

On the enhancement of future gravitational wave laser interferometers and the prospects of probing macroscopic quantum mechanics

Von der Fakultät für Mathematik und Physik

der Gottfried Wilhelm Leibniz Universität Hannover

zur Erlangung des Grades

Doktor der Naturwissenschaften

Dr. rer. nat.

genehmigte Dissertation

von

Dipl. Phys. Henning Rehbein

geboren am 24.07.1978 in Hannover

2009

Referent: Prof. R. Schnabel
Korreferent: Prof. K. Danzmann
Tag der Promotion: 05.12.2008

Abstract

The first generation of a global network of laser interferometric gravitational wave detectors is already in operation. These projects aim at the first direct observation of gravitational wave radiation. The anticipated sensitivity of future detectors might provides an opportunity to open up an entirely new field of gravitational wave astronomy, the key to a deeper understanding of the structure and formation of our universe.

The first part of this thesis deals with potential upgrades for the second generation of observatories, which is currently underway. An innovative concept is elaborated, based on splitting the input laser light into distinct parts. From the resulting modification of the quantum noise budget emerge essentially new physical properties of the detector. It is shown that an appropriate adjustment of directly accessible parameters of the interferometer allows a combination of the signal-recycling and the optical bar scheme. The conjunction of these complementary technologies leads to a significantly improved sensitivity. Further, it is verified that a multi-carrier configuration can be stabilized by the implementation of a feedback control system, which does not affect the noise spectral density in the ideal case. But in practice such a technical component is susceptible to classical noise. An additional investigation aims at the exploitation of multiple carrier fields for an all-optical stabilization scheme. The proposed arrangement is also suitable for compensating certain drawbacks of the signal-recycling technique, which entails a considerable improvement of sensitivity. An intrinsic advantage of all multi-carrier configurations is the increased number of degrees of freedom which can be used for a flexible optimization of the detector for different gravitational wave sources. This is confirmed by a numerical optimization, taking into account a currently estimated classical noise budget of second generation gravitational wave detectors, as well as a more optimistic scenario. In addition, compatibility with other well-known advanced technologies is clarified. These explorations prove the sustainability of the newly developed techniques, i.e. future generations of detectors can also benefit from the concepts presented within the scope of this work.

The second part of this thesis comprises a theoretical basis for testing quantum mechanics in the macroscopic world. It is demonstrated that the presence of realistic decoherence processes, i.e. multiple colored classical noise sources, does not prohibit engineering states of macroscopic objects with nearly vanishing quantum mechanical entropy. A newly developed treatment of a conditional measurement process allows a continuous extraction of information from a realistic system, which represses environmental influences. This concept paves the way for the preparation of entangled states involving either one or two macroscopic parts. During a subsequent free evolution stage, the environment irreversibly disturbs the quantum state. But it persists on short time scales and hence is available for further measurements. The proposed experiments constitute an essential test of quantum mechanics and would push the realm of fascinating quantum physics into the macroscopic world.

Keywords: gravitational wave detector, interferometry, entanglement, macroscopic quantum mechanics

Kurzfassung

Die erste Generation eines weltumspannenden Netzwerks von interferometrischen Gravitationswellendetektoren ist bereits in Betrieb. Diese Projekte sollen den ersten direkten Nachweis der von Albert Einstein 1915 im Rahmen der allgemeinen Relativitätstheorie vorhergesagten Gravitationswellen erbringen. Zukünftige Detektoren könnten durch eine verbesserte Sensitivität eine Gravitationswellen-Astronomie ermöglichen und damit neue Einblicke in die Entstehung und Beschaffenheit unseres Universums bieten.

Der erste Teil dieser Arbeit behandelt potentielle Erweiterungen für die sich im Bau befindliche zweite Generation von Observatorien. Ein vorgestelltes innovatives Konzept basiert auf der Aufteilung des verwendeten Laserlichtes in leicht separierbare Anteile. Dieses erlaubt eine Modellierung und Optimierung der fundamentalen Quanteneffekte, wodurch essentiell neue physikalische Eigenschaften des Detektors hervortreten können. Durch Abstimmung unmittelbar zugänglicher Parameter können die Signal-Recycling Technik und die optische Realisierung von Webers Resonanzantenne in einer Topologie vereinigt werden. Das Zusammenspiel dieser komplementären Technologien kann zu einer signifikanten Steigerung der Empfindlichkeit führen. Es wird belegt, dass ein verlustfreies Kontrollsystem zur Stabilisierung des Interferometers eingesetzt werden kann, ohne die Sensitivität zu beeinflussen. Allerdings ist diese technische Komponente hinsichtlich der Einkopplung klassischen Rauschens als kritisch einzustufen. Im Rahmen einer weiteren Untersuchung werden die zur Verfügung stehenden Eingangsfelder für eine rein optische Stabilisierung des Systems ausgenutzt. Diese Methode kann parallel dazu verwendet werden, bekannte Nachteile der Signal-Recycling Technik auszugleichen und somit die Empfindlichkeit zu verbessern. Ein intrinsischer Vorteil der Verwendung von multiplen Eingangsfeldern ist die erhöhte Anzahl von Freiheitsgraden, die eine flexible Anpassung der Sensitivität des Detektors an verschiedenartige Quellen von Gravitationswellen erlauben. Eine numerische Optimierung bestätigt dieses, wobei neben dem zu erwartenden klassischen Rauschen eines Detektors der zweiten Generation ein optimistischeres Szenarium berücksichtigt wird. Weiterhin wird die Kompatibilität zu anderen bekannten fortschrittlichen Technologien verifiziert. Dadurch wird demonstriert, dass weitere Generationen von Detektoren ebenfalls von den im Rahmen dieser Arbeit vorgestellten Konzepten profitieren können.

Im zweiten Teil der Arbeit wird eine theoretische Grundlage entwickelt, die den Nachweis quantenmechanischer Phänomene auch an makroskopisch schweren Objekten ermöglicht. Erstmals wird gezeigt, dass Zustände präpariert werden können, die eine nahezu verschwindende quantenmechanische Entropie aufweisen, obgleich das jeweilige makroskopische Objekt realistischen Dekohärenzprozessen ausgesetzt ist. Mit Hilfe einer neu entwickelten Methode zur Beschreibung einer konditionierten Messung kann dem entsprechenden System kontinuierlich Information entzogen werden, wodurch der von der Umgebung induzierten Dekohärenz effizient entgegengewirkt wird. Auf der Grundlage dieses Konzeptes wird demonstriert, dass verschränkte Zustände zwischen zwei Systemen erzeugt werden können, wobei ein oder beide involvierten Komponenten makroskopischer Natur sein können. Es zeigt sich, dass nach Abschluss der Präparationsphase der jeweilige quantenmechanische Zustand irreversibel durch die Wechselwirkung mit der Umgebung verändert wird. Dennoch ist es auf kurzen Zeitskalen möglich, den präparierten Zustand weiter zu beobachten. Die vorgeschlagenen Experimente erlauben einen grundlegenden Test der Quantenmechanik und würden erstmals die verblüffenden Paradoxien der Quantenwelt anhand von makroskopisch schweren Objekten demonstrieren.

Stichworte: Gravitationswellendetektor, Interferometrie, Verschränkung, makroskopische Quantenmechanik

Contents

Abstract	i
Kurzfassung	iii
List of abbreviations	ix
1. Introduction	1
2. Fundamentals	3
2.1. Quantized electromagnetic field	3
2.1.1. Maxwell's equations	3
2.1.2. Field quantization	4
2.2. Michelson interferometer	12
2.3. Characterizing optical systems	13
2.3.1. Mathematical framework	14
2.3.2. Linear quantum measurement theory	20
2.3.3. Linear response function	21
2.3.4. Equations of motion	24
2.3.5. Measurement process	30
2.3.6. Quantum Langevin equation	34
2.3.7. Cavity modes	37
2.3.8. Adiabatic elimination	39
3. Gravitational wave spectrum	41
3.1. Detector optimization for binary sources	42
3.2. Broadband optimization	43
3.3. Limitations of detector optimization	44
4. Advanced interferometer concepts	45
4.1. Multi-carrier interferometer	46
4.1.1. Independent carriers	47
4.1.2. Transfer functions	48
4.1.3. Optimal filter functions	51
4.2. Local readout scheme	55
4.2.1. Dynamics, sensing and control	57
4.2.2. Example configurations	59
4.2.3. Implementation issues	67
4.2.4. Combination with advanced technologies	69
4.2.5. Conclusion	71
4.3. Double optical spring interferometer	72

4.3.1. Classical dynamics	74
4.3.2. Dynamics and sensing	78
4.3.3. Example configurations	78
4.3.4. Additional local readout scheme	85
4.3.5. Conclusion	88
4.4. Kerr enhanced interferometer	89
4.4.1. Kerr transfer function	89
4.4.2. Kerr interferometer	93
4.5. Kerr squeezing source	102
4.5.1. Squeezed light	102
4.5.2. Kerr squeezing	102
5. Towards the preparation of macroscopic quantum states	107
5.1. Review of recent experimental results	108
5.2. State preparation with a Michelson interferometer	109
5.2.1. Markovian quantum noise	110
5.2.2. Non-Markovian quantum noise	111
5.2.3. Comment on measured degree of freedom	111
5.3. Gaussian states	112
5.4. Measure of quantumness	114
5.5. Measure of entanglement	115
5.5.1. Non-separability	117
5.5.2. Einstein-Podolsky-Rosen-entanglement	119
5.6. Conditional states	120
5.6.1. Stochastic master equation	121
5.6.2. Quantum Wiener filter	125
5.6.3. State preparation in presence of Markovian noise	130
5.7. Classical control	131
5.7.1. Conditioning and feedback control	131
5.7.2. Controlled states	131
5.8. State Preparation in presence of non-Markovian noise	133
5.8.1. Tuned cavity	134
5.8.2. Detuned cavity	138
5.8.3. Example configuration	139
5.8.4. Optomechanical entanglement	143
5.9. Entanglement of macroscopic test masses	147
5.9.1. Relation between entanglement and SQL	148
5.9.2. Time evolution	150
5.9.3. Non-Markovian noise	152
5.10. Outlook	152
6. Summary and outlook	155
A. Program codes	159
B. Promotion for conditional measurement	167

Bibliography	169
Acknowledgements	181
Curriculum vitae	183
Publications	185

List of abbreviations

BS	beam splitter
BB	broadband
DOS	double optical spring
EPR	Einstein, Podolski, Rosen
ETM	end test mass mirror
GW	gravitational wave
h.c.	hermitian conjugate
ITM	input test mass mirror
LIGO	laser interferometer gravitational wave observatory
LR	local readout
NB	narrowband
QND	quantum non-demolition
RTM	reference test mass mirror
SNR	signal-to-noise ratio
SQL	standard quantum limit
SR	signal-recycling
w.l.o.g.	without loss of generality

1. Introduction

In the year 1881 the physicist Albert Abraham Michelson developed an optical arrangement which is known today as the Michelson interferometer. The original version of this instrument comprises a light source, two mirrors and a beam splitter. An incident beam of light is split into two parts and each part travels a certain distance before it is reflected back by a mirror. After recombining the beams at the beam splitter, a pattern of constructive and destructive interference, influenced by the difference in length of the arms, is produced at the output port. Michelson improved his device and conducted an aether drift experiment in 1887 – the famous Michelson-Morley experiment. The disproof of the aether theory established an important basis for the development of Albert Einstein’s special relativity theory. In 1915, Einstein published an extension of this theory, known as the general relativity theory, which predicts, among other things, the existence of gravitational waves. Beginning in the mid-1970s, it was realized that the differential length change induced by a gravitational wave is ideally measured by an interferometer of the Michelson-type. A major effort was put into the design of new techniques and the precision of interferometric devices was increased by orders of magnitude. Today’s long-baseline laser interferometric gravitational wave observatories have reached their design sensitivities (e.g. $\sqrt{S_x} \sim 2 \times 10^{-23}/\sqrt{\text{Hz}}$ at 150 Hz for the 4 km initial LIGO interferometer [104]) and the first direct observation of gravitational waves is expected shortly. Currently planned second generation gravitational wave laser interferometers such as Advanced LIGO will start operation around 2014. This detector will be nearly quantum noise limited in most of its frequency band (10 Hz to 10 kHz), and it will operate near or at the standard quantum limit, a well-known reference limit for high precision measurements. This limit is enforced when the two fundamental quantum noise contributions – shot noise and radiation pressure noise – are uncorrelated, while it can be surpassed if the two sources exhibit appropriate correlations. The required correlations can, for instance, be established by the injection of non-classical light, modifications of the readout scheme or employing alternative optical configurations. We exploit such techniques for the design of innovative concepts for interferometric gravitational wave detectors in Chap. 4. Our proposed schemes are motivated by the expeditious progress in the development of second generation gravitational wave detectors and they can be regarded as possible upgrades for these forthcoming observatories. The sustainability of the introduced concepts also opens up the possibility of an implementation in third generation detectors. The expected sensitivity of the higher generation antennas allows us to venture out into the field of gravitational wave astronomy, which could potentially give us an amazing insight into the origins of our universe.

In the second part of this theses (Chap. 5), we divert these powerful instruments from their intended use. We exploit strategies aiming at approaching or surpassing the standard quantum limit for the preparation of macroscopic quantum states. The fundamental framework of quantum mechanics was established during the first half of the twentieth

century and various prominent physicists contributed to the development of this theory. The theory was initially worked out in order to provide a better description of effects associated with atoms and light. It was for a long time believed that it is not possible to observe quantum mechanical states of everyday-sized objects, due to the ubiquitous presence of decoherence processes. The natural environment interacts with the object under consideration and perturbs its motion in a thermodynamically irreversible way. The entropy inevitably increases and the system is driven away from a true minimum Heisenberg uncertainty state. An attempt to counteract this effect is based on introducing a strong mechanical damping, in order to repress the environmental influence, i.e. the system is effectively cooled. Such a damping force can be realized in different ways, for instance by the implementation of a feedback control system. This was demonstrated by a recent experiment involving the initial LIGO gravitational wave detector. The eigenfrequency of its suspended mirrors was shifted from 1 Hz up to 140 Hz by a feedback control system. Subsequently the control system was so adjusted that the mechanical mode was damped and a final occupation number of ~ 200 was achieved for the kg-scale oscillator. This result reveals that the test masses in current gravitational wave detectors are still far from a true minimum Heisenberg uncertainty state. But the possibility of a reduced classical noise budget in future detectors motivates our investigation of novel concepts for experiments aiming at probing the quantum nature of macroscopic objects. If we succeed in preparing a state close to the limit set by the Heisenberg uncertainty, it can be used for engineering entangled states involving a single or two macroscopic parts. Such a demonstration of the fascinating phenomena of quantum physics within the realm of the everyday world is a mandatory test of quantum mechanics.

2. Fundamentals

Any physical theory is derived from a small set of basic principles which are taken for granted. A theory should be capable of producing experimental predictions for a certain physical system. The major part of this thesis is based on the theory of classical electromagnetism, widely accepted and described by Maxwell's equations. This theory was consistently and successfully reconciled for more than a century. Only the classical theory is not sufficient for the description of certain phenomena investigated within the scope of this thesis and therefore a quantization of Maxwell's equations is required.

First we derive an expression for the quantized electromagnetic field in terms of the two-photon creation and annihilation operators, which can simultaneously annihilate a photon at frequency $\omega_0 \pm \Omega$ while creating one at frequency $\omega_0 \mp \Omega$. The formalism for two-photon quantum optics was developed by Caves and Schumaker in Ref. [44] and it provides a suitable tool for calculating the propagation of modulation sideband fields within complex optical systems. In practice, such systems are divided into fundamental components, each characterized by a simple linear transfer function in the frequency domain, as discussed in Sec. 2.3.1.

The interferometric configurations considered here can also be regarded as linear quantum measurement devices, which suggests that the force susceptibility formalism of linear quantum measurements applies (cf. Ref. [27]). This formalism is used throughout the thesis at hand, which motivates a detailed review in Sec. 2.3.2.

It is also common to treat optical systems by the quantum Langevin equation, briefly reviewed in Sec. 2.3.6. It is shown that the three formalisms are closely related and describe exactly the same physics.

2.1. Quantized electromagnetic field

2.1.1. Maxwell's equations

The differential form of Maxwell's equations in terms of free charges and currents (see e.g. Ref. [99]) are given in vector form by (SI units):

$$\nabla \cdot \mathbf{B} = 0, \quad (2.1)$$

$$\nabla \cdot \mathbf{D} = \rho, \quad (2.2)$$

$$\nabla \times \mathbf{E} = -\frac{\partial \mathbf{B}}{\partial t}, \quad (2.3)$$

$$\nabla \times \mathbf{H} = \mathbf{J} + \frac{\partial \mathbf{D}}{\partial t}, \quad (2.4)$$

where \mathbf{B} denotes the magnetic field, \mathbf{H} the magnetic induction, \mathbf{E} the electric field, \mathbf{D} the dielectric displacement, \mathbf{J} the free currents in the material and ρ the free charges in the material. Within the framework of this thesis, we primarily consider free electromagnetic

fields, which implies the following simplifications: $\rho = 0$, $\mathbf{J} = 0$, $\mathbf{B} = \mu_0 \mathbf{H}$ and $\mathbf{E} = \mathbf{D}/\epsilon_0$, where μ_0 is the magnetic permeability and ϵ_0 the electric permittivity of the free space, respectively, which obey the relation $\mu_0 \epsilon_0 = c^{-2}$. The electromagnetic field can be expressed in terms of a vector potential \mathbf{A} and a scalar potential ϕ :

$$\mathbf{B} = \nabla \times \mathbf{A}, \quad \mathbf{E} = -\nabla \phi - \frac{\partial \mathbf{A}}{\partial t}. \quad (2.5)$$

There is no unique set of potentials specifying a given electric and magnetic field, since an appropriate gauge transformation does not change the measurable fields. By employing the Coulomb gauge, which is defined by $\nabla \times \mathbf{A} = 0$ and $\phi = 0$, we obtain:

$$\mathbf{B} = \nabla \times \mathbf{A}, \quad \mathbf{E} = -\frac{\partial \mathbf{A}}{\partial t}. \quad (2.6)$$

Now we can deduce a wave equation by substituting Eqs. (2.6) into Eqs. (2.1)-(2.4):

$$\nabla^2 \mathbf{A}(\mathbf{x}, t) = \frac{1}{c^2} \frac{\partial^2 \mathbf{A}(\mathbf{x}, t)}{\partial t^2}. \quad (2.7)$$

2.1.2. Field quantization

Since many aspects associated with the electromagnetic field cannot be described by means of a classical theory, e.g. the double-slit experiment, a quantum mechanical description is required. The quantized electromagnetic field can be obtained by a procedure widely used in literature (cf. e.g. Refs. [81, 166]) which is reviewed in the following.

The vector potential $\mathbf{A}(\mathbf{x}, t)$ can be decomposed into two complex terms

$$\mathbf{A}(\mathbf{x}, t) = \mathbf{A}^{(+)}(\mathbf{x}, t) + \mathbf{A}^{(-)}(\mathbf{x}, t), \quad (2.8)$$

where $\mathbf{A}^{(+)}(\mathbf{x}, t) = (\mathbf{A}^{(-)}(\mathbf{x}, t))^*$ contains all amplitudes which vary as $e^{-i\omega t}$ and $\mathbf{A}^{(-)}(\mathbf{x}, t)$ contains all amplitudes which vary as $e^{i\omega t}$ (we assume $\omega > 0$). It is convenient to deal with a discrete set of variables and extend the discussion to the whole continuum afterwards. For a field restricted to a certain volume, we can expand the vector potential in terms of a discrete set of orthogonal mode functions:

$$\mathbf{A}^{(+)}(\mathbf{x}, t) = \sum_k c_k \mathbf{u}_k(\mathbf{x}) e^{-i\omega_k t}, \quad (2.9)$$

where the Fourier coefficients c_k are constant in the case of a free field. The set of mode functions $\mathbf{u}_k(\mathbf{x})$ is usually determined by physical constraints. Since the volume considered here contains no refractive materials, a mode function corresponding to a frequency ω_k has to satisfy the equation

$$\left(\nabla^2 + \frac{\omega_k^2}{c^2} \right) \mathbf{u}_k(\mathbf{x}) = 0 \quad (2.10)$$

within the volume under consideration. Independent of certain boundary conditions, we assume that the mode functions form a complete orthonormal set

$$\int_V (\mathbf{u}_i(\mathbf{x}))^\dagger \cdot \mathbf{u}_j(\mathbf{x}) d\mathbf{x} = \delta_{ij} \quad (2.11)$$

and also satisfy the transversality condition

$$\nabla \cdot \mathbf{u}(\mathbf{x}) = 0. \quad (2.12)$$

Hence the plane wave mode functions inside a cubic volume $V = L_x L_y L_z$ can be written as

$$\mathbf{u}_k(\mathbf{x}) = \frac{1}{\sqrt{V}} \hat{\mathbf{e}}^{(\lambda)} \exp(i\mathbf{k}^T \cdot \mathbf{x}), \quad (2.13)$$

where $\hat{\mathbf{e}}^{(\lambda)}$ is the unit polarization vector. The index k represents an abbreviation for several discrete variables, i.e. the polarization index ($\lambda = 1, 2$) and the three Cartesian components of the propagation vector \mathbf{k} . The polarization vector must be orthogonal to the propagation vector, which directly follows from Eq. (2.12). The propagation vector takes the form

$$\mathbf{k}^T \equiv (k_x \quad k_y \quad k_z) = (2\pi n_x/L_x \quad 2\pi n_y/L_y \quad 2\pi n_z/L_z), \quad (2.14)$$

with $n_x, n_y, n_z \in \mathbb{Z}$. From Eq. (2.10) we can deduce the relation $\omega_k = c|\mathbf{k}_k|$, which allows us to re-write the vector potential as:

$$\mathbf{A}(\mathbf{x}, t) = \sum_k \left(\frac{\hbar}{2\omega_k \epsilon_0 V} \right)^{1/2} \hat{\mathbf{e}}^{(\lambda)} \left[a_k e^{-i\omega_k t + i\mathbf{k}^T \cdot \mathbf{x}} + a_k^\dagger e^{i\omega_k t - i\mathbf{k}^T \cdot \mathbf{x}} \right], \quad (2.15)$$

where the constant normalization factor is so chosen that the pair of complex conjugate amplitudes a_k and a_k^\dagger are dimensionless. These Fourier amplitudes are complex numbers which can be chosen arbitrarily, but they remain constant in time for a free field. In quantum theory, these Fourier amplitudes are associated with mutually adjoint operators. These operators also remain constant and correspond to the annihilation and creation Schrödinger operators, obeying the well-known boson commutation relations, i.e.

$$[\hat{a}_k, \hat{a}_{k'}] = [\hat{a}_k^\dagger, \hat{a}_{k'}^\dagger] = 0 \quad [\hat{a}_k, \hat{a}_{k'}^\dagger] = \delta_{kk'}. \quad (2.16)$$

The (quantum) electric and magnetic field can easily be obtained from Eq. (2.15):

$$\hat{\mathbf{E}}(\mathbf{x}, t) = i \sum_k \left(\frac{\hbar \omega_k}{2\epsilon_0 V} \right)^{1/2} \hat{\mathbf{e}}^{(\lambda)} \left[\hat{a}_k e^{-i\omega_k t + i\mathbf{k}^T \cdot \mathbf{x}} - \hat{a}_k^\dagger e^{i\omega_k t - i\mathbf{k}^T \cdot \mathbf{x}} \right], \quad (2.17)$$

$$\hat{\mathbf{H}}(\mathbf{x}, t) = i \frac{1}{\mu_0} \sum_k \left(\frac{\hbar}{2\epsilon_0 V \omega_k} \right)^{1/2} (\mathbf{k} \times \hat{\mathbf{e}}^{(\lambda)}) \left[\hat{a}_k e^{-i\omega_k t + i\mathbf{k}^T \cdot \mathbf{x}} - \hat{a}_k^\dagger e^{i\omega_k t - i\mathbf{k}^T \cdot \mathbf{x}} \right]. \quad (2.18)$$

The normalization constant

$$E_0 = \sqrt{\frac{\hbar \omega_k}{2\epsilon_0 V}} \quad (2.19)$$

corresponds to the "electric field per photon". So far, only a finite volume has been considered. The transition to an infinite quantization volume can be accomplished as follows: for $L_x, L_y, L_z \gg 1$, the sum over discrete indices can be replaced by an integral:

$$\sum_k \rightarrow \frac{V}{(2\pi)^3} \sum_\lambda \int d^3\mathbf{k}. \quad (2.20)$$

Quantized beam of light

In the following, only ideal laser beams interacting with optical components will be taken into account. An ideal laser beam is confined to a single dimension and we assume that it propagates w.l.o.g. along the x -axis. The interaction processes considered here are not sensible to polarization, which can therefore be fixed arbitrarily. For a single dimension, the transition to an infinite quantization volume can be accomplished by the substitution [cf. Eq. (2.20)]:

$$\sum_k \rightarrow \frac{L_x}{2\pi} \int dk_x \equiv \frac{L_x}{2\pi c} \int d\omega, \quad (2.21)$$

where the integration variable has been changed from the propagation vector to the optical frequency in the second step. Consequently the electric field can be written as

$$\hat{E}(t, x) = i\sqrt{\frac{L_x}{c}} \left(\frac{L_x}{2\epsilon_0 V c} \right)^{1/2} \int_0^\infty \frac{d\omega}{2\pi} \sqrt{\hbar\omega} \left[\hat{a}(\omega) e^{-i\omega(t-x/c)} - \hat{a}^\dagger(\omega) e^{i\omega(t-x/c)} \right]. \quad (2.22)$$

After defining the cross-sectional area of the beam $\mathcal{A} = V/L_x$ and performing the replacement $i\sqrt{L_x/c} \hat{a}(\omega) \rightarrow \hat{a}(\omega)$, we obtain

$$\hat{E}(t, x) = \sqrt{\frac{1}{2\epsilon_0 \mathcal{A} c}} \int_0^\infty \frac{d\omega}{2\pi} \sqrt{\hbar\omega} \left[\hat{a}(\omega) e^{-i\omega(t-x/c)} + \hat{a}^\dagger(\omega) e^{i\omega(t-x/c)} \right]. \quad (2.23)$$

In the gravitational wave community, it is very common to write this equation in cgs units. It can be converted by using the substitution $\hat{E}(t) \rightarrow \hat{E}(t)/\sqrt{4\pi\epsilon_0}$ (see e.g. Ref. [99]):

$$\hat{E}(t, x) = \sqrt{\frac{2\pi}{\mathcal{A} c}} \int_0^\infty \frac{d\omega}{2\pi} \sqrt{\hbar\omega} \left[\hat{a}(\omega) e^{-i\omega(t-x/c)} + \hat{a}^\dagger(\omega) e^{i\omega(t-x/c)} \right]. \quad (2.24)$$

Note that the annihilation and creation operators now have the dimension of square of time ($\sqrt{\text{sec}}$) and the well-known commutation relation reads

$$[\hat{a}(\omega), \hat{a}^\dagger(\omega')] = 2\pi\delta(\omega - \omega'). \quad (2.25)$$

The electric field operator in Eq. (2.24) has an explicit time dependence and must be regarded as a Heisenberg operator. The representation of the electric field in cgs units serves as the basis for following discussions.

The Hamiltonian can be obtained from the classical expression for the energy of the electromagnetic field via the correspondence principle and it is given by

$$\hat{H} =: \frac{1}{8\pi} \int d\mathbf{x} \left(\hat{E}^2(\mathbf{x}, t) + \hat{H}^2(\mathbf{x}, t) \right) :, \quad (2.26)$$

where $: \ :$ denotes a normal ordering of the operators. Normal ordering is one recipe for deriving the quantized energy. But no unique mapping exists from the classical world to the quantum world and the only way to justify a certain quantization prescription is to check if the quantum theory is able to make accurate predictions. Naturally, there cannot exist a unique mapping, as otherwise one could already figure out all the quantum properties of a system by studying its classical properties!

The Hamiltonian given in Eq. (2.26) can be simplified to

$$\hat{H}_0 = \int_0^\infty \frac{d\omega}{2\pi} \hbar\omega \hat{a}^\dagger(\omega) \hat{a}(\omega) \quad (2.27)$$

in the case of a beam propagating in one dimension. Since the Hamiltonian is time-independent, the conversion of the electric field provided in Eq. (2.24) into the Schrödinger picture can be accomplished by a simple transformation:

$$\hat{E}(x) = e^{-i\hat{H}_0 t} \hat{E}(x, t) e^{i\hat{H}_0 t} \quad (2.28)$$

$$\Leftrightarrow \hat{E}(x) = \sqrt{\frac{2\pi}{\mathcal{A}c}} \int_0^\infty \frac{d\omega}{2\pi} \sqrt{\hbar\omega} \left[\hat{a}(\omega) e^{i\omega x/c} + \hat{a}^\dagger(\omega) e^{-i\omega x/c} \right]. \quad (2.29)$$

However, the creation and annihilation operators are fixed in time. In the case of the Heisenberg representation [cf. Eq. (2.24)] of the electric field, the time dependence has been explicitly factored out. Great importance is attached to the field amplitudes \hat{a} and \hat{a}^\dagger , since most of this thesis deals with the transformation of these amplitudes and not the transformation of the electric field itself.

Modulation picture

Eq. (2.24) is a continuum multi-mode description of the electric field and every mode is excited independently. But some optical devices, such as parametric amplifiers or gravitational wave detectors, can produce a pair of modes at frequencies $\omega_0 \pm \Omega$ simultaneously. For such applications, it is convenient to describe the field in terms of the two-photon formalism introduced by Caves&Schumaker in Ref. [44]. This approach deals with annihilation and creation operators creating simultaneously a photon at $\omega_0 + \Omega$ and annihilating a photon at $\omega_0 - \Omega$ or vice versa. The Heisenberg representation of the electric field [cf. Eq. (2.24)] can be re-written at a fixed point on the optical axis:

$$\hat{E}(t) = \sqrt{\frac{2\pi\hbar\omega_0}{\mathcal{A}c}} e^{-i\omega_0 t} \left(\int_0^\infty \frac{d\Omega}{2\pi} \hat{a}_+ e^{-i\Omega t} + \int_0^{\omega_0} \frac{d\Omega}{2\pi} \hat{a}_- e^{i\Omega t} \right) + \text{h.c.}, \quad (2.30)$$

where h.c. denotes the hermitian conjugate and the new operators occurring in Eq. (2.30) are defined by:

$$\hat{a}_+ = \hat{a}(\omega_0 + \Omega) \sqrt{1 + \frac{\Omega}{\omega_0}}, \quad \hat{a}_- = \hat{a}(\omega_0 - \Omega) \sqrt{1 - \frac{\Omega}{\omega_0}}. \quad (2.31)$$

Note that this decomposition of the electric field is still exactly equivalent to Eq. (2.24). From the relation given in Eq. (2.25) the following non-vanishing commutation relations can be deduced:

$$[\hat{a}_+, \hat{a}_{+'}^\dagger] = 2\pi\delta(\Omega - \Omega') \left(1 + \frac{\Omega}{\omega_0} \right), \quad [\hat{a}_-, \hat{a}_{-'}^\dagger] = 2\pi\delta(\Omega - \Omega') \left(1 - \frac{\Omega}{\omega_0} \right), \quad (2.32)$$

where $\hat{a}_{\pm'}$ accounts for $\hat{a}(\omega_0 \pm \Omega') \sqrt{1 \pm \Omega'/\omega_0}$. In principle it is possible to treat arbitrary sideband frequencies within the framework of the two-photon formalism. But current photo detectors are only qualified for the detection of modulation fields at frequencies

much smaller than the carrier frequency ($\omega_0 \approx 10^{15}$ Hz). In the case of gravitational wave detectors, the relevant information is stored in modulation fields at frequencies $\Omega \approx 10 \dots 1000$ Hz and hence it is reasonable to neglect terms proportional to $\Omega/\omega_0 \ll 1$. It can be shown that this approximation does not affect the final noise spectral densities calculated later (cf. also Ref. [36]). This approximation allows us to extend the integration in Eq. (2.30) from ω_0 to infinity, i.e.

$$\hat{E}(t) = \sqrt{\frac{2\pi\hbar\omega_0}{\mathcal{A}c}} e^{-i\omega_0 t} \int_0^\infty \frac{d\Omega}{2\pi} [\hat{a}_+ e^{-i\Omega t} + \hat{a}_- e^{i\Omega t}] + \text{h.c.} . \quad (2.33)$$

The quadrature field amplitudes of the two-photon modes can then be defined as

$$\hat{a}_1 = \frac{\hat{a}_+ + \hat{a}_-^\dagger}{\sqrt{2}}, \quad \hat{a}_2 = \frac{\hat{a}_+ - \hat{a}_-^\dagger}{\sqrt{2}i} \quad (2.34)$$

according to the Caves&Schumaker formalism [44] and the only non-vanishing commutation relation is given by

$$[\hat{a}_1, \hat{a}_{2'}^\dagger] = -[\hat{a}_2, \hat{a}_{1'}^\dagger] = 2\pi\delta(\Omega - \Omega') . \quad (2.35)$$

It is convenient to combine the quadrature field amplitudes in a vector:

$$\hat{\mathbf{a}} = \begin{pmatrix} \hat{a}_1 \\ \hat{a}_2 \end{pmatrix} . \quad (2.36)$$

Again, the electric field in Eq. (2.33) can be re-written, now in terms of the quadrature phases:

$$\hat{E}(t) = \cos(\omega_0 t) \hat{E}_1(t) + \sin(\omega_0 t) \hat{E}_2(t) , \quad (2.37)$$

where the hermitian quadrature phases $\hat{E}_1(t)$, $\hat{E}_2(t)$ depend on the quadrature field amplitudes:

$$\hat{E}_k(t) = \sqrt{\frac{4\pi\hbar\omega_0}{\mathcal{A}c}} \int_0^\infty \frac{d\Omega}{2\pi} [\hat{a}_k e^{-i\Omega t} + \hat{a}_k^\dagger e^{i\Omega t}] \equiv \sqrt{\frac{4\pi\hbar\omega_0}{\mathcal{A}c}} \int_{-\infty}^\infty \frac{d\Omega}{2\pi} \hat{a}_k e^{-i\Omega t} . \quad (2.38)$$

Note that Eq. (2.38) only describes the quantum part of the electric field. A superposition with a monochromatic classical carrier field with real amplitude Λ and frequency ω_0 gives an extra contribution of $E_c = \Lambda \cos(\omega_0 t - \theta)$. Hence the total electric field reads:

$$\hat{E}(t) = \cos(\omega_0 t) (\hat{E}_1(t) + \Lambda \cos(\theta)) + \sin(\omega_0 t) (\hat{E}_2(t) + \Lambda \sin(\theta)) , \quad (2.39)$$

where θ denotes the phase of the carrier field. As done in Ref. [86] a vector space spanned by basis vectors $\cos(\omega_0 t)$ and $\sin(\omega_0 t)$ can be defined, which allows us to write Eq. (2.39) as

$$\hat{\mathbf{E}}(t) \equiv \underbrace{\begin{pmatrix} \hat{E}_1(t) \\ \hat{E}_2(t) \end{pmatrix}}_{\hat{\mathbf{E}}^{sb}(t)} + \Lambda \underbrace{\begin{pmatrix} \cos(\theta) \\ \sin(\theta) \end{pmatrix}}_{\mathbf{E}^c(t)} . \quad (2.40)$$

A scalar product can then be defined by averaging over time. Since the measurement time τ is much longer compared to an oscillation period of the carrier field ($\tau \gg \omega_0^{-1}$), we can write:

$$\begin{aligned} (\hat{\mathbf{E}}^{sb}(t))^2 &= \hat{E}_1(t) \cos^2(\omega_0 t) + 2\hat{E}_1(t)\hat{E}_2(t) \cos(\omega_0 t) \sin(\omega_0 t) + \hat{E}_2(t) \sin^2(\omega_0 t) \\ &\approx \hat{E}_1^2(t)/2 + \hat{E}_2^2(t)/2, \end{aligned} \quad (2.41)$$

or for the total field given in Eq. (2.39) we find:

$$\hat{\mathbf{E}}^2(t) \approx \Lambda^2/2 + \hat{E}_1^2(t)/2 + \hat{E}_2^2(t)/2 + \Lambda(\hat{E}_1(t) \cos(\theta) + \hat{E}_2(t) \sin(\theta)). \quad (2.42)$$

Properties of the electric field

Special attention is to be paid in the following to certain properties of the electric field, which are important for the subsequent investigations. The energy flux of the electric field is given by the Poynting vector

$$\mathbf{S} = \frac{c}{4\pi} \mathbf{E} \times \mathbf{H} \quad (2.43)$$

which has the dimension energy/(area · time). In our case, only free fields are considered and hence the Poynting vector simplifies to

$$\hat{S} \equiv |\hat{\mathbf{S}}| = \frac{c}{4\pi} \hat{\mathbf{E}}^2(t). \quad (2.44)$$

By employing the time-averaged relation provided in Eq. (2.42), we obtain

$$P = \mathcal{A}S = \frac{\mathcal{A}c}{8\pi} \Lambda^2, \quad (2.45)$$

where we have neglected the quantum part. Hence we can express the amplitude of the classical field in terms of the optical power P :

$$\Lambda = \sqrt{\frac{8\pi P}{\mathcal{A}c}}. \quad (2.46)$$

This allows us to define a "carrier quadrature field" in the following way:

$$\mathbf{D}_j \equiv \sqrt{\frac{\mathcal{A}c}{4\pi}} \mathbf{E}^c = \sqrt{2P_j} \begin{pmatrix} \cos(\theta_j) \\ \sin(\theta_j) \end{pmatrix} \quad (2.47)$$

and hence the whole electric field can be written in terms of quadrature field vectors

$$\hat{\mathbf{a}}_{\text{total}} = \begin{pmatrix} \hat{a}_1 \\ \hat{a}_2 \end{pmatrix} + \sqrt{\frac{2P_a}{\hbar\omega_0}} \begin{pmatrix} \cos(\theta_a) \\ \sin(\theta_a) \end{pmatrix} = \hat{\mathbf{a}} + \frac{1}{\sqrt{\hbar\omega_0}} \mathbf{D}_a, \quad (2.48)$$

which is just the Fourier transform of Eq. (2.40). From the Maxwell energy tensor follows the momentum flow

$$\dot{\hat{p}}_{\text{total}}(t) = \frac{\mathcal{A}}{4\pi} \hat{\mathbf{E}}(t)^2 \quad (2.49)$$

carried by the field. In our case only the quantum part amplified by the classical carrier amplitude is to be taken into account:

$$\dot{\hat{p}}(t) = \Lambda \left(\hat{E}_1(t) \cos(\theta) + \hat{E}_2(t) \sin(\theta) \right) \quad (2.50)$$

and the Fourier transform of the momentum flow reads:

$$\dot{\hat{p}}_j(\Omega) = \sqrt{\frac{\hbar\omega_0}{c^2}} \mathbf{D}_j^T \cdot \hat{\mathbf{j}}(\Omega), \quad (2.51)$$

where $\hat{\mathbf{j}}$ denotes a quadrature field amplitude vector [cf. Eq. (2.36)] and \mathbf{D}_j is the carrier quadrature field [cf. Eq. (2.47)]. We neglect the static (dc) momentum flow associated with the classical carrier field, since it only causes a constant force which does not influence the transfer functions calculated later. Note that the pure quantum part is negligible, since it gives rise to effects beyond the measurable scope.

We aim mainly at the derivation of transfer functions relating the input quadrature field amplitudes to the output quadrature field amplitudes. By employing the relation given in Eq. (2.34) we can convert a linear transformation

$$b_{\pm} = \varphi_{\pm}(\Omega) a_{\pm}(\Omega) \quad \text{with} \quad \varphi_{\pm}(\Omega) \equiv \varphi(\omega_0 \pm \Omega) \quad (2.52)$$

into a transformation of the quadrature field amplitudes:

$$\hat{\mathbf{b}} = \frac{1}{2} \begin{pmatrix} (\varphi_+ + \varphi_-^*) & i(\varphi_+ - \varphi_-^*) \\ -i(\varphi_+ + \varphi_-^*) & (\varphi_+ + \varphi_-^*) \end{pmatrix} \cdot \hat{\mathbf{a}}. \quad (2.53)$$

Free propagation

In order to find a transformation relating the quadrature field operators at distinct locations, we need to compare the electric fields at $(x = 0, t = t_0)$ and $(x = L, t = t_0 + L/c)$. In the absence of losses or refractive media, the electric field at $(x = 0, t = t_0)$ described by the operators \hat{a}_{\pm} should be identical to the electric field at $(x = L, t = t_0 + L/c)$ described by the operators \hat{b}_{\pm} , which leads to the condition [cf. Eq. (2.33)]:

$$\sqrt{\frac{2\pi}{\mathcal{A}c}} e^{-i\omega_0 t_0} \int_0^{\infty} \frac{d\Omega}{2\pi} \sqrt{\hbar\omega_0} [\hat{a}_+ e^{-i\Omega t_0} + \hat{a}_- e^{i\Omega t_0}] \quad (2.54)$$

$$= \sqrt{\frac{2\pi}{\mathcal{A}c}} e^{-i\omega_0(t_0 + L/c)} \int_0^{\infty} \frac{d\Omega}{2\pi} \sqrt{\hbar\omega_0} [\hat{b}_+ e^{-i\Omega(t_0 + L/c)} + \hat{b}_- e^{i\Omega(t_0 + L/c)}], \quad (2.55)$$

from which the linear transformation

$$b_{\pm} = \varphi_{\pm}(\Omega) a_{\pm}(\Omega) \quad \text{with} \quad \varphi_{\pm} = e^{i(\omega_0 \pm \Omega)L/c} \quad (2.56)$$

can be deduced. The transformation of the quadrature fields can be obtained by applying the prescription defined in Eq. (2.53). The matrix for a propagation of the field through a length L is then given by

$$\hat{\mathbf{b}} = e^{i\theta} \mathbf{R}[\phi] \cdot \hat{\mathbf{a}}, \quad (2.57)$$

where $\mathbf{R}[\phi]$ denotes a 2×2 rotation matrix

$$\mathbf{R}[\phi] = \begin{pmatrix} \cos \phi & -\sin \phi \\ \sin \phi & \cos \phi \end{pmatrix} \quad (2.58)$$

and

$$\phi = \frac{\omega_0 L}{c}, \quad \theta = \frac{\Omega L}{c}. \quad (2.59)$$

The rotation angle ϕ (microscopic detuning) corresponds to the phase shift of the carrier light at frequency ω_0 , while θ denotes the phase shift of the modulation sidebands at frequency Ω . Note that the classical carrier quadrature field [cf. Eq. (2.47)] transforms in a different way. A simple rotation relates the classical part of the field at different locations:

$$\mathbf{D}_j \rightarrow \mathbf{R}[\phi] \cdot \mathbf{D}_j. \quad (2.60)$$

Thus a propagation of the total electric field (sideband modulations plus carrier field) requires separate transformations for the two parts of the field.

Coherent and squeezed states

In this thesis, the electric field is described in terms of the two-photon formalism [44]. But before considering two-photon coherent and squeezed states, the one-photon counterparts should be recapitulated. Here we will treat ideal processes, which means that the interaction part of the corresponding Hamiltonian is characterized by a c-number function. Therefore the interaction appears as a generalized classical force acting on the modes of the field. In general, real processes do not exhibit an ideal behavior, e.g. losses and interactions with atoms have to be taken into account. Note that an ideal process does not change the purity of the input state and hence such an interaction does not impurify a minimum uncertainty state.

A coherent state is the closest quantum counterpart to a classical field. It can be regarded as a certain quantum state of a quantum mechanical harmonic oscillator obeying an oscillating behavior similar to a classical harmonic oscillator. Such states are generated from the vacuum state (ground state) by applying the unitary displacement operator:

$$|\alpha\rangle = \hat{D}(\hat{a}, \alpha)|0\rangle \quad \text{with} \quad \hat{D}(\hat{a}, \alpha) = \exp(\alpha\hat{a}^\dagger - \alpha^*\hat{a}). \quad (2.61)$$

It can be easily shown that the generated state is an eigenstate of the annihilation operator

$$\hat{a}|\alpha\rangle = \alpha|\alpha\rangle, \quad (2.62)$$

where α is the complex eigenvalue. If the displacement operator does not act on the vacuum state but on the mode's annihilation operator, one realizes that it is displaced by a c-number, i.e.

$$\hat{D}^\dagger(\hat{a}, \alpha)\hat{a}\hat{D}(\hat{a}, \alpha) = \hat{a} + \alpha. \quad (2.63)$$

A two-photon coherent state can be generated in the following way:

$$|\alpha_+, \alpha_-\rangle = \hat{D}(\hat{a}_+, \alpha_+)\hat{D}(\hat{a}_-, \alpha_-)|0\rangle, \quad (2.64)$$

where $D(\hat{a}_\pm, \alpha_\pm)$ is defined as before in Eq. (2.61) and \hat{a}_\pm corresponds to the annihilation operator for the upper/lower sideband, as introduced in Eq. (2.31). This means that an ideal one-photon process for each of the two modes is involved.

The unitary two-mode squeeze operator is given by

$$\hat{S}(r, \phi_s) = \exp[r(\hat{a}_+\hat{a}_-e^{-2i\phi_s} - \hat{a}_+^\dagger\hat{a}_-^\dagger e^{2i\phi_s})], \quad (2.65)$$

where the real variable r describes the squeezing strength and is therefore called the squeezing factor, while ϕ_s characterizes the squeezing phase. If the two mode squeezing operator acts on the upper or lower mode's annihilation operator, one obtains:

$$\hat{S}^\dagger(r, \phi_s) \hat{a}_\pm \hat{S}(r, \phi_s) = \hat{a}_\pm \cosh(r) + \hat{a}_\mp^\dagger e^{2i\phi_s} \sinh(r). \quad (2.66)$$

We can convert the squeeze operation into a transformation of the quadrature field amplitudes by using Eq. (2.34):

$$\hat{\mathbf{b}} = \begin{pmatrix} \cosh(r) + \sinh(r) \cos(2\phi_s) & \sinh(r) \sin(2\phi_s) \\ \sinh(r) \sin(2\phi_s) & \cosh(r) - \sinh(r) \cos(2\phi_s) \end{pmatrix} \cdot \hat{\mathbf{a}}. \quad (2.67)$$

2.2. Michelson interferometer

The Michelson interferometer was developed by the physicist Albert Abraham Michelson in order to measure the aether wind. The term "aether" was used to describe a medium for the propagation of light. He built a first prototype in 1881 at the Telegraphenberg in Potsdam. Unfortunately this device suffered from various experimental errors and the sensitivity was not sufficient for measuring the aether wind. Later on, in 1887, he built an improved apparatus together with Edward Morley in Cleveland/Ohio. In the same year Michelson and Morley reported in the *American Journal of Science* (vol. 35, 1887, p. 333-345) that they measured a displacement much smaller than that expected due to the aether wind. Even though Morley was not convinced of his own results, many subsequent experiments disproved the aether theory.

The Michelson interferometer once contributed to the disproof of the aether theory. Nowadays one hopes that such an interferometer is an appropriate tool for the confirmation of another theory, which was established by Albert Einstein. He predicted gravitational waves which cause a periodical deformation of space, namely an expansion of space in one direction and a contraction along the orthogonal direction. Even though the existence of gravitational waves was proved indirectly [97], a direct measurement is still outstanding. The Michelson interferometer seems to be an ideal tool for the measurement of the expected differential length change. The crucial point is that a gravitational wave only causes a length change of $\sim 10^{-18}$ m in the case of a kilometer-scale Michelson interferometer. Even though the influence of a gravitational wave can still be thought of as a classical force acting on the end mirrors, such a precise measurement clearly will be influenced by quantum effects. Limits imposed by quantum mechanics and prospects to circumvent these limits will be discussed in Chap. 4.

The essential part of a Michelson interferometer is the beam splitter, as shown in Fig. 2.2, which has four input ports and four output ports. The ingoing quadrature fields $\hat{\mathbf{b}}, \hat{\mathbf{d}}, \hat{\mathbf{f}}$ and $\hat{\mathbf{h}}$ are related to the outgoing fields $\hat{\mathbf{a}}, \hat{\mathbf{c}}, \hat{\mathbf{e}}$ and $\hat{\mathbf{g}}$ via the matrix \mathbf{M}_{BS} in the following way:

$$\begin{pmatrix} \hat{\mathbf{a}} \\ \hat{\mathbf{c}} \\ \hat{\mathbf{e}} \\ \hat{\mathbf{g}} \end{pmatrix} = \mathbf{M}_{\text{BS}} \cdot \begin{pmatrix} \hat{\mathbf{d}} \\ \hat{\mathbf{b}} \\ \hat{\mathbf{h}} \\ \hat{\mathbf{f}} \end{pmatrix}, \quad \text{with} \quad \mathbf{M}_{\text{BS}} = \begin{pmatrix} -\rho & 0 & 0 & \tau \\ 0 & -\rho & \tau & 0 \\ 0 & \tau & \rho & 0 \\ \tau & 0 & 0 & \rho \end{pmatrix}. \quad (2.68)$$

In the simplest case, the north and the east arm each consists of a single mirror. In this thesis more advanced topologies are investigated, where the arms are composed of more than one mirror and certain optical media are also taken into account. However, all the additional components treated in the following give rise to linear transformations of the sideband fields. Therefore the various fields can be related by general linear transfer functions, i.e.

$$\hat{\mathbf{b}} = \mathbf{E} \cdot \hat{\mathbf{a}} + \hat{\mathbf{n}}_b, \quad \hat{\mathbf{h}} = \mathbf{N} \cdot \hat{\mathbf{g}} + \hat{\mathbf{n}}_h, \quad \hat{\mathbf{f}} = \mathbf{W} \cdot \hat{\mathbf{e}} + \hat{\mathbf{n}}_f, \quad \hat{\mathbf{d}} = \mathbf{S} \cdot \hat{\mathbf{c}} + \hat{\mathbf{n}}_d, \quad (2.69)$$

where $\hat{\mathbf{n}}_i$ describes the sideband fields which might be generated during a round trip in the corresponding arm. The set of linear equations can be easily solved in the case of an ideal beam splitter (50:50), open input and output ports ($\mathbf{W} = \mathbf{S} = 0$) and identical arms ($\mathbf{A} := \mathbf{E} = \mathbf{N}$). We obtain for the two output fields:

$$\hat{\mathbf{c}} = \mathbf{A} \cdot \hat{\mathbf{n}}_d + \frac{1}{\sqrt{2}}(\hat{\mathbf{n}}_h - \hat{\mathbf{n}}_b), \quad \hat{\mathbf{e}} = \mathbf{A} \cdot \hat{\mathbf{n}}_f + \frac{1}{\sqrt{2}}(\hat{\mathbf{n}}_h + \hat{\mathbf{n}}_b). \quad (2.70)$$

The outgoing field at the south port (dark port) depends only on the input field at the same port, transformed by the linear transfer function of the arms, and the difference between the additional sideband fields. It should be emphasized that a field injected into the west port (bright port) does not contribute directly to the south port's output. This is due to the fact that the phase relation at the beam splitter has been chosen accordingly. The same is true for fields injected into the south port. A gravitational wave excites the differential mode and hence the corresponding signal can be detected at the dark port. For other applications, it is interesting to also measure the common mode. This requires a detection at the bright port, as one can infer from Eq. (2.70).

The situation changes if the two arms are not exactly equal, e.g. $\mathbf{E} \neq \mathbf{N}$. Due an asymmetry of the arms, sideband fields injected into the bright port can leave the interferometer at the dark port. In this manner, a local oscillator can be provided for a heterodyne detection and various control signals can be extracted for the alignment of the interferometer. In the case of the initial LIGO configuration, the path difference between the beam splitter and the first and second input test mass is approximately 30 cm. Note that higher generation gravitational wave detectors take advantage of additional optics at the dark port, which gives rise to more complicated input-output relations.

2.3. Characterizing optical systems

Optical systems can be characterized in different ways. The various ubiquitous formalisms are so designed that they can provide transfer functions relating the input fields with the output fields of a device, e.g. a simple cavity or a whole laser interferometer. Three different formalisms are to be discussed in the following, all leading to the same results when applied to certain physical systems.

One approach is based on the quantum Langevin formalism [79]. In order to apply this formalism, one has to identify the different parts of a particular device and split the Hamiltonian into the corresponding components:

$$\hat{H}_{\text{total}} = \hat{H}_{\text{sys}} + \hat{H}_{\text{ext}} + \hat{H}_{\text{int}}, \quad (2.71)$$

where \hat{H}_{sys} is the free Hamiltonian of the system, being a function of the internal mode operators. The system has a few degrees of freedom, whereas the external world has many degrees of freedom. The external world is described by the free Hamiltonian \hat{H}_{ext} , which is a function of the bath mode operators. Furthermore \hat{H}_{int} represents the interaction between bath and internal mode operators. By using the quantum Langevin equation (cf. Ref. [79]), the internal mode operators or the output fields can be expressed in terms of the bath mode operators. Even nonlinear systems can be modeled by means of this formalism. Note that the mode operators involved in this formalism do not describe the field at a fix location but the whole mode. On the other hand, the electric field defined in the previous section describes the field at a fix position varying with time. Strictly speaking, a discrete mode is only defined for a closed system. But for nearly closed systems, the proper mode is assumed to be that which is closest to the mode of the corresponding closed system.

Another approach relies on the fact that any optical system is composed of simple subsystems. That means that one can divide a complex device into interconnected elementary subsystems with well-known transfer functions. In the case of linear transfer functions, a very general procedure was developed in Ref. [54], which allows us to derive linear equations for all optical fields propagating between the subsystems. The solution of these equations provides the desired input-output relation. This formalism is also suitable for the development of a numerical code for the simulation of complex optical topologies [54].

It is also possible to treat a system by the linear quantum measurement theory described in Ref. [27], which assumes a linear coupling between the probe (the object intended to measure) and the detector (the measurement apparatus). After identifying these components of a measurement apparatus, the equations of motion of the entire system can be derived. The advantage of this method is that it results in descriptive relations and allows us to include more practical issues, such as feedback control loops, in a simple way.

2.3.1. Mathematical framework

In this section, transfer functions of elementary optical subsystems are considered. The concept presented here follows the scheme suggested by Corbitt et al. in Ref. [54]. But here a slightly generalized version of their formalism is considered, which allows us to treat three dimensional multi-port optical components in a straightforward way. The primary challenge is the determination of the radiation pressure induced motion of optical components. Fluctuating weak modulation sideband fields, amplified by the carrier amplitude, shake mirrors, beam splitters or gratings in a random way. This motion can be calculated by comparing the momentum flow [cf. Eq. (2.51)] of the ingoing and outgoing fields. If the outgoing fields carry less momentum than the ingoing fields, it follows that the difference has been converted into a mechanical motion of the corresponding optical device. Since the general method presented here allows us to treat devices with an arbitrary number of ingoing and outgoing fields with arbitrary directions, one can also take gratings into account. Gratings might replace conventional optical elements in future gravitational wave detectors (see e.g. Refs. [33, 34, 35]) and they can obey complex input-output relations.

The general momentum conservation law reads:

$$-m\Omega^2\hat{\mathbf{x}} = \sum_j \mu_j \dot{\hat{\mathbf{p}}}_j(\Omega), \quad (2.72)$$

with $\mu_j = 1$ for ingoing fields and $\mu_j = -1$ for outgoing fields. By using Eq. (2.51) we

obtain the following expression for the motion of an optical component:

$$\hat{\mathbf{x}} = -\frac{1}{m\Omega^2} \sqrt{\frac{\hbar\omega_0}{c^2}} \sum_j \mu_j \mathbf{e}_j \cdot \mathbf{D}_j^T \cdot \hat{\mathbf{j}} \quad (2.73)$$

where \mathbf{e}_j is a unity vector accounting for the direction of propagation of the field \mathbf{D}_j , e.g. $\mathbf{D}_j \sim \mathbf{e}_j$. Due to a displacement of the optical component, the electric fields have to propagate a longer or shorter distance, which has to be taken into account. Since the radiation pressure induced displacement is very small, the effect on the sideband fields is negligible. Note that the displacement in a certain direction, e.g. \mathbf{e}_k , is simply given by $\hat{\mathbf{x}}^T \cdot \mathbf{e}_k$. We can derive the effect on each carrier quadrature vector by using Eq. (2.60):

$$\mathbf{R}[\hat{\mathbf{x}}^T \cdot \mathbf{e}_m \omega_0 / c] \cdot \mathbf{D}_m = \sum_j \rho^{(j \rightarrow m)} \mathbf{R}[\hat{\mathbf{x}}^T \cdot \mathbf{e}_j \omega_0 / c] \cdot \mathbf{D}_j, \quad (2.74)$$

where $\rho^{(j \rightarrow m)}$ denotes the amplitude reflectivity of the j th field into the m th field and $\tau^{(j \rightarrow m)}$ is the corresponding transmissivity. A possible phase jump can be taken into account by choosing either a positive or negative reflectivity. For a small displacement, we find:

$$\begin{aligned} \mathbf{D}_m &= \sum_j \rho^{(j \rightarrow m)} \mathbf{R}[(\hat{\mathbf{x}}^T \cdot \mathbf{e}_j - \hat{\mathbf{x}}^T \cdot \mathbf{e}_m) \omega_0 / c] \cdot \mathbf{D}_j + \sum_n \tau^{(n \rightarrow m)} \mathbf{D}_n \\ &\approx \sum_j \rho^{(j \rightarrow m)} \left(\mathbf{1} + \frac{\omega_0}{c} (\hat{\mathbf{x}}^T \cdot \mathbf{e}_j - \hat{\mathbf{x}}^T \cdot \mathbf{e}_m) \cdot \mathbf{R}[\pi/2] \right) \cdot \mathbf{D}_j + \sum_n \tau^{(n \rightarrow m)} \mathbf{D}_n \\ &\approx \sum_j \rho^{(j \rightarrow m)} \left(\mathbf{D}_j - \frac{\omega_0}{c} \hat{\mathbf{x}}^T \cdot (\mathbf{e}_j - \mathbf{e}_m) \bar{\mathbf{D}}_j \right) + \sum_n \tau^{(n \rightarrow m)} \mathbf{D}_n, \end{aligned} \quad (2.75)$$

where $\bar{\mathbf{D}}_a = -\mathbf{R}[\pi/2] \cdot \mathbf{D}_a$. For the total field, i.e. the carrier and the sidebands fields, the transformation reads:

$$\begin{aligned} \frac{\mathbf{D}_m}{\sqrt{\hbar\omega_0}} + \mathbf{m} &= \sum_j \rho^{(j \rightarrow m)} \left(\left(\mathbf{j} + \frac{\mathbf{D}_j}{\sqrt{\hbar\omega_0}} \right) - \frac{\omega_0}{c\sqrt{\hbar\omega_0}} \hat{\mathbf{x}}^T \cdot (\mathbf{e}_j - \mathbf{e}_m) \cdot \bar{\mathbf{D}}_j \right) \\ &\quad + \sum_n \tau^{(n \rightarrow m)} \left(\mathbf{n} + \frac{\mathbf{D}_n}{\sqrt{\hbar\omega_0}} \right). \end{aligned} \quad (2.76)$$

Note that the factor $1/\sqrt{\hbar\omega_0}$ has to be taken into account when combining sideband and carrier quadrature field vectors, as clarified in Eq. (2.48). The constant (dc) force resulting from the strong carrier field is neglected here, hence we can write:

$$\mathbf{m} = \sum_j \rho^{(j \rightarrow m)} \left(\mathbf{j} - \frac{\omega_0}{c\sqrt{\hbar\omega_0}} \hat{\mathbf{x}}^T \cdot (\mathbf{e}_j - \mathbf{e}_m) \cdot \bar{\mathbf{D}}_j \right) + \sum_n \tau^{(n \rightarrow m)} \mathbf{n}. \quad (2.77)$$

Inserting Eq. (2.73) into Eq. (2.77) gives a set of linear equations which have to be solved in order to obtain the input-output relation for the optical device under consideration. In the following, the general formalism is applied to two widely used optical components.

Example: mirror

For a mirror of mass m which interacts with two incoming fields (cf. Fig. 2.1), the unity vectors required for Eq. (2.73) are given by

$$\mathbf{e}_a = (1), \quad \mathbf{e}_b = (-1), \quad \mathbf{e}_c = (1), \quad \mathbf{e}_d = (-1) \quad (2.78)$$

and hence we find for the displacement of the mirror:

$$\hat{x}(\Omega) = -\frac{1}{m\Omega^2} \sqrt{\frac{\hbar\omega_0}{c^2}} \left[\mathbf{D}_a^T \cdot \hat{\mathbf{a}} - \mathbf{D}_d^T \cdot \hat{\mathbf{d}} + \mathbf{D}_b^T \cdot \hat{\mathbf{b}} - \mathbf{D}_c^T \cdot \hat{\mathbf{c}} \right]. \quad (2.79)$$

Since there are only two outgoing fields, Eq. (2.77) reduces to

$$\hat{\mathbf{b}} = \rho \hat{\mathbf{a}} + \tau \hat{\mathbf{d}} - \frac{2\rho\omega_0 \hat{x}}{c\sqrt{\hbar\omega_0}} \bar{\mathbf{D}}_a, \quad (2.80)$$

$$\hat{\mathbf{c}} = -\rho \hat{\mathbf{d}} + \tau \hat{\mathbf{a}} - \frac{2\rho\omega_0 \hat{x}}{c\sqrt{\hbar\omega_0}} \bar{\mathbf{D}}_d. \quad (2.81)$$

Inserting Eq. (2.79) into Eqs. (2.80)-(2.81) yields

$$\hat{\mathbf{b}} - \mathcal{K} \left((\bar{\mathbf{D}}_a \cdot \mathbf{D}_b^T) \cdot \hat{\mathbf{b}} - (\bar{\mathbf{D}}_a \cdot \mathbf{D}_c^T) \cdot \hat{\mathbf{c}} \right) = \mathcal{K} \left((\bar{\mathbf{D}}_a \cdot \mathbf{D}_a^T) \cdot \hat{\mathbf{a}} - (\bar{\mathbf{D}}_a \cdot \mathbf{D}_d^T) \cdot \hat{\mathbf{d}} \right) + \rho \hat{\mathbf{a}} + \tau \hat{\mathbf{d}} \quad (2.82)$$

and

$$\hat{\mathbf{c}} - \mathcal{K} \left((\bar{\mathbf{D}}_d \cdot \mathbf{D}_b^T) \cdot \hat{\mathbf{b}} - (\bar{\mathbf{D}}_d \cdot \mathbf{D}_c^T) \cdot \hat{\mathbf{c}} \right) = \mathcal{K} \left((\bar{\mathbf{D}}_d \cdot \mathbf{D}_a^T) \cdot \hat{\mathbf{a}} - (\bar{\mathbf{D}}_d \cdot \mathbf{D}_d^T) \cdot \hat{\mathbf{d}} \right) - \rho \hat{\mathbf{d}} + \tau \hat{\mathbf{a}} \quad (2.83)$$

with

$$\mathcal{K} = \frac{2\rho\omega_0}{m\Omega^2 c^2}. \quad (2.84)$$

If we shine a single carrier light on one side, e.g. the left side, of a perfectly reflecting mirror ($\rho = 1$), Eqs. (2.82)-(2.83) reduce to

$$\hat{\mathbf{b}} + \mathcal{K}(\bar{\mathbf{D}}_a \cdot \mathbf{D}_b^T) \cdot \hat{\mathbf{b}} = \hat{\mathbf{a}} + \mathcal{K}(\bar{\mathbf{D}}_a \cdot \mathbf{D}_a^T) \cdot \hat{\mathbf{a}}. \quad (2.85)$$

In this case the ingoing and outgoing fields have the same power, i.e. $\mathbf{D}_a = \mathbf{D}_b$ (provided that there is no phase jump). Now we assume w.l.o.g. that the classical field only exhibits an excitation in the amplitude quadrature ($\theta_a = \theta_b = 0$), which allows us to simplify Eq. (2.85):

$$\hat{\mathbf{b}} - 2\mathcal{K}P_a \begin{pmatrix} 0 & 0 \\ -1 & 0 \end{pmatrix} \cdot \hat{\mathbf{b}} = \hat{\mathbf{a}} + 2\mathcal{K}P_a \begin{pmatrix} 0 & 0 \\ -1 & 0 \end{pmatrix} \cdot \hat{\mathbf{a}}. \quad (2.86)$$

This set of linear equations can be easily solved:

$$\begin{aligned} \hat{b}_1 &= \hat{a}_1, \\ \hat{b}_2 &= \hat{a}_2 - \frac{1}{m\Omega^2} \frac{8\omega_0 P_a}{c^2} \hat{a}_1, \end{aligned} \quad (2.87)$$

and we obtain from Eq. (2.79) an expression for the motion of the mirror:

$$\hat{x}(\Omega) = -\frac{1}{m\Omega^2} \sqrt{\frac{8P_a \omega_0 \hbar}{c^2}} \hat{a}_1. \quad (2.88)$$

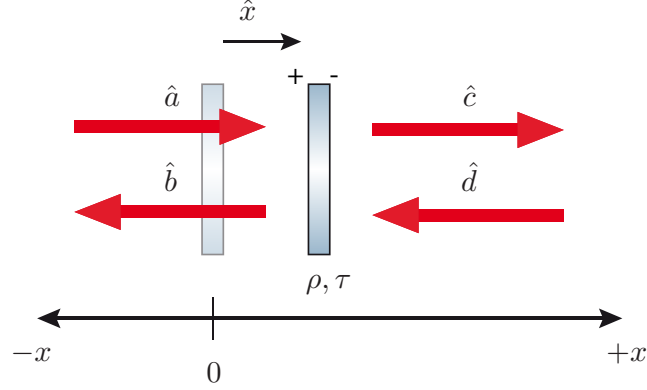


Figure 2.1.: Mirror is displaced by \hat{x} due to the influence of optical fields.

Example: beam splitter

An analogous relation can be found for a beam splitter subject to radiation pressure fluctuations. We have to deal with eight different fields, as shown in Fig. 2.2. It is convenient to treat the displacements in x - and y - directions separately. For the beam splitter, the unity vectors required for Eq. (2.73) are given by

$$\mathbf{e}_a = \begin{pmatrix} 0 \\ 1 \end{pmatrix}, \quad \mathbf{e}_b = \begin{pmatrix} 0 \\ -1 \end{pmatrix}, \quad \mathbf{e}_c = \begin{pmatrix} 1 \\ 0 \end{pmatrix}, \quad \mathbf{e}_d = \begin{pmatrix} -1 \\ 0 \end{pmatrix}, \quad (2.89)$$

$$\mathbf{e}_e = \begin{pmatrix} 0 \\ -1 \end{pmatrix}, \quad \mathbf{e}_f = \begin{pmatrix} 0 \\ 1 \end{pmatrix}, \quad \mathbf{e}_g = \begin{pmatrix} -1 \\ 0 \end{pmatrix}, \quad \mathbf{e}_h = \begin{pmatrix} 1 \\ 0 \end{pmatrix}, \quad (2.90)$$

and therefore we obtain for the motion:

$$\hat{x}_x = -\frac{1}{m\Omega^2} \sqrt{\frac{\hbar\omega_0}{c^2}} \left[-\mathbf{D}_c^T \cdot \hat{\mathbf{c}} - \mathbf{D}_d^T \cdot \hat{\mathbf{d}} + \mathbf{D}_g^T \cdot \hat{\mathbf{g}} + \mathbf{D}_h^T \cdot \hat{\mathbf{h}} \right], \quad (2.91)$$

$$\hat{x}_y = -\frac{1}{m\Omega^2} \sqrt{\frac{\hbar\omega_0}{c^2}} \left[-\mathbf{D}_a^T \cdot \hat{\mathbf{a}} - \mathbf{D}_b^T \cdot \hat{\mathbf{b}} + \mathbf{D}_e^T \cdot \hat{\mathbf{e}} + \mathbf{D}_f^T \cdot \hat{\mathbf{f}} \right]. \quad (2.92)$$

Since a displacement in x -direction has the same effect as a displacement of the same amount in y -direction, it is common to define a total displacement by $\hat{x}_{\text{tot}} = \hat{x}_x + \hat{x}_y$ which accounts for the extra length each light field has to travel. However, from Eq. (2.77) a set of linear equations can be deduced

$$\hat{\mathbf{a}} = -\rho\hat{\mathbf{d}} + \tau\hat{\mathbf{f}} - \frac{\rho\omega_0\hat{x}_{\text{tot}}}{c\sqrt{\hbar\omega_0}} \bar{\mathbf{D}}_d, \quad \hat{\mathbf{c}} = -\rho\hat{\mathbf{b}} + \tau\hat{\mathbf{h}} - \frac{\rho\omega_0\hat{x}_{\text{tot}}}{c\sqrt{\hbar\omega_0}} \bar{\mathbf{D}}_b \quad (2.93)$$

$$\hat{\mathbf{e}} = \rho\hat{\mathbf{h}} + \tau\hat{\mathbf{b}} - \frac{\rho\omega_0\hat{x}_{\text{tot}}}{c\sqrt{\hbar\omega_0}} \bar{\mathbf{D}}_h, \quad \hat{\mathbf{g}} = \rho\hat{\mathbf{f}} + \tau\hat{\mathbf{d}} - \frac{\rho\omega_0\hat{x}_{\text{tot}}}{c\sqrt{\hbar\omega_0}} \bar{\mathbf{D}}_f, \quad (2.94)$$

and the corresponding solution gives the desired input-output relation. The most general expression is obvious but cumbersome and, we therefore omit it.

In the following, different interferometer designs will be considered. But all configurations have in common that a laser source is injected from one side of the beam splitter

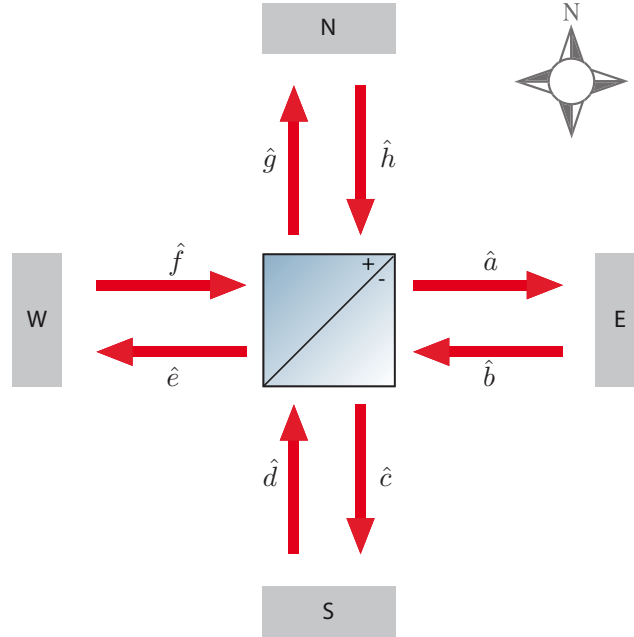


Figure 2.2.: Beam splitter exposed to different quadrature fields.

and, in the case of no losses, all light is reflected back to this port. This implies the following simplifications:

$$P_c = P_d = 0, \quad P := P_a = P_b = P_g = P_h = P_f/2, \quad (2.95)$$

where we have assumed a 50:50 beam splitter ($\tau = \rho = 1/\sqrt{2}$). Furthermore \mathbf{g} , \mathbf{h} and \mathbf{a} , \mathbf{b} respectively, are each connected via certain linear transfer functions, which describe the two arms of the interferometer. In terms of these transfer functions, one can obtain simple formulas for the motion of the beam splitter.

In the previous two examples we have only considered the motion of optical components in one or two dimensions. But the formalism allows us to treat optical devices reflecting light into arbitrary directions in a straightforward way.

Detuned cavity

So far, only single optical components have been discussed. In the following, we derive the input-output relation for an optical resonator consisting of two mirrors separated by a distance L . We consider a detuned cavity with a fixed input mirror and a suspended end mirror of mass m . The output quadrature field vector $\hat{\mathbf{o}}$ depends linearly on the input vacuum field $\hat{\mathbf{i}}$. There might be other contributions influencing the output, e.g. a signal generated by a force acting on the suspended mirror, vacuum fields due to losses or simply laser noise. But first, these additional effects are disregarded and the moveable mirror is assumed to be perfectly reflecting. According to Eq. (2.80) the fields at the movable end mirror are related in the following way:

$$\hat{\mathbf{b}} = \hat{\mathbf{a}} + \frac{2\omega_0 \hat{x}}{c\sqrt{\hbar\omega_0}} \bar{D}_a. \quad (2.96)$$

Since the cavity is detuned by $\phi = \omega_0 L/c$, a rotation [cf. Eq. (2.57)] of the quadrature fields has to be taken into account. Therefore the relation between the fields inside and outside the cavity reads:

$$\hat{\mathbf{o}} = -\rho \hat{\mathbf{i}} + \tau e^{i\theta} \mathbf{R}[\phi] \cdot \hat{\mathbf{b}}, \quad (2.97)$$

$$e^{-i\theta} \mathbf{R}[-\phi] \cdot \hat{\mathbf{a}} = \tau \hat{\mathbf{i}} + \rho e^{i\theta} \mathbf{R}[\phi] \cdot \hat{\mathbf{b}}, \quad (2.98)$$

where τ and ρ are the transmissivity and reflectivity of the input mirror, respectively. One is free to choose an appropriate phase of the carrier field at the end mirror, since the phase of the incoming field can be chosen arbitrarily. For the sake of simplicity, it is convenient to assume

$$\mathbf{D}_a = \mathbf{D}_b = \sqrt{2P_c} \begin{pmatrix} 1 \\ 0 \end{pmatrix}. \quad (2.99)$$

The solution of Eqs. (2.96)-(2.98) can then be easily calculated and in leading order in τ^2 , $\theta \equiv \Omega L/c$ and $\lambda \equiv \phi L/c$ the transfer function reads

$$\hat{\mathbf{o}} = \frac{1}{\Omega_{\text{opt}}^2} \begin{pmatrix} \lambda^2 - \epsilon^2 - \Omega^2 & 2\lambda\epsilon \\ -2\lambda\epsilon & \lambda^2 - \epsilon^2 - \Omega^2 \end{pmatrix} \cdot \hat{\mathbf{i}} + \hat{x} \sqrt{\frac{\epsilon\theta^2 m}{2\hbar}} \frac{1}{\Omega_{\text{opt}}^2} \begin{pmatrix} \lambda \\ \epsilon - i\Omega \end{pmatrix}, \quad (2.100)$$

where the definition of the cavity's half bandwidth has been used, namely

$$\epsilon = \frac{\tau^2 c}{4L}. \quad (2.101)$$

The (complex) optical resonance frequencies are given by the roots of

$$\Omega_{\text{opt}}^2 = (\Omega - \lambda + i\epsilon)(\Omega + \lambda + i\epsilon). \quad (2.102)$$

The coupling strength of the mirror's motion \hat{x} into the output field is proportional to

$$\theta^2 = \frac{16\omega_0 P_c}{mLc}, \quad (2.103)$$

which has the unit $1/\text{sec}^3$ and where P_c refers to the circulating power. The circulating power is related to the input power P_{in} by

$$P_c = \frac{\tau^2}{1 + (1 - \tau^2) - 2\sqrt{1 - \tau^2} \cos(2\lambda L/c)} P_{\text{in}} \approx \frac{4c^2 \tau^2}{c^2 \tau^4 + 16L^2 \lambda^2} P_{\text{in}}. \quad (2.104)$$

The motion of the end mirror [cf. Eq. (2.79)] due to the fluctuating vacuum fields is given by

$$\hat{x}(\Omega) = -\frac{1}{m\Omega^2} \sqrt{\frac{\hbar\omega_0}{c^2}} \left[\mathbf{D}_a^T \cdot \hat{\mathbf{a}} + \mathbf{D}_b^T \cdot \hat{\mathbf{b}} \right]. \quad (2.105)$$

After expressing $\hat{\mathbf{a}}$ in terms of the ingoing fields $\hat{\mathbf{i}}$ and performing the same approximation as for Eq. (2.100), one obtains

$$\hat{x}(\Omega) = -\frac{1}{m\Omega^2} \frac{1}{\Omega_{\text{opt}}^2} \left[\sqrt{\frac{\epsilon\hbar\theta^2 m}{2}} \begin{pmatrix} i\Omega - \epsilon & \lambda \end{pmatrix} \cdot \hat{\mathbf{i}} + \frac{\theta^2 m}{4} \lambda \hat{x}(\Omega) \right]. \quad (2.106)$$

Substituting the solution of Eq. (2.106) into Eq. (2.100) reveals the transfer function

$$\hat{\mathbf{o}} = \frac{1}{M} \begin{pmatrix} 4\Omega^2(\lambda^2 - \epsilon^2 - \Omega^2) - \theta^2\lambda & 8\lambda\epsilon\Omega^2 \\ 2\epsilon(\theta^2 - 4\lambda\Omega^2) & 4\Omega^2(\lambda^2 - \epsilon^2 - \Omega^2) - \theta^2\lambda \end{pmatrix} \cdot \hat{\mathbf{i}}, \quad (2.107)$$

with

$$M = \theta^2\lambda + 4\Omega^2\Omega_{\text{opt}}^2, \quad (2.108)$$

which determines the resonances of the system.

Signal transfer

So far the mirror motion has been influenced solely by radiation pressure fluctuations. Usually the mirror is also subject to signal forces which should be measured. Such a force acts on the mirror and causes a Fourier domain displacement $\mathbf{s}(\Omega)$ in a certain direction. This term can be added in Eq. (2.73) and one obtains:

$$\hat{\mathbf{x}} = -\frac{1}{m\Omega^2} \sqrt{\frac{\hbar\omega_0}{c^2}} \sum_j \mathbf{e}_j \mu_j \mathbf{D}_j^T \cdot \hat{\mathbf{j}} + \mathbf{s}. \quad (2.109)$$

Optical losses

An ideal, i.e. perfectly reflecting mirror, satisfies the relation $\tau^2 + \rho^2 = 1$. This is not feasible in a real experimental set-up and the unavoidable losses can be described by the relation

$$\tau^2 + \rho^2 + A = 1, \quad (2.110)$$

in the case of a (power) loss A . Eq. (2.110) can easily be extended to more complex optical components. The part of the field lost to an optical component is replaced by a coherent vacuum field $\hat{\mathbf{v}}$. This additional field has to be included in Eq. (2.77) and we finally obtain:

$$\begin{aligned} \hat{\mathbf{m}} = & \sum_j \rho^{(j \rightarrow m)} \left(\hat{\mathbf{j}} - \frac{\omega_0}{c\sqrt{\hbar\omega_0}} (\mathbf{e}_j - \mathbf{e}_m) \cdot \hat{\mathbf{x}}^T \cdot \bar{\mathbf{D}}_j + \frac{\sqrt{A^{(j \rightarrow m)}}}{\rho^{(j \rightarrow m)}} \hat{\mathbf{v}}_j \right) \\ & + \sum_n \left(\tau^{(n \rightarrow m)} \hat{\mathbf{n}} + \sqrt{A^{(n \rightarrow m)}} \hat{\mathbf{v}}_n \right). \end{aligned} \quad (2.111)$$

Therefore Eqs. (2.82)-(2.83) and Eqs. (2.93)-(2.94) can easily be extended by including in each case an additional contribution of the form $\sqrt{A^n} \hat{\mathbf{v}}_n$.

2.3.2. Linear quantum measurement theory

This section deals with the measurement of a classical observable, which is indirectly accessible via a probe. The classical observable influences the probe and therefore the construction of an appropriate detector is required, which is coupled to the probe. The detection scheme allows us to obtain classical data which can be saved by a conventional storage device. Quantum-domain measurements of this kind are characterized by the dynamical interaction between the probe and the detector, which can establish correlations

between the states of these two systems. The detector produces an output containing information about the probe's state with a certain measurement error and it can influence the probe due to the backaction of the measurement. In the case of a linear quantum measurement, these two aspects do not depend on the probe's initial quantum state. Within the scope of this thesis, only linear measurement processes are investigated. Therefore it is of interest to identify any universal quantitative features of the measurement process independent of a certain physical realization of the detector and the measured system. An extensive analysis of linear quantum measurements can be found in Ref. [27]; the application to signal-recycled gravitational wave interferometers is discussed in detail by Buonanno and Chen in Ref. [37]. Since this formalism is suitable for the description of many different interferometer topologies, the main aspects are to be recapitulated in the following. The analysis adopts the notation used in Ref. [37], where the equations of motion in the frequency domain are given in terms of linear response functions (cf. Sec. 2.3.3).

It should be emphasized that it is more straightforward to derive the transfer functions of an optical device by means of the simple modular matrix formalism introduced in the previous section. This formalism is able to provide an input-output relation, but the resulting formulas are in general rather unsystematic expressions. It is more instructive to derive the equations of motion within the framework of the linear quantum measurement formalism, since one gains more insight into the dynamics of the system. For example, the concept of the optical spring could not be understood intuitively by considering only the input-output relation derived by means of the formalism presented in Sec. 2.3.1.

This section is organized as follows: first the idea of the linear response function is explained by means of a driven harmonic oscillator. Then it is shown that it is possible to measure arbitrary small forces acting on such a harmonic oscillator by exploiting a time-dependent readout scheme. Then the linear quantum measurement formalism is applied to a detuned signal-recycling interferometer.

2.3.3. Linear response function

It is instructive to start with a simple example. We consider a quantum mechanical harmonic oscillator with eigenfrequency ω_m , velocity damping γ_m and mass m . If the oscillator is driven by an external force $\hat{F}(t)$, the corresponding inhomogeneous second-order linear differential equation for the location $\hat{x}(t)$ reads:

$$m \left(\ddot{\hat{x}}(t) + \gamma_m \dot{\hat{x}}(t) + \omega_m^2 \hat{x}(t) \right) = \hat{F}(t). \quad (2.112)$$

After defining the quantities

$$a \equiv \frac{1}{2} \sqrt{4\omega_m^2 - \gamma_m^2} \quad \text{and} \quad b \equiv \gamma_m/2, \quad (2.113)$$

a straightforward calculation yields the solution of Eq. (2.112):

$$\hat{x}(t) = e^{-bt} \left[\hat{x}_0 \cos(at) + \left(\frac{\hat{p}_0}{am} + \frac{b}{a} \hat{x}_0 \right) \sin(at) \right] + \frac{1}{ma} \int_{-\infty}^t dt' e^{-b(t-t')} \sin(a(t-t')) \hat{F}(t') \quad (2.114)$$

$$\equiv \hat{x}^{(0)}(t) + \int_{-\infty}^t dt' C_{x^{(0)}x^{(0)}}(t, t') \hat{F}(t'). \quad (2.115)$$

The first term in Eq. (2.114) – abbreviated by $x^{(0)}(t)$ in Eq. (2.115) – is the homogeneous solution and describes the free evolution. The second term in Eq. (2.114) is due to the external driving force. This inhomogeneous solution can be expressed in terms of the so called linear response function given by

$$C_{x^{(0)}x^{(0)}}(t, t') = \frac{1}{ma} e^{-b(t-t')} \sin(a(t-t')). \quad (2.116)$$

This describes the response of the position of the harmonic oscillator to an external force. This response depends not only on present but also on past values of $\hat{F}(t)$. A weighted sum of the previous values of $\hat{F}(t)$, with the weights given by the linear response function $C_{x^{(0)}x^{(0)}}(t, t')$, contributes to current values of $\hat{x}(t)$. The linear response function has many applications in information theory, physics and engineering. There exist alternative names for specific linear response functions, such as susceptibility or impedance. In the linear quantum measurement theory the term "susceptibility" is commonly used. Since the susceptibility given in Eq. (2.116) depends only on the time difference $t - t'$, the Fourier transform of Eq. (2.115) can be calculated easily:

$$\hat{x}(\Omega) = \hat{x}^{(0)}(\Omega) + R_{xx}(\Omega) \hat{F}(\Omega), \quad (2.117)$$

where the Fourier domain susceptibility is given by

$$R_{xx}(\Omega) = -\frac{1}{m(\Omega - (a - ib))(\Omega - (-a - ib))}. \quad (2.118)$$

The eigenfrequencies of the system are given by the poles of the susceptibility $R_{xx}(\Omega)$

$$\Omega_{\pm} = \pm a - ib, \quad (2.119)$$

which are obviously complex. The real part corresponds to the oscillatory part in the time domain solution, while the negative imaginary part accounts for the exponential decay [cf. Eq. (2.114)]. A positive imaginary part would imply an exponential growth towards the future, i.e. the system would be unstable. Hence the stability of a system can be checked by analyzing the roots of the Fourier domain susceptibility defined in general by:

$$R_{AB}(\Omega) \equiv \frac{i}{\hbar} \int_0^{+\infty} d\tau e^{i\Omega\tau} C_{AB}(0, -\tau). \quad (2.120)$$

Measurement of a classical force

We consider a harmonic oscillator without damping ($\gamma_m = 0$) as a quantum probe exposed to an external classical force. By employing an appropriate detector one can measure the force with a certain degree of accuracy. The question arises whether it is possible to detect arbitrary weak forces. From the general uncertainty principle

$$\Delta \hat{A} \Delta \hat{B} \geq \frac{1}{2} |\langle [\hat{A}, \hat{B}] \rangle| \quad (2.121)$$

and Eq. (2.114) (with $\gamma_m = 0$), follows the two-time uncertainty relation for the coordinate of the harmonic oscillator:

$$\Delta \hat{x}(t) \Delta \hat{x}(t') \geq \frac{\hbar}{2m\omega_m} |\sin(\omega_m(t-t'))|, \quad (2.122)$$

where the commutator $[x, p] = i\hbar$ has been used. The product of the uncertainties vanishes periodically for

$$t - t' = n \frac{\pi}{\omega_m}, \quad \text{for } n \in \mathbb{N}. \quad (2.123)$$

This means that a measurement at time t can be carried out without influencing the measurement at a later time $t + n\pi/\omega_m$. For a suspended mirror, a stroboscopic measurement (cf. Ref. [152]) of its position can be realized by switching the laser source on and off at appropriate time intervals. This causes the oscillator's wave function to breath. A measurement at time t perturbs the oscillator's momentum, due to the ponderomotive light pressure. The wave function gets wider and reaches a maximum at time $t + \pi/(2\omega_m)$. After this it shrinks and reaches its original value at time $t + \pi/\omega_m$, regardless of the perturbation at time t . Therefore it is in principle possible to detect arbitrary small forces. A more precise measurement usually causes more backaction, but it does not influence the measurement output in the case of such a stroboscopic measurement. The general backaction evasion criterion, given by

$$[\hat{x}, \hat{H}_I] = 0, \quad (2.124)$$

is satisfied. Here, \hat{H}_I describes the pulsed interaction between probe and detector and \hat{x} is the detector observable.

For high precision measurements one would need to control high laser powers very fast, which is not suitable from an experimental point of view. A more sophisticated method would be a time-dependent change of the readout quadrature, this technique also allows us to realize a scheme which is nearly backaction free.

We can deduce from Eq. (2.87) the time domain equations of motion for the simple measurement of a suspended mirror:

$$\begin{aligned} \hat{b}_1(t) &= a_1(t), \\ \hat{b}_2(t) &= a_2(t) + \frac{\alpha}{\hbar} \hat{x}(t) \end{aligned} \quad (2.125)$$

with

$$\alpha = \sqrt{\frac{8P\hbar\omega_0}{c^2}}. \quad (2.126)$$

In the absence of damping the oscillator's coordinate $\hat{x}(t)$ is given by Eq. (2.114) (with $\gamma_m = 0$), where the force exerted on the mirror consists of a classical signal part, which we want to measure, and a quantum backaction part due to the ponderomotive light force:

$$\hat{F}(t) = F_{\text{sig}}(t) + \alpha \hat{a}_1(t). \quad (2.127)$$

In order to measure the signal, the outgoing field is mixed with a local oscillator light with amplitude $A(t)$, which exhibits a time-dependent phase $\eta(t)$:

$$A(t) = A_0 \cos(\eta(t)) \cos(\omega_0 t) + A_0 \sin(\eta(t)) \sin(\omega_0 t). \quad (2.128)$$

Shining the superposed light on a photodiode gives rise to a photocurrent which is filtered by the response function $\Phi(t)$ of the electronics employed for the postprocessing of the generated current. A real detector cannot furnish an instantaneous measurement, hence

one has to integrate over a certain time interval T in order to obtain the final output \hat{Y} . After defining

$$g_1(t) = A_0\Phi(t)\cos(\eta(t)), \quad g_2(t) = A_0\Phi(t)\sin(\eta(t)), \quad (2.129)$$

the required integration over a time interval T very much larger than ω_0^{-1} can be written as:

$$\hat{Y} = \int_0^T dt [g_1(t)\hat{b}_1(t) + g_2(t)\hat{b}_2(t)] \quad (2.130)$$

$$= \int_0^T dt [g_1(t)\hat{a}_1(t) + g_2(t)(\hat{a}_2(t) + \frac{\alpha}{\hbar}(\hat{x}_0 \cos(\omega_m t) + \frac{\hat{p}_0}{m\omega_m} \sin(\omega_m t)) + \frac{\alpha}{m\hbar\omega_m} \int_0^t dt' \sin(\omega_m(t-t'))(F_{\text{sig}}(t') + \alpha\hat{a}_1(t')))]. \quad (2.131)$$

Obviously we can get rid of the backaction part [term proportional to $\alpha a_1(t)$] by demanding

$$g_1(t) + \frac{\alpha^2}{m\hbar\omega_m} \int_t^T dt' \sin(\omega_m(t'-t))g_2(t') = 0. \quad (2.132)$$

The radiation pressure fluctuations are completely canceled out and it seems that the classical signal force can be measured with an arbitrary accuracy. This scheme was first proposed by Vyatchanin et al. in Ref. [165], who pointed out that the light introduces some kind of damping to the harmonic oscillator. This damping is proportional to the coupling constant α and it prevents the measurement from being perfect. Furthermore, this scheme is only suitable for signals with known arrival times and is therefore not applicable to gravitational wave laser interferometers. However the stroboscopic measurement as well as the time-dependent homodyne detection scheme clarify the possibility of measuring small forces without any restrictions emanating from the Heisenberg uncertainty relation. In contrast to a conventional detection scheme, one avoids seeing the backaction induced perturbation by observing an appropriate quadrature or measuring in proper time intervals. Note that the detection schemes presented are strictly speaking not QND measurements. For a real QND observable $\hat{q}(t)$, the commutator at different times must always vanish, i.e.

$$[\hat{q}(t), \hat{q}(t')] = 0 \quad \text{for all } t, t'. \quad (2.133)$$

The vanishing commutator indicates that all measured values of $\hat{q}(t)$ can be stored as pieces of classical data.

2.3.4. Equations of motion

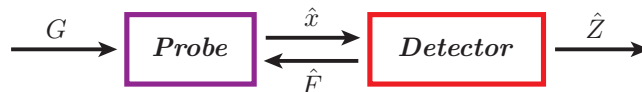


Figure 2.3.: General scheme for a linear measurement system

In the following, a linear measurement scheme as shown in Fig. 2.3 and discussed in Ref. [27] is recapitulated. The probe \mathcal{P} , which belongs to the Hilbert space $\mathcal{H}_{\mathcal{P}}$, is exposed

to a classical force G (e.g. a gravitational wave) influencing its coordinate \hat{x} . In order to measure the classical force, an appropriate detector \mathcal{D} is attached to the probe. The detector belongs to the Hilbert space $\mathcal{H}_{\mathcal{D}}$ and is so coupled to the probe that it measures the coordinate \hat{x} . The detector can also exert a backaction force \hat{F} on the probe. The detector's output observable \hat{Z} contains some quantum noise caused by the probe and the detector as well as a classical signal depending on the classical observable G . The total Hamiltonian belonging to the combined Hilbert space $\mathcal{H} = \mathcal{H}_{\mathcal{D}} \otimes \mathcal{H}_{\mathcal{P}}$ is given by

$$\hat{H} = [(\hat{H}_{\mathcal{P}} - \hat{x}G) + \hat{H}_{\mathcal{D}}] - \hat{x}\hat{F}, \quad (2.134)$$

where $\hat{H}_{\mathcal{D}}$ and $\hat{H}_{\mathcal{P}}$ describe the free evolution of the detector and the probe, respectively. The interaction between the classical force and the probe is taken into account by the term $\hat{x}G$, while the term $\hat{x}\hat{F}$ denotes the interaction between the detector and the probe. Note that the structure of the Hamiltonian in Eq. (2.134) resembles that of Hamiltonians analyzed within the scope of dissipative quantum dynamics based on system-reservoir coupling models, if we regard the detector as the reservoir. Such coupled systems were extensively investigated (see, e.g. Ref. [166]) and it was shown that the dynamics of the system are independent of a specific reservoir realization. This is in accordance with the quantum measurement theory where the probe's dynamics are also independent of a particular implementation of the detector. Furthermore the measurement's backaction causes a decoherence of the probe, which is also similar to the reservoir induced decoherence. Even though the reservoir is influenced by the system, it is assumed to be in thermal equilibrium and hence any changes are supposed to be unobservable. This is the main difference from a quantum measurement process, since the intended purpose of a detector is the acquisition of some information about the probe's behavior. Furthermore, the detector can be regarded as an amplifier, since a weak force is converted into a detectable classical output signal, which cannot be accomplished by a system in thermal equilibrium.

The linear quantum measurement scheme introduced in Ref. [27] was applied by Buonanno and Chen in Ref. [37] to a signal-recycled gravitational wave detector. The probe is provided by the motion of the suspended mirrors or, more precisely, by the antisymmetric mode of motion of the four arm cavity mirrors. The optical system is coupled to the probe and produces the output observable \hat{Z} . The whole optical system can be regarded as the detector. The total Hamiltonian is at most quadratic in the canonical coordinates and momenta and therefore the system is a linear one. For such a linear system, the commutator of operators corresponding to arbitrary linear observables at two times is a c-number:

$$C_{AB}(t, t') = [\hat{A}(t), \hat{B}(t')], \quad \text{with } \hat{A}, \hat{B} \in \{\hat{x}, \hat{F}, \hat{Z}\} \text{ and } C_{AB}(t, t') \in \mathbb{C}. \quad (2.135)$$

These commutators are also known as the system's susceptibilities, since it can be shown that the exact Heisenberg evolution for any linear observable \hat{P} of the probe's Hilbert space and \hat{D} of the detector's Hilbert space is given by

$$\hat{P}_H(t) = \hat{P}_H^{(0)}(t) + \frac{i}{\hbar} \int_{-\infty}^t C_{Px}(t, t') \hat{F}_H(t'), \quad (2.136)$$

$$\hat{D}_H(t) = \hat{D}_H^{(0)}(t) + \frac{i}{\hbar} \int_{-\infty}^t C_{DF}(t, t') \hat{x}_H(t'), \quad (2.137)$$

where $\hat{P}_H^{(0)}(t)$ and $\hat{D}_H^{(0)}(t)$ account for the free evolution, respectively. This is analogous to the simple example discussed in Sec. 2.3.3. For an arbitrary system, the perturbed time evolution is an infinite series which stops after the first-order only in the case of a linear system. For a time-independent zeroth order Hamiltonian the susceptibility in Eq. (2.135) solely depends on the time difference $t-t'$ and hence the equations of motion in the Fourier domain can easily be obtained by employing the definition given in Eq. (2.120):

$$\hat{x}^{(1)}(\Omega) = \hat{x}^{(0)}(\Omega) + R_{xx}(\Omega)\hat{F}^{(1)}(\Omega) + Lh(\Omega), \quad (2.138)$$

$$\hat{F}^{(1)}(\Omega) = \hat{F}^{(0)}(\Omega) + R_{FF}(\Omega)\hat{x}^{(1)}(\Omega), \quad (2.139)$$

$$\hat{Z}^{(1)}(\Omega) = \hat{Z}^{(0)}(\Omega) + R_{ZF}(\Omega)\hat{x}^{(1)}(\Omega). \quad (2.140)$$

Note that the susceptibilities are obviously defined with respect to the free evolution operators. The displacement due to a gravitational wave is given by $Lh(t)$, where L is the length of the arm cavities and $h(t)$ is the differential strain induced by the gravitational wave (see Eq. (2.15) of Ref. [37]). The set of linear equations, i.e. Eqs. (2.138)-(2.140), can be solved easily and a rather straightforward calculation reveals the explicit expressions for the different observables $\{\hat{x}^{(1)}, \hat{F}^{(1)}, \hat{Z}^{(1)}\}$ depending on the input fields $\hat{i}_{1,2}$. By means of Eqs. (2.138)-(2.139) we can also derive the differential equation of motion for the antisymmetric mode of motion of the four arm cavity mirrors in the frequency domain:

$$-\frac{m}{4}\Omega^2\hat{x}^{(1)}(\Omega) - R_{FF}(\Omega)\hat{x}^{(1)}(\Omega) = -\frac{m}{4}\Omega^2\hat{x}^{(0)}(\Omega) + \hat{F}^{(0)}(\Omega) + \text{GW force}, \quad (2.141)$$

where the free mass susceptibility $R_{xx} = -4/(m\Omega^2)$ was used. The mass of a single mirror is denoted by m . The structure of the above Eq. (2.141) is similar to the equation of motion of a simple harmonic oscillator [cf. Eq. (2.112)]. The fluctuating radiation pressure force $\hat{F}^{(0)}$, the gravitational wave strain and the quantized force $-m/4\Omega^2\hat{x}^{(0)}(\Omega)$ can be regarded as driving forces acting on an oscillator with a frequency-dependent spring constant $K_{\text{pond}}(\Omega) = -R_{FF}(\Omega)$. The term *optical spring* emerged from this structure of Eq. (2.141). In the case of a tuned signal-recycled interferometer, the ponderomotive rigidity vanishes ($R_{FF}(\Omega) = 0$) and the different forces simply act on a free mass.

It was also shown in Ref. [37] that a detuned signal-recycled Michelson interferometer is completely equivalent to a single detuned cavity with one movable mirror (cf. Sec. 2.3.1). This allows us to obtain directly from Eqs. (2.100) and (2.106) explicit expressions for the operators $\{\hat{F}^{(0)}, \hat{Z}^{(0)}\}$ introduced above. In order to switch from a simple cavity to a whole detuned signal-recycled interferometer, the following substitutions are necessary:

$$\begin{aligned} \lambda &\longrightarrow \lambda = \gamma_o \frac{2\rho_{\text{SR}} \sin(2\phi)}{1 + \rho_{\text{SR}}^2 + 2\rho_{\text{SR}} \cos(2\phi)}, & \theta &\longrightarrow \theta = \sqrt{8P_{\text{arm}}\omega_0/(mLc)}, \\ \epsilon &\longrightarrow \epsilon = \gamma_o \frac{1 - \rho_{\text{SR}}^2}{1 + \rho_{\text{SR}}^2 + 2\rho_{\text{SR}} \cos(2\phi)}, & m &\longrightarrow m/4, \end{aligned} \quad (2.142)$$

where ρ_{SR} is the reflectivity of the signal-recycling mirror, ϕ the detuning phase of the signal-recycling cavity and P_{arm} the circulating power in each arm cavity.

The operator $\hat{F}^{(0)}(\Omega)$ used in Eqs. (2.138)-(2.139) describes the radiation pressure forces emanating from the ingoing vacuum fields, which would act on fixed mirrors. The operator $\hat{Z}^{(0)}(\Omega)$ in Eq. (2.139) accounts for the outgoing fluctuations in the quadratures

in the case of fixed mirrors. In the language of Ref. [38], $\hat{F}^{(0)}(\Omega)$ and $\hat{Z}^{(0)}(\Omega)$ are *free* quantities which are given by

$$\hat{F}^{(0)}(\Omega) = \sqrt{\frac{\epsilon\theta^2 m \hbar}{2}} \frac{(i\Omega - \epsilon)\hat{i}_1 + \lambda\hat{i}_2}{(\Omega - \lambda + i\epsilon)(\Omega + \lambda + i\epsilon)}, \quad (2.143)$$

$$\hat{Z}_1^{(0)}(\Omega) = \frac{(\lambda^2 - \epsilon^2 - \Omega^2)\hat{i}_1 + 2\lambda\epsilon\hat{i}_2}{(\Omega - \lambda + i\epsilon)(\Omega + \lambda + i\epsilon)}, \quad (2.144)$$

$$\hat{Z}_2^{(0)}(\Omega) = \frac{-2\lambda\epsilon\hat{i}_1 + (\lambda^2 - \epsilon^2 - \Omega^2)\hat{i}_2}{(\Omega - \lambda + i\epsilon)(\Omega + \lambda + i\epsilon)}, \quad (2.145)$$

with $\hat{Z}^{(0)}(\Omega) = \hat{Z}_1^{(0)}(\Omega) \sin \zeta + \hat{Z}_2^{(0)}(\Omega) \cos \zeta$, where ζ denotes the homodyne detection angle. Here \hat{i}_1 (\hat{i}_2) is the amplitude (phase) quadrature operator of the incoming vacuum field at the dark port [108]. The susceptibilities are given by (cf. Ref. [38]):

$$R_{FF}(\Omega) = \frac{\theta^2 m}{4} \frac{\lambda}{(\Omega - \lambda + i\epsilon)(\Omega + \lambda + i\epsilon)}, \quad (2.146)$$

$$R_{Z_1 F}(\Omega) = \sqrt{\frac{\epsilon\theta^2 m}{2\hbar}} \frac{\lambda}{(\Omega - \lambda + i\epsilon)(\Omega + \lambda + i\epsilon)}, \quad (2.147)$$

$$R_{Z_2 F}(\Omega) = -\sqrt{\frac{\epsilon\theta^2 m}{2\hbar}} \frac{\epsilon - i\Omega}{(\Omega - \lambda + i\epsilon)(\Omega + \lambda + i\epsilon)}, \quad (2.148)$$

$$R_{Z_\zeta F}(\Omega) = R_{Z_1 F}(\Omega) \sin \zeta + R_{Z_2 F}(\Omega) \cos \zeta. \quad (2.149)$$

The susceptibility $R_{FF}(\Omega)$ describes the optical spring [36] and $R_{Z_i F}(\Omega)$ are optical transfer functions from the differential mode to the outgoing quadrature fields.

In order to compare different interferometer topologies, it is useful to normalize the output observable $\hat{Z}^{(1)}(\Omega)$ to unit signal, which means that the solution of the linear equations (2.138)-(2.140) for $\hat{Z}^{(1)}(\Omega)$ is divided by the term in front of the signal part $Lh(\Omega)$. The resulting equation

$$\hat{O}(\Omega) = \hat{\mathcal{N}} + Lh \quad (2.150)$$

$$= \hat{Z}(\Omega) + R_{xx}(\Omega)\hat{\mathcal{F}}(\Omega) + \hat{x}^{(0)}(\Omega) + Lh(\Omega) \quad (2.151)$$

is a relation between the signal-referred quantum noise $\hat{\mathcal{N}}$, the gravitational wave signal and the output observable \hat{O} . The new quantities used here are defined as follows:

$$\hat{Z}(\Omega) = \frac{\hat{Z}^{(0)}(\Omega)}{R_{ZF}(\Omega)}, \quad \hat{\mathcal{F}}(\Omega) = \hat{F}^{(0)}(\Omega) - R_{FF}(\Omega) \frac{\hat{Z}^{(0)}(\Omega)}{R_{ZF}(\Omega)}. \quad (2.152)$$

One can infer from the commutation relations of the observables $\hat{Z}(\Omega)$ and $\hat{\mathcal{F}}(\Omega)$ that they can be regarded at each instant of time as the canonical momentum and coordinate of different effective monitors.

Note that Eqs. (2.141) and (2.150) depend on the quantized coordinate $\hat{x}^{(0)}(\Omega)$ of the unperturbed test masses. This term can be disregarded, since it has been shown by Braginsky et al. in Ref. [24] that no additional noise arises from the quantization of the test masses. In order to remove the influence of the test masses' quantization from the final noise spectral density, one has to filter the output data appropriately. Applying such a

filter is quite reasonable, since one is only interested in measuring the change of position of the interferometer's test masses induced by a classical force, namely a gravitational wave, while the initial quantum state of the test masses is unimportant. This fact simplifies the investigation of the performance of current and future gravitational wave detectors, since only the quantum noise arising from the light has to be examined.

Furthermore, the photocurrent generated by output field [cf. Eq. (2.150)] can be recorded directly on any storage device. This is possible, since the photocurrent, which is proportional to the output field, can be regarded as purely classical due to the vanishing commutator at different times:

$$[\hat{\mathcal{O}}(t), \hat{\mathcal{O}}(t')] = 0, \quad \text{for all } t, t'. \quad (2.153)$$

Noise spectral density

The two time correlation matrix given by

$$Q_{AB}(t, t') \equiv \langle \hat{A}(t) \hat{B}(t') \rangle_{\text{sym}} = \frac{1}{2} \langle \hat{A}(t) \hat{B}(t') + \hat{B}(t') \hat{A}(t) \rangle \quad (2.154)$$

yields a quantitative measure of the internal fluctuations of a given system. Even though the correlation matrix completely characterizes these fluctuations, it is more convenient for many applications to consider the equivalent noise spectral density. According to the Wiener-Khinchine theorem, the single-sided (cross-) noise spectral density $S_{AB}(\Omega)$ is given by

$$Q_{AB}(t, t') = \frac{1}{2} \int_{-\infty}^{\infty} S_{AB}(\Omega) e^{-i\Omega(t-t')} \frac{d\Omega}{2\pi}. \quad (2.155)$$

For a double-sided noise spectral density, the factor 1/2 in front of the integral can be dropped. Both definitions, i.e. the single-sided as well as the double-sided noise spectral density, are commonly used in the literature. Throughout this thesis, however, the single-sided convention is employed, which is preferably used by the gravitational wave community. The Fourier transform of Eq. (2.155) is given by

$$\frac{1}{2} \langle \hat{A}(\Omega) \hat{B}^\dagger(\Omega') + \hat{B}^\dagger(\Omega') \hat{A}(\Omega) \rangle = \frac{1}{2} 2\pi \delta(\Omega - \Omega') S_{AB}(\Omega). \quad (2.156)$$

In the case of a gravitational wave detector, the expectation value is defined with respect to the input state, which is a vacuum state, either coherent or squeezed. Assuming a usual vacuum input state $|0\rangle$, the (signal-referred) noise spectral density of the output observable $\hat{\mathcal{O}}(\Omega)$ [cf. Eq. (2.150)] is given by

$$S_h(\Omega) = \frac{1}{L^2} (S_{ZZ}(\Omega) + 2R_{xx}(\Omega) \Re[S_{\mathcal{F}Z}(\Omega)] + R_{xx}^2(\Omega) S_{\mathcal{F}\mathcal{F}}(\Omega)), \quad (2.157)$$

which depends on the different spectra of the observables defined in Eq. (2.152). These spectra can easily be calculated by using

$$\frac{1}{2} \langle 0 | \hat{i}_l(\Omega) \hat{i}_k^\dagger(\Omega') + \hat{i}_k^\dagger(\Omega') \hat{i}_l(\Omega) | 0 \rangle = \frac{1}{2} 2\pi \delta(\Omega - \Omega') \delta_{kl}, \quad (2.158)$$

or they can be found explicitly in Ref. [38].

We consider a simple example in order to clarify the meaning of the noise spectral density: if we assume $t = t'$ and $A = B$ [which implies that $S_{AA}(\Omega) = S_{AA}(-\Omega)$], we have

$$\Delta\hat{A}^2(t) = Q_{AA}(t, t) = \int_0^\infty S_{AA}(\Omega) \frac{d\Omega}{2\pi}, \quad (2.159)$$

which means that the variance of the observable \hat{A} is obtainable by integrating its noise spectral density over all positive frequencies.

Standard quantum limit

The standard quantum limit (SQL) [23, 27, 45] is a well-known reference limit in conventional interferometric gravitational wave detectors, more generally speaking, it limits any conventional high precision measurement. An interferometer measures the change in the test mass mirror's relative positions. The position observable, however, does not commute at different times and the associated commutation relation in the case of a free mass reads:

$$[\hat{x}^{(0)}(t), \hat{x}^{(0)}(t')] = \frac{i\hbar(t-t')}{\mu} = \frac{i\hbar\tau}{\mu}, \quad (2.160)$$

where μ is the reduced mass. This evokes the uncertainty relation

$$\Delta x^{(0)}(t) \Delta x^{(0)}(t') \geq \frac{\hbar|t-t'|}{2\mu} = \frac{\hbar\tau}{2\mu}. \quad (2.161)$$

If the measurement time τ is interpreted as the bandwidth of the measurement, the minimum noise spectral density at frequency $\Omega = 2/\tau$ is given by $\Delta x^{(0)}(t) = \Delta x^{(0)}(t') \simeq \sqrt{S_x(\Omega)/\tau}$ (cf. Chap. 6.2 in [27]). From these considerations, we can directly infer the SQL, i.e.

$$S_h^{\text{SQL}}(\Omega) = \frac{2\hbar}{\mu\Omega^2 L^2}. \quad (2.162)$$

This derivation of the SQL is simply based on the quantum mechanics of the interferometer's test masses, while other features are not taken into account. The same result can be obtained by focusing on the meter's properties, i.e. the laser light measuring the differential mode of motion, without paying attention to the quantum mechanics of the test masses. A generalized Heisenberg inequality relates the second-order noise moments of the pair of canonically conjugate variables $\hat{\mathcal{F}}(\Omega)$, $\hat{\mathcal{Z}}(\Omega)$:

$$S_{\mathcal{Z}\mathcal{Z}}(\Omega)S_{\mathcal{F}\mathcal{F}}(\Omega) - S_{\mathcal{Z}\mathcal{F}}(\Omega)S_{\mathcal{F}\mathcal{Z}}(\Omega) \geq \hbar^2. \quad (2.163)$$

In the case of uncorrelated shot noise and radiation pressure force noise, i.e. $S_{\mathcal{F}\mathcal{Z}}(\Omega) = S_{\mathcal{Z}\mathcal{F}}(\Omega) = 0$, one obtains from Eq. (2.157) and Eq. (2.163) a lower boundary for the noise spectral density:

$$S_h(\Omega) \geq S_h^{\text{SQL}}(\Omega) = \frac{2|R_{xx}(\Omega)|\hbar}{L^2} = \frac{2\hbar}{\mu\Omega^2 L^2}, \quad (2.164)$$

which coincides with Eq. (2.162). In the case of a LIGO interferometer, the reduced mass is $\mu = m/4$ where m is the mass of a single mirror. These two derivations of the SQL are completely different and the question arises how they are related. This was extensively investigated by Braginsky et al. in Ref. [24], who found that the true origin

Symbol	physical meaning	AdvLIGO NB	AdvLIGO BB
m	single mirror mass	40 kg	40 kg
$2\pi c/\omega_0$	laser wavelength	1064 nm	1064 nm
P	circulating power	800 kW	800 kW
L	interferometer arm length	4 km	4 km
ϕ	detuning phase of SR cavity	2π 0.242	2π 0.247
ρ_{SR}	SR mirror reflectivity	$\sqrt{0.93}$	$\sqrt{0.93}$
γ_o	cavity half bandwidth	2π 15 Hz	2π 15 Hz
ζ	detection angle	2π 0.347	2π 0.45
ϵ	effective half bandwidth	2π 120 Hz	2π 395 Hz
λ	effective detuning	2π 290 Hz	2π 411 Hz

Table 2.1.: Parameter values for Advanced LIGO [1] configurations used throughout this thesis. The parameters were obtained by means of the optimization procedure introduced in Sec. 3.1. The narrowband (NB) configuration is optimized for NS-NS binaries, using the current Advanced LIGO noise budget (cf. also Fig. 3.1). For the broadband (BB) operational mode, we allow 10% decrease in detectable distance for NS-NS binaries, while maximizing the contribution to the SNR from frequencies above 500 Hz.

of the SQL is noise due to the quantization of the meter, not the test masses. But the inherent connection between the meter and the test masses ensures that the SQL can be derived either way. This connection is a consequence of the vanishing commutation relation of the output observables [cf. Eq. (2.153)]. The quantized test masses cause a non-vanishing contribution to this commutator, which is canceled by the shot noise and radiation pressure noise contributions. This cancelation explains the identical results obtained by the different derivations of the SQL.

After a rather controversial debate, it was eventually realized that the SQL can in principle be surpassed either by putting the meter into a certain initial state or by measuring an appropriately chosen linear combination of the probe's observables. In gravitational wave detectors, the former case corresponds to the injection of squeezed light, while the latter accounts for a variational measurement of the output field. Such techniques are called quantum non-demolition (QND) measurements.

2.3.5. Measurement process

The noise spectral density of an output field leaking from a given device can be deduced directly from the properties of the input field and the transfer function of the optical system under consideration. From an experimental point of view, an appropriate photo-sensitive measurement of the output field must be accomplished in order to obtain a noise spectral density. A photo detector converts the outgoing field into a photocurrent which is subsequently analyzed. The required electronic circuit exhibits a well-defined response function which also determines the final measurement result. These experimental aspects are discussed e.g. by Yurke in Ref. [173]. Here the discussion is restricted to ideal photo detection schemes providing a photocurrent directly proportional to the power spectrum

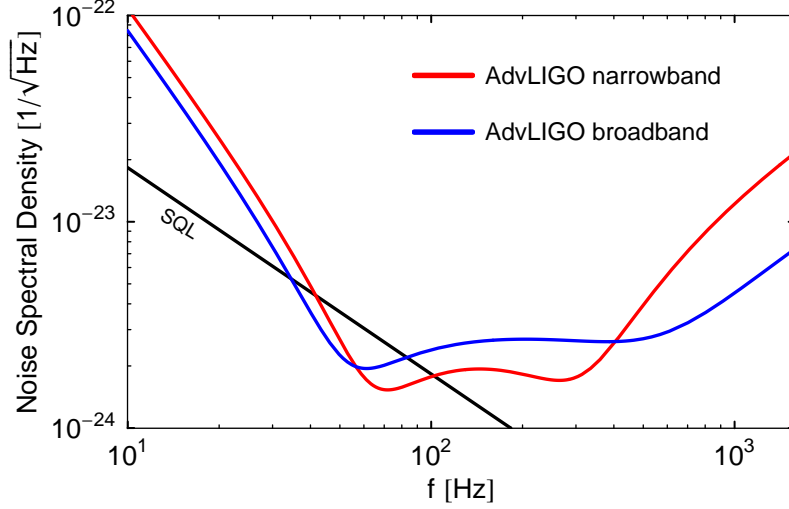


Figure 2.4.: Quantum noise spectral densities of two Advanced LIGO interferometer configurations. The parameters for the narrowband as well as for the broadband operational mode are given in Tab. 2.1.

of the incident light.

The signal intended to be measured is encoded in the sideband fields around the carrier frequency ω_0 . The bandwidth of the detection apparatus is limited and therefore a cut-off in the frequency domain has to be introduced, which discards the Fourier components of the electromagnetic field outside a certain range. However, in general a small frequency band around ω_0 contains the relevant signal and hence the cut-off does not significantly influence the overall sensitivity. Adopting the notation introduced in Ref. [40], we can write the output field as follows

$$\hat{S}^{\Omega_c}(\omega_0; t) = \sqrt{\frac{2\pi\hbar\omega_0}{\mathcal{A}c}} \int_{\omega_0 - \Omega_c}^{\omega_0 + \Omega_c} \frac{d\omega}{2\pi} \hat{a}(\omega) e^{-i\omega t} + \text{h.c.} \quad (2.165)$$

$$= \hat{S}_1^{\Omega_c}(\omega_0; t) \cos(\omega_0 t) + \hat{S}_2^{\Omega_c}(\omega_0; t) \sin(\omega_0 t), \quad (2.166)$$

where $S_{1,2}^{\Omega_c}(\omega_0; t)$ are the quadrature phases introduced in Eq. (2.38). The superscript Ω_c indicates that only frequencies within the interval $[\omega_0 - \Omega_c, \omega_0 + \Omega_c]$ are taken into account.

For many applications, only a weak signal light leaks out from the output port, which cannot be detected directly by simply shining it on a photodiode. Furthermore a direct measurement would yield a photocurrent proportional to the square of the field given in Eq. (2.166), which would cause a mixing of signal contributions at different sideband frequencies. This cannot easily be reversed when postprocessing the measurement data. It is therefore necessary to combine the outgoing signal light with an intense local oscillator in order to enhance the weak signal and avoid a mixing of the different frequency contributions. This can be achieved by employing a homodyne or heterodyne readout scheme, both of which are discussed in this section.

Homodyne detection

A homodyne detector is operated by a local oscillator which consists of a monochromatic wave with amplitude $L(t)$ and a fluctuating part $\delta L(t)$. This fluctuating part is usually not shot noise limited, but the additional noise can be removed from the final measurement output by using a balanced detection scheme, as shown e.g. in Ref. [173]. The signal field $\hat{S}^{\Omega_c}(\omega_0; t)$ is combined at a 50:50 beam splitter with the local oscillator $E_{\text{LO}}(t) = L(t) + \delta L(t)$. The combined fields, which propagate towards the two photodiodes, are given by

$$\hat{A}_1(t) = \frac{1}{\sqrt{2}} \left(\hat{S}^{\Omega_c}(\omega_0; t) + E_{\text{LO}}(t) \right), \quad \hat{A}_2(t) = \frac{1}{\sqrt{2}} \left(\hat{S}^{\Omega_c}(\omega_0; t) - E_{\text{LO}}(t) \right). \quad (2.167)$$

Since the photodiodes measure the intensity of the incident light, the corresponding photocurrents are proportional to the squared field amplitudes:

$$\hat{I}_1(t) \propto \hat{A}_1^2(t) = \frac{1}{2} \left(L^2(t) + 2L(t)(\delta L(t) + \hat{S}^{\Omega_c}(\omega_0; t)) + (\delta L(t) + \hat{S}^{\Omega_c}(\omega_0; t))^2 \right) \quad (2.168)$$

$$\hat{I}_2(t) \propto \hat{A}_2^2(t) = \frac{1}{2} \left(L^2(t) + 2L(t)(\delta L(t) - \hat{S}^{\Omega_c}(\omega_0; t)) + (\delta L(t) - \hat{S}^{\Omega_c}(\omega_0; t))^2 \right). \quad (2.169)$$

From these equations we can infer that fluctuations introduced by the local oscillator give rise to a common mode signal. These fluctuations can be canceled out by considering only the difference of the photocurrents generated by the distinct photodiodes, i.e.:

$$\hat{\mathcal{O}}_{\text{PD}} \equiv \hat{A}_1^2(t) - \hat{A}_2^2(t) = 2L(t)\hat{S}^{\Omega_c}(\omega_0; t) + 2\delta L(t)\hat{S}^{\Omega_c}(\omega_0; t), \quad (2.170)$$

where $\hat{\mathcal{O}}_{\text{PD}} \propto \hat{I}_1(t) - \hat{I}_2(t)$. The second term on the right hand side is usually negligible since $L(t) \gg \delta L(t)$. Such a detection scheme therefore provides a direct measurement of the signal field, amplified by the local oscillator's amplitude. The noise spectral density of the photocurrent is proportional to the noise spectral density of the signal field. We have to demand that the local oscillator oscillates at the same carrier frequency ω_0 as the signal light, i.e.

$$L(t) = A \cos(\omega_0 t - \theta), \quad (2.171)$$

where θ denotes the phase of the local oscillator. Inserting Eqs. (2.166) and (2.171) into Eq. (2.170) and applying a low pass filter reveals the differential photocurrent

$$\hat{I}_1(t) - \hat{I}_2(t) \propto \hat{\mathcal{O}}_{\text{PD}} = A \left(\hat{S}_1^{\Omega_c}(\omega_0; t) \cos(\theta) + \hat{S}_2^{\Omega_c}(\omega_0; t) \sin(\theta) \right). \quad (2.172)$$

The measured quadrature of the signal field can be varied by adjusting the phase of the local oscillator.

Heterodyne detection

Currently operating gravitational wave detectors use the heterodyne readout scheme. This detection strategy requires that the carrier field injected into the interferometer exhibits phase modulation sidebands at frequencies $\omega_0 \pm \omega_{sm}$, the so-called Schnupp sideband fields with $\Omega_c < \omega_{sm} < \omega_0$. Due to an asymmetry between the interferometer's arms, the modulation sidebands will not exactly satisfy the dark fringe condition [cf. Eq. (2.70)],

even though a monochromatic carrier would satisfy it. For this reason the sideband modulation fields partially leak out from the dark port and provide a local oscillator (at frequencies $\omega_0 \pm \omega_{sm}$) which is represented by

$$L(t) = \Lambda_- \cos[(\omega_0 - \omega_{sm})t - \theta_-] + \Lambda_+ \cos[(\omega_0 + \omega_{sm})t - \theta_+], \quad (2.173)$$

where Λ_{\pm} and θ_{\pm} are the amplitude and phase, respectively, belonging to the upper (+) or lower (−) modulation sideband. The signal intended to be measured is contained in the sideband fields around ω_0 . It can easily be shown that sideband fields around frequencies $\omega_0 \pm 2\omega_{sm}$ also contribute to the final measurement output, hence it is convenient to split the signal field into the following relevant parts:

$$\begin{aligned} \hat{S}^{\Omega_c}(t) = & \hat{S}_1^{\Omega_c}(\omega_0 - 2\omega_{sm}, t) \cos[(\omega_0 - 2\omega_{sm})t] + \hat{S}_2^{\Omega_c}(\omega_0 - 2\omega_{sm}, t) \sin[(\omega_0 - 2\omega_{sm})t] \\ & + \hat{S}_1^{\Omega_c}(\omega_0; t) \cos[\omega_0 t] + \hat{S}_2^{\Omega_c}(\omega_0; t) \sin[\omega_0 t] \\ & + \hat{S}_1^{\Omega_c}(\omega_0 + 2\omega_{sm}, t) \cos[(\omega_0 + 2\omega_{sm})t] + \hat{S}_2^{\Omega_c}(\omega_0 + 2\omega_{sm}, t) \sin[(\omega_0 + 2\omega_{sm})t] \\ & + \text{contributions from irrelevant frequency bands.} \end{aligned} \quad (2.174)$$

The total output field $\hat{S}^{\Omega_c}(t) + L(t)$ needs to be squared and demodulated (multiplied with $\cos(\omega_{sm}t + \phi_D)$). The result is composed of several parts oscillating at different frequencies. By applying a low pass filter, all oscillating parts are discarded and the resulting photocurrent is proportional to:

$$\hat{O}_{PD} = \frac{1}{2} \Lambda_0 \left[\frac{\Lambda_-}{\Lambda_0} \hat{S}_{\phi_D + \theta_-}^{\Omega_c}(\omega_0 - 2\omega_{sm}, t) + \hat{S}_{\theta_0}^{\Omega_c}(\omega_0; t) + \frac{\Lambda_+}{\Lambda_0} \hat{S}_{-\phi_D + \theta_+}^{\Omega_c}(\omega_0 + 2\omega_{sm}, t) \right], \quad (2.175)$$

with

$$\Lambda_0 = \left| \Lambda_+ e^{-i(\phi_D + \theta_+)} + \Lambda_- e^{i(\phi_D - \theta_-)} \right| \quad \theta_0 = \arg \left[\Lambda_+ e^{-i(\phi_D + \theta_+)} + \Lambda_- e^{i(\phi_D - \theta_-)} \right]. \quad (2.176)$$

and

$$\hat{S}_{\zeta}^{\Omega_c}(\omega; t) = \hat{S}_1^{\Omega_c}(\omega; t) \cos(\zeta) + \hat{S}_2^{\Omega_c}(\omega; t) \sin(\zeta). \quad (2.177)$$

The middle term $\hat{S}_{\theta_0}^{\Omega_c}(\omega_0; t)$ in Eq. (2.175) contains the signal and it is directly accessible via a homodyne measurement. In the case of a heterodyne detection scheme, additional noise contributions originating from vacuum fluctuations around the frequencies $\omega_0 \pm 2\omega_{sm}$ can disturb measurement.

In principle, the Schnupp modulation sideband fields also acquire a gravitational wave signal. But as long as only a small fraction of the total power is pumped into the modulation sideband fields this effect is negligible and therefore only the additional quantum noise needs to be considered. One can also disregard classical laser noise since currently used laser sources are quantum noise limited at sufficiently high modulation frequencies ω_{sm} . The final noise spectral density can be split into a homodyne detection part and a contribution from the heterodyne detection:

$$S_n^{\text{het}}(\phi_D, \Omega) = S_n^{\text{hom}}(\phi_D, \Omega) + S_n^{\text{add}}(\phi_D, \Omega), \quad (2.178)$$

with

$$S_n^{\text{add}}(\phi_D, \Omega) = \frac{\Lambda_+^2 + \Lambda_-^2}{\Lambda_0^2}. \quad (2.179)$$

In the case of a balanced modulation, i.e. $\Lambda_+ = \Lambda_-$, only one quadrature determined by the Schnupp modulation phase is measured:

$$\theta_0 = \frac{1}{2}(\theta_+ + \theta_-), \quad (2.180)$$

with an additional noise of

$$S_n^{\text{add}}(\phi_D, \Omega) = \frac{1}{2}, \quad (2.181)$$

provided that an optimal demodulation phase is chosen:

$$\phi_D = \frac{1}{2}(-\theta_+ + \theta_-). \quad (2.182)$$

Employing a heterodyne detection scheme introduces additional noise but it permits the simultaneous detection of different quadratures. A closer look on the totally unbalanced case in which either Λ_+ or Λ_- is zero clarifies this. E.g. for $\Lambda_- = 0$ the detected quadrature is given by

$$\theta_0 = \phi_D + \theta_+, \quad (2.183)$$

which means that one can flexibly adjust the detection angle by simply adapting the demodulation phase ϕ_D . Therefore the noise spectral density can be optimized for each sideband frequency, which cannot easily be accomplished by a homodyne detection scheme (cf. Ref. [108]). But even an optimal heterodyne quadrature readout is not able to enhance the QND performance of a conventional interferometer, as shown in in Ref. [40].

Note that for a heterodyne detection at the interferometer's output port only one photodiode is required. Alternatively one can renounce the modulation of the interferometer's input field and superpose the output field at a beam splitter with an appropriately modulated field. In this case the set-up resembles that required for the homodyne detection scheme.

2.3.6. Quantum Langevin equation

The quantum Langevin formalism provides a third method for the derivation of equations of motion for operators belonging to a well defined system \mathcal{S} , which in turn belongs to the Hilbert space $\mathcal{H}_{\mathcal{S}}$. This system is influenced by a "heat bath" \mathcal{B} consisting of an assembly of harmonic oscillators. The corresponding mode operators of the bath act on the Hilbert space $\mathcal{H}_{\mathcal{B}}$. Any operator associated with a single Hilbert space corresponds to an operator acting on the combined Hilbert space

$$\mathcal{H} = \mathcal{H}_{\mathcal{S}} \otimes \mathcal{H}_{\mathcal{B}}. \quad (2.184)$$

For the derivation of the quantum Langevin equation, carried out in detail by Gardiner and Collett in Ref. [79], three assumptions are essential:

- Couplings between system \mathcal{S} and bath \mathcal{B} are linear in the operators belonging to the bath \mathcal{B} .
- The rotating wave approximation removes infinite effects and serves as a renormalization.

- The bath spectrum is flat (white) and the Markov approximation ensures that the bath-system coupling constant is frequency independent.

The total Hamiltonian is given by

$$\hat{H}_{\text{tot}} = \hat{H}_{\mathcal{S}} + \hat{H}_{\mathcal{B}} + \hat{V}, \quad (2.185)$$

where $\hat{H}_{\mathcal{S}}$ is a function of the internal mode operators of the system \mathcal{S} , while $\hat{H}_{\mathcal{B}}$ is the free Hamiltonian of the bath. The coupling between \mathcal{S} and \mathcal{B} is described by the interaction Hamiltonian \hat{V} . It was shown in Ref. [79] that the quantum Langevin equation for an arbitrary Heisenberg operator $\hat{a} \in \mathcal{S}$ is given by

$$\dot{\hat{a}} = -\frac{i}{\hbar}[\hat{a}, \hat{H}_{\mathcal{S}}] - \left([\hat{a}, \hat{c}^\dagger] \left(\frac{\gamma}{2}\hat{c} - \sqrt{\gamma}\hat{b}_{\text{in}}\right) - \left(\frac{\gamma}{2}\hat{c} - \sqrt{\gamma}\hat{b}_{\text{in}}\right) [\hat{a}, \hat{c}^\dagger]\right), \quad (2.186)$$

where \hat{c} describes the particular internal mode of the system \mathcal{S} which couples to the bath \mathcal{B} and γ corresponds to an internal damping of the system. The other modes belonging to the system only couple indirectly through \hat{c} with the bath. An ingoing field is defined by $\hat{b}_{\text{in}}(t)$, which satisfies the commutation relation

$$[\hat{b}_{\text{in}}(t), \hat{b}_{\text{in}}^\dagger(t')] = \delta(t - t'). \quad (2.187)$$

Note that Eq. (2.186) only provides a differential equation for an arbitrary internal mode, which is in general not directly accessible. Only the fields leaving the system \mathcal{S} are detectable by an appropriate device. These outgoing fields can be obtained via the time-reversed Langevin equation:

$$\hat{b}_{\text{out}}(t) = \hat{b}_{\text{in}}(t) - \sqrt{\gamma}\hat{c}(t). \quad (2.188)$$

For applications in quantum optics the "heat bath" is given by an electromagnetic field equivalent to an assembly of harmonic oscillators. In the case of a detuned cavity or equivalently a whole detuned signal-recycled interferometer, the probe (test masses) as well as the detector (optical system) belong to the system \mathcal{S} . In contrast to the linear quantum measurement approach discussed in Sec. 2.3.4, there is no distinction between these two components. Note that the quantum Langevin formalism also applies to systems exhibiting nonlinear interactions between the internal modes. Neither the explicit form of $\hat{H}_{\mathcal{S}}$ is constrained nor are the properties of the system operators or their commutation relations.

For a detuned cavity, the system Hamiltonian was derived first in Ref. [112] and was frequently used in the literature. In more recent publications, e.g. Refs. [161, 162], a slightly different notation was introduced, which we adopt here. Accordingly, the system Hamiltonian reads:

$$\hat{H}_{\mathcal{S}} = \hbar\omega_c\hat{a}^\dagger\hat{a} + \frac{1}{2m}\hat{p}^2 + \frac{m\omega_m}{2}\hat{x}^2 - \hbar\frac{\omega_0}{L}\hat{a}^\dagger\hat{a}\hat{x} - F\hat{x} + i\hbar E \left(e^{-i\omega_0 t}\hat{a}^\dagger - e^{i\omega_0 t}\hat{a}\right). \quad (2.189)$$

The first term describes the cavity mode with optical frequency ω_c , where \hat{a} ($[\hat{a}, \hat{a}^\dagger] = 1$) is the corresponding annihilation operator. The second and third term account for the end mirror, which is treated as a quantized simple harmonic oscillator. The position and momentum operators (\hat{x}, \hat{p}) describe a suspended end mirror with mass m and pendulum

eigenfrequency ω_m and they obey the commutation relation $[\hat{x}, \hat{p}] = i$. The fourth term accounts for the radiation pressure force and is proportional to the number of photons within the cavity of length L . The fifth term specifies an external classical force acting on the mirror. In the case of a gravitational wave with strain $h(t)$, the force is given by $F(t) = mL\ddot{h}(t)$. The last two terms describe the driving laser with frequency ω_0 , which is assumed to be quantum noise limited. The complex quantity E is related to the input laser power P_{in} by $|E| = \sqrt{P_{\text{in}}\gamma/(\hbar\omega_0)}$ where γ is the photon decay rate. By defining dimensionless position and momentum variables, namely $\hat{x} \rightarrow \hat{x}\sqrt{\hbar/(m\omega_m)}$ and $\hat{p} \rightarrow \hat{p}\sqrt{\hbar m\omega_m}$, one obtains the Hamiltonian

$$\hat{H}_S = \hbar\omega_c\hat{a}^\dagger\hat{a} + \frac{\hbar\omega_m}{2}(\hat{p}^2 + \hat{x}^2) - \hbar G\hat{a}^\dagger\hat{a}\hat{x} - L\sqrt{\frac{m\hbar}{\omega_m}}\ddot{h}(t)\hat{x} + i\hbar E \left(e^{-i\omega_0 t}\hat{a}^\dagger - e^{i\omega_0 t}\hat{a} \right), \quad (2.190)$$

with the coupling constant given by $G = (\omega_0/L)\sqrt{\hbar/(m\omega_m)}$. Converting the cavity mode operator from the Heisenberg picture into the interaction picture and using Eq. (2.186) yields a set of coupled quantum Langevin equations:

$$\dot{\hat{x}}(t) = \omega_m\hat{p}(t), \quad (2.191)$$

$$\dot{\hat{p}}(t) = -\omega_m\hat{x}(t) - \gamma_m\hat{p}(t) + G\hat{a}^\dagger(t)\hat{a}(t) + k\ddot{h}(t) + \hat{\xi}(t), \quad (2.192)$$

$$\dot{\hat{a}}(t) = -\left(\frac{\gamma}{2} + i\omega_c + i\omega_0\right)\hat{a}(t) + iG\hat{x}(t)\hat{a}(t) + E + \sqrt{\gamma}\hat{a}_{\text{in}}(t), \quad (2.193)$$

where γ_m corresponds to a mechanical damping giving rise to additional fluctuations described by the Brownian noise operator $\hat{\xi}$. Furthermore the quantity k was introduced: $k = L\sqrt{m/(\hbar\omega_m)}$. Now the operators can be linearized around the steady state:

$$\hat{a} = \alpha_s + \delta\hat{a}, \quad \hat{x} = x_s + \delta\hat{x}, \quad \hat{p} = p_s + \delta\hat{p}. \quad (2.194)$$

Inserting Eq. (2.194) into Eqs. (2.191)-(2.193) yields a set of decoupled equations. By solving the equations for the steady state one obtains:

$$p_s = 0, \quad x_s = G|\alpha_s|^2/\omega_m, \quad \alpha_s = E/(\gamma/2 + i\Delta), \quad (2.195)$$

with $\Delta = \omega_c - \omega_0 - G^2|\alpha_s|^2/\omega_m$. After defining the quadratures

$$\hat{X} = \frac{1}{\sqrt{2}}(\delta\hat{a} + \delta\hat{a}^\dagger), \quad \hat{Y} = \frac{1}{i\sqrt{2}}(\delta\hat{a} - \delta\hat{a}^\dagger), \quad (2.196)$$

$$\hat{X}_{\text{in}} = \frac{1}{\sqrt{2}}(\hat{a}_{\text{in}} + \hat{a}_{\text{in}}^\dagger), \quad \hat{Y}_{\text{in}} = \frac{1}{i\sqrt{2}}(\hat{a}_{\text{in}} - \hat{a}_{\text{in}}^\dagger), \quad (2.197)$$

we obtain the well-known linearized quantum Langevin equations:

$$\delta\dot{\hat{x}} = \omega_m\delta\hat{p}, \quad \delta\dot{\hat{p}} = -\omega_m\delta\hat{x} - \gamma_m\delta\hat{p} + \kappa\delta\hat{x} + k\ddot{h}(t) + \hat{\xi}, \quad (2.198)$$

$$\dot{\hat{X}} = -\frac{\gamma}{2}\hat{X} + \Delta\hat{Y} + \sqrt{\gamma}\hat{X}_{\text{in}}, \quad \dot{\hat{Y}} = -\frac{\gamma}{2}\hat{Y} - \Delta\hat{X} + \kappa\delta\hat{x} + \sqrt{\gamma}\hat{Y}_{\text{in}}, \quad (2.199)$$

with $\kappa = \sqrt{2}G\alpha_s$. Note that the phase of E was so chosen that α_s is real. Applying the following substitutions

$$\gamma \rightarrow 2\epsilon, \quad \Delta \rightarrow -\lambda, \quad \kappa \rightarrow \frac{\theta}{4\omega_m} \quad (2.200)$$

to Eqs. (2.198)-(2.199), where ϵ , λ and θ are defined as in Sec. 2.3.1, and converting the equations into the Fourier domain yields:

$$\begin{aligned} -i\Omega\delta\hat{x} &= \omega_m\delta\hat{p}, & -i\Omega\delta\hat{p} &= -\omega_m\delta\hat{x} - \gamma_m\delta\hat{p} + \frac{\theta}{4\omega_m}\hat{x} - \Omega^2kh + \hat{\xi}, \\ -i\Omega\hat{X} &= -\epsilon\hat{X} - \lambda\hat{Y} + \sqrt{2\epsilon}\hat{X}_{\text{in}}, & -i\Omega\hat{Y} &= -\epsilon\hat{Y} + \lambda\hat{X} + \frac{\theta}{4\omega_m}\delta\hat{x} + \sqrt{2\epsilon}\hat{Y}_{\text{in}}. \end{aligned} \quad (2.201)$$

Solving this set of linear equations yields a solution for the field inside the cavity, e.g. the cavity mode. After employing Eq. (2.188) in order to obtain the outgoing field we find the final solution which exactly agrees with that already provided in Eq. (2.107).

2.3.7. Cavity modes

The operators \hat{a} , \hat{a}^\dagger used in Eq. (2.190) are cavity mode operators and describe the whole field inside the resonator. Strictly speaking, one has to distinguish between the normal and the cavity mode: the cavity mode describes the real field inside an arbitrary resonator, while normal modes are only defined for a closed system, e.g. a perfect cavity. This means that the idea of normal and cavity modes only coincide in the case of a closed system. Despite this difference, the Langevin formalism always deals with normal modes. Any kind of damping which makes the resonator imperfect, e.g. optical losses or a transmitting mirror, are taken into account by introducing a coupling of the normal modes to a reservoir. This method was originally introduced by Senitzky [142], refined by Gardiner and Collett [50, 80, 81] and nicely recapitulated and extended by Dutra and Nienhuis [67]. However, a leaky cavity is an open system and the question arises whether it is really possible to describe the intra-cavity field by an expansion into the undamped normal modes of a closed system. Since the normal modes of a perfect cavity form a complete orthonormal set [cf. Eq. (2.11)], defined for the space inside the resonator, any field can be expanded in terms of these modes. This can be deduced directly from the theory of Fourier series. But due to the boundary conditions of a closed system, the normal modes have to vanish at both ends of the resonator. In the case of a cavity with a transmitting mirror, the field does not necessarily satisfy this condition and consequently cannot be correctly described at the boundaries by a normal mode expansion. This is the main reason why the Langevin formalism can break down for low finesse cavities. One then has to use various approaches discussed extensively in the literature: the cavity mode can be defined intuitively by identifying the parts of the field which are self-repeating, apart from a decay factor in a complete round trip inside a leaky cavity. This leads to the theory of the so-called Fox-Li cavity modes [76, 77] used in laser physics. These modes are not necessarily orthogonal, which is important for the explanation of so-called excess noise, where the Schawlow-Townes linewidth of a laser is enhanced (cf. Ref. [131]). Even more sophisticated formalisms are presented for instance in Refs. [66, 67], where the authors give up the idea of commuting reservoir and system operators. However, it was also pointed out that the normal modes used within the framework of the Langevin approach are a good approximation in the case of a high finesse cavity.

In Sec. 5.8.4, entanglement between a cavity mode and test masses will be investigated. In the literature, the Langevin formalism is commonly used for the derivation of the required cavity mode. But since the formalisms introduced in Secs. 2.3.1 and 2.3.4 are used throughout this thesis, it is not convenient to switch to the Langevin formalism.

Remember that, in contrast to the Langevin approach, the previous sections have dealt with transfer functions for the continuous quadrature amplitude operators of quantized beams of light. The mathematical representation of such a beam has been obtained by choosing an infinite quantization volume. Despite the infinite quantization volume, this concept provides an appropriate description of the field inside a finite cavity volume. One can think of an infinite propagating wave reflected back and forth by the two end mirrors of the resonator. Alternatively one could imagine an infinite beam of light manipulated at certain locations, which corresponds to reflections on mirrors or interactions with other optical components. However, by adopting the concept of an infinite beam of light, one can calculate the effective time-dependent quadrature amplitudes at a certain location within the cavity, consisting of a superposition of the back and forth reflected beam. The question arises how the quadrature amplitudes at a certain location are related to the cavity mode.

First it should be demonstrated how a certain mode can be extracted from an electric field restricted to a finite quantization volume. If this finite quantization volume comprises a single dimension, one obtains the following expression from Eq. (2.17):

$$\hat{E}(t - x/c) = i \sum_k \left(\frac{2\pi\hbar\omega_k}{A2L} \right)^{1/2} \left[\hat{a}_k e^{-i\pi kc/Lt} - \hat{a}_k^\dagger e^{i\pi kc/Lt} \right]. \quad (2.202)$$

Note that the quantization length is now given by $2L$, where L is the length of the cavity. Obviously, the time and spatial evolution of the field are equivalent and the following mode functions can be defined in analogy to Eq. (2.13):

$$u_n(t) = \sqrt{\frac{c}{2L}} e^{-i\pi nc/Lt}, \quad n \in \mathbb{N}. \quad (2.203)$$

These mode functions form a complete set and with respect to the scalar product

$$(\psi, \phi) = \int_{t'}^{2L/c+t'} dt \psi^*(t) \phi(t) \quad (2.204)$$

they are orthonormal, e.g. $(u_n, u_{n'}) = \delta_{n,n'}$. The n th mode of the electric field given in Eq. (2.202) can be extracted by evaluating the following expression:

$$\hat{E}_n(t') = (u_n(t), \hat{E}(t)) u_n(t') + \text{h.c.}, \quad (2.205)$$

where the field at $x = 0$ was considered.

Now we pass to the case where the field is described by an infinite beam of light. Consequently the field inside the resonator is no longer expressed by such normal modes, as in Eq. (2.202), but by the continuous annihilation and creation operators

$$\hat{E}(t) = \sqrt{\frac{2\pi}{Ac}} \int_0^\infty \frac{d\omega}{2\pi} \sqrt{\hbar\omega} \hat{a}(\omega) e^{-i\omega t} + \text{h.c.} \quad (2.206)$$

A particular mode can be extracted by the same procedure as before. As already mentioned, the normal modes form a complete orthonormal set and consequently even the field inside a leaky cavity can be approximately described by an expansion into these

normal modes of a closed system. According to the previous considerations, this requires the evaluation of the following scalar products:

$$(u_n(t), \hat{E}(t)) = \sqrt{\frac{2\pi}{\mathcal{A}c}} \int_0^\infty \frac{d\omega}{2\pi} \sqrt{\hbar\omega} \hat{a}(\omega) \sqrt{\frac{c}{2L}} \int_{t'}^{2L/c+t'} dt e^{i(-\omega + \pi n c/L)t}. \quad (2.207)$$

The continuous mode operator $a(\omega)$ only gives a significant contribution around $\omega \approx \omega_0$ and therefore it is sufficient to consider a particular scalar product with $\omega_{\text{res}} \equiv \pi n_{\text{res}} c/L = \omega_0 - \lambda$ where n_{res} is so chosen that λ is minimized. Here, $\lambda \ll \omega_0$ denotes the detuning of the cavity. Then one obtains:

$$(u_{n_{\text{res}}}(t), \hat{E}(t)) \approx \sqrt{\frac{2\pi}{\mathcal{A}c}} \sqrt{\frac{2L}{c}} \int_0^\infty \frac{d\omega}{2\pi} \sqrt{\hbar\omega} \hat{a}(\omega) e^{-i\omega t'} e^{i\omega_{\text{res}} t'}, \quad (2.208)$$

which leads to the expression:

$$\hat{E}_{n_{\text{res}}}(t') = (u_{n_{\text{res}}}(t), \hat{E}(t)) u_{n_{\text{res}}}(t') + \text{h.c.} \approx \sqrt{\frac{2\pi}{\mathcal{A}c}} \int_0^\infty \frac{d\omega}{2\pi} \sqrt{\hbar\omega} \hat{a}(\omega) e^{-i\omega t'} + \text{h.c.}, \quad (2.209)$$

being in agreement with Eq. (2.206). This means that Eq. (2.206) already approximately describes a certain mode of the field, originating from the assumption that the continuous mode operator only gives a significant contribution around the carrier frequency. The experienced reader might already be aware of this trivial interrelation. From Eq. (2.206) one can deduce that the cavity mode operators are only re-normalized continuous mode operators:

$$\hat{a}_i \rightarrow \sqrt{\frac{2L}{c}} \hat{a}_i \quad \text{with } i \in \{1, 2\}, \quad (2.210)$$

where we have already passed to the quadrature amplitudes.

After calculating the output field quadrature amplitudes $\hat{\mathbf{a}}_{\text{out}}$ of a cavity in terms of the ingoing quadrature amplitudes $\hat{\mathbf{a}}_{\text{in}}$, one can obtain the intra-cavity mode by the following important rule:

$$\hat{\mathbf{a}}_{\text{cav}} = \sqrt{\frac{2L}{c}} \sqrt{\frac{1}{T}} (\hat{\mathbf{a}}_{\text{out}} + \hat{\mathbf{a}}_{\text{in}}). \quad (2.211)$$

This is an important relation which will be used frequently in the following investigations and it coincides with the relation already given in Eq. (2.188).

2.3.8. Adiabatic elimination

The Hamiltonian associated with a simple cavity [cf. Eq. (2.190)] describes two degrees of freedom, the cavity mode and the suspended mirror, which couple through radiation pressure fluctuations. For many experimental scenarios, these coupled degrees of freedom have different dynamical time scales. If one scale is very much faster than the other, the dynamics of the fast variable are *slaved* to the slow variable. This means that the quick system *adiabatically* follows the slow one. For a measurement performed in the large cavity bandwidth limit [$\epsilon \gg \omega_m, \theta/(4\omega_m)$], the cavity mode adiabatically follows the mirror dynamics, i.e. equilibrium is reached quasi-instantaneously. Therefore an adiabatic process is also called quasi-static. This implies that the cavity mode dynamics can be eliminated by discarding the corresponding derivatives in Eqs. (2.198)-(2.199).

The resulting equations of motion in the Fourier domain can easily be solved and one obtains:

$$\hat{X} = \hat{X}_{\text{in}}, \quad (2.212)$$

$$\hat{Y} = \hat{Y}_{\text{in}} + \frac{2}{\sqrt{T}} \sqrt{\frac{8P\omega_0\hbar}{c^2}} \frac{1}{\hbar} \hat{x}, \quad (2.213)$$

$$\hat{x} = -\frac{1}{m\Omega^2} \frac{2}{\sqrt{T}} \sqrt{\frac{8P\omega_0\hbar}{c^2}} \hat{X}_{\text{in}} + s, \quad (2.214)$$

where P is the circulating power inside the resonator. The factor $2/\sqrt{T}$ accounts for the averaged number of round trips of a photon inside the cavity. In comparison to the result obtain for a simple mirror in Eqs. (2.88) and (2.87), the susceptibility of the phase quadrature to the mirror motion as well as the susceptibility of the mirror motion to the fluctuating amplitude quadrature is amplified by the number of round trips. In the case of negligible cavity dynamics the implementation of a resonator only gives rise to a higher effective power and consequently a stronger coupling between the field and the mirror motion compared to a single mirror.

3. Gravitational wave spectrum

In 1915 Albert Einstein formulated the general theory of relativity, which is the geometric theory of gravitation [68]. Even before it was fully developed, it was clear that this theory would have to predict gravitational waves. In order to preserve compatibility with the special relativity theory, gravity must be causal. This means that the time-varying gravitational field of accelerated masses is distributed in spacetime no faster than the speed of light. This motivates the idea that there exists some kind of "gravitational radiation". The Einstein field equations form the basis of the general relativity theory. By introducing certain simple assumptions, it is possible to rewrite these equations so that they take the form of wave equations. The associated waves are ripples in the curvature of spacetime [75, 119] and are generated by massive bodies, so moving that they generate a quadrupole moment. Note that monopole waves would violate mass-energy conservation, while dipole waves violate momentum conservation. It should be emphasized that there is a close analogy between electromagnetic and gravitational radiation: gravitational waves (GWs) originate from accelerated masses, while electromagnetic waves arise from accelerated charges. The basic properties of gravitational waves were worked out by Einstein within months after completing his general relativity theory [69, 70]. His final result is known today as the *quadrupole formula* for the emission of gravitational wave radiation [75]. It turned out that only very large astrophysical objects moving at relativistic speeds are candidates for interesting gravitational wave sources. A discussion of various sources is found, for instance, in Ref. [75]. After emission, gravitational waves interact only very weakly with matter and thus they propagate as though in a vacuum, which makes their detection extremely challenging. A detailed introduction to the topic of general relativity is provided in Refs. [89, 119] or in Ref. [88], which is more stringent from a mathematical point of view.

A gravitational wave alters the distance between widely separated objects, i.e. it causes a change δL_{GW} in the proper distance L between two spacetime events [11], which can be described by the dimensionless quantity

$$h = \frac{2\delta L_{\text{GW}}}{L}, \quad (3.1)$$

the so-called gravitational wave amplitude (or GW strain). In contrast to the electromagnetic field, the quantity h falls off as $1/r$. This is due to the fact that the total energy flowing through large spheres must be conserved. The lowest order contribution depends on the source's time-varying quadrupole moment Q and on the distance r to the source:

$$h = \frac{2G}{c^4} \frac{1}{r} \ddot{Q} \quad (3.2)$$

where G is Newton's gravitational constant and c the speed of light. In order to obtain a rough estimation [16, 95] the quadrupole moment can be approximated by $\ddot{Q} \simeq 2Mv^2 \simeq 4E_{\text{kin}}^{\text{ns}}$ where v is the internal velocity of the source and $E_{\text{kin}}^{\text{ns}}$ the non-spherical part of

its internal kinetic energy. For a neutron star binary system located in a distance of 100 Megaparsecs (Mpc) with a total mass of $E_{\text{kin}}^{\text{ns}}/c^2 = 2.8$ solar masses one obtains

$$h \sim 10^{-20}. \quad (3.3)$$

This implies that we have to measure the change in distance between two test masses separated by 4 km with an accuracy of one-tenth of a femtometer, which is one millionth of an atom width. This elucidates why no attempt to directly detect gravitational waves has yet been successful. Only an indirect proof was furnished by means of the neutron star binary system PSR1913+16 (cf. e.g. Ref. [97]).

Currently operating gravitational wave detectors are optimized for the observation of merging compact binary systems. Such astrophysical objects consist of two neutron stars (NS-NS), a neutron star and a black hole (NS-BH) or two black holes (BH-BH). Signals from the adiabatic phase of a binary inspiral can be modeled very accurately with post-Newtonian methods. This allows us to carry out an optimization for the detection of such sources, which is recapitulated in Sec. 3.1. The detection of more speculative sources, for which no analytical waveforms are available, requires a broadening of the detection band. A possible optimization procedure is proposed in Sec. 3.2. The inevitable classical noise floor limits the sensitivity of gravitational wave detectors at certain frequencies. We provide a tool which allows us to test the exploitation of a given classical noise budget in Sec. 3.3

3.1. Detector optimization for binary sources

In order to quantify the performance of various gravitational wave detector configurations an appropriate assessment criterion is required. For this purpose we consider inspiraling binary systems consisting of compact astrophysical objects such as neutron stars and/or black holes. For these GW sources we will calculate the matched-filtering signal-to-noise ratio (SNR) or the detectable distance for a given threshold SNR. For known waveforms $h(f)$ (in the frequency domain), the optimal SNR, achievable by correlating the data with a known template, is (cf. Ref. [74])

$$\rho^2 = 4 \int_0^\infty df \frac{|h(f)|^2}{S_h(f)}, \quad (3.4)$$

where $S_h(f)$ is the single-sided noise spectral density of the interferometer. For compact binary objects one obtains (see, e.g. Ref. [57])

$$|h(f)| = \frac{G^{5/6} \mu^{1/2} M^{1/3}}{\sqrt{30} \pi^{2/3} c^{3/2} D} f^{-7/6} \Theta(f_{\text{max}} - f) \quad (3.5)$$

with

$$M = (M_1 + M_2) \quad \text{and} \quad \mu = \frac{M_1 M_2}{M_1 + M_2}, \quad (3.6)$$

where μ , M , M_1 and M_2 are the reduced, total and single masses of the binary system and D is the distance from the source to the detector. Note that the amplitude $|h(f)|$ is that where the rms average over all directions is already taken into account. There is an upper cut-off frequency, f_{max} , in Eq. (3.5), beyond which the systems undergo a

transition from adiabatic inspiral to non-adiabatic merger, and Eq. (3.5) is no longer a valid approximation. This frequency is usually taken to be the GW frequency at the last stable circular orbit given, for a test mass in a Schwarzschild space time with mass M (cf. Ref. [41]), by

$$f_{\max} \approx 4400 \text{ Hz} \left(\frac{M_{\odot}}{M} \right). \quad (3.7)$$

A lower cut-off frequency also needs to be taken into account for integration in Eq. (3.4). Below f_{\min} it is no longer possible to treat the system as stationary and we take $f_{\min} \approx 7$ Hz. This frequency almost agrees with the limit imposed by seismic noise on the detector. Usually we focus on the optimization for NS-NS binary inspirals, which have a total mass of 2.8 solar masses. For such systems, the last stable circular orbit gives an upper frequency limit of $f_{\max} = 1570$ Hz. Considering binaries of averaged orientation, the observable distance for a given SNR ρ_0 reaches

$$D = \sqrt{\frac{2}{15} \frac{G^{5/6} \mu^{1/2} M^{1/3}}{\pi^{2/3} c^{3/2} \rho_0}} \sqrt{\int_{f_{\min}}^{f_{\max}} df \frac{f^{-7/3}}{S_h(f)}}. \quad (3.8)$$

Here we assume that the event rate is roughly proportional to the cube of the radius of the detectable range, i.e.,

$$\mathcal{R} \propto D^3. \quad (3.9)$$

Note that we have only considered the lowest Post-Newtonian approximation, which imposes certain limits on the application of the presented formulas. But in Chap. 4 only the relative performance of different topologies is investigated, so that the formulas are sufficient for our purposes.

3.2. Broadband optimization

Note that the optimization strategy discussed in the previous section tends to focus on the low frequency regime at the expense of sensitivity at higher frequencies – due to the rather steep power law of $f^{-7/3}$ in Eq. (3.5). Performing an optimization in this way yields a good sensitivity for binary systems, but the search for GWs should also be extended to the so-called GW bursts with not well modeled properties. These sources include supernova explosions in our Galaxy, mergers of compact binary systems, gamma ray burst engines and other energetic sources [3, 4, 5]. Since the waveforms of GWs from such sources are poorly known, a more broadband optimization needs to be carried out in order to achieve a better sensitivity in the high frequency regime. This can be accomplished in the following way: first a narrowband optimization, described in the previous section, is performed, where we keep all configurations obeying an event rate which is at least a certain fraction of the optimal event rate for binary systems. In a second step these configurations are explored in the high frequency regime by considering a smaller frequency integration interval, i.e. [500 Hz; 1570 Hz], and selecting the optimal signal-to-noise ratio on this interval. Note that we use the same power law for this frequency interval as before. There are alternative approaches with different power laws, e.g. cf. Ref. [106], but their methods yield comparable results.

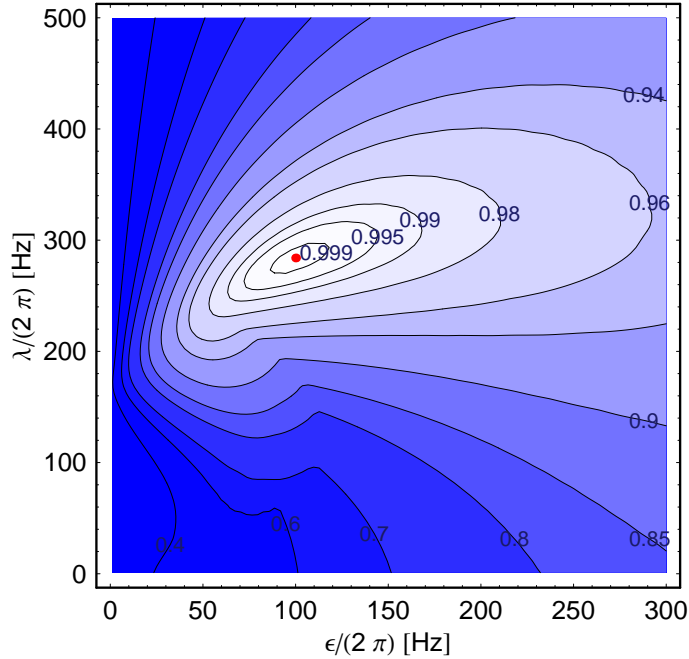


Figure 3.1.: Contour plot illustrates the sensitivity of Advanced LIGO in the (ϵ, λ) -plane: red dot marks the Advanced LIGO narrowband configuration (cf. Tab. 2.1) yielding a maximum event rate for the detection of NS-NS binary systems. Labels of contour lines indicate the percentage of the achievable event rate compared to the maximal event rate, i.e. $(D(\epsilon, \lambda)/D_{\max}^{\text{AdvNB}})^3$ [cf. Eq. (3.8)]. For each point in the (ϵ, λ) -plane the detection angle has been optimized. Residual parameters are given in Tab. 2.1

3.3. Limitations of detector optimization

The inevitable presence of classical noise imposes a limit on the sensitivity of a GW detector. We need another assessment criterion in order to quantify the exploitation of this limit by a certain detector design and a given set of parameters. The total classical noise budget obtained by adding up all different classical noise contributions needs to be compared with the final noise spectral density of a detector where both, classical and quantum noise, are taken into account. Let us define

$$\begin{aligned} \eta(f_{\text{up}}) &\equiv \int_{f_{\text{min}}}^{f_{\text{up}}} \frac{f^{-7/3}}{S_h(f)} df / \int_{f_{\text{min}}}^{f_{\text{up}}} \frac{f^{-7/3}}{S_h^{\text{cl}}(f)} df \\ &\equiv \frac{\bar{S}_h^{\text{cl}}}{\bar{S}_h} = \frac{\bar{S}_h^{\text{cl}}}{\bar{S}_h^{\text{cl}} + \bar{S}_h^{\text{q}}}, \end{aligned} \quad (3.10)$$

where \bar{S}_h^{cl} , \bar{S}_h^{q} and \bar{S}_h are the weighted averages of the classical, quantum, and total noise spectrum in the in the frequency interval $[7 \text{ Hz}; f_{\text{up}}]$, respectively. If the newly defined quantity $\eta \in [0; 1]$ is close to unity, it is indicated that the quantum noise is only a small fraction of the total noise. This implies that the noise spectral density almost follows the borderline set by the classical noise up to the frequency f_{up} .

4. Advanced interferometer concepts

Beginning in the mid-1970s, a major effort has been made to establish an international array of long-baseline laser interferometers to detect gravitational waves. First generation ground-based observatories, i.e. LIGO [144], VIRGO [73], GEO [169] and TAMA [9], are already operating. They are aimed at the detection of gravitational waves in the audio frequency band ($10 - 10^4$ Hz), within which they are reaching their design sensitivities. These large-scale laser interferometers are based upon the original simple Michelson interferometer topology (cf. Sec. 2.2) and measure relative changes in locations of mirror-endowed, nearly free test masses. But instead of single mirrors they are equipped with Fabry-Pérot cavities in the arms. Furthermore a so-called power-recycling (PR) mirror is placed at the laser input port in order to recycle unused laser light leaking out from the bright port. The GEO detector is the only exception, since it does not use arm cavities but dual-recycling [91].

Currently planned second generation gravitational wave laser interferometers such as Advanced LIGO [1] will start operation around 2014. Advanced LIGO will exploit the extensively investigated signal-recycling (SR) technique: an additional mirror is placed behind the dark port of the interferometer, which results in a modified resonance structure. The optical resonance frequency and bandwidth can be altered by changing the location and reflectivity of the SR mirror, which provides some flexibility in aiming at the detection of different astrophysical sources. If the SR cavity formed by the input test mass mirrors of the arm cavities and the SR mirror is neither resonant nor anti-resonant with respect to the carrier frequency, the optical configuration is called *detuned signal-recycling*. As demonstrated theoretically by Buonanno and Chen [36, 37, 38] and experimentally by Somiya et al. [147] and Miyakawa et al. [120], the power inside a detuned SR interferometer depends on the motion of the mirrors, which gives rise to the so-called *optical spring*. This effect can entail a second resonance besides the optical one, which is known as the optomechanical resonance: the eigenfrequency of the suspended test masses can be shifted from the pendulum frequency (~ 1 Hz) up to the detection band. The detector can gain sensitivity around both resonances. The general principle underlying the optical spring effect is identical to that explained by Braginsky and Khalili [26] for a single detuned cavity (cf. Ref. [38]), employed in their proposal of the *optical bar* detection scheme [25].

One concern using the optical spring is that the quantum noise limited sensitivity at frequencies below the optomechanical resonance is significantly lower than that of non-optical-spring interferometers. The reason for this inherent drawback is clarified in Sec. 4.2 and a possible way out is presented, relying on a local measurement of the position of the arm cavities' input mirrors by an independent carrier light.

A second concern is the instability introduced by the optical spring due to the anti-damping associated with the optical force. This instability can be cured by incorporating a linear feedback control system, which ideally would not modify the noise spectral density of a gravitational wave detector as shown by Buonanno and Chen in Ref. [37]. In Sec. 4.3

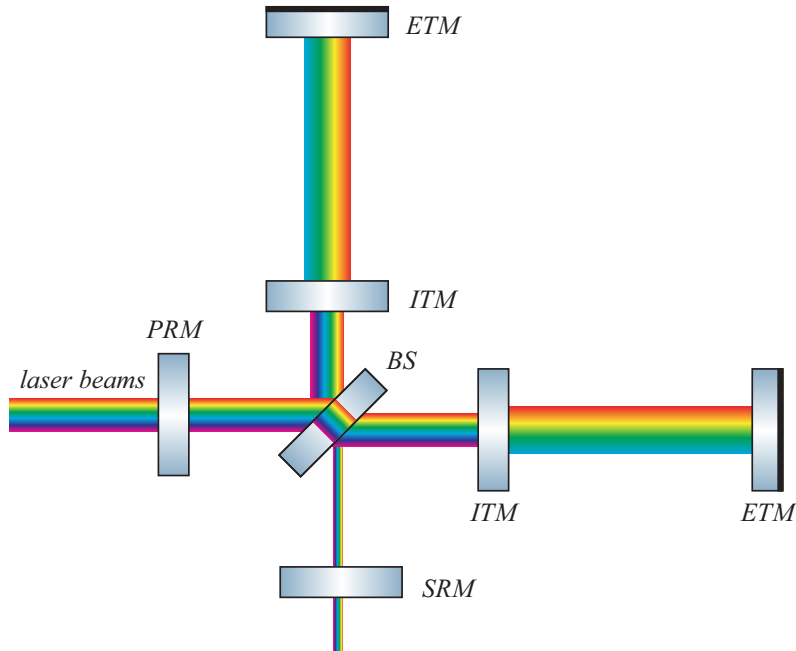


Figure 4.1.: Artistic impression of a multi-carrier power- and signal-recycling Michelson interferometer equipped with arm-cavities. Some carrier fields resonate in the arm-cavities while others are directly reflected from the ITMs.

an alternative all-optical stabilization scheme is introduced, employing a second optical spring. The local readout as well as the double optical spring scheme can be considered as upgrade options for the Advanced LIGO detector or concepts for third generation detectors. Both proposals involve two carrier lights, which increases the possibility of re-shaping the noise spectral density. We optimize each configuration for a detection of neutron star binary systems and additionally a broadband optimization is carried out. Such layouts might also solve the parametric instability problem (cf. Refs. [28, 29]) which can occur in the case of a high laser power buildup in the arm cavities.

The investigations are brought into a more general context in Sec. 4.1 by the formulation of a universal theoretical framework for the treatment of multi-carrier interferometers. All main issues, including the optimal combination of the multiple output channels, are explored for an arbitrary number of carrier fields.

Finally an interferometric configuration comprising Kerr-nonlinear arm-cavities is investigated in Sec. 4.4. Such a system might apply for future gravitational wave detectors or simply for a continuous-wave source of squeezed light.

4.1. Multi-carrier interferometer

In the following we investigate signal-recycling laser interferometers operated by multiple independent carrier lights. Such a configuration is shown schematically in Fig. 4.1. Different laser sources need to be merged before injection into the input port of the interferometer. By choosing either distinct polarizations or frequencies, we can ensure that there is no direct coupling between the fields, i.e. no interference effects occur between

them. This is verified in Sec. 4.1.1 for an arbitrary number of carrier lights. Using this result, we can effectively obtain a multiplicity of interferometers in one scheme, where parameters such as detuning and mirror reflectivities can be chosen independently for each individual interferometer.

The outgoing sideband fields, associated with the different carrier lights, are split and each is sensed separately by a homodyne detection scheme. The various outputs need to be combined in an optimal way, which requires the implementation of an appropriate filtering procedure. In Sec. 4.1.3 a general expression for the optimal filter functions is provided.

These general results are used for the investigation of two concrete scenarios: the *local readout enhancement of detuned SR interferometers* [136] in Sec. 4.2 and the *double optical spring enhancement for gravitational wave detectors* [137] in Sec. 4.3. Finally a combination of both techniques is considered in Sec. 4.3.4.

4.1.1. Independent carriers

In this section we consider a light field composed of various independent ideal laser beams. We assume that the free propagation of each contribution can be treated independently and in the same manner as discussed in Sec. 2.1.2. But the question arises whether there are interference effects when n carrier fields impinge on a mirror and couple optomechanically. The total field composed of the different carrier lights and the corresponding quantum noise parts [cf. also Eq. (2.39)] is given by

$$\begin{aligned}\hat{E}_{\text{tot}}(t) &= \sum_{i=1}^n \left[\Lambda^{(i)} \cos(\omega_0^{(i)} t - \theta^{(i)}) \right] + \cos(\omega_0 t) \hat{E}_1(t) + \sin(\omega_0 t) \hat{E}_2(t) \\ &= \sum_{i=1}^n \left[\cos(\omega_0^{(i)} t) (\hat{E}_1^{(i)}(t)/n + \Lambda^{(i)} \cos(\theta^{(i)})) + \sin(\omega_0^{(i)} t) (\hat{E}_2^{(i)}(t)/n + \Lambda^{(i)} \sin(\theta^{(i)})) \right],\end{aligned}\quad (4.1)$$

$$(4.2)$$

i.e. there is a unique quantum noise floor replenished by the n carrier fields. The quantum noise part can be centered around an arbitrary frequency ω_0 , since it can always be shifted by an appropriated integral substitution. In order to clarify this, it is convenient to switch to the representation of the electromagnetic field given in Eq. (2.33):

$$\hat{E}^{\text{sb}}(t) = \sqrt{\frac{2\pi\hbar\omega_0}{\mathcal{A}c}} \int_{-\infty}^{\infty} \frac{d\Omega}{2\pi} \hat{a}(\omega_0 + \Omega) e^{-i\Omega t} + \text{h.c.} \quad (4.3)$$

$$\stackrel{\Omega \rightarrow \Omega - \omega_0 + \omega'_0}{=} \sqrt{\frac{2\pi\hbar\omega'_0}{\mathcal{A}c}} \int_{-\infty}^{\infty} \frac{d\Omega}{2\pi} \hat{a}(\omega'_0 + \Omega) e^{-i\Omega t} + \text{h.c.} \quad (4.4)$$

In this way Eq. (4.2) is obtained: the common quantum noise contribution has been divided into n parts and each one has been centered at one of the n carrier frequencies $\omega_0^{(i)}$. A careful calculation reveals the total momentum flow [cf. Eq. (2.49)]:

$$\dot{p}_{\text{total}}(t) = \frac{\mathcal{A}}{4\pi} (\hat{E}_{\text{tot}}(t))^2 = \sum_{i=1}^n \left[\Lambda^{(i)} (\hat{E}_1^{(i)}(t) \cos(\theta^{(i)}) + \hat{E}_2^{(i)}(t) \sin(\theta^{(i)})) \right], \quad (4.5)$$

where we have taken only first-order terms into account, i.e. the quantum part amplified by the classical carrier amplitudes [cf. also Eq. (2.51)]. Obviously no cross terms occur and consequently even fields with the same polarization show no interference effects when impinging on a mirror. There is no direct coupling between the fields, which provides an important basis for the following investigations.

4.1.2. Transfer functions

This section is closely related to Sec. 2.3.4, where we have recapitulated a detuned signal-recycling interferometer operated by a single carrier light. All previously introduced quantities need to be redefined for an appropriate treatment of a multi-carrier configuration.

We assume a general configuration as shown in Fig. 4.1, where the carrier fields $i = 1, \dots, k$ enter the arm cavities, while the carrier fields $i = k + 1, \dots, n$ only impinge on the input test mass mirrors. This implies that we need to consider the differential motion of the end test mass mirrors (ETMs) and the input test mass mirrors (ITMs) separately, since they are exposed to different optical fields. Additionally, the beam splitter (BS) motion normal to its reflective surface has to be taken into account. In the following we list the Heisenberg equations of motions in frequency domain [36, 37, 38, 54, 108] for the differential mode of motion of the ETMs (\hat{x}_{ETM}) and the ITMs (\hat{x}_{ITM}), respectively, as well as for the BS (\hat{x}_{BS}):

$$\hat{x}_{\text{ETM}} = R_{xx}^{\text{ETM}}(\Omega) \sum_{i=1}^k \left[\hat{F}^{(i)}(\Omega) + R_{FF}^{(i)}(\Omega)(\hat{x}_{\text{ETM}} - \hat{x}_{\text{ITM}}) \right] + L h + \hat{\xi}_{\text{ETM}}, \quad (4.6)$$

$$\begin{aligned} \hat{x}_{\text{ITM}} = & - R_{xx}^{\text{ITM}}(\Omega) \left\{ \sum_{i=1}^k \left[\hat{F}^{(i)}(\Omega) + R_{FF}^{(i)}(\Omega)(\hat{x}_{\text{ETM}} - \hat{x}_{\text{ITM}}) \right] \right. \\ & \left. - \sum_{i=k+1}^n \left[\hat{F}^{(i)}(\Omega) + R_{FF}^{(i)}(\Omega)(\hat{x}_{\text{ITM}} + \sqrt{2}\hat{x}_{\text{BS}}) \right] \right\} + \hat{\xi}_{\text{ITM}}, \end{aligned} \quad (4.7)$$

$$\hat{x}_{\text{BS}} = R_{xx}^{\text{BS}}(\Omega) \left\{ \sum_{i=k+1}^n \left[\hat{F}^{(i)}(\Omega) + R_{FF}^{(i)}(\Omega)(\hat{x}_{\text{ITM}} + \sqrt{2}\hat{x}_{\text{BS}}) \right] + \sum_{i=1}^n \hat{F}_{\text{BP}}^{(i)}(\Omega) \right\} + \hat{\xi}_{\text{BS}}. \quad (4.8)$$

Here we act on the assumption that gravitational waves with amplitude h incident from right above the detector plane exhibit a polarization that maximizes the response of our L -shaped Michelson interferometer. Furthermore we have used the fact that the free propagation of each field can be treated separately and no interference effects occur, as verified in the previous section. All the fields couple directly to the mirrors, which in turn implies that the fields are coupled indirectly. This indirect coupling of the fields via the mirror motion is taken into account by Eqs. (4.6)-(4.8).

The output associated with the n carrier fields [cf. also Eq. (2.140)] is given by

$$\begin{aligned}\hat{y}^{(i)}(\Omega) &= \hat{Y}_1^{(i)}(\Omega) \sin \zeta^{(i)} + \hat{Y}_2^{(i)}(\Omega) \cos \zeta^{(i)} \\ &\quad + [R_{Y_1 F}^{(i)}(\Omega) \sin \zeta^{(i)} + R_{Y_2 F}^{(i)}(\Omega) \cos \zeta^{(i)}](\hat{x}_{\text{ETM}} - \hat{x}_{\text{ITM}}) \quad \text{for } i \in [1, k], \quad (4.9) \\ \hat{y}^{(i)}(\Omega) &= \hat{Y}_1^{(i)}(\Omega) \sin \zeta^{(i)} + \hat{Y}_2^{(i)}(\Omega) \cos \zeta^{(i)} \\ &\quad + [R_{Y_1 F}^{(i)}(\Omega) \sin \zeta^{(i)} + R_{Y_2 F}^{(i)}(\Omega) \cos \zeta^{(i)}](\hat{x}_{\text{ITM}} + \sqrt{2}\hat{x}_{\text{BS}}) \quad \text{for } i \in [k+1, n]. \quad (4.10)\end{aligned}$$

It should be emphasized again that \hat{x}_{ITM} and \hat{x}_{ETM} account for the differential motion between two mirrors, while \hat{x}_{BS} describes the motion of a single mirror tilted 45 deg. This justifies the factor of $\sqrt{2}$ in front of the BS motion. Each optical component has its own mechanical susceptibility, namely

$$R_{xx}^{\text{ITM}}(\Omega) = R_{xx}^{\text{ETM}}(\Omega) = -\frac{2}{m\Omega^2} \quad \text{and} \quad R_{xx}^{\text{BS}}(\Omega) = -\frac{\sqrt{2}}{m_{\text{BS}}\Omega^2}, \quad (4.11)$$

where we assumed that ETMs, ITMs and BS can be treated as free masses and the ETMs and ITMs all have the same weight. The classical noise acting on these components is described by the operators $\hat{\xi}_m$ with $m \in [\text{ETM}, \text{ITM}, \text{BS}]$. According to Ref. [37] the free quantities (cf. also Sec. 2.3.4) $F^{(i)}(\Omega)$ and $\hat{Y}_j^{(i)}(\Omega)$ are related to the incoming amplitude and phase quadratures, $\hat{a}_1^{(i)}$ and $\hat{a}_2^{(i)}$, as follows:

$$\hat{F}^{(i)}(\Omega) = \sqrt{\frac{\epsilon^{(i)}\theta^{(i)}m\hbar}{2}} \frac{i\Omega - \epsilon^{(i)} \hat{a}_1^{(i)} + \lambda^{(i)} \hat{a}_2^{(i)}}{(\Omega + i\epsilon^{(i)})^2 - (\lambda^{(i)})^2}, \quad (4.12)$$

$$\hat{Y}_1^{(i)}(\Omega) = \frac{[(\lambda^{(i)})^2 - (\epsilon^{(i)})^2 - \Omega^2] \hat{a}_1^{(i)} + 2\lambda^{(i)}\epsilon^{(i)} \hat{a}_2^{(i)}}{(\Omega + i\epsilon^{(i)})^2 - (\lambda^{(i)})^2}, \quad (4.13)$$

$$\hat{Y}_2^{(i)}(\Omega) = \frac{-2\lambda^{(i)}\epsilon^{(i)} \hat{a}_1^{(i)} + [(\lambda^{(i)})^2 - (\epsilon^{(i)})^2 - \Omega^2] \hat{a}_2^{(i)}}{(\Omega + i\epsilon^{(i)})^2 - (\lambda^{(i)})^2}. \quad (4.14)$$

As aforementioned, the carrier lights $i = k+1, \dots, n$ are completely reflected from the ITMs and therefore they only perceive a Michelson interferometer without cavities in the arms. According to Ref. [87], the dark port vacuum fluctuations associated with these carriers are primarily responsible for the motion of the BS. It should be emphasized that the outputs corresponding to the subset of carrier lights which enter the arm cavities, i.e. $i = 1, \dots, k$, are only marginally influenced by seismic, thermal and radiation pressure noise introduced at the beam splitter. This can be explained as follows: the carrier fields entering the arm cavities generally exhibit a lower power incident on the BS than those not entering the arm cavities. Further, fluctuations associated with the carriers $i = 1, \dots, k$ do not build up as much as those associated with the carriers $i = k+1, \dots, n$, both in common and in differential mode.

The incoming bright port amplitude fluctuations associated with the n carrier fields are described by the operators $b_1^{(i)}$. These fluctuations cause an additional motion of the BS, which gives rise to the second sum in Eq. (4.8), where the involved quantities are given

by

$$\hat{F}_{\text{BP}}^{(i)} = \gamma_0 \frac{L\sqrt{\theta^{(i)}m\hbar(1 - (\rho_{\text{PR}}^{(i)})^2)\gamma_0}}{\sqrt{2}c(-\gamma_0(1 - \rho_{\text{PR}}^{(i)}) + i(1 + \rho_{\text{PR}}^{(i)})\Omega)} b_1^{(i)} \quad \text{for } i \in [1, k], \quad (4.15)$$

$$\hat{F}_{\text{BP}}^{(i)} = \sqrt{\frac{\theta^{(i)}ml\hbar(1 + \rho_{\text{PR}}^{(i)})}{2c(1 - \rho_{\text{PR}}^{(i)})}} b_1^{(i)} \quad \text{for } i \in [k + 1, n]. \quad (4.16)$$

Here L is the length of the arm cavities, while l accounts for the distance between the BS and an ITM. The optical transfer functions (cf. Ref. [38] or Sec. 2.3.4) are given by

$$R_{Y_1F}^{(i)}(\Omega) = \sqrt{\frac{\epsilon^{(i)}\theta^{(i)}m}{2\hbar}} \frac{\lambda^{(i)}}{(\Omega + i\epsilon^{(i)})^2 - (\lambda^{(i)})^2}, \quad (4.17)$$

$$R_{Y_2F}^{(i)}(\Omega) = -\sqrt{\frac{\epsilon^{(i)}\theta^{(i)}m}{2\hbar}} \frac{\epsilon^{(i)} - i\Omega}{(\Omega + i\epsilon^{(i)})^2 - (\lambda^{(i)})^2}, \quad (4.18)$$

and the ponderomotive rigidity is described by the susceptibility

$$R_{FF}^{(i)}(\Omega) = \frac{m\theta^{(i)}}{4} \frac{\lambda^{(i)}}{(\Omega - \lambda^{(i)} + i\epsilon^{(i)})(\Omega + \lambda^{(i)} + i\epsilon^{(i)})}. \quad (4.19)$$

The optical resonance frequency of the differential optical mode (to be precise, that which is closest to this carrier) is defined for each carrier field separately and is given by $\omega_0^{(i)} - \lambda^{(i)} - i\epsilon^{(i)}$ where, in terms of interferometer parameters, $\lambda^{(i)}$ and $\epsilon^{(i)}$ are given by (cf. Ref. [38] or Sec. 2.3.4):

$$\lambda^{(i)} = \gamma_o \frac{2\rho_{\text{SR}}^{(i)} \sin(2\phi^{(i)})}{1 + (\rho_{\text{SR}}^{(i)})^2 + 2\rho_{\text{SR}}^{(i)} \cos(2\phi^{(i)})} \quad \text{and} \quad \epsilon^{(i)} = \gamma_o \frac{1 - (\rho_{\text{SR}}^{(i)})^2}{1 + \rho_{\text{SR}}^2 + 2\rho_{\text{SR}}^{(i)} \cos(2\phi^{(i)})}, \quad (4.20)$$

for $i \in [1, k]$ or

$$\lambda^{(i)} = c\phi^{(i)}/l \quad \text{and} \quad \epsilon^{(i)} = (1 - (\rho_{\text{SR}}^{(i)})^2)c/(4l), \quad (4.21)$$

for $i \in [k + 1, n]$. This implies that each carrier field can sense a different detuning of the SR cavity and a different SR mirror reflectivity.

Note that we have assumed in Eq. (4.9) that the carriers $i = 1, \dots, k$ only sense a differential cavity length, i.e. $\hat{x}_{\text{ETM}} - \hat{x}_{\text{ITM}}$, while we have ignored the slight difference between the sensitivities to ITMs and ETMs as well as motion of the BS. In Eq. (4.10), the carriers $i = k + 1, \dots, n$ only sense the differential motion between the ITMs and the BS, since these fields do not enter the arm cavities.

The operators $\hat{\xi}_{\text{ITM}}$, $\hat{\xi}_{\text{ETM}}$ and $\hat{\xi}_{\text{BS}}$ introduced in Eqs. (4.6)-(4.8) model the classical noise at ITMs, ETMs and BS, respectively. We assume that the noise contributions are uncorrelated but all have the same spectrum, namely one fourth of the total classical noise spectrum generally pre-estimated for the differential mode of motion in Advanced

LIGO [1]. The only non-vanishing correlation functions are given by

$$\begin{aligned}
\langle \hat{a}_k^{(i)}(\Omega) (\hat{a}_l^{(j)})^\dagger(\Omega') \rangle_{\text{sym}} &= \pi \delta(\Omega - \Omega') \delta_{ij} \delta_{kl}, \\
\langle \hat{b}_1^{(i)}(\Omega) (\hat{b}_1^{(j)})^\dagger(\Omega') \rangle_{\text{sym}} &= \pi \delta(\Omega - \Omega') \delta_{ij} S_1^{(i)}(\Omega), \\
\langle \hat{\xi}_{\text{ITM}}(\Omega) (\hat{\xi}_{\text{ITM}})^\dagger(\Omega') \rangle_{\text{sym}} &= 2\pi \delta(\Omega - \Omega') S_{\text{cl}}(\Omega), \\
\langle \hat{\xi}_{\text{ETM}}(\Omega) (\hat{\xi}_{\text{ETM}})^\dagger(\Omega') \rangle_{\text{sym}} &= 2\pi \delta(\Omega - \Omega') S_{\text{cl}}(\Omega), \\
\langle \hat{\xi}_{\text{BS}}(\Omega) (\hat{\xi}_{\text{BS}})^\dagger(\Omega') \rangle_{\text{sym}} &= \pi \delta(\Omega - \Omega') S_{\text{cl}}(\Omega),
\end{aligned} \tag{4.22}$$

from which we can obtain the single-sided noise spectral densities. The incoming bright- and dark port fluctuations associated with the different carrier fields are uncorrelated, while in each case they exhibit the same correlations. Here $S_1^{(i)}(\Omega)$ denotes the spectrum of technical input laser noise, while $S_{\text{cl}}(\Omega)$ characterizes the spectrum of all other classical noise sources in the gravitational wave strain. For the classical noise sources, we use the current noise budget of Advanced LIGO, as pre-estimated by the simulation tool *Bench* [2]; the various contributions, such as suspension thermal noise, seismic noise, thermal fluctuations in the coating and gravity gradient noise, are shown e.g. in Fig. 4.8.

4.1.3. Optimal filter functions

The outgoing sideband fields around the n different carriers are detected independently via homodyne detections. Thus a certain combination of the amplitude and phase quadrature (described by the phase $\zeta^{(i)}$ with $i \in [1, n]$) of each field is measured. We seek an optimal linear combination of the n measurement output channels in order to maximize the sensitivity to gravitational waves. In practice, an appropriate postprocessing of the n classical data streams has to be performed.

The input-output relations provided by Eqs. (4.6)- (4.10) can be rewritten in the form:

$$\hat{y}^{(i)}(\Omega) \equiv \mathbf{n}_i^T(\Omega) \cdot \boldsymbol{\nu}(\Omega) + s_i(\Omega)h(\Omega), \tag{4.23}$$

where $\boldsymbol{\nu}$ is a column vector with $3n + 3$ entries which account for $2n$ quadrature operators, n operators associated with the amplitude quadrature of the incoming bright port fluctuations and three operators modeling the classical noise:

$$\boldsymbol{\nu}^T = \left(\hat{a}_1^{(1)} \quad \hat{a}_2^{(1)} \quad \dots \quad \hat{a}_1^{(n)} \quad \hat{a}_2^{(n)} \quad \hat{b}_1^{(1)} \quad \dots \quad \hat{b}_1^{(n)} \quad \hat{\xi}_{\text{ITM}} \quad \hat{\xi}_{\text{ETM}} \quad \hat{\xi}_{\text{BS}} \right). \tag{4.24}$$

The column vector \mathbf{n}_i describes the noise transfer functions from the input noise channels $\boldsymbol{\nu}$ into the output channels $\hat{y}^{(i)}$. The transfer of the GW strain h is characterized by the functions s_i . The combination of the n output fields reads:

$$\hat{y}(\Omega) = \sum_{i=1}^n K_i(\Omega) \hat{y}^{(i)}(\Omega), \tag{4.25}$$

and one has to identify n optimal filter functions K_i , which minimize the combined signal-referred noise spectral density of \hat{y} :

$$S_h(\Omega) = \frac{\sum_{i,j=1}^n (\mathbf{N})_{ij} K_i K_j^*}{\sum_{i,j=1}^n (\mathbf{S})_{ij} K_i K_j^*}. \tag{4.26}$$

The matrices $\mathbf{S}, \mathbf{N} \in \mathbb{C}^{(n,n)}$ are given by

$$(\mathbf{S})_{ij} = s_i s_j^* \quad \text{and} \quad (\mathbf{N})_{ij} = \sum_{s,k=1}^{3n+3} (\mathbf{n}_i^T)_s S_{\nu_s \nu_k} (\mathbf{n}_j^\dagger)_k. \quad (4.27)$$

Here $S_{\nu_s \nu_k}$ is the (cross) spectral density between ν_s and ν_k [cf. Eq. (4.22)], with

$$\langle \nu_s(\Omega) \nu_k^\dagger(\Omega') \rangle = \pi \delta(\Omega - \Omega') S_{\nu_s \nu_k}(\Omega) \quad (4.28)$$

The inverse of the largest eigenvalue of the $n \times n$ -matrix

$$\mathbf{M} = \mathbf{N}^{-1} \cdot \mathbf{S}. \quad (4.29)$$

provides the resulting minimum noise spectral density and the corresponding eigenvector gives the n optimal filter functions K_i . Additionally we define the symmetrized and normalized filter matrix

$$(\mathbf{K}(\mathbf{X}))_{ij} = \frac{K_i(\mathbf{X})_{ij} K_j^*}{\sum_{l=1}^n |K_l|^2(\mathbf{X})_{ll}} \quad (4.30)$$

where the k th diagonal element gives the percentage of how much GW strain ($\mathbf{X} \equiv \mathbf{S}$), noise ($\mathbf{X} \equiv \mathbf{N}$) or overall output ($(\mathbf{X})_{ij} \equiv 1$) the k th output channel contributes to the combined output. The off-diagonal elements, or more precisely

$$2\Re [(\mathbf{K}(\mathbf{X}))_{ij}], \quad \text{for } i \neq j, \quad (4.31)$$

account for the correlations between the different outputs.

In the following section we apply the formalism introduced to a simple example configuration.

Radiation pressure noise cancelation

As a motivation for the investigation of the local readout scheme (cf. Sec. 4.2), a simple double-carrier configuration is considered in the following (cf. Fig. 4.2). The relative position of a suspended ETM is measured with respect to a fixed ITM as well as a suspended RTM. We are primarily interested in a relative length change between the ITM and the ETM which is sensed by means of the main carrier field. The phase quadrature of the corresponding output field is detected in order to maximize the signal which might contain a gravitational wave signal. This signal can be masked by radiation pressure noise in the low frequency regime. But the motion of the ETM is additionally sensed by an optomechanical sensor composed of a short cavity. The information gained by this second independent measurement can be used to cancel out the radiation pressure noise introduced by the main carrier, which allows us to improve sensitivity at low-frequencies (cf. Refs. [55, 56, 90, 105]). Note that such a scheme is also capable of canceling parts of classical noise contributions.

For the subsequent theoretical discussion we assume that the cavity mode can be eliminated adiabatically (cf. Sec. 2.3.8). Then the equation of motion for the ETM reads

$$\hat{x}_{\text{ETM}}(\Omega) = -\frac{1}{m\Omega^2} \left(\alpha^{(1)} \hat{a}_1^{(1)}(\Omega) - \alpha^{(2)} \hat{a}_1^{(2)}(\Omega) \right) + Lh(\Omega) \quad (4.32)$$

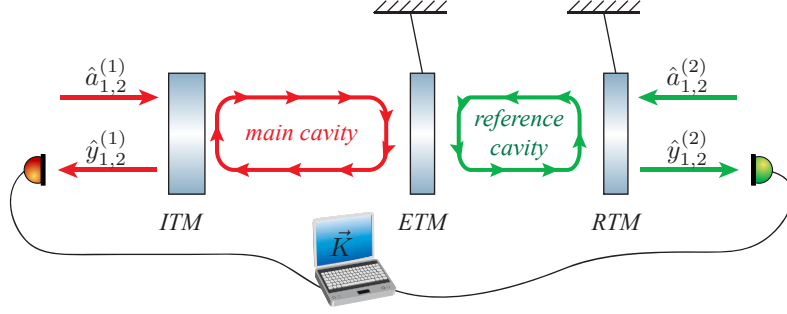


Figure 4.2.: The length of a Fabry-Pérot cavity with a fixed input test mass mirror (ITM) and a suspended end test mass mirror (ETM) with mass m is measured. An optomechanical sensor, composed of the ETM and a reference test mass mirror (RTM) with the same mass as the ETM, measures the motion of the ETM independently.

and for the RTM we obtain:

$$\hat{x}_{\text{RTM}}(\Omega) = -\frac{1}{m\Omega^2} \left(\alpha^{(2)} \hat{a}_1^{(2)}(\Omega) \right) + Lh(\Omega), \quad (4.33)$$

where the quantity $\alpha^{(i)} = 2/\tau^{(i)} \sqrt{8\hbar\omega_0 P^{(i)}/c} \equiv \sqrt{\hbar m} \Omega_q^{(i)}$ denotes measurement strength [cf. Eq. (2.212)]. The measurement outputs corresponding to the two carrier fields are given by

$$\hat{y}^{(1)}(\Omega) = \hat{a}_2^{(1)}(\Omega) + \frac{\alpha^{(1)}}{\hbar} \hat{x}_{\text{ETM}}(\Omega), \quad (4.34)$$

$$\hat{y}^{(2)}(\Omega) = \hat{a}_1^{(2)}(\Omega) \sin \zeta^{(2)} + \left[\hat{a}_2^{(2)}(\Omega) + \frac{\alpha^{(2)}}{\hbar} (\hat{x}_{\text{RTM}}(\Omega) - \hat{x}_{\text{ETM}}(\Omega)) \right] \cos \zeta^{(2)}. \quad (4.35)$$

The combined sensitivity depends crucially on the detected quadrature $\zeta^{(2)}$ of the output field of the reference cavity. Three distinct scenarios are considered in the following:

(i) The most obvious measurement strategy would be a frequency-dependent homodyne detection, such that the sensitivity of the optomechanical sensor is only limited by shot noise, as proposed by Heidmann et al. in Refs. [55, 90]. We assume that both devices exhibit the same measurement strength, i.e. $\Omega_q \equiv \Omega_q^{(1)} = \Omega_q^{(2)}$. After re-scaling ($\Omega \rightarrow \Omega\Omega_q$) and using the detection angle $\zeta_{\text{sub}}^{(2)} = \arctan(1/\Omega^2)$, the two outputs are given by

$$\hat{y}^{(1)}(\Omega) = \frac{1}{\Omega^2} \left(-\hat{a}_1^{(1)}(\Omega) + \hat{a}_1^{(2)}(\Omega) \right) + \hat{a}_2^{(1)}(\Omega) + \sqrt{2}h, \quad (4.36)$$

$$\hat{y}^{(2)}(\Omega) = \frac{1}{\sqrt{1+\Omega^2}} \left(\hat{a}_1^{(1)}(\Omega) - \hat{a}_1^{(2)}(\Omega) + \hat{a}_2^{(2)}(\Omega)\Omega^2 \right). \quad (4.37)$$

Note that the signal h has been normalized to the SQL at Ω_q in Eq. (4.36). The combined output is free from radiation pressure noise if the filter functions

$$\mathbf{K}_{\text{sub}}^T = \frac{1}{N(\Omega)} \left(\Omega^2 \quad \sqrt{1+\Omega^2} \right) \quad (4.38)$$

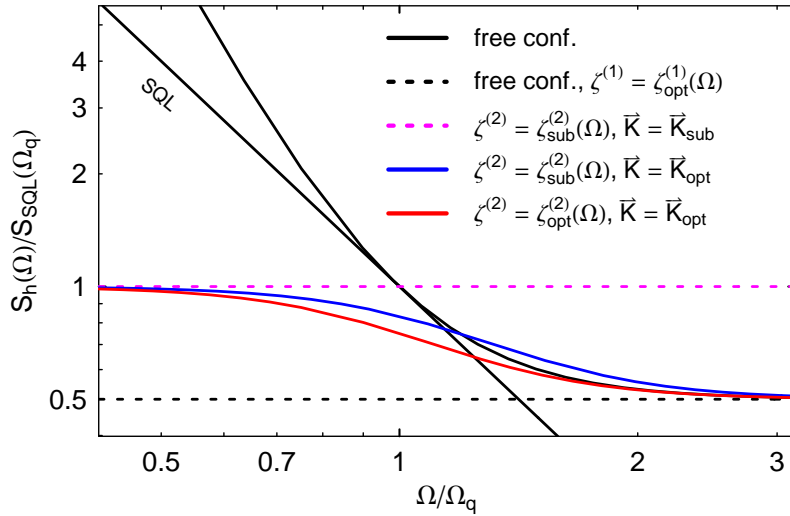


Figure 4.3.: Comparison of noise spectral densities of different configurations: single readout with phase quadrature detection (black solid line); single readout with optimal frequency-dependent homodyne detection (black dashed line); three distinct scenarios are considered for a configuration comprising an independent readout of ETM's motion: (i) suboptimal readout of second output field and suboptimal filter (dashed magenta line) (ii) suboptimal readout of second output field and optimal filter (blue line) and (iii) both optimized (red line). The phase quadrature of the main output field is detected.

are used, where $N(\Omega)$ accounts for a normalization. We obtain for the combined output

$$\hat{y}(\Omega) = \frac{1}{N(\Omega)} \left(\hat{a}_2^{(1)}(\Omega) - \hat{a}_2^{(2)}(\Omega) + \sqrt{2}h \right) \Omega^2, \quad (4.39)$$

which entails a constant noise spectral density, i.e. $S_h(\Omega)/S_{\text{SQL}}(\Omega_q) = 1$. The combined noise spectral density is influenced by the shot noise level of both measurement devices. Note that these intuitively chosen filter functions do not minimize the overall noise spectral density.

(ii) The optimal filter functions calculated by means of the formalism presented in Sec. 4.1.3 read:

$$\mathbf{K}_{\text{opt}}^T = \frac{1}{N(\Omega)} \left(\Omega^2(2 + \Omega^4) \quad 2\sqrt{1 + \Omega^2} \right). \quad (4.40)$$

These filter functions agree with Eq. (4.38), for $\Omega \ll 1$ which ensures that radiation pressure noise is still canceled in the low frequency regime. In the high frequency regime, only the output corresponding to the main carrier is used. The shot noise level of the optomechanical sensor does not contribute to the combined output, which obeys the noise spectral density

$$S_h(\Omega)/S_{\text{SQL}}(\Omega_q) = \frac{1}{2} + \frac{1}{2 + \Omega^2}. \quad (4.41)$$

(iii) A straightforward minimization reveals that the optimal frequency-dependent detection angle is given by $\zeta_{\text{opt}}^{(2)} = \arctan(1/\Omega^2 - \Omega^2)$ which results in a slightly improved

combined noise spectral density (cf. also Fig. 4.3):

$$S_h(\Omega)/S_{\text{SQL}}(\Omega_q) = \frac{\Omega^4 + 2}{2\Omega^4 + 2}, \quad (4.42)$$

The optimal filter functions in the case of this detection strategy can again be obtained by means of the formalism introduced in Sec. 4.1.3:

$$\mathbf{K}_{\text{opt}}^T = \frac{1}{N(\Omega)} \left(\Omega^2(1 + \Omega^4) \quad 2\sqrt{1 - \Omega^4 + \Omega^8} \right). \quad (4.43)$$

4.2. Local readout scheme

Currently planned high power detuned signal-recycling (SR) laser interferometers (for example Advanced LIGO [1]) are characterized by two resonances within the detection band. One resonance is optical in nature and the other is caused by the optical spring, which can shift the pendulum eigenfrequency of the suspended mirrors up to the detection band. This gives rise to the optomechanical resonance around which the sensitivity of the detector is enhanced, as around the optical resonance. For such an interferometer, the free mass SQL [27] is no longer applicable and it can be surpassed around the optomechanical resonance frequency. But below this resonance frequency, the sensitivity of a detuned SR interferometer is significantly lower than that of non-optical-spring configurations with comparable circulating power. Such a drawback can also compromise high-frequency sensitivity, when a broadband optimization is performed on the overall sensitivity of the interferometer with respect to a wide class of gravitational wave sources. This deterioration of sensitivity is caused by the optical spring, which rigidly connects the input test mass mirror (ITM) and the end test mass mirror (ETM) of each arm cavity at frequencies below the optomechanical resonance. The general principle underlying this effect was already explained by Braginsky and Khalili in Ref. [26], where they proposed the *optical bar* detection scheme [25]. They pointed out that the optical spring behaves like a rigid optical bar, which can connect the end mirrors of a L -shaped Michelson interferometer with an intra-cavity mirror. By attaching a local meter to the intra-cavity mirror, the motion transferred from the end mirrors to this mirror can be read out. Therefore Braginsky and Khalili can take advantage of the same effect that limits the detuned SR interferometer at frequencies substantially below the optomechanical resonance. The ITM and ETM of each arm cavity are stuck together and hence also behave like a rigid optical bar. This implies that the carrier light, which only senses the change in arm cavity length, i.e. the difference in ITM and ETM motion, cannot be used to measure GW efficiently at these frequencies. In order to understand this more conveniently, we need to use the local inertial frame of the beam splitter (BS). In this frame, the effect of GWs can be described completely as a tidal force field, which only exerts forces on the ETMs, not on the ITMs. Here we make the approximation that the ITMs and the BS are collocated. This means that the light propagating between these optical components is unaffected by GWs. Since the ITM and the ETM are rigidly connected, both move in the local inertial frame of the BS by 1/2 of the extent the ETM would have moved had there been no optical spring present. Here and below we assume that the ITMs and ETMs have equal masses. To illustrate this situation, we contemplate an incident low-frequency GW with amplitude h from right above the detector plane. In the local inertial frame of the BS, an ETM

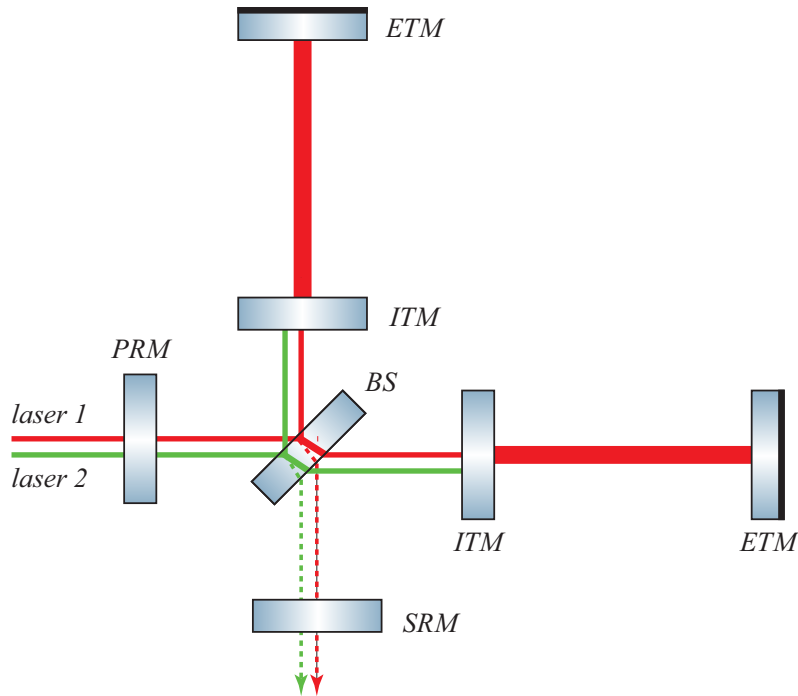


Figure 4.4.: Schematic plot of a power- and signal recycled Michelson interferometer equipped with arm cavities and double-readout. The added local meter is realized by a secondary laser which does not enter the arm cavities. It senses only the differential motion of the input test mass mirrors.

inside a non-optical-spring interferometer would move a distance Lh , where L is the arm length of the interferometer. In the case of an optical spring interferometer below the optomechanical resonance the ITM and the ETM both move by $\sim Lh/2$. For this reason, we propose to measure the local motion of the ITM by using an additional *local readout* (LR) scheme which allows us to dramatically recover the low-frequency sensitivity. Note that the local meter senses an effective mass of the ITM which is equal to the total mass of the ITM and the ETM. The optical-bar scheme proposed by Braginsky et al. is equivalent to only measuring the ITM's motion locally [25]. In this sense our proposal can be considered as directly incorporating the optical-bar scheme into currently planned second generation GW interferometers.

Local readout schemes have also been proposed for interferometers without an optical spring, as discussed in Sec. 4.1.3. But the motivation was entirely different, since the mirrors can still be considered as independent objects, whose motion with respect to their local inertial frames is merely caused by radiation-pressure noise, provided that only signal and quantum noise sources are taken into account. A local readout scheme can thus be used to (partially) cancel radiation-pressure noise and improve low-frequency sensitivity [55, 56, 90, 105]. Additionally, such schemes are able to cancel parts of the classical noise. The following investigations can also be regarded as a generalization of these schemes, because the results discussed in Sec. 4.1.3 can be recovered by setting the detuning to zero.

From an astrophysical point of view, the implementation of the LR scheme broadens the

detection band. This allows the interferometer to search for multiple sources simultaneously as well as to examine a wider frequency range of the same source. As an example, we will explore how the increase in detection bandwidth allows us to detect more efficiently the population of compact binary objects with a broad range of masses (and hence signal frequency band).

In order to construct the local meter, we consider a scheme where a second carrier is injected into the bright port of a detuned SR interferometer. This auxiliary carrier light does not enter the arm cavities as in Fig. 4.4. Instead, it senses the differential motion of the ITMs. It would also be conceivable to apply a LR scheme to the ETMs, similar to the set-up discussed in Sec. 4.1.3. The same sensitivity recovery would be possible, since the ETMs would also move with respect to free collocated mirrors by $-Lh/2$. These two strategies are quite equivalent in the ideal situation, but differ from each other in terms of the difficulty in implementation and in terms of quantum noise, since additional mirrors need to be introduced. Moreover, such a scheme might also be more susceptible to technical noise sources such as laser noise.

The following aspects of the LR scheme are discussed in this section: first we study the dynamics, sensing and control of the double-readout interferometer in Sec. 4.2.1. By means of the results obtained in the previous Sec. 4.1.3 the joint Heisenberg equations of motion for test masses, beam splitter and optical fields are obtained and the optimal combined GW sensitivity of the two readout channels is calculated. Further, it is proved that the use of control schemes does not affect this sensitivity. Afterwards, in Sec. 4.2.2, we illustrate how our proposed scheme can be used to improve the sensitivity of the planned Advanced LIGO interferometer. Various scenarios are considered and a realistic classical noise budget is taken into account. Then we discuss practical issues for a possible implementation in Advanced LIGO in Sec. 4.2.3. A combination with other QND techniques, i.e. squeezed light input and variational homodyne detection is discussed in Sec. 4.2.4. We conclude with a summary of the main results.

4.2.1. Dynamics, sensing and control

Equations of motion

We investigate a signal- and power-recycled Michelson interferometer with arm cavities and equipped with a supplementary readout of the differential motion of the ITMs (cf. Fig. 4.4). Such a layout comprises two interferometers, the large-scale main interferometer and a small interferometer which has the ITMs as its end mirrors. Choosing at least different frequencies or polarizations for the two carrier lights allows us an independent treatment of the two interferometers, as pointed out in Sec. 4.1.1. We assume that the parameters, e.g. detunings or mirror reflectivities, can be chosen independently for each interferometer. Remember that the ingoing bright- and dark port fluctuations associated with the two lasers are uncorrelated. The Heisenberg equations of motion can be obtained directly from the general formalism presented in Sec. 4.1.3 by choosing $n = 2$ and $k = 1$. Then the equations of motion for the differential motion of the ITMs (\hat{x}_{ITM}) and the ETMs (\hat{x}_{ETM}), respectively, as well as for the BS motion \hat{x}_{BS} normal to its reflective

surface, are given by

$$\begin{aligned} \hat{x}_{\text{ITM}} = & -R_{xx}(\Omega) \left[\hat{F}^{(1)}(\Omega) + R_{FF}^{(1)}(\Omega) (\hat{x}_{\text{ETM}} - \hat{x}_{\text{ITM}}) \right. \\ & \left. - \hat{F}^{(2)}(\Omega) - R_{FF}^{(2)}(\Omega) (\hat{x}_{\text{ITM}} + \sqrt{2} \hat{x}_{\text{BS}}) \right] + \hat{\xi}_{\text{ITM}}, \end{aligned} \quad (4.44)$$

$$\hat{x}_{\text{ETM}} = R_{xx}(\Omega) \left[\hat{F}^{(1)}(\Omega) + R_{FF}^{(1)}(\Omega) (\hat{x}_{\text{ETM}} - \hat{x}_{\text{ITM}}) \right] + L h + \hat{\xi}_{\text{ETM}}, \quad (4.45)$$

$$\begin{aligned} \hat{x}_{\text{BS}} = & R_{xx}^{\text{BS}}(\Omega) \left[\hat{F}^{(2)}(\Omega) + R_{FF}^{(2)}(\Omega) (\hat{x}_{\text{ITM}} + \sqrt{2} \hat{x}_{\text{BS}}) \right. \\ & \left. + \hat{F}_{\text{BP}}^{(1)}(\Omega) + \hat{F}_{\text{BP}}^{(2)}(\Omega) \right] + \hat{\xi}_{\text{BS}}, \end{aligned} \quad (4.46)$$

and for the two measurement outputs $\hat{y}^{(i)}$ we obtain:

$$\begin{aligned} \hat{y}^{(1)} = & \hat{Y}_1^{(1)}(\Omega) \sin \zeta^{(1)} + \hat{Y}_2^{(1)}(\Omega) \cos \zeta^{(1)} \\ & + \left[R_{Y_1F}^{(1)}(\Omega) \sin \zeta^{(1)} + R_{Y_2F}^{(1)}(\Omega) \cos \zeta^{(1)} \right] (\hat{x}_{\text{ETM}} - \hat{x}_{\text{ITM}}), \end{aligned} \quad (4.47)$$

$$\begin{aligned} \hat{y}^{(2)} = & \hat{Y}_1^{(2)}(\Omega) \sin \zeta^{(2)} + \hat{Y}_2^{(2)}(\Omega) \cos \zeta^{(2)} \\ & + \left[R_{Y_1F}^{(2)}(\Omega) \sin \zeta^{(2)} + R_{Y_2F}^{(2)}(\Omega) \cos \zeta^{(2)} \right] (\hat{x}_{\text{ITM}} + \sqrt{2} \hat{x}_{\text{BS}}). \end{aligned} \quad (4.48)$$

All the quantities used here are listed in Sec. 4.1.3 and the parameters are given in Tab. 4.1. For the subsequent discussion we assume that the mass of the BS coincides with the mass of a single mirror, i.e. $m_{\text{BS}} = m$. Note that we can obtain two input-output relations from the equations of motion given in Eqs. (4.44)-(4.48) and write them, according to Sec. 4.1.3, in the following compact form:

$$\hat{y}^{(1)} = \mathbf{n}_1^T \cdot \boldsymbol{\nu} + s_1 h, \quad \hat{y}^{(2)} = \mathbf{n}_2^T \cdot \boldsymbol{\nu} + s_2 h, \quad (4.49)$$

where $\boldsymbol{\nu}^T = (\hat{a}_1^{(1)}, \hat{a}_2^{(1)}, \hat{a}_1^{(2)}, \hat{a}_2^{(2)}, \hat{b}_1^{(1)}, \hat{b}_1^{(2)}, \hat{\xi}_{\text{ITM}}, \hat{\xi}_{\text{ETM}}, \hat{\xi}_{\text{BS}})$. Here the two vectors $\mathbf{n}_{1,2}$ are the linear transfer functions from the noise channels $\boldsymbol{\nu}$ into the two output channels, while the two functions $s_{1,2}$ are the linear transfer functions from the signal, i.e. the GW strain h , into the output channels. The combined optimal noise spectral density can be deduced directly from Eq. (4.26).

Control

It has been shown by Buonanno and Chen in Refs. [36, 37, 38] that the optical spring introduces an instability which has to be cured by employing an appropriate feedback control system. This instability is also discussed in detail in Sec. 4.3, where an alternative all-optical stabilization scheme is proposed. In the case of a single-carrier system, it is easy to show that a control system does not give rise to any fundamental change in sensitivity with regard to GW signals [36, 37, 38]. This can be understood intuitively since signal and noise portions are fed back equally onto the test masses. The proposed double-readout system is more complex, but the same intuition still applies. If we define $\mathbf{x}^T \equiv (\hat{x}_{\text{ITM}}, \hat{x}_{\text{ETM}}, \hat{x}_{\text{BS}})$ and $\mathbf{y}^T \equiv (\hat{y}^{(1)}, \hat{y}^{(2)})$, the equations of motion, i.e. Eqs. (4.44)-(4.48), can be re-written as follows:

$$\mathbf{x} = \mathbf{A}(\Omega) \cdot \mathbf{x} + \mathbf{B}(\Omega) \cdot \boldsymbol{\nu} + \mathbf{c}(\Omega)h + \mathbf{D}(\Omega) \cdot \mathbf{y}, \quad (4.50)$$

$$\mathbf{y} = \mathbf{F}(\Omega) \cdot \mathbf{x} + \mathbf{G}(\Omega) \cdot \boldsymbol{\nu}. \quad (4.51)$$

Symbol	physical meaning	value
m_{BS}	beam splitter mass	40 kg
ρ_{PR}	power-recycling mirror reflectivity	$\sqrt{0.94}$
$2\pi c/\omega_0^{(2)}$	laser wavelength of 2 nd carrier	1064 nm
$P^{(2)}$	circulating power of 2 nd carrier	1 kW
$\lambda^{(2)}$	detuning for 2 nd carrier	0 Hz
$\epsilon^{(2)}$	cavity half bandwidth for 2 nd carrier	2π 1 kHz
$\zeta^{(2)}$	detection angle for 2 nd carrier	0

Table 4.1.: Parameters values relevant for the second carrier field injected into the bright port of an interferometer (cf. Fig. 4.4). These parameter values are always used for the local meter and the parameter values given in Tab. 2.1 (narrowband configuration) for the first carrier, unless otherwise stated.

In Eq. 4.50 the matrix \mathbf{A} accounts for the mirror dynamics, the matrix \mathbf{B} describes how the noise sources combined in $\boldsymbol{\nu}$ are applied as forces onto the mirrors and the vector \mathbf{c} denotes how the GW signal h directly influences the mirrors. In Eq. 4.51 the matrix \mathbf{F} describes how the output channels \mathbf{y} depend on the motions summarized in \mathbf{x} , the matrix \mathbf{G} describes sensing noise in \mathbf{y} , and finally the matrix \mathbf{D} accounts for the required feedback. By solving Eqs. (4.50) and (4.51) jointly, we obtain

$$\mathbf{y} = [\mathbb{1}_2 - \mathbf{H} \cdot \mathbf{D}]^{-1} \cdot [[\mathbf{H} \cdot \mathbf{B} + \mathbf{G}] \cdot \boldsymbol{\nu} + \mathbf{H} \cdot \mathbf{c} h], \quad (4.52)$$

where the matrix $\mathbf{H} \equiv \mathbf{F} \cdot (\mathbb{1}_2 - \mathbf{A})^{-1}$ was defined. It can be seen from Eq. (4.52) that the only dependance of \mathbf{y} on the control system is through \mathbf{D} , which only appears in the first factor on the right-hand side. The optimal sensitivity, obtained by maximizing the signal-referred noise spectrum of $(K_1, K_2) \cdot \mathbf{y}$ is then clearly invariant with respect to the control system \mathbf{D} .

4.2.2. Example configurations

Quantum noise example

To begin, we study the quantum noise spectral density of the proposed LR scheme for different parameter regimes. Introducing a second carrier as illustrated by Fig. 4.4 does not affect the signal-transfer function of the large-scale interferometer and it still reads:

$$s^{(1)}(\Omega) = \frac{R_{Y_1F}^{(1)}(\Omega) \sin \zeta^{(1)} + R_{Y_2F}^{(1)}(\Omega) \cos \zeta^{(1)}}{1 - 2R_{FF}^{(1)}(\Omega)R_{xx}(\Omega)} \xrightarrow{\Omega \rightarrow 0} 0, \quad (4.53)$$

where we have assumed that the SR cavity is tuned with respect to the second carrier. Otherwise a second optical spring would inevitably change the signal transfer function given in Eq. (4.53). The signal-transfer function of the tuned local meter is given by

$$s^{(2)}(\Omega) = -\frac{R_{FF}^{(1)}(\Omega)R_{xx}(\Omega)R_{Y_2F}^{(2)}(\Omega)}{1 - 2R_{FF}^{(1)}(\Omega)R_{xx}(\Omega)} \xrightarrow{\Omega \rightarrow 0} \frac{\theta^{(2)}}{\sqrt{2\epsilon^{(2)}\hbar}}, \quad (4.54)$$

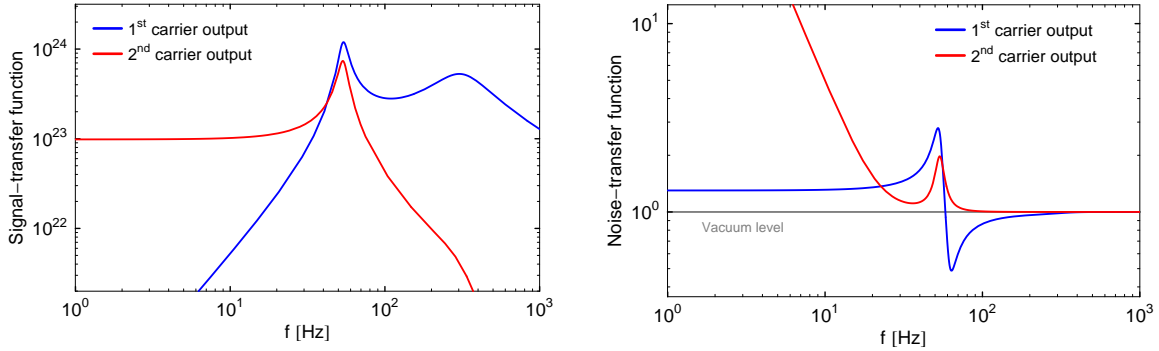


Figure 4.5.: Example of signal (left panel) and noise (right panel) transfer functions of the local readout configuration. For each carrier the associated transfer function is shown separately. Parameters are given in Tabs. 2.1 and 4.1 but with $\zeta^{(1)} = 0$.

provided that its phase quadrature is detected. Note that both transfer functions depend crucially on the susceptibility $R_{FF}^{(1)}(\Omega)$ offered by the first carrier: in the case of the large-scale interferometer it is responsible for the optomechanical resonance around which the signal transfer is strongly enhanced, but it also causes a diminished sensitivity at low frequencies. Remember that the poles of Eq. (4.53) correspond to the optical and the optomechanical resonance. On the other hand, the local meter can only sense a signal if the large-scale interferometer provides a non-vanishing ponderomotive rigidity, i.e. $R_{FF}^{(1)}(\Omega) \neq 0$ is required. Note that, in contrast to the large-scale interferometer, the signal transfer function of the local meter stays constant for low frequencies. This behavior is further illustrated by Fig. 4.5 where the individual signal- and noise-transfer functions associated with the first and second carrier are shown. We use the parameters for an Advanced LIGO narrowband configuration provided in Tab. 2.1, but with phase quadrature detection, i.e. $\zeta^{(1)} = 0$. The parameter values for the local meter are given in Tab. 4.1. Fig. 4.5 confirms that the large-scale interferometer mainly senses frequencies above the optical spring resonance, while the signal transfer function decreases considerably at lower frequencies. The local meter offers complementary sensitivity for frequencies below the optical spring resonance, when the ITM is dragged together with the ETM by the optical spring. The corresponding filter functions shown in the left panel of Fig. 4.6 mirror this behavior. The curves shown in this figure indicate the percentage of GW strain (solid lines) or noise (dashed lines) fed from the large-scale interferometer (red lines) or the local meter (blue lines) into the combined output [cf. Eq. (4.30)]. The green curves in Fig. 4.6 account for the correlations [cf. Eq. (4.31)] between the two outputs. At frequencies above the optical spring resonance, the optimal combination depends mainly on the first readout, while at frequencies below the optical spring resonance mainly on the second readout. This plot illustrates that the local readout scheme can directly improve the sensitivity only below the optomechanical resonance frequency. Note that the noise spectral density of both output channels can be above the optimally combined noise spectral density at certain frequencies. This is due to the fact that there are correlations between the two output fields, since they are coupled indirectly via the motion of the ITMs. The optimal filter functions are able to exploit these correlations (cf. green curve in the left panel of Fig. 4.6). This also means that the additional radiation pressure noise

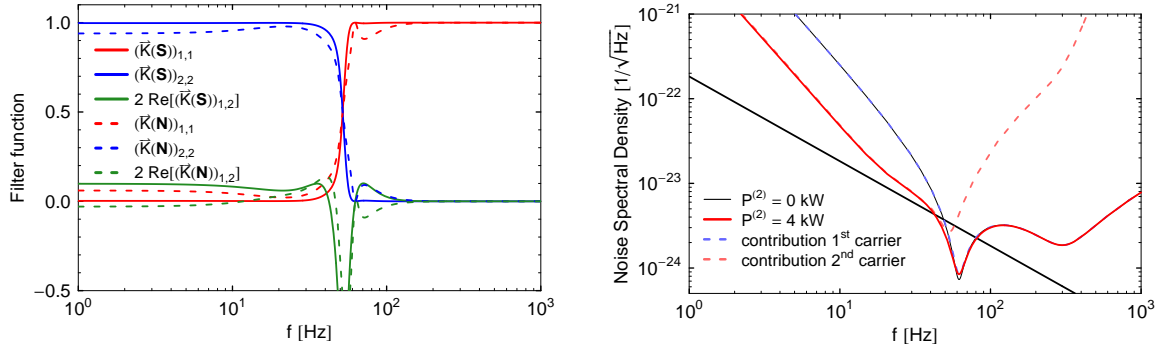


Figure 4.6.: Left panel: squared absolute values and cross correlations of the optimal filter functions [cf. Eq. (4.30)]. The percentage of GW strain (solid lines) or noise (dashed lines) contributed by the large-scale interferometer (red lines) and the local meter (blue lines) is depicted. The green lines account for the correlations between the two outputs. Right panel: the resulting combined noise spectral density as well as the contributions associated with the individual carriers are shown. The same parameters as in Fig. 4.5 were used.

imposed on the ITMs by the local meter can be partly canceled out. But a small fraction remains, which can be seen in the right panel of Fig. 4.6, where a slightly deteriorated sensitivity can be observed around the optomechanical resonance compared to the usual detuned SR interferometer without LR.

The local meter provides additional degrees of freedom usable for a fine tuning of the noise spectral density of the interferometer. Note that the cavity mode associated with the local meter can be eliminated adiabatically due to the short arm length and the low finesse considered here. This implies that the corresponding output only depends on the ratio between the circulating power $P^{(2)}$ and the half bandwidth $\epsilon^{(2)}$, which can be inferred e.g. from Eq. (2.212). Remember that we assume that the SR mirror reflectivity for each carrier light can be adjusted independently. This allows us to decrease the circulating power required for operating the local meter, which facilitates the implementation of the proposed technique. For example, if we assume a circulating power of only $P^{(2)} = 1$ kW in each arm of the local meter, it is still possible to recover all curves shown in Fig. 3 (left panel) of our Ref. [136], where a circulating power of up to $P^{(2)} = 16$ kW was considered. This is illustrated in Fig. 4.7, where the combined noise curves for a fixed power but variable bandwidth are plotted.

Beside the half bandwidth $\epsilon^{(2)}$, the residual degrees of freedom are the detection angle $\zeta^{(2)}$ and detuning $\lambda^{(2)}$ of the local meter. Detuning the SR cavity with respect to the second carrier field gives rise to a second pair of resonances. Since the additional optical resonance usually occurs beyond the cavities' half line width, where the local meter does not give any contribution to the combined noise spectral density, we can effectively exploit three resonances. Note that the newly established optomechanical resonance also needs to be stabilized by a feedback control system which does not influence the sensitivity according to Sec. 4.2.1. Due to the low power circulating in the local meter the second optomechanical resonance occurs at considerably lower frequencies than the first. In this regime one cannot have much advantage from a peaked response, since the interferometer is clearly dominated by classical noise. Consequently, we do not extend the analysis to

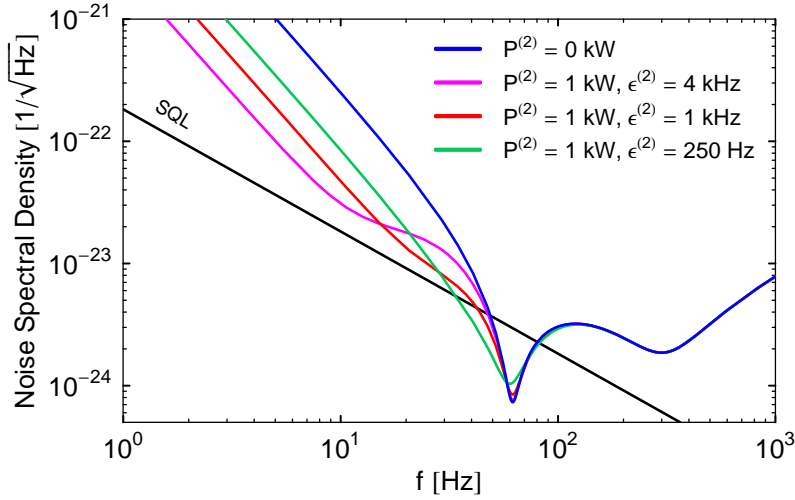


Figure 4.7.: Quantum noise curves for the proposed local readout scheme. Different curves correspond to different choices of the half bandwidth $\epsilon^{(2)}$. The other parameters are the same as in Fig. 4.5. Since the cavity mode of the local meter can be eliminated adiabatically we can conclude that its performance only depends on the ratio $P^{(2)}/\epsilon^{(2)}$.

a non-zero detuning associated with the local meter. Finally, the homodyne detection angle $\zeta^{(2)}$ provides another degree of freedom, which can be used for an optimization. In particular a frequency-dependent homodyne detection scheme might be a matter of special interest since it can be implemented without much effort for such a small-scale interferometer. This will be discussed in detail in Sec. 4.2.4.

It should also be mentioned that the combination of a signal-recycled Michelson interferometer with a local meter may indirectly help to improve the sensitivity at high frequencies or to increase the detection bandwidth. Such a broadband optimization is also carried out in the following. A broadband configuration exploits the effect that the sensitivity of the large-scale interferometer can be shifted to higher frequencies by so adjusting its detection angle that it is closer to the phase quadrature, while the local meter helps to maintain sensitivity at low frequencies. This will be studied more closely in Sec. 4.2.2.

Classical noise dominated regime

Sensing noise is usually negligible in the low frequency regime and the motion of the mirrors and the beam splitter is dominated by classical force noise. With this assumption the first carrier offers the following output:

$$\hat{y}^{(1)} \propto \hat{\xi}_{\text{ETM}} - \hat{\xi}_{\text{ITM}} + Lh, \quad (4.55)$$

where $\hat{\xi}_{\text{ETM}}$ and $\hat{\xi}_{\text{ITM}}$ account for the classical noise acting on ETMs and ITMs, respectively [cf. Eq. (4.22)]. The output of the second carrier is proportional to

$$\hat{y}^{(2)} \propto \hat{\xi}_{\text{ETM}} + \hat{\xi}_{\text{ITM}} + 2\sqrt{2}\hat{\xi}_{\text{BS}} + Lh, \quad (4.56)$$

where $\hat{\xi}_{\text{BS}}$ accounts for the classical noise acting on the BS. Suppose again that $\hat{\xi}_{\text{ITM}}$, $\hat{\xi}_{\text{ETM}}$, and $\hat{\xi}_{\text{BS}}$ correspond to independent noise contributions, at the same level for ITMs

and ETMs but half as high for the BS [cf. Eq. (4.22)]. Calculating the optimal filter functions by means of the formalism introduced in Sec. 4.1.3 yields that 3/4 of the large-scale interferometer's and one fourth of the local meter's output should be used. This is in contrast to the optimal filter functions we obtain when only quantum noise is taken into account, as in the left panel of Fig. 4.6. The combined output for the classical noise dominated regime is given by

$$\hat{y} \propto \hat{\xi}_{\text{ETM}} - \frac{1}{2}\hat{\xi}_{\text{ITM}} + \frac{1}{\sqrt{2}}\hat{\xi}_{\text{BS}} + Lh. \quad (4.57)$$

For the ratio between the noise spectral densities of a single large-scale interferometer [cf. Eq. (4.55)] and the optimally combined local readout configuration [cf. Eq. (4.57)] we obtain $\frac{3}{2}/2$, i.e. classical noise in the combined output is reduced by 25%. This corresponds to an improvement in event rate by a factor of $(\sqrt{4/3})^3$, i.e. $\sim 54\%$, which can also be seen in Fig. 4.10: for high binary masses the dashed curves meet at a factor of $(4/3)^{3/2}$ below the solid curves. This plot is explained in detail in the following section. The above considerations also clarify why the improvement in event rate for binary systems with a high total mass does not significantly exceed 54% (cf. Tab. 4.2).

Optimized configurations with Advanced LIGO classical noise budget

Now we employ the tools reviewed and introduced in Sec. 3.1 for an optimization of our proposed configuration. Different binary inspirals are considered and the signal-to-noise ratio (SNR) is maximized with respect to certain interferometer parameters. For this optimization a realistic classical noise budget as given by *Bench* [2] is taken into account. The different noise contributions are shown for instance in Fig. 4.8, where they are represented by grey lines. Here we use the usual Advanced LIGO narrowband configuration with parameters given in Tab. 2.1 as a reference. Remember that these parameters were obtained by optimizing the interferometer for neutron star - neutron star (NS-NS) binary systems, i.e. binary systems with a total mass of $M = (1.4 + 1.4) M_{\odot}$. But in the following we extend our analysis to binary systems with a higher total mass, which results in a shortened integration interval according to Eq. (3.7). In any case, considering different binary sources requires in each instance an optimization of the LR and the Advanced LIGO configuration in order to conduct an appropriate comparison. Each optimization of the Advanced LIGO configuration is accomplished in the same way as before, i.e. optical power $P^{(1)}$, effective detuning $\lambda^{(1)}$, effective half bandwidth $\epsilon^{(1)}$ and detection angle $\zeta^{(1)}$ are so adjusted that the SNR is maximized for a given binary system with a certain total mass (cf. Tab. 4.2). When optimizing the LR scheme, we maximize the SNR by varying the same set of parameters of the large-scale interferometer. Additionally the half bandwidth $\epsilon^{(2)}$ and the detection angle $\zeta^{(2)}$ of the local meter are subject to our optimization routine (cf. Tab. 4.2). We impose a fixed circulating power on the second carrier, i.e. $P^{(2)} = 1 \text{ kW}$ and require it to be resonant in the signal-recycling cavity ($\lambda^{(2)} = 0$). If we optimize both systems for a certain binary system and compare the expected event rates for this particular astrophysical source, we find moderate improvements in event rates (cf. last column in Tab. 4.2). The improvement in event rate increases for higher binary masses since the local meter mainly helps to enhance sensitivity at low frequencies. But the classical noise budget imposes a limit on achievable improvement which can be verified by means of the function introduced in

M/M_{\odot}	$P^{(1)}$ [kW]	$\lambda^{(1)}$ [Hz]	$\epsilon^{(1)}$ [Hz]	$\zeta^{(1)}$ [rad]	$\epsilon^{(2)}$ [Hz]	$\zeta^{(2)}$ [rad]	Improve
2.8	800	2π 290	2π 120	2π 0.35	-	-	43%
	800	2π 250	2π 75	2π 0.34	2π 200	2π 0.02	
20	400	2π 175	2π 35	2π 0.26	-	-	47.6%
	600	2π 180	2π 30	2π 0.25	2π 200	2π 0.02	
30	200	2π 125	2π 20	2π 0.25	-	-	48.2%
	250	2π 125	2π 15	2π 0.27	2π 200	2π 0.02	
40	100	2π 95	2π 10	2π 0.27	-	-	49%
	200	2π 105	2π 10	2π 0.22	2π 200	2π 0.02	
80	100	2π 85	2π 20	2π 0.16	-	-	56.4%
	100	2π 80	2π 10	2π 0.18	2π 200	2π 0.5	
120	150	2π 295	2π 195	2π 0.47	-	-	55.6%
	100	2π 100	2π 20	2π 0.16	2π 200	2π 0.5	
160	100	2π 270	2π 185	2π 0	-	-	53.43%
	100	2π 135	2π 30	2π 0.14	2π 200	2π 0.48	
200	200	2π 295	2π 185	2π 0.14	-	-	53.42%
	250	2π 480	2π 85	2π 0.14	2π 200	2π 0.5	

Table 4.2.: Parameters obtained when optimizing the usual Advanced LIGO type configuration (first row) and the proposed LR scheme (second row) for different binary systems (first column). The last column shows the improvement in event rate achievable by the LR scheme, i.e. the performance of the two configurations optimized for the same binary system with a certain total mass (given in the first column) is compared. Reasonable errors in the different parameters may decrease the event rate – but not more than 1%.

Eq. (3.10). If we consider for instance the LR configuration optimized for $M = 2.8M_{\odot}$ we obtain

$$\eta(f_{\text{up}} = 250 \text{ Hz}) = 0.85, \quad (4.58)$$

which reveals that the interferometer is almost limited by classical noise within the frequency interval [7 Hz; 250 Hz]. In the case of the Advanced LIGO narrowband configuration, we only obtain $\eta(f_{\text{up}} = 250 \text{ Hz}) = 0.73$.

Note that in our Ref. [136] all parameters of the tuned local meter were fixed for optimization, namely we used a bandwidth of $\epsilon^{(2)} = 2\pi$ 4 kHz, a circulating power of $P^{(2)} = 4$ kW and the phase quadrature associated with the second carrier was detected, i.e. $\zeta^{(2)} = 0$. We only varied the circulating power $P^{(1)}$, detection angle $\zeta^{(1)}$ and detuning phase $\phi^{(1)}$ of the large-scale interferometer. Here the optimization is extended to six degrees of freedom. The doubled number of variable parameters gives rises to an additional improvement in sensitivity which becomes apparent when comparing Tab. 4.2 with Tab. 2 in Ref. [136].

The advantage of the local readout scheme can be better appreciated when one realizes that there are different populations of likely sources (i.e., the total binary mass M can reside in a range \mathcal{M}), where the signals extend to different frequency bands. We need to investigate how well a certain configuration, optimized for a particular system with total

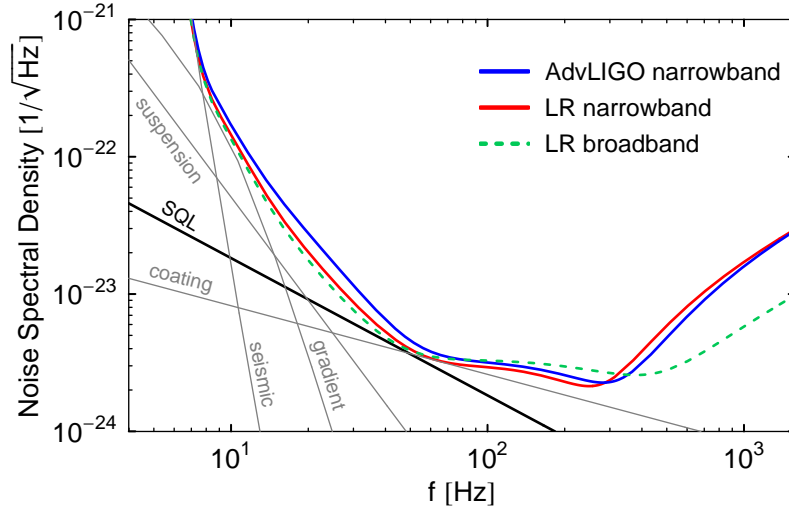


Figure 4.8.: Noise spectral densities of Advanced LIGO narrowband and two different LR configurations. Both narrowband configurations are optimized for binary systems with total mass $M = 2.8 M_{\odot}$ and parameters are given in Tab. 4.2. The LR broadband configuration was obtained by means of the optimization procedure introduced in Sec. 3.2, which produced the following set of parameters: $\lambda^{(1)} = 2\pi \cdot 360$ Hz, $\epsilon^{(1)} = 2\pi \cdot 245$ Hz, $\zeta^{(1)} = 2\pi \cdot 0.43$, $\epsilon^{(2)} = 2\pi \cdot 200$ Hz, $\zeta^{(2)} = 2\pi \cdot 0.02$ and residual parameters are given in Tab. 2.1 or 4.1. When using the Advanced LIGO narrowband configuration as a reference, one obtains an improvement in event rate for NS-NS binary systems of 43% in the case of the LR narrowband and 32.7% in the case of the LR broadband configuration. Classical noise (grey lines) is included here. Contributions are labeled according to their appearance: suspension thermal noise results from the fluctuations in the suspension system; seismic noise is due to motion of the ground; thermal fluctuations in the coating dominate over fluctuations in the substrate; gravity gradient noise accounts for time-changing Newtonian gravitational forces.

mass M , would perform for other possible systems with masses in \mathcal{M} . Here we consider $\mathcal{M} = [1 M_{\odot}, 630 M_{\odot}]$ with a maximum mass determined by the condition $f_{\max} = f_{\min}$ [cf. Eq. (3.7)]. Such a comparison is shown in Fig. 4.10 which illustrates the improvements in event rates obtainable by differently optimized Advanced LIGO configurations (dashed lines) and LR configurations (solid lines). Both schemes were optimized specifically for binary systems with total masses $M = 2.8 M_{\odot}$ (red), $40 M_{\odot}$ (green) and $120 M_{\odot}$ (blue). Note that the expected event rates are normalized to the performance of the Advanced LIGO narrowband configuration (cf. Tab. 2.1). In Figs. 4.8 and 4.11, we also show the corresponding noise spectral densities of these configurations, together with the classical noise contributions. These figures suggest at least two possible applications of the local readout scheme:

Detector with broader frequency band. Fig. 4.8 shows the Advanced LIGO narrowband (solid blue curve) and the LR narrowband (solid red curve) configurations which are both optimized for binary systems with a total mass of $2.8 M_{\odot}$. The local readout scheme provides an event rate which is 43% above that obtainable by Advanced LIGO. A comparison of these two narrowband schemes for other binary masses $M \in \mathcal{M}$ reveals that

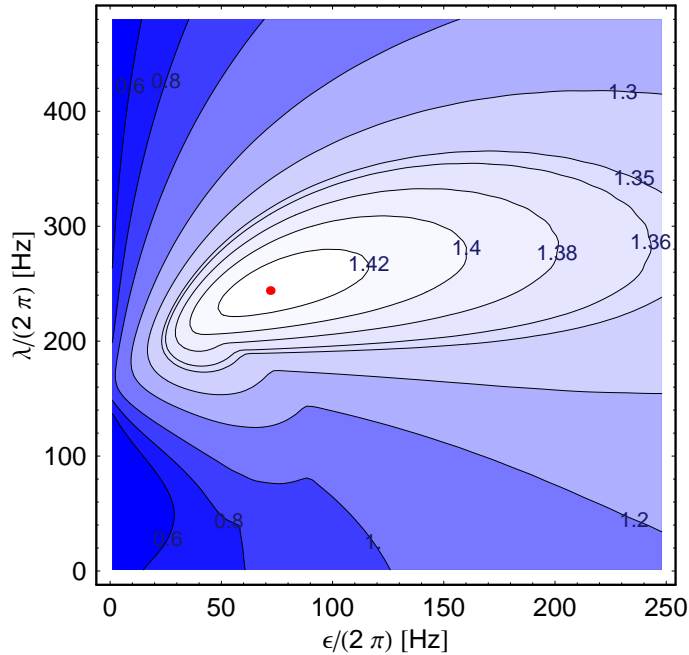


Figure 4.9.: Contour plot illustrates the sensitivity of proposed LR scheme compared to Advanced LIGO narrowband configuration (cf. Tab. 2.1) versus $\epsilon^{(1)}$ and $\lambda^{(1)}$: red dot marks the LR configuration which yields a maximum event rate for the detection of NS-NS binary systems, namely an improvement of 43% is achieved compared to the Advanced LIGO narrowband configuration. Labels of contour lines indicate how much improvement in event rate is maintained when parameters are varied, i.e. $(D(\epsilon^{(1)}, \lambda^{(1)})/D_{\max}^{\text{AdvNB}})^3$ [cf. Eq. (3.8)] is shown. There exists a large region with only a slightly deteriorated event rate, where broadband configurations can be found. For each point in the $(\epsilon^{(1)}, \lambda^{(1)})$ -plane the two detection angles $(\zeta^{(1)}, \zeta^{(2)})$ and the effective half bandwidth $(\epsilon^{(2)})$ of the LR configuration were optimized.

the LR narrowband scheme is globally better since it always offers a higher event rate, as illustrated by Fig. 4.10. The same figure also highlights that the LR narrowband configuration, for instance, performs even better for binary systems with $M = 40 M_{\odot}$ than an Advanced LIGO configuration specifically optimized for such binary systems (vide dashed green line in Fig. 4.10).

Alternatively, one can apply the broadband optimization scheme introduced in Sec. 3.2 to the LR scheme (dashed green curve in Fig. 4.8). This allows us to shift the sensitivity by a well-defined amount from the low frequency regime to higher frequencies. Fig. 4.8 reveals that it is possible to achieve a better sensitivity than the Advanced LIGO narrowband configuration in the frequency band [500 Hz; 1570 Hz], while still improving the event rate for NS-NS binary systems by 32.7%. It can be seen that this configuration is much broader in band, which demonstrates that when an overall optimization is performed the LR scheme can indirectly improve the sensitivity at higher frequencies. Even though the event rate for NS-NS binary systems is slightly decreased compared to the LR narrowband configuration, this configuration is potentially interesting for detecting other sources above 300 Hz, e.g. pulsars and low-mass X-ray binaries. Fig. 4.9 shows that there exists a large

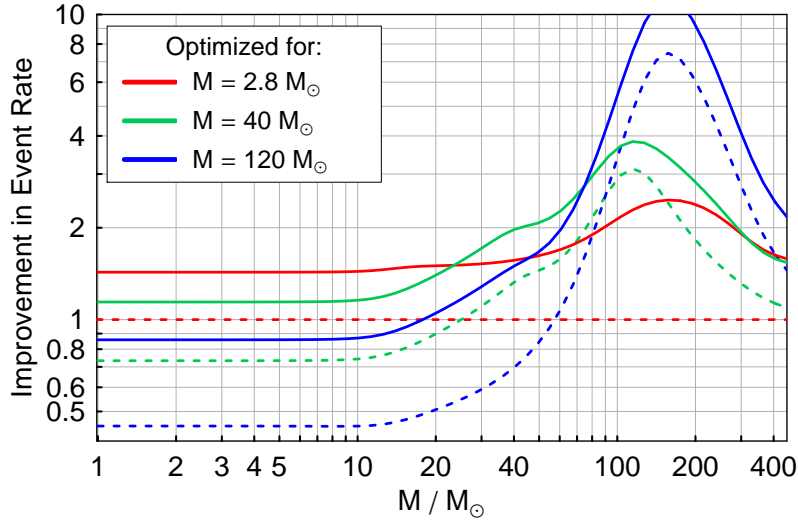


Figure 4.10.: Improvement in the event rate compared to the Advanced LIGO narrowband configuration versus total binary mass. The optimization parameters are fixed for each curve. Local readout configurations (solid lines) as well as Advanced LIGO configurations (dashed lines) are optimized for three different total binary masses. Corresponding parameters can be found in Tab. 4.2.

region in the $(\epsilon^{(1)}, \lambda^{(1)})$ -plane where the optimal event rate for NS-NS binary systems is nearly maintained. Within this region, possible broadband configurations can be found.

Detector for intermediate-mass black-hole binaries. The LR configuration optimized for $40 M_{\odot}$ systems (green curve in Fig. 4.10) has the same sensitivity to low-mass binary systems as the Advanced LIGO narrowband configuration (up to $M = 10 M_{\odot}$), while improving event rates for $60 M_{\odot} - 300 M_{\odot}$ by factors of 2 – 4.5. This allows us to build a detector sensitive to the more speculative (yet in some sense astrophysically more interesting) intermediate-mass black-hole binaries, without sacrificing sensitivity at low-mass systems which are more likely to exist. As we can infer from the dashed curves in Fig. 4.10, such a broad improvement of sensitivity for systems with different total masses is not achievable by single-readout Advanced LIGO type configurations. It is also interesting to note that this LR configuration requires a circulating power of only 200 kW in the arms.

The improvement in event rate increases significantly for higher binary masses (cf. blue curve in Fig. 4.10), since the local meter helps to enhance sensitivity mainly at low frequencies. But if we optimize for such high masses, the sensitivity for lower mass systems cannot keep up with the Advanced LIGO narrowband configuration.

4.2.3. Implementation issues

In this section the possibility of implementing the proposed LR technique explicitly in the Advanced LIGO detector is discussed. In fact, the so-called Michelson degree of freedom of the detector already needs to be measured (cf. e.g. Ref. [116]) in order to keep the signal-extraction port of the interferometer at dark fringe. But this is exactly what our local readout scheme proposes to measure. However, the sensitivity of the current

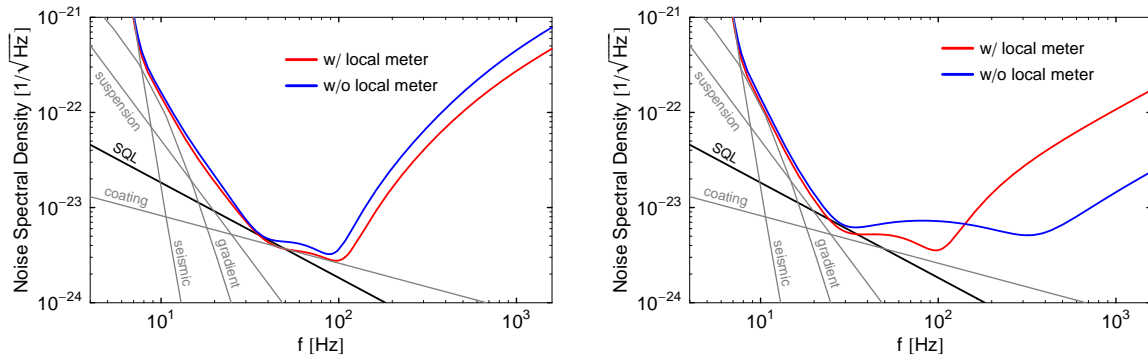


Figure 4.11.: Noise curves for the schemes with and without local readout both optimized for binary systems with a total, equally distributed mass of $M = 40 M_{\odot}$ (left) and $M = 120 M_{\odot}$ (right). Parameters obtained by the optimization are given in Tab. 4.2 and all other parameters can be found in Tab. 4.2. Note that classical noise (grey lines) is included here.

Michelson control signal needs to be dramatically improved in order to expand into our regime. It should also be realized that a more precise measurement of the Michelson degree of freedom additionally helps to decrease the control-loop noise, which is shot noise imposed on the control signal and coupling to the main signal due to unavoidable imbalances, as discussed in Ref. [148].

Optical Power. In the Advanced LIGO baseline design, a pair of radio frequency (RF) sidebands created around the main carrier frequency will be injected in order to probe the motion of the ITMs, as already done in current detectors. But only about 1% of total power at the input port is pumped into the RF sidebands that resonate in the power-recycling cavity but not in the arms. Taking into account the fact that the RF sidebands do not enter the arm cavities and thus suffer from less optical losses, the power of these sidebands at the ITMs is currently planned to be ~ 34 W. This is not sufficient for the implementation of our proposed local readout scheme. In the Advanced LIGO baseline design, the input power is 125 W, which is amplified to ~ 1.0 kW at each ITM, due to power-recycling. The same power at the ITMs is required for the local readout scheme and consequently the input power needs to be raised by a factor ~ 30 , if one enforces an implementation by using 1% of the carrier light for the RF sidebands. An alternative and more realistic realization is to use a phase-locked secondary laser, with its frequency shifted by an odd number of half free spectral ranges from the primary laser in order to be off-resonant in the arm cavities. Furthermore, the sub-carrier should almost satisfy the dark fringe condition at the signal-extraction port and additionally it should be resonant in both recycling cavities. A circulating power of $P^{(2)} = 1$ kW for the sub-carrier can be achieved by using a perceptibly lower input power than for the primary laser, namely ~ 36 W.

The parametric instability [28, 29] in the arm cavities might set a limit for the power of the primary laser. Therefore it is also conceivable to use the higher power laser for the sub-carrier, while the other one could replace the primary laser source. Indeed, a circulating power of $P^{(2)} = 1$ kW is less than the carrier power of the current GEO [91] detector, which strongly resembles the local meter.

Detection. Each signal at the dark port should be extracted with some reference field, which will be another set of RF sidebands in a RF readout scheme, or DC offset light in a DC readout scheme. The former leaks from the dark port via a macroscopic asymmetry in the central Michelson interferometer and the latter via a microscopic asymmetry between the two arm cavities. The reference fields associated with the two carriers should be isolated in both cases before photo-detection, otherwise the reference field which is not used for the signal extraction will just impose extra shot noise. One way to solve this problem is to make use of orthogonal polarizations. Before photo-detection the carrier and the sub-carrier accompanied by the reference fields can be separated by a polarized beam splitter, which is all-reflective to one polarization and transmissive to the other one. In addition, it is easy to combine the two beams lossless before injection into the bright port. An alternative method is to use two carrier lights which differ in frequency. An appropriate cavity can separate the beams at different frequencies, where one resonates in the cavity while the other does not. Such a cavity, a so-called output-mode-cleaner, is already planned to be used at the signal-extraction port in Advanced LIGO. In the same way, an input-mode-cleaner cavity can be used to combine the two beams before injection into the interferometer.

Alternative configuration. The local meter can also be placed around the ETMs. In this case, a single laser beam, which can be different in frequency from the carrier light, should be split and sent to each end of the arm cavities. This method guarantees that the additional laser noise can be canceled out by subtracting the measurement records corresponding to the two mirrors. It is also possible to implement a reference cavity, as proposed for a radiation-pressure-noise reduction in Refs. [55, 105]. In this way, the secondary laser for the local readout does not need such high power and there is no concern about a heat problem at the BS and the ITMs. However, a realization of this configuration would require more additional optical components.

4.2.4. Combination with advanced technologies

It was shown by KLMTV in Ref. [108] that the quantum noise spectral density of a conventional interferometer without signal-recycling can benefit from either a frequency-dependent squeezed light input or a frequency-dependent homodyne readout. Furthermore KLMTV pointed out that both techniques can be combined in order to achieve an additional improvement in sensitivity. In this section, the local readout scheme in conjunction with these two QND techniques is to be investigated. The injection of squeezed vacuum states [117, 159] into the dark port [39, 86] and the frequency-dependent homodyne detection scheme are only applied to the local meter. Of course it is also possible to supplement the large-scale interferometer with these advanced tools. This can be accomplished in the same manner as proposed in Refs. [39, 134], where the authors considered a detuned SR interferometer without local readout. But since the arms of the local meter are short and the SR cavity is tuned (with respect to the second carrier), its input and/or output optics can be modified without much effort, as shown in the following.

Variational homodyne detection

In the case of a tuned local meter, a frequency-dependent homodyne detection of the corresponding output field can disburden the measurement from radiation pressure noise

caused by vacuum fluctuations entering from the dark port. Therefore one might expect that the local meter exhibits a flat noise spectral density which coincides with its signal referred shot noise level. But Fig. 4.12 reveals that the combined noise spectral density still increases at low frequencies, even though only the local meter is used in this regime. This can be explained as follows: we can infer from Eq. (4.46) that laser noise entering from the bright port is also taken into account. At best, the laser source shows no technical noise, i.e. it is quantum noise limited. Nevertheless, the vacuum field entering from the bright port gives rise to radiation pressure forces acting on the BS. Such a contribution cannot be canceled by a variational homodyne detection, but by decreasing the power-recycling gain it is possible to reduce the effect. However, due to the classical noise present in the low frequency regime, this coupling from the bright port to the dark port does not impose a meaningful limitation on the final sensitivity of the detector.

In order to achieve optimal sensitivity, a rather complex frequency dependance of the detection angle is required around the optomechanical resonance. But for Fig. 4.12 the readout angle was approximated by

$$\tan \zeta_{\text{opt}}^{(2)}(\Omega) \approx \frac{3(\theta^{(2)})^2}{2m\epsilon^{(2)}\Omega^2}, \quad (4.59)$$

where $m_{\text{BS}} = m$ was used. Furthermore we have assumed that $\Omega \ll \epsilon^{(2)}$, which is satisfied for the parameter regime considered here. The prescription for the detection angle can be realized experimentally by implementing a single filter cavity with the complex resonance frequency

$$\Omega_{\text{res}} = \omega_0 - \frac{\sqrt{3}\theta^{(2)}}{2\sqrt{m\epsilon^{(2)}}} - i\frac{\sqrt{3}\theta^{(2)}}{2\sqrt{m\epsilon^{(2)}}}. \quad (4.60)$$

This expression can be obtained by using the KLMTV filter formalism introduced in Ref. [108] and generalized in Refs. [39, 134]. Note that a frequency-dependent detection of the output of the large-scale interferometer is much more challenging, since this would require at least two long filter cavities.

Squeezed light

As shown in Ref. [108] for a conventional and in Refs. [39, 86, 134] for detuned SR configurations, a frequency-dependent squeezed light input can reduce the overall noise spectral density by a factor of e^{-2r} where $r \geq 0$ is the squeezing parameter. The optimal squeezing angle α_{opt} can be obtained by so choosing it that the noise spectral density has only terms proportional to e^{-2r} . If we just consider the vacuum fluctuations associated with the local meter, the optimal squeezing angle is simply given by

$$\tan \alpha_{\text{opt}}^{(2)}(\Omega) \approx \frac{2m\epsilon^{(2)}\Omega^2}{3(\theta^{(2)})^2} \quad (4.61)$$

where $m_{\text{BS}} = m$ and $\Omega \ll \epsilon^{(2)}$ were again assumed. The frequency dependance of the squeezing angle can also be realized easily by implementing a single filter cavity. But it should be emphasized that the prescription given in Eq. (4.61) does not necessarily minimize the combined noise spectral density around the optomechanical resonance. This becomes apparent in Fig. 4.12, where the sensitivity around the optomechanical resonance

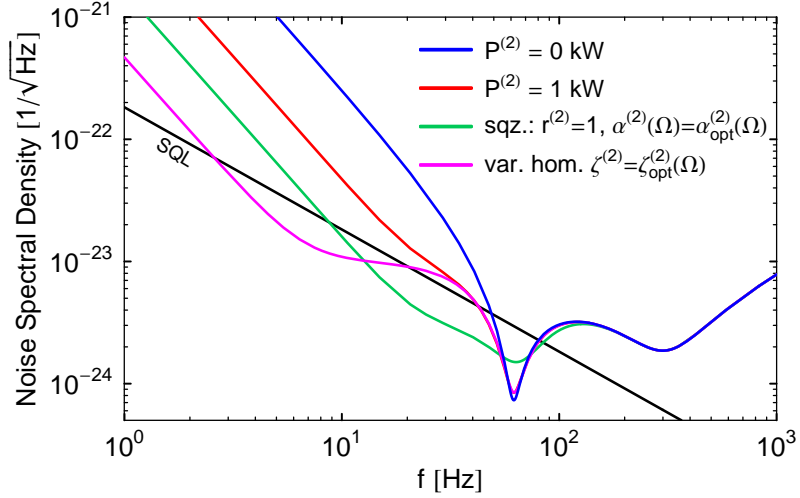


Figure 4.12.: Quantum noise spectral densities of Advanced LIGO narrowband configuration (blue) with phase quadrature readout (cf. also Tab. 2.1) and different LR configurations: (*red*) configuration agrees with the one already shown in Fig. 4.7, i.e. $P^{(2)} = 1$ kW and $\epsilon^{(2)} = 2\pi$ 1 kHz; (*green*) same configuration as before but with frequency-dependent squeezed input (10 dB) associated with second carrier; (*magenta*) again the same LR configuration but with frequency-dependent homodyne detection of the output of the local meter.

is slightly deteriorated compared to the same configuration without a squeezed light input. This is due to the fact that the resonance resides within the scope of the shot noise dominated regime of the local meter. In this regime, the phase quadrature is squeezed while the amplitude quadrature is anti-squeezed, which gives rise to additional radiation pressure forces acting on the ITMs. This additional noise can be found in the output of the large-scale interferometer. However, a more stringent minimization of the combined noise spectral density with respect to the squeezing angle would result in a rather complex expression. The corresponding frequency dependence cannot be realized by means of a single KLMTV filter. Remember that operating the large-scale interferometer with a squeezed light input would demand at least two long filter cavities.

4.2.5. Conclusion

Motivated by the optical-bar schemes [25] and the quantum-locking schemes [55, 56, 90, 105], we have proposed the injection of a second laser beam into a detuned signal-recycled Michelson interferometer. By means of this auxiliary light field, a measurement of the differential motion of the input test mass mirrors is accomplished. With this local readout technique we can overcome the sensitivity limitation imposed by the rigid optical spring at frequencies below the optomechanical resonance. We have derived the optimally combined sensitivity of the local readout scheme, and demonstrated that it is invariant with respect to the implementation of a feedback control system.

Taking into account the currently predicted classical noise budget of Advanced LIGO as well as constraints on the optical power, we performed an optimization of our local readout scheme for the detection of different compact binary systems. The proposed local

readout scheme allows us either to broaden the detection band, i.e. the sensitivity at high frequencies is indirectly improved, or to detect of intermediate-mass black-hole binaries with a broad frequency range, without sacrificing sensitivity to neutron-star binaries and stellar-mass black-hole binaries.

We have also briefly discussed how the sensing of the central Michelson degree of freedom in the current baseline design of Advanced LIGO can be made dramatically more sensitive and turned into our local readout configuration.

Finally, it has been shown that the local readout scheme can be combined without much effort with other QND techniques, namely the injection of squeezed vacuum states or the variational homodyne detection of the output field. Both advanced tools allow us a further improvement in sensitivity, as we have shown for the quantum noise limited regime. A full optimization in the presence of classical noise should be carried out.

4.3. Double optical spring interferometer

Most of the candidate Advanced LIGO configurations are designed to have two resonances within the detection band around which the sensitivity is enhanced: a stable optical resonance and an unstable optomechanical resonance – which is upshifted from the pendulum frequency due to the so-called *optical spring* effect. One concern that arises in conjunction with the optical spring is that it always causes instability: depending on the sign of the detuning, the optical force either brings anti-damping or creates an anti-spring. The instability can be cured by employing an appropriate linear feedback control system which does not modify the noise spectral density of the GW detector in the ideal case, as shown by Buonanno and Chen in Ref. [37]. But in practice, the required control within the detection band can cause undesirable complexity in the control system or additional classical noise.

In this section, an alternative all-optical way to suppress the instability is investigated. The proposed scheme requires the injection of a second carrier field into the bright port of the interferometer, as depicted in Fig. 4.13. We assume that the two carriers exhibit different polarizations and/or frequencies as in the local readout scheme considered in Sec. 4.2. This ensures that there is no direct coupling between the two carrier fields (cf. Sec. 4.1.1), although they both couple directly to the mirrors. The two outputs associated with the carrier lights have to be separated behind the dark port in order to perform an independent homodyne detection of each field. Thereafter the two output channels need to be combined by means of appropriate filter functions.

In contrast to the local readout scheme, the second carrier also resonates in the arm cavities. Nevertheless, each carrier can sense an individual reflectivity of the SR mirror and detuning of the SR cavity. One purpose of the second carrier is to create a second optical spring that, together with the first, forms a stable optical spring — even though each individual optical spring, acting alone, would be unstable. That means that the test masses are trapped by a stable ponderomotive potential well induced by two carrier light fields whose detunings have opposite signs. Such a stable, double optical spring (DOS) can be realized at least in two ways. The first possibility (*weak stabilization*) relies on the observation that the ratio between the real part of the optical spring constant (strength of spring/anti-spring) and its imaginary part (strength of damping/anti-damping) depends on the detuning frequency of the carrier. This suggests that the detunings of the two

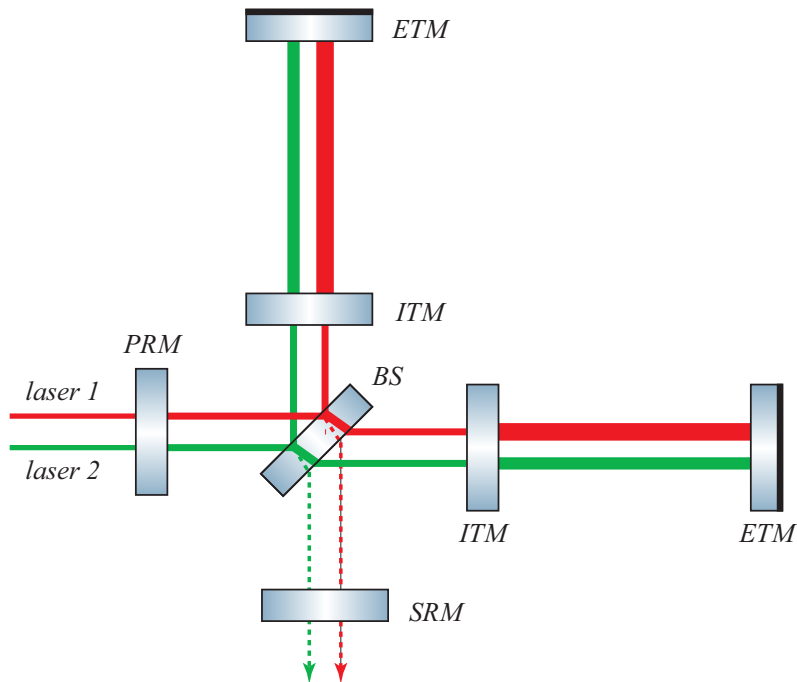


Figure 4.13.: Schematic plot of a double-carrier Michelson interferometer equipped with arm cavities as well as power- and signal-recycling mirrors. The two carrier lights are split at the beam splitter (BS) before they are transmitted through the input test mass mirrors (ITMs) into the arm cavities. Both carrier fields resonate in the arm cavities and together they can provide a stable double optical spring (DOS).

carriers can be so arranged that the first carrier features a stronger spring and weaker anti-damping, while the second offers a weaker anti-spring and stronger damping. In this case a stable regime can be reached with a weak second carrier, which does not much affect the sensitivity of the interferometer. The second way (*annihilation*) requires the two carriers to have equal power and exactly opposite detunings. In this case the corresponding optical springs exactly cancel each other, so that the differential motion of the test masses again behaves as a free mass. Interestingly, the noise spectrum of this configuration agrees with that expected by the GW community [84] at a time an interferometer with detuned signal-recycling had not been thoroughly studied, i.e. before Refs. [36, 37, 38] were published.

The weak stabilization and annihilation regimes are by no means the only possibilities. One can also profit from the DOS technique in the sense that it increases flexibility in shaping noise curves: for any specific GW source, the noise spectrum can be optimized correspondingly over the parameter subspace of the two carriers, with the constraint that the resulting dynamics must be stable. The optimization carried out here is restricted to neutron star binary inspirals, i.e. binary systems with a total mass of $M = 2.8M_{\odot}$. The currently predicted noise budget of Advanced LIGO is employed for the optimization procedure, as well as a plausible noise budget of interferometers just after the second generation.

The DOS technique can also be used for the stabilization of the optical-spring pondero-

motive squeezer introduced in Refs. [53, 124]. The proposed set-up aims at the generation of frequency-independent squeezed vacuum states below the optical spring resonance frequency. The stable optomechanical resonance has already been demonstrated experimentally in our Ref. [52].

This section is organized as follows: first, the stabilization process is demonstrated by studying the classical dynamics of DOS systems in Sec. 4.3.1. In the following section, the input-output relation of a DOS interferometer is calculated. In Sec. 4.3.3, different applications of the DOS scheme are discussed. The DOS scheme can be enhanced further by the implementation of the previously proposed local readout technique, which is discussed in Sec. 4.3.4. Finally, in Sec. 4.3.5, we summarize the main results.

4.3.1. Classical dynamics

In this section, we study the classical dynamics of the double optical spring stabilization process. The mechanical degree of freedom of the interferometer shown in Fig. 4.13 is given by

$$x \equiv x_{\text{antisym}} = (x_{\text{ETM}}^{(n)} - x_{\text{ITM}}^{(n)}) - (x_{\text{ETM}}^{(e)} - x_{\text{ITM}}^{(e)}), \quad (4.62)$$

which describes the differential motion between the four test masses. All test mass mirrors are suspended as pendulums and we assume that each has an eigenfrequency of ~ 1 Hz in the absence of an optical field. Since this eigenfrequency is far below the detection band, we will simply treat the mirrors as free masses. The effective mass of the differential mode is $m/4$, where m is the mass of each individual mirror.

Two carrier fields with angular frequencies $\omega_0^{(i)}$ with $i \in [1, 2]$ establish the optical part of the set-up. A differential arm length change gives rise to a signal which can be found in both output fields corresponding to the two carrier lights. When the mirrors are held fixed, the optical resonance frequency of the differential optical mode is given by $\omega_0^{(i)} - \lambda^{(i)} - i\epsilon^{(i)}$, where $\epsilon^{(i)}$ and $\lambda^{(i)}$ can be found in Eq. (4.20) in terms of interferometer parameters, i.e. the detuning phase $\phi^{(i)}$, the amplitude reflectivity $\rho_{\text{SR}}^{(i)}$ of the SR mirror and the half line width γ_o of the arm cavities. Since the two carriers should both be resonant in the arm cavities, their detuning phases must differ by

$$\Delta\phi = \phi^{(2)} - \phi^{(1)} = \frac{2\pi n l_{\text{SR}}}{c} (\Delta\nu)_{\text{FSR}}, \quad n = 0, \pm 1, \pm 2, \dots \quad (4.63)$$

where $(\Delta\nu)_{\text{FSR}}$ is the free spectral range of an arm cavity and l_{SR} the length of the SR cavity. This constraint must be taken into account in practical designs of DOS interferometers. Later, however, we assume that the detuning phases can take arbitrary values which can be accomplished experimentally by changing the length of the SR cavity. Before treating the two optical springs jointly let us consider first the optomechanical coupling for each detuned carrier separately. Provided that the mirrors can initially be treated as free masses, the classical equation of motion for the differential mode in the case of a single detuned carrier can be written in frequency domain as:

$$-\frac{m}{4}\Omega^2 x(\Omega) = -K_{\text{os}}^{(i)}(\Omega) x(\Omega) + F_{\text{ext}}, \quad i \in [1, 2], \quad (4.64)$$

where $m/4$ is the reduced mass and F_{ext} accounts for any external classical force. The radiation pressure force exerted on the mirrors becomes linearly dependent on the differential length x [cf. Eq. (4.62)] of the arm cavities, analogous to a mechanical spring. This

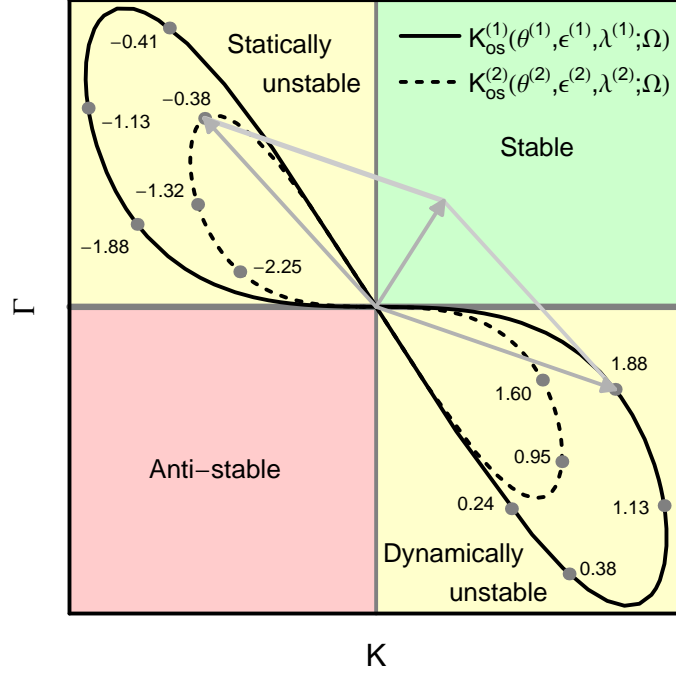


Figure 4.14.: Real and imaginary parts of two different spring constants in the weakly coupled regime [cf. Eq. (4.66)]. For each trajectory the circulating power, bandwidth and sideband frequency are fixed to a certain value while detuning varies from $-\infty$ to ∞ . The outer trajectory corresponds to an optical spring with a higher circulating power, i.e. $\theta^{(1)} > \theta^{(2)}$. Example values of $\lambda^{(i)}/\epsilon^{(i)}$ are marked on each trajectory.

is only the case for a detuned SR cavity, while in the case of a tuned configuration the motion of the differential mode is solely influenced by radiation pressure fluctuations and classical noise. The frequency-dependent optical spring constant $K_{\text{os}}^{(i)}(\Omega)$ is given by [38]:

$$K_{\text{os}}^{(i)}(\Omega) = -R_{FF}^{(i)}(\Omega), \quad i \in [1, 2], \quad (4.65)$$

where the susceptibility $R_{FF}^{(i)}(\Omega)$ can be found in Eq. (4.19).

Before treating a full-power interferometer, it is instructive to first consider to a *weakly coupled regime*, assuming that optical frequency scales, i.e. the effective detuning $\lambda^{(i)}$ and the effective bandwidth $\epsilon^{(i)}$, are much larger than the resulting optomechanical resonance frequency. In this weakly coupled regime, one can expand the optical spring constant (cf. e.g. Ref. [37]) as

$$K_{\text{os}}^{(i)}(\Omega) \approx \frac{m\theta^{(i)}\lambda^{(i)}}{4((\epsilon^{(i)})^2 + (\lambda^{(i)})^2)} \left(1 + i \frac{2\epsilon^{(i)}\Omega}{((\epsilon^{(i)})^2 + (\lambda^{(i)})^2)} \right) \equiv K^{(i)} - i\Omega\Gamma^{(i)}, \quad i \in [1, 2]. \quad (4.66)$$

where $K^{(i)}$ and $\Gamma^{(i)}$ are both real constants. Analogous to a mechanical spring, $K^{(i)}$ accounts for the restoring force while $\Gamma^{(i)}$ denotes the damping. The real and imaginary parts of the optical spring constant are proportional to $\theta^{(i)}$, which in turn is proportional to the carrier power $P^{(i)}$. Inserting Eq. (4.66) into Eq. (4.64) reveals that the

optomechanically coupled system is stable if

$$K^{(i)} > 0 \quad \text{and} \quad \Gamma^{(i)} > 0, \quad (4.67)$$

i.e. a positive spring constant and positive damping is required.

From Eq. (4.66) one can readily deduce that the stability condition, i.e. Eq. (4.67), can never be satisfied by a single optical system, since a positive detuning always produces anti-damping ($\Gamma^{(i)} < 0$) while a negative detuning always comes along with an anti-restoring force ($K^{(i)} < 0$). This is also illustrated by Fig. 4.14: we plot the trajectory mapped out by (K, Γ) for fixed circulating power and effective line width ($\epsilon^{(i)}$) as the effective detuning ($\lambda^{(i)}$) shifts from $-\infty$ to ∞ . This figure shows two different trajectories corresponding to two optical springs with different optical power, where the outer one [i.e. $K_{\text{os}}^{(1)}(\theta^{(1)}, \epsilon^{(1)}, \lambda^{(1)}; \Omega)$] belongs to a higher power. Each individual spring, as we change its detuning frequency, has its own ∞ -shaped trajectory which is confined within quadrants with $K^{(i)} \cdot \Gamma^{(i)} < 0$. But when the two optical springs are combined, their complex spring constants add up, which corresponds to a vector addition as depicted in Fig. 4.14. By appropriately adjusting the detunings for first and second carrier, it is possible to find many stable compositions; one of them is shown in Fig. 4.14. In this configuration, a relatively strong optical spring is stabilized by a relatively weak anti-spring generated by a lower power. This can be explained as follows: the stronger optical spring is generated by a carrier with relatively high optical quality factor, $|\lambda^{(1)}/\epsilon^{(1)}|$, which tends to yield a stronger restoring (or anti-restoring) than a damping (or anti-damping) force. The weak anti-spring is generated by a carrier with low optical quality factor $|\lambda^{(2)}/\epsilon^{(2)}|$, which tends to yield a stronger damping (or anti-damping) than restoring (or anti-restoring) force. Hence a lower optical power of the second carrier allows the damping force of the second spring to match that of the first, while it makes the anti-restoring force of the second spring much weaker than the restoring force of the first spring. Mathematically, this *weak stabilization* can be summarized as

$$\frac{|K^{(1)}|}{|\Gamma^{(1)}|} \gg \frac{|K^{(2)}|}{|\Gamma^{(2)}|}, \quad |\Gamma^{(1)}| \sim |\Gamma^{(2)}| \Rightarrow |K^{(1)}| \gg |K^{(2)}|. \quad (4.68)$$

Now we turn to another rather extreme example of a stable DOS regime. When the two carriers have the same power and bandwidth but opposite detunings, their optical spring constants exactly cancel each other. In fact, this cancelation, or annihilation, is valid for an arbitrarily strong coupling. Mathematically, this can be summarized as

$$K_{\text{os}}^{(1)}(\theta^{(1)}, \epsilon^{(1)}, \lambda^{(1)}; \Omega) + K_{\text{os}}^{(2)}(\theta^{(2)}, \epsilon^{(2)}, -\lambda^{(2)}; \Omega) = 0. \quad (4.69)$$

As stated above, the stability condition given in Eq. (4.67) is an approximation which is only valid in the weakly coupled regime. A more precise statement regarding the stability of the two carrier system is given by the condition that all roots of the characteristic equation

$$-\frac{m}{4}\Omega^2 + K_{\text{os}}^{(1)}(\Omega) + K_{\text{os}}^{(2)}(\Omega) = 0 \quad (4.70)$$

must have negative imaginary parts [cf. discussion e.g. before Eq. (2.120)]. In Fig. 4.15, we rigorously explore the high-power DOS stabilization process by tracing the real and imaginary parts of the optomechanical eigenfrequency obtained by numerically solving

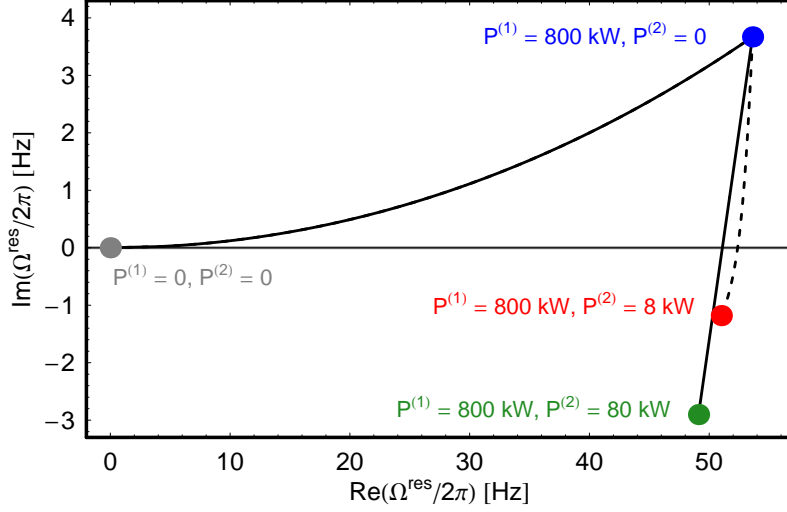


Figure 4.15.: Trajectories of the optomechanical resonance frequency in the complex plane [cf. Eq. (4.70)] illustrate the DOS stabilization process. The test masses are assumed to be initially free masses (gray dot). Fixing the power of the first carrier light to different values between 0 and 800 kW yields the trajectory from the left gray dot to the upper blue dot, i.e. the mechanical resonance frequency is upshifted and a mild anti-damping is introduced (Advanced LIGO narrowband parameters given in Tab. 2.1 were used). The trajectory ends at the blue dot, with a circulating power of $P^{(1)} = 800$ kW. Subsequently, the optical power of the second carrier is fixed to different values between 0 and 8 kW or 0 and 80 kW, respectively. It introduces a damping while slightly downshifting the optomechanical resonance frequency. For $\epsilon^{(2)} = 2\pi$ 9Hz, $\lambda^{(2)} = -2\pi$ 55Hz, the trajectory ends at the red dot, with a circulating power of $P^{(2)} = 8$ kW; while for $\epsilon^{(2)} = 2\pi$ 60Hz, $\lambda^{(2)} = -2\pi$ 60Hz the trajectory ends at the green dot, with circulating power of $P^{(2)} = 80$ W.

Eq. (4.70). We first consider a single optical spring configuration with a power increasing from $P^{(1)} = 0$ to 800 kW (from the left most dot to the top dot). In this case the real part of the optomechanical resonance frequency as well as the anti-damping increase. We then fix the first carrier at $P^{(1)} = 800$ kW and increase the second carrier to $P^{(2)} = 8$ kW and $P^{(2)} = 80$ kW, respectively, for two different choices of line width and detuning. Finally, we achieve a stable system by adding damping while only slightly decreasing the optomechanical resonance frequency by a few Hz (from the top dot to the two lower-right dots). Here we do not plot the optical resonance, because it remains stable for the circulating powers considered here.

Before ending this section, we note that, when the pendulum eigenfrequency is not neglected, a stable single optical spring regime exists, i.e. an increase in mechanical resonance frequency is associated with an increase in damping. But this requires the optical frequency scales to be lower than the pendulum eigenfrequency (~ 1 Hz), which is not desirable in the case of GW detectors. Such a regime was experimentally investigated by Schliesser et al. in Ref. [140].

4.3.2. Dynamics and sensing

In this section, we investigate the sensitivity of a stable DOS interferometer like that shown in Fig. 4.13. According to Sec. 4.1.1, such a set-up effectively contains two independent interferometers in one scheme, if the two carrier lights exhibit at least different frequencies or polarizations. Both sense the same differential mode defined in Eq. (4.62). But the input optical vacuum fluctuations associated with the two carriers are independent. We assume that the optical detuning and SR mirror reflectivity can be varied independently for each carrier. The Heisenberg equations of motion in frequency domain (cf. Refs. [36, 37, 38, 54, 108]) can be obtained directly from the general formalism presented in Sec. 4.1.3 by choosing $n = 2$ and $k = 2$. Then the equations of motion for the antisymmetric mode of motion of the four arm cavity mirrors is given by

$$\hat{x} = -R_{xx}(\Omega)[\hat{F}^{(1)}(\Omega) + \hat{F}^{(2)}(\Omega) + (R_{FF}^{(1)}(\Omega) + R_{FF}^{(2)}(\Omega)) \hat{x}] + L h + \hat{\xi}_{\text{noise}}, \quad (4.71)$$

and for the two measurement outputs $\hat{y}^{(i)}$ we obtain:

$$\hat{y}^{(1)} = \hat{Y}_1^{(1)}(\Omega) \sin \zeta^{(1)} + \hat{Y}_2^{(1)}(\Omega) \cos \zeta^{(1)} + [R_{Y_1F}^{(1)}(\Omega) \sin \zeta^{(1)} + R_{Y_2F}^{(1)}(\Omega) \cos \zeta^{(1)}] \hat{x}, \quad (4.72)$$

$$\hat{y}^{(2)} = \hat{Y}_1^{(2)}(\Omega) \sin \zeta^{(2)} + \hat{Y}_2^{(2)}(\Omega) \cos \zeta^{(2)} + [R_{Y_1F}^{(2)}(\Omega) \sin \zeta^{(2)} + R_{Y_2F}^{(2)}(\Omega) \cos \zeta^{(2)}] \hat{x}. \quad (4.73)$$

Note that we have labeled all quantities with superscripts (1) and (2) for the first carrier and the second carrier, respectively. All the quantities used here are listed in Sec. 4.1.3. In contrast to the local readout scheme (cf. Sec. 4.2) it is no longer necessary to treat ITMs and ETMs separately, hence the mechanical susceptibility of the differential mode is now given by $R_{xx} \equiv -4/(m\Omega^2)$ and the classical noise at the four mirrors can be handled by a single operator $\hat{\xi}_{\text{noise}}$. Two input-output relations are obtainable from the equations of motion given in Eqs. (4.71)-(4.73) and these can be written in the compact form introduced in Sec. 4.1.3:

$$\hat{y}^{(1)} = \mathbf{n}_1^T \cdot \boldsymbol{\nu} + s_1 h, \quad \hat{y}^{(2)} = \mathbf{n}_2^T \cdot \boldsymbol{\nu} + s_2 h, \quad (4.74)$$

where $\boldsymbol{\nu}^T = (\hat{a}_1^{(1)}, \hat{a}_2^{(1)}, \hat{a}_1^{(2)}, \hat{a}_2^{(2)}, \hat{\xi}_{\text{noise}})$. Here the two vectors $\mathbf{n}_{1,2}$ account for the linear transfer functions from the noise channels $\boldsymbol{\nu}$ into the two output channels, while the two functions $s_{1,2}$ are the linear transfer functions from the signal, i.e. the GW strain h , into the two output channels. The combined optimal noise spectral density can be deduced directly from Eq. (4.26).

4.3.3. Example configurations

In this section, different example configurations of a DOS interferometer are discussed. First we restrict our investigations to quantum noise in order to clarify the two distinct regimes, weak stabilization and annihilation already mentioned at the beginning. Next, different configurations are optimized for neutron star binary inspirals taking into account a realistic classical noise budget. Finally, the classical noise budget is lowered by a certain amount and we explore whether DOS configurations can take full advantage of this technical improvement. The proposed DOS configuration is designated as an upgrade candidate for the forthcoming Advanced LIGO detector.

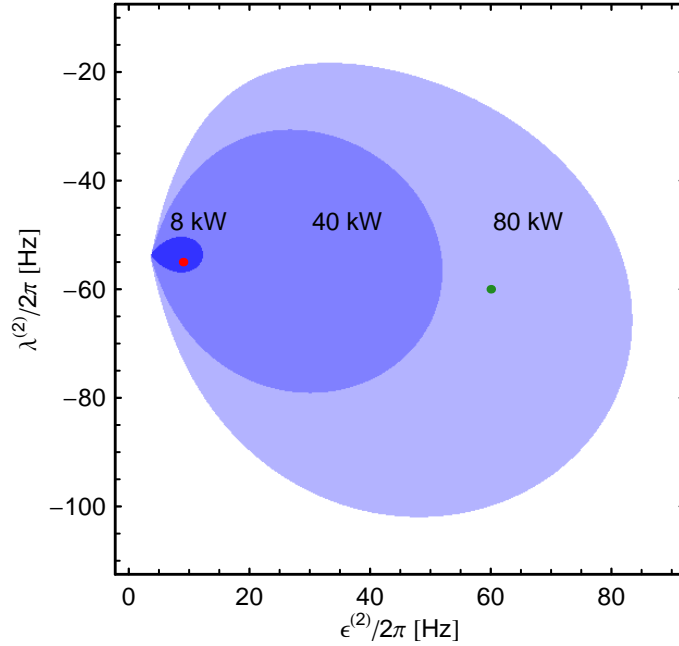


Figure 4.16.: Weak stabilization regime: stable regions versus effective half bandwidth ($\epsilon^{(2)}$) and effective detuning ($\lambda^{(2)}$) associated with the second carrier in the case of three different circulating powers, i.e. $P^{(2)} = 8 \text{ kW}$, 40 kW and 80 kW . The colored regions indicate that the Advanced LIGO narrowband configuration (cf. Tab. 2.1) with a circulation power of 800 kW is turned into a stable DOS configuration. The small red and green dots mark the configurations whose trajectories of the optomechanical resonance frequencies are shown in Fig. 4.15.

Quantum noise examples

Here we study the quantum noise spectrum of two special regimes of the DOS scheme: weak stabilization and annihilation. Both cases have already been discussed within the framework of classical dynamics in Sec. 4.3.1.

Weak stabilization. In this scenario, we use a relatively weak second carrier to stabilize a typical Advanced LIGO configuration. This corresponds to the regime illustrated by Fig. 4.15, where a second carrier with circulating powers of $P^{(2)} = 8 \text{ kW}$ and 80 kW , respectively, has been employed to stabilize an interferometer with a high circulating power ($P^{(1)} = 800 \text{ kW}$). These two stable example configurations are also marked in Fig. 4.16, which shows the region of all possible second carriers in the $(\lambda^{(2)}, \epsilon^{(2)})$ – plane for circulating powers of $P^{(2)} = 8 \text{ kW}$, 40 kW and 80 kW .

In Fig. 4.17 we plot the noise spectral densities of two DOS configurations which correspond to the two stable configurations treated in Fig. 4.15. Remember that we use the parameters of the Advanced LIGO narrowband operational mode for the first carrier (cf. Tab. 2.1). The optical resonance frequencies and powers for the second carrier can be found in the caption of Fig. 4.15, and we assume that the phase quadrature is detected, i.e. $\zeta^{(2)} = 0$. As we see from Fig. 4.17, in both cases the DOS noise spectral densities do not much differ from that of the usual Advanced LIGO narrowband interferometer.

Annihilation. Now we turn to a different regime, where the Advanced LIGO circulat-

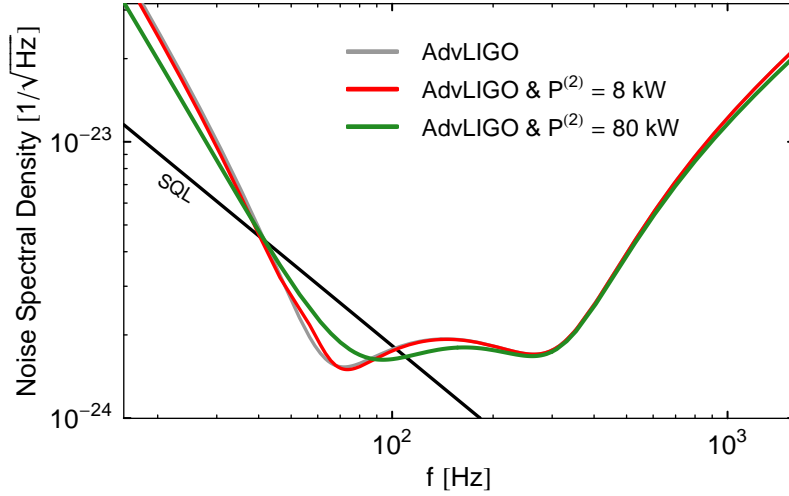


Figure 4.17.: Noise spectral densities of weak stabilization DOS configurations, with parameters corresponding to configurations treated in Fig. 4.15 or marked in Fig. 4.16. The parameters associated with the first carrier agree with those of the Advanced LIGO narrowband operational mode (cf. Tab. 2.1). The two choices of parameter values for the stabilizing second carrier are: (i) $P^{(2)} = 8 \text{ kW}$, $\epsilon^{(2)} = 2\pi \text{ 9Hz}$, $\lambda^{(2)} = -2\pi \text{ 55Hz}$ and (ii) $P^{(2)} = 80 \text{ kW}$, $\epsilon^{(2)} = 2\pi \text{ 60Hz}$, $\lambda^{(2)} = -2\pi \text{ 60Hz}$. Phase quadrature is detected in both cases ($\zeta^{(2)} = 0$).

ing power is equally distributed to the two carrier fields, namely $P^{(1)} = P^{(2)} = 400 \text{ kW}$, and where the two detunings are exactly opposite. In this case the two optical springs cancel each other, i.e. the total effective ponderomotive rigidity vanishes completely. For Fig. 4.18 the two detection angles also have opposite signs, while the *absolute* values of the two detunings as well as the two detection angles agree with the corresponding values of the Advanced LIGO narrowband configuration (cf. Tab. 2.1). All other parameters are unchanged.

Fig. 4.18 shows that the sensitivity does not change in the high frequency regime where shot noise is the limiting factor. This is because, generally, the noise spectral density of the shot noise remains unchanged when reversing the signs of the detuning and the detection angle, respectively. With the optimal filter functions (cf. Fig. 4.19), we obtain the same shot noise level as the usual Advanced LIGO narrowband configuration, since the total power is conserved. It should be emphasized that the noise spectral density, of each output separately can be above the optimally combined noise spectral density as depicted by Fig. 4.18. This is possible because the filter functions are able to exploit correlations between the two outputs, which is indicated by the green curves in Fig. 4.19.

In the low frequency regime, sensitivity is slightly improved compared to the single optical spring configuration. As discussed in detail in Sec. 2.3.3, the quantum noise limited sensitivity of single optical spring interferometers at frequencies below the optomechanical resonance is dramatically lower than the sensitivity of non-optical-spring interferometers. This is due to the strong restoring force established by the single optical spring, which suppresses the response of the differential mode to GWs. In a double optical spring interferometer, the second carrier usually gives rise to a less rigid or completely canceled

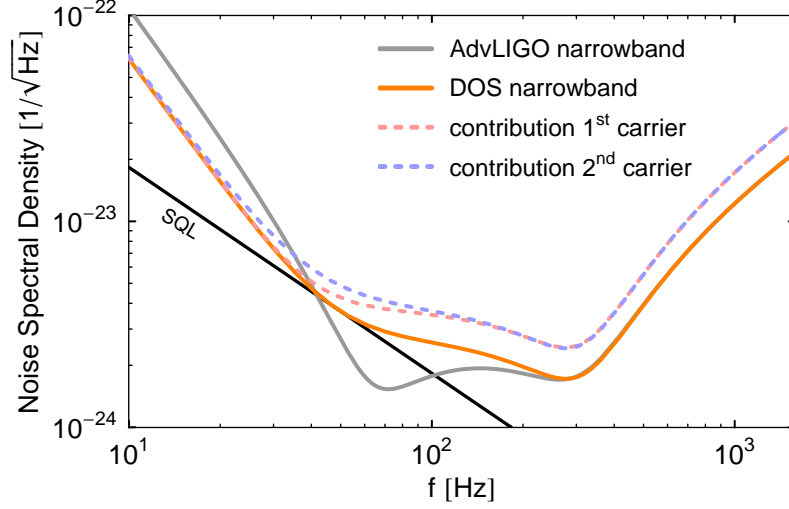


Figure 4.18.: Noise spectral density of annihilation DOS configuration (canceled optical spring) with parameters based on the Advanced LIGO narrowband operational mode (cf. Tab. 2.1). Detuning and detection angle of the first carrier are identical to that of Advanced LIGO narrowband configuration, while those of the second are opposite. The total power is equally divided into two parts, i.e. $P^{(1)} = P^{(2)} = 400$ kW. Other parameters are left unchanged. The contributions corresponding to the two carrier lights are also itemized (light red and blue curves). The contributions correspond to measuring one of the outputs alone without filtering – but still in presence of both carriers.

effective optical spring. This effect has already appeared in the first example, where only a weak second carrier light was employed (cf. Fig. 4.17) and it becomes more significant in the case of canceled optical springs (cf. Fig. 4.18). For intermediate frequencies, sensitivity deteriorates due to the absence of an optomechanical resonance gain. In this regime, the output associated with the carrier having positive detuning usually provides a better sensitivity than the other. The optimal filter functions are chosen accordingly, as illustrated by Fig. 4.19.

In the case of the annihilation regime the optomechanical resonance disappears completely and the noise spectral density of such a configuration is equal to

$$S_h(\Omega) = S_{\text{shot}}(\Omega) + \frac{S_{\text{SQL}}^2(\Omega)}{4S_{\text{shot}}(\Omega)}. \quad (4.75)$$

Here $S_{\text{shot}}(\Omega)$ denotes the shot-noise spectral density of a detuned single carrier interferometer with the same total power as in the canceled optical spring configuration. Remember that the free-mass standard quantum limit (SQL) [27] for detecting the gravitational wave strain h with a Michelson interferometer equipped with arm cavities is given by

$$S_{\text{SQL}}(\Omega) = \sqrt{\frac{8\hbar}{m\Omega^2 L^2}}. \quad (4.76)$$

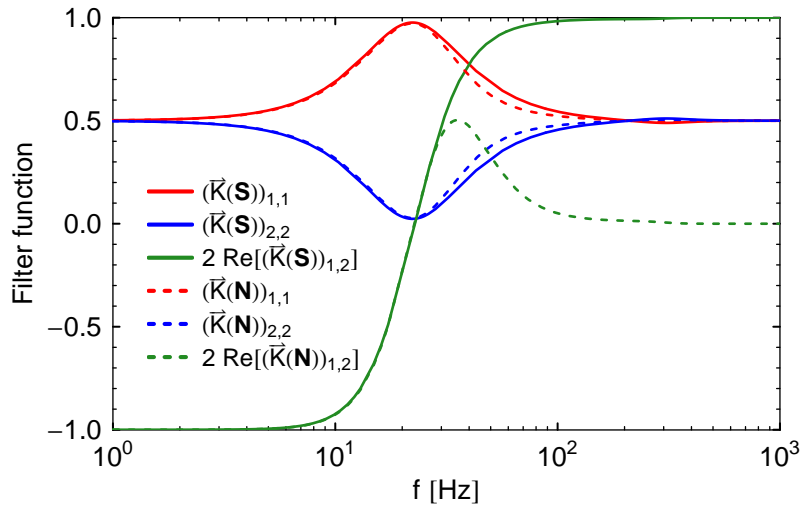


Figure 4.19.: Squared absolute values and cross correlations of filter functions [cf. Eq. (4.30)]. The percentage of GW strain (solid lines) or noise (dashed lines) contributed by the output corresponding to the first carrier (red lines) and the second (blue lines) carrier is depicted. The green lines account for the correlations between the two outputs.

Optimized configurations with Advanced LIGO classical noise budget

In the following we optimize the proposed DOS interferometer for neutron star - neutron star (NS-NS) inspirals by means of the tools introduced and reviewed in Sec. 3.1. For such systems with a total mass of $M = (1.4 + 1.4)M_{\odot}$ the last stable circular orbit gives an upper frequency limit of $f_{\max} \approx 1570$ Hz and seismic noise defines a lower bound of $f_{\min} \approx 7$ Hz. Furthermore a broadband optimization is carried out, studied in detail in Sec. 3.2. In the first instance, we use the current Advanced LIGO classical noise budget (as given in *Bench* [2]) for the optimization. Each contribution to the total classical noise budget, i.e. suspension thermal noise, seismic noise, thermal fluctuations in the coating and gravity gradient noise, is shown separately in Figs. 4.20–4.21.

In addition to stabilizing the interferometer, the second carrier can also help to improve sensitivity. If we assume that both carriers sense the same SR mirror reflectivity, the gain in NS-NS sensitivity is maximized when the two optical springs totally cancel each other (Fig. 4.20). This requires the total power to be equally distributed to the two carrier fields.

Experimentally more challenging is the implementation of a SR mirror which yields different reflectivities for the two carrier lights. This additional degree of freedom allows a further improvement in sensitivity, namely it can be used to so optimize each sub-interferometer for a different frequency regime that they complement each other. In this case the annihilation scenario is no longer the optimal choice, but distributing the total power equally is still close to an optimal arrangement (cf. Tab. 4.3). The combined noise spectral density of such a configuration is shown in Fig. 4.21 together with the spectra of the individual output channels. These individual contributions reveal that one carrier (with negative detuning) ensures a good sensitivity in the low frequency regime while the other (with positive detuning) gives the main contribution at frequencies above the

	$P^{(i)}$ [kW]	$\lambda^{(i)}$ [Hz]	$\epsilon^{(i)}$ [Hz]	$\zeta^{(i)}$ [rad]	Improvement
	800	2π 290	2π 120	2π 0.347	-
	-	-	-	-	-
high classical noise	750	2π 190	2π 50	2π 0.125	7.3%
	50	-2π 70	2π 20	2π 0.075	
	700	2π 190	2π 40	2π 0.0625	22.6%
	100	-2π 50	2π 30	2π 0.475	
	600	2π 180	2π 30	2π 0.0125	22.6%
	200	-2π 40	2π 50	2π 0.3875	
	500	2π 150	2π 45	2π 0.0125	36.3%
	300	-2π 50	2π 60	2π 0.375	
	450	2π 160	2π 30	2π 0	35.5%
	350	-2π 10	2π 40	2π 0.3	
400	2π 140	2π 20	2π 0.01	35.5%	
400	-2π 20	2π 55	2π 0.31		

Table 4.3.: Parameters for DOS scheme optimized for NS-NS binary systems with a total power fixed at 800 kW. The last column gives the improvement in event rate of the proposed DOS scheme compared to an optimized Advanced LIGO configuration (parameters provided in the first row). Each upper (lower) row shows the parameters associated with the first (second) carrier. We adopted the current Advanced LIGO classical noise budget.

optomechanical resonance. It should be emphasized that the combined noise spectral density is close to the limit set by the classical noise level at low frequencies, and an improvement in event rate of 35.5% can be achieved for NS-NS inspirals for which the optimization has been carried out. As a more general optimization is performed, with a variable distribution of the total power, which is still fixed at 800 kW, it turns out that $P^{(1)} = 500$ kW, $P^{(2)} = 300$ kW achieves a slightly better improvement in event rate, namely 36.3%. Results for different power distributions are listed in Tab. 4.3.

The sensitivity of all optimized configurations is basically improved at low frequencies at the expense of the high frequency regime. By means of the broadband optimization procedure introduced in Sec. 3.2 one can find a certain trade-off. This is exemplified by Fig. 4.21, where we achieve a sensitivity comparable to Advanced LIGO within the [500 Hz, 1570 Hz] frequency band, while maintaining an improvement in the event rate (integrating again from f_{\min}) of 16.4% compared to Advanced LIGO (cf. violet line in Fig. 4.21).

After adding up all classical noise contributions shown in Figs. 4.20 and 4.21, it turns out that the noise spectral density of the double optical spring configuration – in contrast an ordinary single optical spring set-up – almost follows the borderline set by classical noise in the low frequency regime, which can be tested by means of the function introduced in Eq. (3.10). For the $P^{(1)} = P^{(2)} = 400$ kW-configuration shown in Fig. 4.21, we obtain

$$\eta(f_{\text{up}} = 250 \text{ Hz}) \approx 0.85. \quad (4.77)$$

This indicates that at low frequencies (i.e., below 250 Hz), the quantum noise is already

	$P^{(i)}$ [kW]	$\lambda^{(i)}$ [Hz]	$\epsilon^{(i)}$ [Hz]	$\zeta^{(i)}$ [rad]	Improve
	800	2π 170	2π 10	2π 0.263	-
	-	-	-	-	-
low classical noise	700	2π 165	2π 5	2π 0.48	31.1%
	100	-2π 75	2π 25	2π 0.02	
	600	2π 150	2π 5	2π 0.01	52.2%
	200	-2π 20	2π 45	2π 0.36	
	500	2π 140	2π 5	2π 0.03	74.3%
	300	-2π 20	2π 45	2π 0.33	
	450	2π 135	2π 5	2π 0.01	83.4%
	350	-2π 25	2π 50	2π 0.33	
	400	2π 127	2π 4	2π 0.01	110%
	400	-2π 11	2π 46	2π 0.3	

Table 4.4.: The same comparison as in Tab. 4.3 but for a reduced classical noise budget: the gravity gradient noise and the suspension thermal noise are reduced by a factor of ten and the coating thermal by a factor of three (in amplitude).

a small fraction of the total noise. Improving the quantum noise spectral density further does not significantly improve the overall efficiency of the detector. Qualitatively, starting with a level of $\eta = 0.85$ and further lowering the overall quantum noise \bar{S}_h^q [cf. Eq. (3.10)] by a factor of 2 only improves η from 0.85 to 0.9, which entails an increase in event rate by 22%.

Optimized configurations with reduced classical noise budget

It is likely that developments in technology will lead in the future to a reduced classical noise floor. In order to explore the sustainability of our proposed DOS configuration, we analyze its performance in the presence of a reduced classical noise budget. For instance, the gravity gradient noise is a limiting factor at low frequencies before, at even lower frequencies, the seismic noise becomes dominant. Fluctuations in the mass distribution surrounding the suspended test masses induce an unwanted differential arm length change. As suggested in Ref. [96], this effect can be removed from the recorded data by performing independent measurements of the density fluctuations of the ground near each test mass. Even though it is conceivable to completely cancel out gravity gradient noise, we assume it to be one-tenth (in amplitude) of the current estimation for Advanced LIGO [8]. Another limiting factor is established by thermal noise in the suspension system and mirrors. Here we assume that the suspension thermal noise can be lowered by a factor of ten in amplitude, while the internal thermal noise of the mirrors can be lowered by a factor of three in amplitude [8]. Such improvements might be realized by (i) optimizing the design of the mirror coating structure and the suspension wires, (ii) improving mechanical quality factors of mirror coatings, substrate and suspension materials, and (iii) applying cryogenic techniques [18, 35, 84, 155, 156].

In order to conduct a proper comparison of the sensitivity to NS-NS binary systems, we optimize the usual single optical spring configuration as well as the DOS layout for

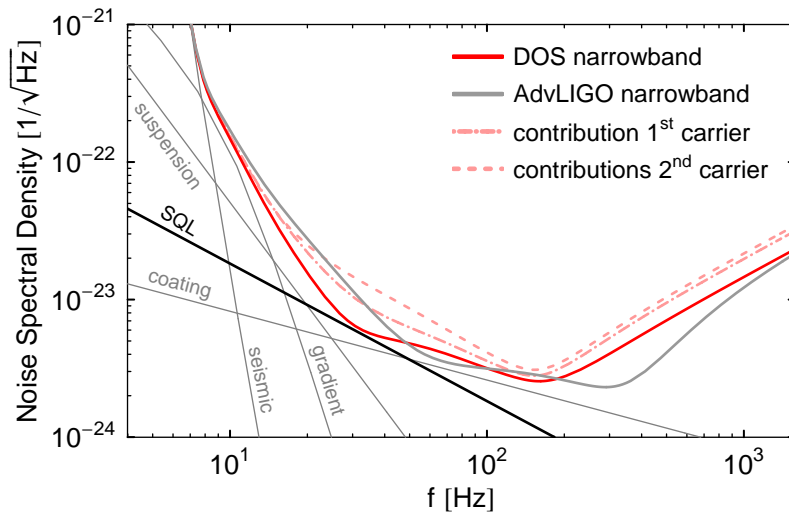


Figure 4.20.: Comparison of single optical spring Advanced LIGO narrowband configuration (cf. Tab. 2.1) with our proposed DOS scheme. The annihilation regime is illustrated in the presence of classical noise. The same reflectivity of the SR mirror is assumed for both carriers. We obtain 15% improvement in event rate for a DOS interferometer by using the following optimized parameters: $P^{(1)} = P^{(2)} = 400$ kW, $\lambda^{(1)} = -\lambda^{(2)} = 2\pi$ 128 Hz, $\epsilon^{(1)} = \epsilon^{(2)} = 2\pi$ 43 Hz, $\zeta^{(1)} = 2\pi$ 0.433 and $\zeta^{(2)} = 2\pi$ 0.5.

the modified classical noise budget. Only now does the potential of the DOS interferometer become apparent: if we use the Advanced LIGO narrowband configuration (cf. Tab. 2.1), in the presence of the new classical noise budget as a reference, we can achieve an improvement in event rate of only 61% with an optimized single optical spring configuration. Whereas an optimization of the DOS interferometer reveals an improvement of 238%. Comparing the single optical spring and the DOS configuration when both are optimized for the new classical noise budget, one obtains an improvement in event rate of 110% (cf. Tab. 4.4). The corresponding noise spectral densities of both optimized layouts are presented in Fig. 4.22. The big gap between the total noise curve of the single optical spring system and the classical noise budget shows that the single optical spring configuration is not limited by classical noise at low frequencies. This gap can be partially filled by the double optical spring configuration, but there is still room for further improvement. For the DOS configuration shown in Fig. 4.22 we evaluate

$$\eta(f_{\text{up}} = 250 \text{ Hz}) \approx 0.51. \quad (4.78)$$

In this case, lowering quantum noise by a factor of 2 still improves the event rate by 69%. A further improvement can be obtained by injecting even more than two carrier lights into the interferometer and combining the corresponding output channels in an optimal way (cf. Sec. 4.1).

4.3.4. Additional local readout scheme

As shown in the previous section, the DOS scheme does not fully exploit a possible lower classical noise budget which might be achieved by certain technical improvements

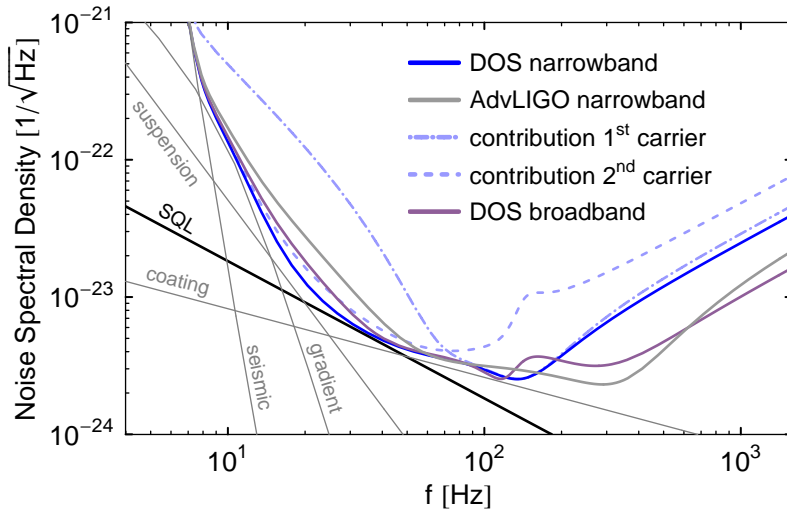


Figure 4.21.: Comparison of Advanced LIGO narrowband configuration (cf. Tab. 2.1) with two DOS configurations where different SR mirror reflectivities for first and second carrier are allowed. Parameters are given in detail in the last row of the first block in Tab. 4.3 for the DOS narrowband configuration. For the DOS broadband configuration we use the parameters: $\lambda^{(1)} = 2\pi \cdot 130$ Hz, $\epsilon^{(1)} = 2\pi \cdot 5$ Hz, $\zeta^{(1)} = 2\pi \cdot 0.01$, $\lambda^{(2)} = -2\pi \cdot 230$ Hz, $\epsilon^{(2)} = 2\pi \cdot 155$ Hz and $\zeta^{(2)} = 2\pi \cdot 0.02$. We obtain 35.5% improvement in event rate for the DOS narrowband configuration and 16.4% for the broadband configuration.

of the Advanced LIGO baseline design. Under such circumstances, the implementation of additional advanced tools, e.g. the injection of squeezed vacuum states [39, 86, 117, 159, 158] or a variational homodyne detection [39, 108, 134], can become inevitable. Both techniques were already investigated in conjunction with the local readout scheme in Sec. 4.2.4. Here, a third alternative should be considered, namely the combination of the DOS scheme with a local meter which senses the differential motion of the ITMs. This requires the injection of three carrier fields into the bright port, which so differ in frequency and/or polarization that they can be treated independently, as discussed in Sec. 4.1.1. Two carriers enter the arm cavities and the corresponding parameters (i.e. the two effective detunings and bandwidths) should be so adjusted that they provide a stable double optical spring. Note that it is not reasonable to approach the annihilation regime because the presence of an optical spring is required for transferring the motion of the ETMs to the ITMs in order to provide a signal for the third carrier which does not enter the arm cavities (cf. also Sec. 4.2).

Again the equations of motion can be easily obtained by means of the general formalism introduced in Sec. 4.1, namely one has to choose $n = 3$ and $k = 2$. In the case of a tuned local meter (third carrier) the stability condition is still given by Eq. (4.70), which depends only on the two carriers entering the arm cavities. But in general, all carriers can sense a detuned SR cavity and hence another optical spring can occur. The associated

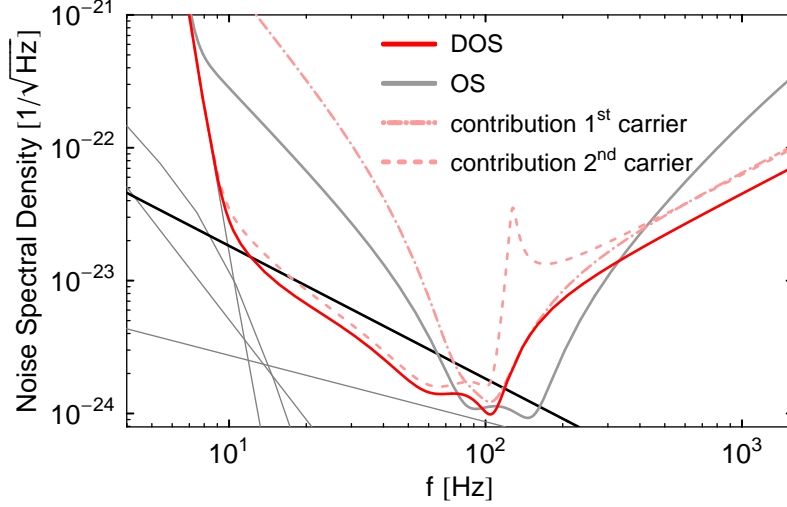


Figure 4.22.: Noise spectral densities of DOS and single optical spring configurations both optimized for NS-NS binaries with respect to a reduced classical noise budget. Compared to Fig. 4.20 suspension thermal noise and gravity gradient noise are lowered by a factor of 10 and coating thermal noise by a factor of 3. With respect to the Advanced LIGO narrowband configuration an improvement in event rate of 238% can be achieved by the DOS configuration, while the single optical spring configuration can only achieve 61%. The corresponding parameters can be found in in Tab. 4.4.

optomechanical resonances are stable if all roots of the characteristic equation

$$\begin{aligned}
 &1 + R_{FF}^{(3)}(\Omega) \left(R_{FF}^{(1)}(\Omega) (R_{xx}(\Omega))^2 - \sqrt{2} R_{xx}^{\text{BS}}(\Omega) \right) - R_{xx}(\Omega) \left[2R_{FF}^{(1)}(\Omega) + R_{FF}^{(2)}(\Omega) \right. \\
 &\left. + R_{FF}^{(3)}(\Omega) - \sqrt{2} \left(2R_{FF}^{(1)}(\Omega) + R_{FF}^{(2)}(\Omega) \right) R_{FF}^{(3)}(\Omega) R_{xx}^{\text{BS}}(\Omega) \right] = 0
 \end{aligned} \tag{4.79}$$

have negative imaginary parts [cf. also Eq. (4.70)]. However, here we restrict the investigations to a tuned local meter.

Fig. 4.23 shows a stable three-carrier configuration roughly optimized for NS-NS systems in the presence of the lowered classical noise budget discussed in Sec. 4.3.3. Compared to Fig. 4.22, a further improvement can be observed and we obtain

$$\eta(f_{\text{up}} = 250 \text{ Hz}) \approx 0.56. \tag{4.80}$$

which indicates that we converge to the limit set by the classical noise budget [cf. Eq. (4.78)]. Comparing the single optical spring and the DOS configuration, when both are optimized for the new classical noise budget, one obtains an improvement in event rate of 169%. The grid search method (cf. App. A) employed for the optimization of all presented interferometer configurations is not suitable for a three-carrier set-up because of the multiplicity of degrees of freedom. The plot shown in Fig. 4.23 can only be understood as a preliminary result and a more sophisticated optimization needs to be carried out.

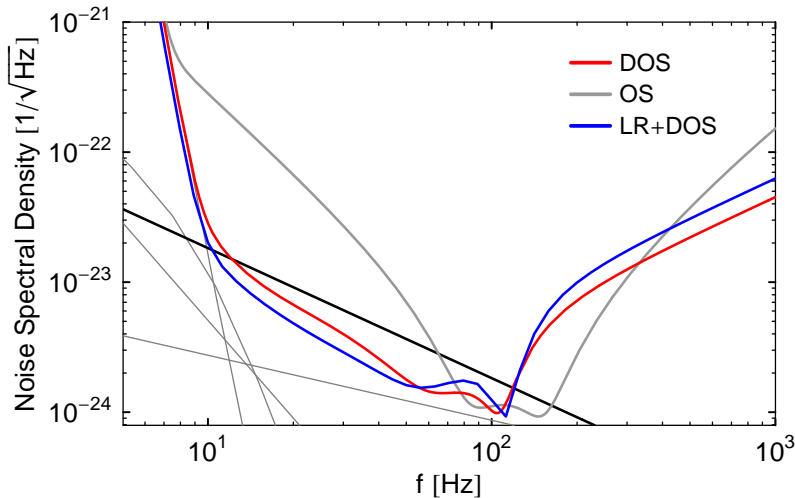


Figure 4.23.: Noise spectral density of DOS in combination with a local readout scheme in comparison with configurations introduced in Fig. 4.22. With respect to the Advanced LIGO narrowband configuration an improvement in event rate of 333% can be achieved by the corporate configuration. Parameters: DOS: $P^{(1)} = 400$ kW, $\lambda^{(1)} = 2\pi \cdot 130$ Hz, $\epsilon^{(1)} = 2\pi \cdot 2$ Hz, $\zeta^{(1)} = 2\pi \cdot 0.45$, $P^{(2)} = 400$ kW, $\lambda^{(2)} = -2\pi \cdot 5$ Hz, $\epsilon^{(2)} = 2\pi \cdot 45$ Hz, $\zeta^{(2)} = 2\pi \cdot 0.288$; local meter: $P^{(3)} = 4$ kW, $\lambda^{(3)} = 2\pi \cdot 0$ Hz, $\epsilon^{(3)} = 2\pi \cdot 1000$ Hz, $\zeta^{(3)} = 2\pi \cdot 0.363$.

4.3.5. Conclusion

We have theoretically investigated the benefit of a double optical spring configuration for second generation gravitational wave detectors, in particular in a follow-up experiment to Advanced LIGO. It should be emphasized that the proposed technique also applies to small-scale experimental set-ups. A stable optomechanical resonance has already been demonstrated experimentally by Corbitt et al. in Ref. [52]. In the double optical spring configuration, a second laser beam is injected into the bright port of a signal-recycled interferometer. The additional carrier field is, like the first carrier, resonant in the arm cavities and is also detuned in the signal-recycling cavity. The corresponding two outputs are optimally filtered and combined. By choosing appropriate detunings of the signal-recycling cavity and homodyne detection angles, it is possible to achieve a stable double optical spring system while additionally improving the sensitivity.

Taking into account the currently pre-estimated classical noise budget for the Advanced LIGO detector, as well as constraints on the optical power, we have performed an optimization of our double carrier scheme with respect to the detection of neutron star binary systems. The double optical spring scheme allows an improvement of 36% in event rate, and we have shown that further improvement will largely be limited by classical noise. When considering a more optimistic classical noise budget, a double optical spring interferometer is much more capable than a single optical spring interferometer of taking advantage of this improvement: compared with 61% improvement in event rate achievable by an optimized single optical spring configuration, the optimized double optical spring layout allows 238%. Nevertheless, the reduced classical noise level leaves further room for an improvement of sensitivity, which can be exploited by employing additional

advanced tools. The proposed double optical spring layout can easily be combined with existing schemes, e.g. the injection of squeezed vacuum states [39, 86, 117, 159, 158] or a variational homodyne detection [39, 108, 134]. But here the combination with the local readout scheme (cf. Sec. 4.2) proposed in our Ref. [136] has been considered. Such a three carrier interferometer is able to exploit a possible future classical noise budget more efficiently.

4.4. Kerr enhanced interferometer

It is well-known that cavities containing a nonlinear crystal can provide an improved response to phase signals and that quantum noise can become (Kerr) squeezed [51, 109]. In the following it is shown that this effect can be used to enhance the performance of higher generation gravitational wave detectors. A conventional Michelson interferometer with Kerr media placed in the tuned arm cavities was already analyzed Bondurant et al. in Ref. [19] and by Pace et al. in Ref. [128]. These authors have shown that radiation pressure noise can be canceled at certain sideband frequencies by exploiting the nonlinearity of the Kerr medium, which allows the interferometer to surpass the standard quantum limit (SQL) [27]. In contrast to their proposals, a detuned configuration, e.g. Advanced LIGO [1], with Kerr nonlinear arm cavities is considered here, and signal and noise transfer functions are derived. It should also be emphasized that we employ a slightly different theoretical approach, namely the two-photon formalism [44], which is based on linearized transformations of the quadrature field operators. In this formalism, linear transfer functions map quadrature field operators, which act at positive modulation frequencies around an optical carrier frequency ω_0 . By adopting this formalism, it is possible to describe complex optical configurations (cf. also Sec. 2.3).

The Kerr effect can also help indirectly to improve the performance of a gravitational wave detector, since it can provide the central component of a continuous wave squeezed light source. We discuss such a set-up at the end of this section.

4.4.1. Kerr transfer function

In the first instance we derive a linear transformation which relates the electromagnetic field incident on a Kerr medium and the outgoing field. Here, a more general description is presented [47] than in our Ref. [135], which clarifies more rigorously the connection to the two-photon formalism. As always, we have to ensure that the quantum noise fluctuations compared to the expectation value of the field are small, otherwise it would not be possible to linearize the Heisenberg equations of motion.

We consider only non-magnetic materials without free charges and currents, i.e. $\rho = 0$ and $\mathbf{J} = 0$. If such a material is exposed to an external electric field \mathbf{E} , the positive and negative charges of each molecule inside the material are shifted and therefore a dipole moment is created. The dipole moment of each molecule contributes to an additional internal electric field, which is orientated in the opposite direction to the external field. This internal electric field is characterized by the (macroscopic) polarization \mathbf{P} and the dielectric displacement (in cgs units) is then given by

$$\mathbf{D} = \mathbf{E} + 4\pi\mathbf{P}. \quad (4.81)$$

The polarization can be expressed as a power-series expansion in the electric field \mathbf{E} :

$$\begin{aligned} \mathbf{P}(t) = & \int \chi^{(1)}(t-t_1) \cdot \mathbf{E}(t_1) dt_1 + \iint \chi^{(2)}(t-t_1, t-t_2) : \mathbf{E}(t_1) \mathbf{E}(t_2) dt_1 dt_2 \\ & + \iiint \chi^{(3)}(t-t_1, t-t_2, t-t_3) : \mathbf{E}(t_1) \mathbf{E}(t_2) \mathbf{E}(t_3) dt_1 dt_2 dt_3 + \dots, \end{aligned} \quad (4.82)$$

where $\chi^{(1)}(t)$ is the first-order time domain susceptibility tensor, which describes a regime where the properties of the medium are independent of the intensity of the field. Accordingly, $\chi^{(2)}(t)$ and $\chi^{(3)}(t)$ are the second and third-order susceptibility tensors, respectively, which account for intensity dependent effects. Note that the quantities $\chi^{(i)}$ are $(i+1)$ -rank tensors. In the following, we will assume that the polarization at time t depends only on the instantaneous values of the electric field strength, which allows us to simplify Eq. (4.82):

$$\mathbf{P}(t) = \chi^{(1)} \cdot \mathbf{E}(t) + \chi^{(2)} : \mathbf{E}(t) \mathbf{E}(t) + \chi^{(3)} : \mathbf{E}(t) \mathbf{E}(t) \mathbf{E}(t) + \dots \quad (4.83)$$

According to the Kramers-Kronig relation (see e.g. Ref. [114]), the assumption that the medium responds instantaneously also implies that the medium is lossless and non-dispersive. A rigorous treatment can be found in standard textbooks, e.g. in Refs. [22, 42].

Many phenomena in nonlinear optics can be treated in a classical way, but here we aim at the modification of quantum noise by a nonlinear medium and therefore a consistent quantum mechanical description is required. We can deduce the Kerr Hamiltonian (cf. Refs. [17, 64]) from Eq. (4.83) via the correspondence principle

$$\hat{H} = : \int_V d\mathbf{x} \left[\frac{1}{8\pi} (\hat{\mathbf{E}}^2 + \hat{\mathbf{B}}^2) + \frac{1}{2} \chi^{(1)} \cdot \hat{\mathbf{E}} \hat{\mathbf{E}} + \frac{1}{3} \chi^{(2)} : \hat{\mathbf{E}} \hat{\mathbf{E}} \hat{\mathbf{E}} + \frac{1}{4} \chi^{(3)} : \hat{\mathbf{E}} \hat{\mathbf{E}} \hat{\mathbf{E}} \hat{\mathbf{E}} \right] :, \quad (4.84)$$

where $: \ :$ denotes normal ordering and $V = \mathcal{A}L_{\text{op}}$ is the interaction volume. The beam impinging on the Kerr medium has a cross-sectional area \mathcal{A} and it travels a length L_{op} through the medium. Second-order nonlinear optical interactions can only occur in non-centrosymmetrical materials [22, 92], i.e. in materials which do not show inversion symmetry, whereas third-order nonlinear interactions can occur in centrosymmetrical and non-centrosymmetrical media. In the following, we assume that the material under consideration is isotropic, which implies that it is also centrosymmetrical, so that the quadratic term in Eq. (4.83) vanishes. Furthermore, the linear susceptibility should be disregarded, since it does not influence the physical phenomena investigated here. Note that a third-order polarization can lead to a variety of effects involving different carrier frequencies. However, we restrict the discussion to a single frequency, namely the frequency of the incident carrier field ω_0 . Here the third-order polarization is only associated with intensity dependent effects, i.e. self-modulation.

It is convenient to re-write the quantized beam of light [cf. Eq. (2.33)] propagating in one dimension as:

$$\hat{E}(t, z) = \sqrt{\frac{2\pi\hbar\omega_0}{\mathcal{A}c}} \left(\hat{a}(t, z) + \hat{a}^\dagger(t, z) \right), \quad (4.85)$$

where the annihilation operator is given by

$$\hat{a}(t, z) = e^{-i\omega_0(t-z/c)} \left(\int_{-\infty}^{+\infty} \frac{d\Omega}{2\pi} \hat{a}_+(\Omega) e^{-i\Omega(t-z/c)} + \frac{\Lambda}{2} e^{i\theta} \sqrt{\frac{\mathcal{A}c}{2\pi\hbar\omega_0}} \right) \quad (4.86)$$

$$\equiv e^{-i\omega_0(t-z/c)} (\hat{v}(t, z) + \Lambda_0). \quad (4.87)$$

Here the spacial dependance as well as the classical field amplitude Λ [cf. Eq. (2.46)] are explicitly taken into account. W.l.o.g. we assume that the electric field propagates in z -direction and for the initial phase of the carrier field we choose $\theta = 0$. Note that $\hat{E}(t, z)$ and $\hat{a}(t, z)$ are Heisenberg operators and the only non-vanishing equal-time commutation relation of the field amplitudes is given by

$$[\hat{a}(t, z), \hat{a}^\dagger(t, z')] = c\delta(z' - z). \quad (4.88)$$

Inserting the representation of the field introduced in Eq. (4.85) into the Hamiltonian given in Eq. (4.84) yields for the zeroth order part:

$$H_0 =: \frac{1}{8\pi} \int_V d\mathbf{x} (\hat{\mathbf{E}}^2 + \hat{\mathbf{B}}^2) := \frac{\hbar\omega_0}{c} \int_0^{L_{\text{op}}} dz \hat{a}^\dagger(t, z) \hat{a}(t, z), \quad (4.89)$$

which describes the free propagation and agrees with Eq. (2.27). In the same way, one obtains for the third-order interaction part:

$$H_1 =: \int_V d\mathbf{x} \frac{1}{4} \chi^{(3)} \hat{\mathbf{E}} \hat{\mathbf{E}} \hat{\mathbf{E}} \hat{\mathbf{E}} := \frac{\hbar}{2} \chi \int_0^{L_{\text{op}}} dz \hat{a}^\dagger(t, z) \hat{a}^\dagger(t, z) \hat{a}(t, z) \hat{a}(t, z), \quad (4.90)$$

where we have redefined the nonlinearity $\chi^{(3)}$ in the following way:

$$\chi = \chi^{(3)} \frac{6\pi^2 \hbar \omega_0^2}{\mathcal{A}c^2}. \quad (4.91)$$

Now we switch to the interaction picture which can be accomplished by applying the substitution

$$\hat{a}(t, z) \rightarrow e^{i\omega_0(t-z/c)} \hat{a}_I(t, z). \quad (4.92)$$

By using the commutation relation given in Eq. (4.88), the Heisenberg equation of motion in the interaction picture for the annihilation operator \hat{a}_I can be easily derived:

$$i\hbar \frac{d\hat{a}_I(t, z)}{dt} = i\hbar \frac{\partial \hat{a}_I(t, z)}{\partial t} + i\hbar c \frac{\partial \hat{a}_I(t, z)}{\partial z} = \hbar c \chi \hat{a}_I^\dagger(t, z) \hat{a}_I(t, z) \hat{a}_I(t, z). \quad (4.93)$$

We can define $\xi = t - z/c$ and use (ξ, z) as a new set of variables in which Eq. (4.93) reads:

$$\left. \frac{\partial \hat{a}_I(\xi, z)}{\partial z} \right|_{\xi} = -i\chi \hat{a}_I^\dagger(\xi, z) \hat{a}_I(\xi, z) \hat{a}_I(\xi, z). \quad (4.94)$$

The new variable ξ is a constant along the light ray which propagates through the Kerr medium. Therefore Eq. (4.94) exactly describes how the field amplitude changes along its propagation. We call the new coordinates (ξ, z) *co-moving coordinates*. Solving the

differential equation (4.94) yields for the annihilation operator \hat{a}_1 after propagation of length L_{op} :

$$\hat{a}_1(\xi, L_{\text{op}}) = e^{-i\chi L_{\text{op}} \hat{a}_1^\dagger(\xi, 0) \hat{a}_1(\xi, 0)} \hat{a}_1(\xi, 0). \quad (4.95)$$

According to Eq. (4.86), the interaction annihilation operator decomposes into its (real) expectation value and a noise amplitude operator, i.e. $\hat{a}_1(t, z) = \hat{v}(t, z) + \Lambda_0$. Keeping only first-order terms of the small fluctuations \hat{v} , we obtain from Eq. (4.95):

$$\hat{v}(\xi, L_{\text{op}}) = e^{-i\chi L_{\text{op}} \Lambda_0^2} \left[\hat{v}(\xi, 0) - i\chi L_{\text{op}} \Lambda_0^2 \left(\hat{v}(\xi, 0) + \hat{v}^\dagger(\xi, 0) \right) \right]. \quad (4.96)$$

Switching back from the co-moving coordinate system to the previous (t, z) coordinate system yields:

$$\hat{v}(t + L_{\text{op}}/c, L_{\text{op}}) = e^{-i\mathcal{K}_{\text{op}}/2} \left[\hat{v}(t, 0) - i\frac{\mathcal{K}_{\text{op}}}{2} \left(\hat{v}(t, 0) + \hat{v}^\dagger(t, 0) \right) \right] \quad (4.97)$$

with the coupling constant

$$\mathcal{K}_{\text{op}} = 2\chi L_{\text{op}} \Lambda_0^2. \quad (4.98)$$

In order to convert Eq. (4.97) into the sideband picture, one needs to define [cf. relation given in Eq. (2.54)]:

$$\hat{v}(t, 0) = \int_{-\infty}^{\infty} \frac{d\Omega}{2\pi} \hat{a}_+ e^{-i\Omega t}, \quad \hat{v}(t + L_{\text{op}}/c, L_{\text{op}}) = \int_{-\infty}^{\infty} \frac{d\Omega}{2\pi} \hat{b}_+ e^{-i\Omega(t + L_{\text{op}}/c)}. \quad (4.99)$$

With these definitions we can re-write Eq. (4.97):

$$\hat{b}_+ = e^{i\Omega L_{\text{op}}/c - i\mathcal{K}_{\text{op}}/2} \left[\hat{a}_+ - i\frac{\mathcal{K}_{\text{op}}}{2} \left(\hat{a}_+ + \hat{a}_-^\dagger \right) \right]. \quad (4.100)$$

This expression can be converted into a relation between the quadrature field amplitudes by means of Eq. (2.34):

$$\begin{pmatrix} \hat{b}_1 \\ \hat{b}_2 \end{pmatrix} = e^{i\Omega L_{\text{op}}/c} \underbrace{\mathbf{R}[\mathcal{K}_{\text{op}}/2]}_{\mathbf{K}} \cdot \begin{pmatrix} 1 & 0 \\ -\mathcal{K}_{\text{op}} & 1 \end{pmatrix} \cdot \begin{pmatrix} \hat{a}_1 \\ \hat{a}_2 \end{pmatrix}, \quad (4.101)$$

where \mathbf{R} is the rotation matrix defined in Eq. (2.57). One sees that the linearized Kerr transformation consists of a rotation as well as a conversion of amplitude quadrature fluctuations into phase quadrature fluctuations. The phase factor in front of the right side of Eq. (4.101) takes the phase shift of the modulation sideband fields into account, which in most cases is negligible since one tends to use short media ($\Omega L_{\text{op}} \ll c$). Strictly speaking, one has to take into account a second rotation of the quadrature field amplitudes, given by $\mathbf{R}[\omega_0 L_{\text{op}}/c]$ due to the free propagation of the field. Recall that we have switched to the interaction picture which suppresses the contribution of free propagation. The following investigations deal with Kerr media placed in a resonator and therefore (free) rotation and conventional detuning can be merged into a single quantity.

In Eq. (4.98) the Kerr coupling constant was defined, which characterizes the effect of the Kerr medium. In the case of a Kerr nonlinear crystal (*electro-optical* Kerr effect) the coupling constant is frequency independent over a broad spectrum and reads

$$\mathcal{K}_{\text{op}} = 2\chi L_{\text{op}} \Lambda_0^2 = \chi^{(3)} \frac{12\pi^2 \omega_0 L_{\text{op}}}{\mathcal{A}c^2} P = \frac{n_2 \omega_0 L_{\text{op}} P}{\mathcal{A}c} \equiv \theta_{\text{op}} P, \quad (4.102)$$

where Eqs. (2.46), (4.91) and (4.86) have been used. Here $n_2 = 12\pi^2\chi^{(3)}/c$ (cf. e.g. Ref. [22]) is the nonlinear refractive index with units m^2/W . P denotes the light power inside the Kerr medium.

Note that radiation pressure effects as well as a thermal expansion due to the absorption of light and a temperature dependent refractive index of substrates also result in intensity dependent phase shifts and can therefore be described by the formalism introduced. In analogy to Eq. (4.102), these effects may be described by appropriate coupling parameters \mathcal{K}_{rp} and \mathcal{K}_{th} , respectively. For example, one can infer the radiation pressure coupling constant from Eq. (2.87), where a beam of light interacting with a single mirror was considered:

$$\mathcal{K}_{\text{rp}} = \frac{1}{m\Omega^2} \sqrt{\frac{8P\omega_0\hbar}{c^2}}. \quad (4.103)$$

The similarity between the Kerr effect and optomechanical coupling was already pointed out by Loudon in Ref. [113]. An intrinsic difference is that the radiation pressure induced nonlinear phase shift decreases with increasing frequency, while the Kerr effect is frequency independent. In the following section it will be shown how the Kerr effect can be used for reshaping the quantum noise budget of higher generation GW detectors. Later on a Kerr squeezing source will be investigated.

4.4.2. Kerr interferometer

By comparing Eq. (2.87) with Eq. (4.102), it becomes apparent that the optomechanical coupling and the Kerr effect act in a similar manner. Both equations refer to a single interaction, i.e. a single pass through a Kerr medium and a single reflection of a free mirror, respectively. Now the previous results are to be extended to a nonlinear detuned cavity, i.e. a detuned cavity containing a Kerr medium. As shown by Buonanno et al. in Ref. [38], a detuned cavity with a movable end mirror is completely equivalent to a detuned signal-recycling (SR) interferometer. It can be seen that the same is true for a detuned Kerr nonlinear cavity. For this reason the Kerr medium can be placed in the tuned arm cavities of a SR interferometer while detuning is passed on the SR cavity.

Classical dynamics

The recapitulation of the classical aspects of such a system (see e.g. Ref. [32] or standard textbooks already cited above) already suggests the implementation of a nonlinear Fabry-Pérot resonator. Such a device obeys a nonlinear relation between the input power P_{in} and the intra-cavity power P given by

$$P = \frac{\tau_1^2}{1 + \rho_1^2\rho_2^2 - 2\rho_1\rho_2 \cos(2\phi + \theta_{\text{op}}P)} P_{\text{in}}. \quad (4.104)$$

where ϕ accounts for the detuning. For $\theta_{\text{op}} = 0$, one obtains the intra-cavity power in the case of a conventional (linear) resonator [cf. Eq. (2.104)]. In the left panel of Fig. 4.24, the intra-cavity power is shown as a function of the cavity detuning for three different nonlinear susceptibilities θ_{op} . The corresponding phase shifts of the light reflected from the Kerr cavity are shown in the right panel of Fig. 4.24. Both graphs reveal that a critical choice of parameters exists: at the edge of a *multi-stable* behavior, where an infinite slope occurs for a specific value of the detuning. We call this state the *critical*

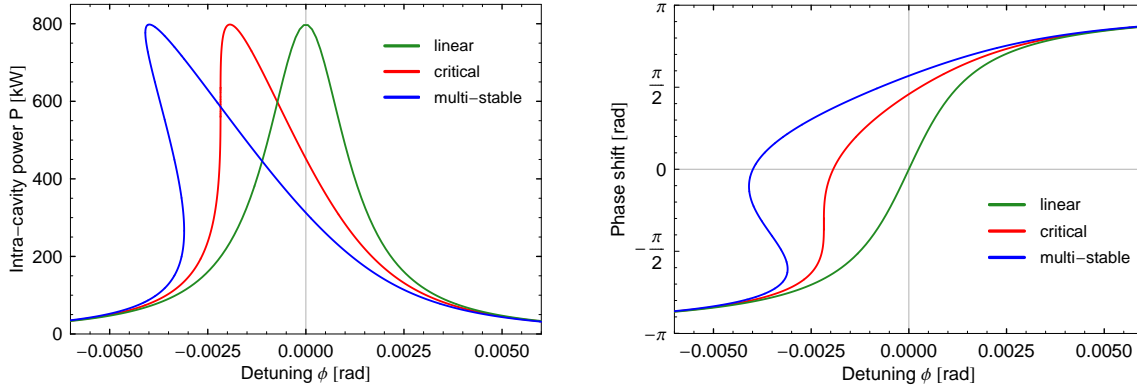


Figure 4.24.: (*left panel*) Intra cavity power and (*right panel*) phase shift of reflected light for three different values of the nonlinear susceptibility (linear: $\theta_{\text{op}} = 0 \text{ W}^{-1}$, critical: $\theta_{\text{op}} = 4.85 \cdot 10^{-9} \text{ W}^{-1}$ and multi-stable: $\theta_{\text{op}} = 10^{-8} \text{ W}^{-1}$) of the Kerr medium. The critical state is characterized by an infinite slope for a particular detuning. Residual parameters: $P_{\text{in}} = 1 \text{ kW}$, $T = 0.005$

state. The critical state is considered to be promising with regard to enhancing sensitivity for detection of signals induced by a cavity length change and the reduction of quantum noise. By calculating the slope of the implicit function given in Eq. (4.104), we can find a condition for the turning points where an infinity slope occurs:

$$1 + \rho_1^2 \rho_2^2 - 2\rho_1 \rho_2 [\cos(2\phi + \theta_{\text{op}} P) + \theta_{\text{op}} P \sin(2\phi + \theta_{\text{op}} P)] = 0. \quad (4.105)$$

By assuming that the end mirror is lossless, ($\rho_2 = 1$) and $\phi, \theta_{\text{op}} \ll 1$, one can solve Eq. (4.105) for the detuning:

$$\phi = -\mathcal{K}_{\text{op}} \pm \frac{1}{4} \sqrt{-T^2 + 4\mathcal{K}_{\text{op}}^2}, \quad (4.106)$$

where $T = 1 - \rho_1^2$ and the definition of the Kerr coupling constant \mathcal{K}_{op} given in Eq. (4.102) were used. We can directly infer from Eq. (4.106) that we have to distinguish between three regimes depicted in Fig. 4.24: (*i*) For $|\mathcal{K}_{\text{op}}| < T/2$ neither the critical state nor the multi-stable region is accessible and hence the system is close to a linear one. (*ii*) For $|\mathcal{K}_{\text{op}}| = T/2$, it is possible to reach the critical state by choosing the detuning according to Eq. (4.106). (*iii*) If the nonlinear coupling constant exceeds the critical value, i.e. $|\mathcal{K}_{\text{op}}| > T/2$, one arrives at the multi-stable regime and there are two points exhibiting an infinite slope.

Input-output relation and noise spectral density

For a rigorous quantum mechanical treatment of a Kerr interferometer, the Heisenberg equations of motion need to be considered. The goal is to obtain a transfer function relating the ingoing vacuum field with the outgoing field. As always, we assume that the gravitational waves (GWs) with amplitude h incident from directly above the detector plane exhibit a polarization that maximizes the response of the L-shaped Michelson interferometer. In the following, the Heisenberg equations of motion in frequency domain

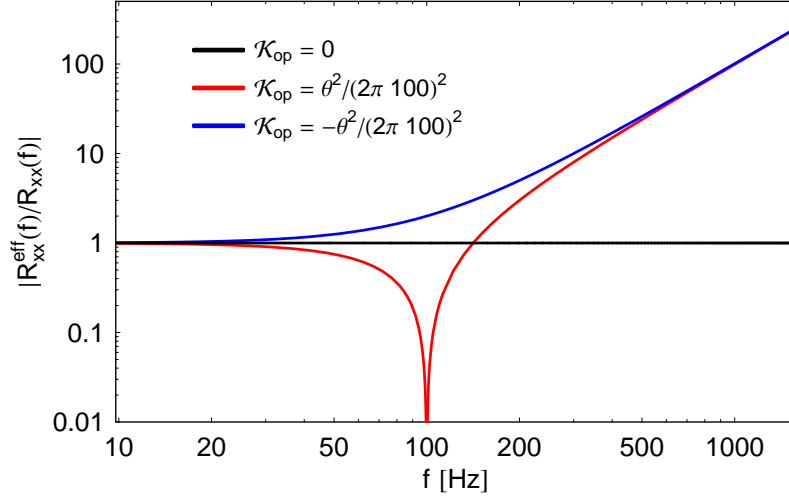


Figure 4.25.: The effective mechanical susceptibility defined in Eq. (4.112), normalized by the usual mechanical susceptibility. Three different Kerr coupling constants are considered. A positive coupling constant gives rise to a dip, i.e. the effective mechanical susceptibility vanishes for a certain frequency and hence the output of the interferometer is free from radiation pressure noise at that frequency (cf. Fig. 4.26). A negative coupling constant entails an increased mechanical susceptibility, which corresponds to a reduced mirror mass. Advanced LIGO parameters were used (cf. Tab. 2.1).

[36, 37, 38, 54, 108] for the antisymmetric mode of motion \hat{x} of the four arm cavity mirrors, for the Kerr effect \hat{k} and for the output \hat{y} of the interferometer are listed:

$$\hat{x} = R_{xx}(\Omega)[\hat{F}(\Omega) + R_{FF}(\Omega) \hat{x}] + hL + \hat{\xi}_{\text{noise}}, \quad (4.107)$$

$$\hat{k} = \tilde{\mathcal{K}}_{\text{op}} \frac{4}{\theta^2} [\hat{F}(\Omega) + R_{FF}(\Omega) \hat{k}], \quad (4.108)$$

$$\hat{y} = \hat{Y}_1(\Omega) \sin \zeta + \hat{Y}_2(\Omega) \cos \zeta + [R_{Y_1F}(\Omega) \sin \zeta + R_{Y_2F}(\Omega) \cos \zeta](\hat{x} + \hat{k}), \quad (4.109)$$

where $\tilde{\mathcal{K}}_{\text{op}} = \mathcal{K}_{\text{op}}L/c$ and the quantities defined in Sec. 2.3.4 have been used, but without the superscripts. The operator $\hat{F}(\Omega)$ characterizes the radiation pressure forces arising from the vacuum fluctuations coupling into the dark port, which would act on fixed mirrors. The operators $\hat{Y}_i(\Omega)$ account for the outgoing fluctuations in the quadratures in the case of fixed mirrors. Since the incoming vacuum fields are modified in a related way by the Kerr medium and the optomechanical coupling, both effects can be characterized in terms of the same operators $\hat{F}(\Omega)$ and $\hat{Y}_i(\Omega)$ [cf. Eqs. (4.107) and (4.108)]. The function $R_{Y_iF}(\Omega)$ accounts for the optical transfer from the differential mode \hat{x} and the Kerr effect \hat{k} to the outgoing quadrature fields. The operator $\hat{\xi}_{\text{noise}}$ describes the classical displacement noise of the differential mode. Finally, the susceptibility $R_{FF}(\Omega)$ corresponds to the optical spring constant. Note that the equations of motion (4.107)-(4.109) are valid either for a detuned cavity with a single movable end mirror or for a detuned SR interferometer. With the relations given in Sec. 2.3.4, one can switch between these configurations.

According to the linear quantum measurement formalism (cf. Sec. 2.3.4), the Kerr effect described by \hat{k} can be considered as a probe observable like the generalized displacement \hat{x} . Since both observables couple in the same way with the detector, it is convenient to

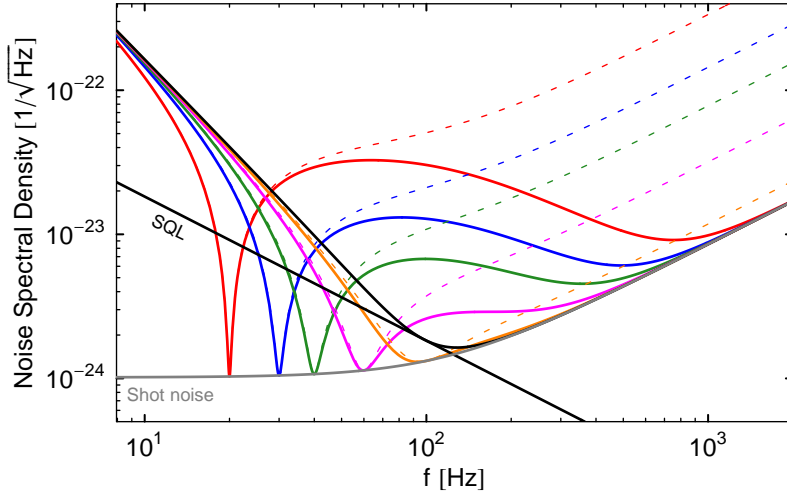


Figure 4.26.: Comparison between radiation pressure noise cancelation due to Kerr effect (thick solid lines) and optimized homodyne detection angle (thin dashed lines) for a tuned Advanced LIGO configuration (cf. Tab. 2.1). For equal colored curves the detection angle as well as the Kerr coupling constant were so chosen that radiation pressure noise is canceled at the same frequency. A tuned configuration with phase quadrature readout is also shown (black curve). The Kerr coupling constants can be inferred from frequencies where the signal-referred shot noise spectrum is touched.

define a new effective probe observable

$$\hat{x}^{\text{eff}} \equiv \hat{x} + \hat{k}, \quad (4.110)$$

which allows us to replace Eqs. (4.107) and (4.108) by a single equation, namely

$$\hat{x}^{\text{eff}} = R_{xx}^{\text{eff}}(\Omega)[\hat{F}(\Omega) + R_{FF}(\Omega) \hat{x}^{\text{eff}}] + hL + \hat{\xi}_{\text{noise}}, \quad (4.111)$$

where the effective mechanical susceptibility defined by

$$R_{xx}^{\text{eff}}(\Omega) \equiv R_{xx}(\Omega) + \tilde{\mathcal{K}}_{\text{op}} \frac{4}{m\theta^2} \quad (4.112)$$

has been used. The usual mechanical susceptibility of the differential mode of the four arm cavity mirrors is given by $R_{xx}(\Omega) = -4/(m\Omega^2)$, where we assume that the mirrors can be treated as free masses. The effective mechanical susceptibility normalized by the free mass mechanical susceptibility is shown in Fig. 4.25 for different Kerr coupling constants. By virtue of Eq. (4.112), the signal-referred noise spectral density of the Kerr enhanced interferometer can be deduced analogously to Eq. (2.157):

$$S_h(\Omega) = \frac{1}{L^2} \left(S_{ZZ}(\Omega) + 2R_{xx}^{\text{eff}}(\Omega) \Re[S_{\mathcal{F}\mathcal{Z}}(\Omega)] + (R_{xx}^{\text{eff}})^2(\Omega) S_{\mathcal{F}\mathcal{F}}(\Omega) \right). \quad (4.113)$$

We can already draw some important conclusions from Eqs. (4.112) and (4.113): the effective susceptibility vanishes for an arbitrary frequency Ω_{op} ($R_{xx}^{\text{eff}}(\Omega_{\text{op}}) = 0$), if the nonlinear coupling constant is positive and is chosen as follows:

$$\tilde{\mathcal{K}}_{\text{op}} = \frac{\theta^2}{\Omega_{\text{op}}^2}. \quad (4.114)$$

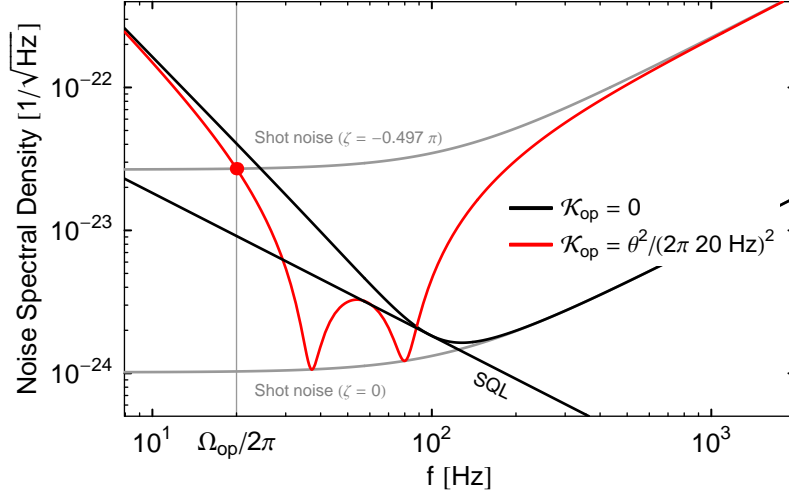


Figure 4.27.: Kerr supplemented tuned configuration (red curve) with homodyne detection angle ($\zeta = -0.497\pi$) so chosen that radiation pressure noise is canceled at $\Omega = 2\pi \cdot 90$ Hz. The signal-referred shot noise spectrum corresponding to this detection angle is intersected at $\Omega_{\text{op}} = 2\pi \cdot 20$ Hz due to radiation pressure noise cancellation caused by the Kerr effect. A conventional tuned Advanced LIGO configuration with phase quadrature detection and parameters given in Tab. 2.1 is also shown (black curve). For the Kerr configuration, we used Advanced LIGO parameters, if not stated otherwise.

It can be seen in Fig. 4.25 that a dip occurs at frequency Ω_{op} . Exactly for this frequency, the configuration is equivalent to an interferometer with infinite heavy mirrors, hence the outgoing field is free from radiation pressure noise. The corresponding signal-referred noise spectral density touches the hypothetical shot noise limited sensitivity curve at Ω_{op} , as shown in Fig. 4.26 for a tuned configuration. This regime was already investigated by Pace et al. in Ref. [128]. Strictly speaking, radiation pressure noise cannot be completely canceled, since the mechanical susceptibility shows a small imaginary part due to the finite quality factor of the suspension [cf. Eq. (2.118)], not compensable by the Kerr nonlinearity. Note that the coupling constant defined in Eq. (4.98) includes a factor which is proportional to the circulating power, i.e. $\tilde{\mathcal{K}}_{\text{op}} \sim \theta^2$. Consequently the effective mechanical susceptibility is independent of the circulating power. This implies that canceling radiation pressure noise at a chosen frequency requires a certain Kerr crystal with a nonlinear refractive index n_2 , regardless of the circulating power. Recall that radiation pressure noise can also be canceled at arbitrary frequencies by choosing an appropriate homodyne detection angle, which can be implemented in a more straightforward way. Both techniques are depicted in Fig. 4.26, here equal colored curves exhibit radiation pressure noise cancellation at equal frequencies, either due to the Kerr effect or to the optimized homodyne detection angle. Remember that the signal-referred shot noise spectrum is minimized by detecting the phase quadrature. In general, the homodyne detection angles optimized for certain frequencies are different from the phase quadrature, hence sensitivity at high frequencies is deteriorated. On the other hand the Kerr configuration allows us to maintain sensitivity in the shot noise dominated regime.

It seems appropriate to combine both techniques, i.e. varying the homodyne detection angle of the Kerr interferometer. Despite the presence of a Kerr nonlinearity, the detection angle can be so optimized that the signal-referred shot noise spectrum is touched at an arbitrary but fixed frequency Ω_ζ . The corresponding optimal detection angle reads:

$$\zeta(\Omega_\zeta) = \arctan \left[\frac{2\epsilon(\theta^2 - \tilde{\mathcal{K}}_{\text{op}}\Omega_\zeta^2)}{\Omega_\zeta^2(\epsilon^2 + \Omega_\zeta^2)} \right]. \quad (4.115)$$

At the same time, the Kerr effect can be used to cancel radiation pressure noise at another chosen frequency Ω_{op} . Clearly, the noise spectral density of the Kerr interferometer intersects the signal-referred shot noise spectrum exactly at the frequency Ω_{op} (cf. Fig. 4.27), but it is the shot noise spectrum related to the actual configuration. We have chosen a detection angle according to Eq. (4.115) which entails an increased signal-referred shot noise level. Consequently one finds a deteriorated sensitivity at Ω_{op} . But Fig. 4.27 also reveals that the minimal signal-referred shot noise level is still touched at two distinct frequencies, where one is given by Ω_ζ and the other determined by

$$\Omega_{\text{add}}^2 = \frac{(\epsilon^2 + \Omega_\zeta^2)\Omega_{\text{op}}}{\Omega_\zeta^2 - \Omega_{\text{op}}^2} \quad (4.116)$$

in the case of a positive Kerr coupling constant as given in Eq. (4.114). In contrast to a conventional interferometer, the mechanical susceptibility of a tuned Kerr interferometer is no longer a monotonic function over frequency, which can be seen in Fig. 4.25. Hence the same amount of radiation pressure noise can occur at two distinct frequencies. This implies that canceling radiation pressure noise at one frequency Ω_ζ accompanies canceled radiation pressure noise at a second frequency Ω_{add} , provided that $\Omega_\zeta > \Omega_{\text{op}}$. Remember that in the case of a tuned conventional cavity the detection angle can only be optimized for a single frequency when radiation pressure noise is canceled at the expense of sensitivity at other frequencies. The Kerr nonlinearity helps to maintain sensitivity over a broader frequency range. When performing a frequency-dependent homodyne detection, both the conventional and the Kerr interferometer noise spectral density agree with the shot noise limited sensitivity curve. It should be emphasized that the dips which the noise spectral densities feature in Figs. 4.26 and 4.27 do not correspond to resonances of the system, consequently the stability of a tuned configuration is maintained without introducing a feedback mechanism as required for a detuned SR interferometer. Note that for a tuned configuration it is not desirable to choose a negative Kerr coupling constant since this would completely remove the effort put into the design of heavy test masses, which can also be seen in Fig. 4.25.

Either for a positive or negative Kerr coupling constant it is reasonable to choose Ω_{op} well within the half linewidth of the configuration because of the following arguments: (i) Below Ω_{op} the effective mechanical susceptibility deviates marginally from the free mass mechanical susceptibility (cf. Fig. 4.25). (ii) Above the half linewidth, where shot noise is the dominating noise source, the output is susceptible neither to radiation pressure noise nor to the Kerr effect. This implies that choosing $\Omega_{\text{op}} > \epsilon$ leaves the output nearly unaffected. One cannot hope to achieve an improvement above the half linewidth unless additional techniques are introduced (cf. Ref. [135]). This argumentation is true for a tuned as well as for a detuned configuration, which will be explored in detail in the following paragraph.

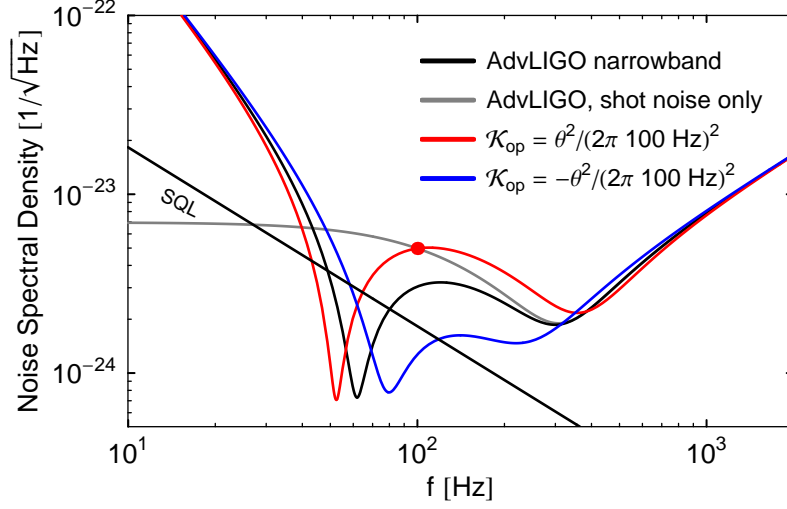


Figure 4.28.: Comparison between Advanced LIGO and Kerr supplemented configurations. For positive Kerr coupling constant (red curve) radiation pressure noise is canceled at 100 Hz, for this reason the shot noise spectrum is intersected (red dot). The optomechanical resonance is shifted to lower frequencies. For negative Kerr coupling constant (blue curve) radiation pressure noise is not canceled, instead the optomechanical resonance is shifted to higher frequencies. Phase quadrature of all configurations is detected. For the Kerr configuration we used Advanced LIGO narrowband parameters, if not stated otherwise.

In the case of a detuned configuration, it is not always desirable to cancel radiation pressure noise. Due to cross correlations between shot noise and radiation pressure noise, the signal-referred noise spectral density can surpass the shot noise limited sensitivity curve. When canceling radiation pressure noise, these correlations obviously vanish and therefore the sensitivity is eventually deteriorated, as depicted in Fig. 4.28 where $\Omega_{\text{op}} = 100$ Hz is chosen.

The resonances of a detuned SR interferometer equipped with Kerr media in the arm cavities can be obtained from the condition

$$1 - R_{FF}(\Omega_{\text{res}})R_{xx}^{\text{eff}}(\Omega_{\text{res}}) = 0. \quad (4.117)$$

Note that introducing a Kerr nonlinearity does not change the number of resonances of our system. Nevertheless, the resonant structure is modified by the effective mechanical susceptibility defined in Eq. (4.112). The condition given in Eq. (4.117) simplifies for $\Omega_{\text{res}} < \epsilon$ and one easily obtains an expression for the optomechanical resonance frequency:

$$(\Omega_{\text{res}}^{\text{opt}})^2 = \frac{\theta^2 \lambda}{\epsilon^2 + \lambda(\lambda + \tilde{\mathcal{K}}_{\text{op}})} \quad \text{with} \quad \tilde{\mathcal{K}}_{\text{op}} = \pm \frac{\theta^2}{\Omega_{\text{op}}^2}, \quad (4.118)$$

where both signs of the Kerr coupling constant were taken into account. For a positive Kerr coupling constant it turns out that $\Omega_{\text{res}}^{\text{opt}} \lesssim \Omega_{\text{op}}$, i.e. the optomechanical resonance occurs near the frequency where radiation pressure noise is completely canceled. However, the optomechanical resonance cannot be pushed beyond Ω_{op} since the effective susceptibility vanishes for this frequency. This corresponds to an infinite mirror mass which provides some kind of barrier to the optomechanical resonance.

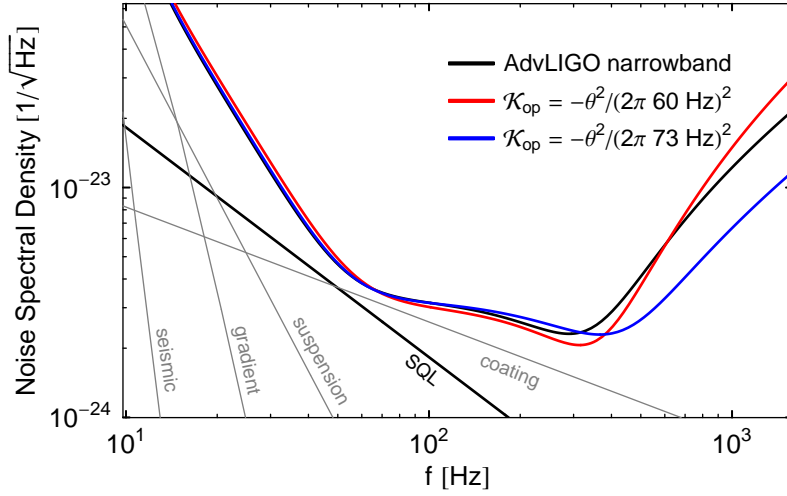


Figure 4.29.: Comparison between Advanced LIGO narrowband (cf. Tab. 2.1) and Kerr supplemented configurations. The narrowband configuration (red curve) yields 4% improvement in event rate. Parameters: $\Omega_{\text{op}} = 2\pi 60 \text{ Hz}$, $\lambda = 2\pi 495 \text{ Hz}$, $\epsilon = 2\pi 75 \text{ Hz}$ and $\zeta = 2\pi 0.325$. The broadband (blue curve) configuration maintains event rate of Advanced LIGO narrowband and improves the high frequency sensitivity. Parameters: $\Omega_{\text{op}} = 2\pi 73 \text{ Hz}$, $\lambda = 2\pi 495 \text{ Hz}$, $\epsilon = 2\pi 185 \text{ Hz}$ and $\zeta = 2\pi 0.41$. For the Kerr configuration we used Advanced LIGO parameters, if not stated otherwise.

By reversing the sign of the Kerr coupling constant, the mechanical susceptibility can be increased for frequencies above Ω_{op} which is also depicted in Fig. 4.25. By so choosing $\tilde{\mathcal{K}}_{\text{op}}$ that the mechanical susceptibility is increased around the optomechanical resonance, while it is marginally affected in the radiation pressure dominated low frequency regime, an improvement of sensitivity around the resonance can be observed. The susceptibility to forces acting on the mirror is increased, which amplifies the optomechanical coupling and hence also the effect of the optical spring. A further shift of the optomechanical resonance to higher frequencies is induced. These effects are illustrated in Figs. 4.28 and 4.30.

Even in the case of a positive detuned SR configuration it is possible that the restoring optical spring vanishes completely due to the Kerr effect. Only if the condition

$$\mathcal{K}_{\text{op}} > -\frac{\epsilon^2 + \lambda^2}{\lambda} \quad (4.119)$$

is satisfied, the noise spectral density does feature an optomechanical resonance. It is not desirable to leave this regime, since one can no longer take advantage of the optomechanical resonance gain. Furthermore, sensitivity suffers from strong radiation pressure noise within the detection band due to a strongly increased effective mechanical susceptibility. Fig. 4.30 shows that sensitivity is significantly deteriorated, when one leaves the regime defined in Eq. (4.119).

There remains a small frequency window, where the Kerr nonlinearity can help to improve the sensitivity. Namely, one has to concentrate on the frequency regime below the half linewidth of the set-up and around or above the optomechanical resonance frequency. But in this regime, an interferometer obeys rather complex dynamics, for which reason a

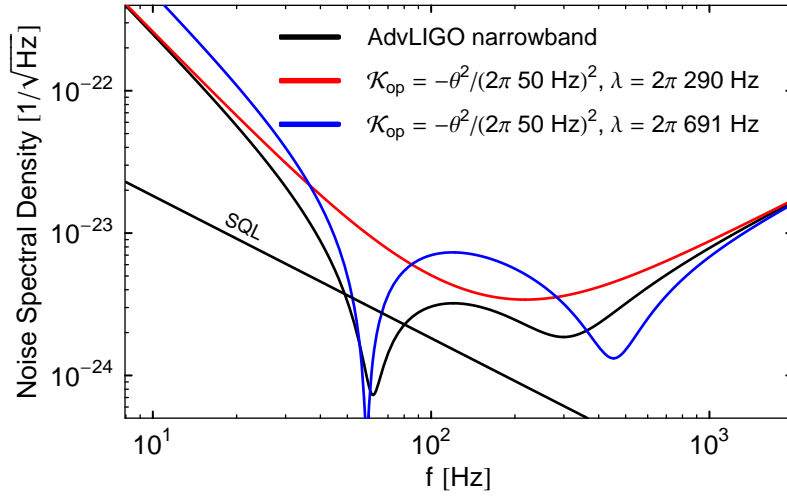


Figure 4.30.: Comparison between Advanced LIGO and two Kerr interferometer configurations: (blue curve) Optomechanical resonance is strongly enhanced due to Kerr amplified effective susceptibility. (red curve) Condition given in Eq. 4.119 is no longer satisfied, which causes a rather poor sensitivity within the detection band. Phase quadrature of all configurations is detected. For the Kerr configuration we used Advanced LIGO parameters, if not stated otherwise.

numerical optimization has to be carried out (cf. App. A). The Kerr nonlinearity provides an additional parameter which can be used for reshaping the noise budget. Such an optimization has revealed that a minor improvement in sensitivity for the detection of neutron star binary systems can be achieved by employing a Kerr medium, as shown in Fig. 4.29. For the optimization, the current Advanced LIGO classical noise budget was taken into account (as given by the simulation tool *Bench* [2]): each contribution to the total classical noise budget, i.e. suspension thermal noise, seismic noise, thermal fluctuations in the coating and gravity gradient noise, is presented in Fig. 4.29. Additionally a broadband optimization was performed in order to achieve a better sensitivity in the high frequency regime (cf. Sec. 3.2): all configurations of the Kerr interferometer obeying an event rate at least equal to that of Advanced LIGO were selected. In a second step, these configurations were explored in the high frequency regime by considering a smaller frequency integration interval, namely [500 Hz; 1570 Hz]. The configuration with an optimal signal-to-noise ratio with respect to this frequency interval is also shown in Fig. 4.29. It illustrates that a broadband configuration benefits moderately from the Kerr effect.

The preceding classical considerations suggest that there is a critical state which is accompanied by a huge improvement in sensitivity. Due to the infinite slope which occurs in Fig. 4.24 for a certain detuning, the critical state is characterized by an infinite response to a length change of the cavity. The question arises whether this effect also occurs in the quantum mechanical description of the Kerr interferometer. The experienced readers might know that any configuration showing a restoring optical spring naturally approaches the critical states at a certain frequency. This is due to the fact that the optomechanical coupling provides a frequency-dependent coupling constant which varies from zero to

infinity. This suggests that the system passes the critical state for a particular frequency. We have to look for a peaked response to a driving force at a certain frequency, which is by definition a resonance computable, by using the condition provided in Eq. (4.117). In other words, the optomechanical resonance can already be interpreted as the point where a detuned SR interferometer approaches the critical state (cf. also Ref. [62]). But in general, Eq. (4.117) yields a complex solution for the optomechanical resonance frequency where the imaginary part characterizes the bandwidth of the resonance. Therefore it is not feasible to realize an infinite response, because we cannot exactly meet the condition given in Eq. (4.117). Introducing a Kerr medium does not change the resonant structure fundamentally and therefore it is not possible to achieve an infinite response of the system to a length change. But in the case of a negligible optomechanical coupling, i.e. $m \rightarrow \infty$, Eq. (4.117) yields for the resonances:

$$\Omega_{\text{res}}^{1,2} = 0, \quad \Omega_{\text{res}}^{3,4} = i\epsilon \pm \sqrt{\lambda(\tilde{\mathcal{K}}_{\text{op}} + \lambda)}. \quad (4.120)$$

This implies that for fixed mirrors the condition for the critical state can be satisfied, but only for $\Omega = 0$ and no infinity response can occur for all other frequencies. This will be discussed in more detail in Sec. 4.5.

4.5. Kerr squeezing source

4.5.1. Squeezed light

Pure squeezed states represent a class of minimum-Heisenberg states which show reduced noise in one quadrature component compared to a coherent state. It is well-known that squeezed light may exhibit sub-Poissonian photon counting statistics and therefore the statistical properties of such states cannot be calculated using techniques established in classical probability theory.

There is a huge variety of applications for squeezed light that have emerged from the field of quantum optics. Especially for high precision quantum measurements, e.g. for the improvement of laser interferometric GW detectors as suggested by Caves in Ref. [43], squeezed light might become a standard tool. The first generation of GW detectors was widely limited by classical noise, which makes it unfeasible to exploit quantum correlations. But it is very likely that quantum noise will be one of the major noise sources in higher generation GW detectors (e.g., Advanced LIGO [1]), which explains a considerably increased interest in nonclassical techniques. Additionally, continuous variable quantum communication and information theory gain in importance where squeezed states are also an indispensable tool. For instance squeezed light was employed for the generation of entangled states of light [20, 78] and for the demonstration of teleportation [30, 151].

For small-scale devices it is favorable to use a monolithic design which ensures that radiation pressure noise is negligible. Only then we can take full advantage of the Kerr nonlinearity since the optomechanical coupling and the Kerr nonlinearity are competing effects [113].

4.5.2. Kerr squeezing

In Sec. 4.4, an interferometer equipped with Kerr nonlinear arm cavities has been investigated, with mirrors suspended as pendulums. As long as the analysis is aimed at the

improvement of GW detectors, it is reasonable to treat the end mirror as a quasi free mass, legitimated by the low mechanical eigenfrequency (~ 1 Hz). Therefore a strong optomechanical coupling can occur which is frequency-dependent and competes against the constant Kerr nonlinearity. The parameters can be so chosen that the system approaches the critical state for a single frequency, but for all other frequencies radiation pressure forces drive the system away from this state. For the realization of an efficient Kerr squeezing source, the use of a monolithic experimental set-up suggests itself, which intrinsically does not suffer from radiation pressure noise. Note that it is also conceivable to consider a device with a sufficiently high mechanical eigenfrequency. As long as one focuses on sideband frequencies far below the mechanical eigenfrequency ω_m , the mechanical susceptibility is approximately constant:

$$R_{xx}(\Omega) = -\frac{1}{m(\Omega^2 - i\gamma_m\Omega + \omega_m^2)} \rightarrow \frac{1}{m\omega_m^2} \quad \text{for } \Omega, \gamma_m \ll \omega_m, \quad (4.121)$$

where γ_m denotes the velocity damping [cf. also Eq. (2.112)]. We can infer from Eq. (4.121) that the optomechanical coupling only gives a frequency-independent contribution, which can be compensated by means of the Kerr nonlinearity [cf. Eq (4.112)]. This suggests that a micromechanical oscillator equipped with a Kerr nonlinearity can also provide an appropriate basis for the generation of squeezed states. Such a device in the form of a toroid cavity, which generally shows a mechanical eigenfrequency up to a few MHz, was investigated i.e. by Kippenberg et al. in Refs. [140, 170].

But for the sake of simplicity, we assume a monolithic design for the following investigations. The input-output relation can be obtained from Eqs. (4.107)-(4.109):

$$\begin{aligned} \hat{\boldsymbol{o}} = \frac{1}{M} & \begin{pmatrix} (\lambda^2 - \epsilon^2 - \Omega^2) + \tilde{\mathcal{K}}_{\text{op}}\lambda & 2\lambda\epsilon \\ 2\epsilon(-\tilde{\mathcal{K}}_{\text{op}} - 4\lambda) & (\lambda^2 - \epsilon^2 - \Omega^2) + \tilde{\mathcal{K}}_{\text{op}}\lambda \end{pmatrix} \cdot \hat{\boldsymbol{i}} \\ & + \sqrt{S_x} \frac{1}{M} \sqrt{\frac{m\theta^2\epsilon}{2\hbar}} \begin{pmatrix} \lambda \\ \epsilon - i\Omega \end{pmatrix}, \end{aligned} \quad (4.122)$$

where

$$M = -\tilde{\mathcal{K}}_{\text{op}}\lambda + \Omega_{\text{opt}}^2 \quad \text{with} \quad \Omega_{\text{opt}}^2 = (\Omega - \lambda + i\epsilon)(\Omega + \lambda + i\epsilon). \quad (4.123)$$

Alternatively, this relation can also be obtained from Eq. (2.107) by replacing the optomechanical coupling by the Kerr coupling, i.e. $\theta^2 \rightarrow -4\Omega^2\tilde{\mathcal{K}}_{\text{op}}$. The second term in Eq. (4.122) accounts for the classical displacement noise, i.e. it summarizes the displacement caused by various classical noisy forces imposing a total displacement noise spectral density S_x on the mechanical oscillator. But first the discussion should be restricted to quantum noise, in order to clarify the general principle underlying a Kerr squeezing source.

The condition for infinite squeezing is given by

$$M = 0, \quad (4.124)$$

which means that the quantum fluctuations of each output quadrature of $\hat{\boldsymbol{o}}$ diverge. Therefore a quadrature exists, exhibiting an infinite uncertainty associated with a vanishing uncertainty in another quadrature, since we are dealing with quantum noise, i.e.

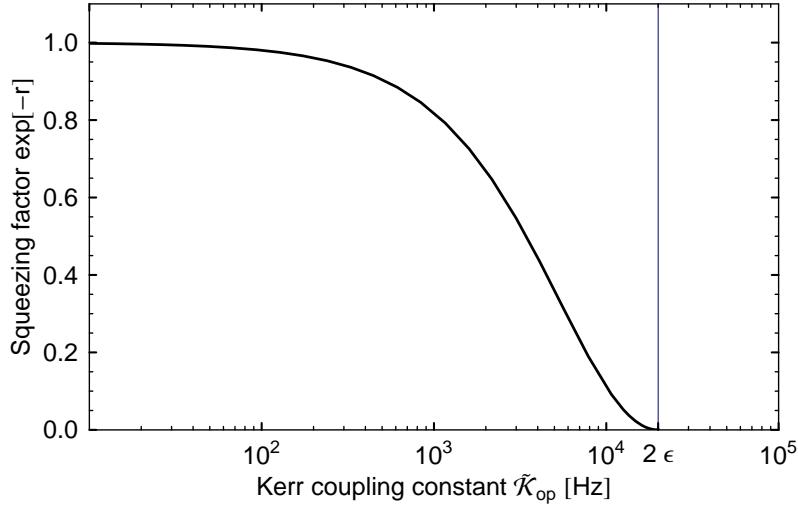


Figure 4.31.: Squeezing factor for zero sideband frequency versus Kerr coupling constant. A nonlinear cavity is considered with a half bandwidth of $\epsilon = 2\pi$ 10 kHz and the detuning is chosen according to Eq. (4.128) with $\Omega_0 = 0$. The linearized formalism used here gradually breaks down when $\tilde{\mathcal{K}}_{\text{op}}$ approaches 2ϵ and it is not applicable anymore for $\tilde{\mathcal{K}}_{\text{op}} \geq 2\epsilon$

pure states. Solving Eq. (4.124) for the detuning yields:

$$\lambda_{1,2} = \frac{1}{2} \left(-\tilde{\mathcal{K}}_{\text{op}} \pm \sqrt{\tilde{\mathcal{K}}_{\text{op}}^2 - 4(\epsilon - i\Omega)^2} \right), \quad (4.125)$$

which reveals that infinite squeezing is only accessible for $\Omega = 0$. In this case Eq. (4.125) exactly agrees with the classical condition for the critical state given in Eq. (4.106), provided that the additional rotation due to the Kerr medium is taken into account: namely the substitution $\lambda \rightarrow \lambda + \tilde{\mathcal{K}}_{\text{op}}/2$ is required.

First we optimize the configuration for a vanishing sideband frequency, i.e. we set $\Omega = 0$ in Eq. (4.125). Then we have to distinguish between three different regimes: (i) For $|\tilde{\mathcal{K}}_{\text{op}}| < 2\epsilon$ it is not possible to generate infinite squeezing since the condition given in Eq. (4.124) cannot be satisfied, which follows directly from Eq. (4.125). The system is close to a linear configuration. In this regime, the squeezing factor is continuously improved for an increasing nonlinear coupling constant as illustrated by Fig. 4.31. The amplitude quadrature exhibits maximal squeezing. There are two opportunities for the optimal detuning which can be obtained by taking the real part of the solution provided in Eq. (4.125). (ii) For $|\tilde{\mathcal{K}}_{\text{op}}| = 2\epsilon$ our model predicts an infinite squeezing factor at $\Omega = 0$ since Eq. (4.125) yields a real valued optimal detuning. By using this value, one obtains for the minimal noise spectrum:

$$S_{\text{min}}(\Omega) = \frac{\Omega^2}{4\epsilon^2 + \Omega^2}, \quad (4.126)$$

which was also found by Collett and Walls in Ref. [51]. The minimal noise spectrum occurs for a fixed homodyne detection angle, namely the amplitude quadrature. From Eq. (4.126) one can infer that strong squeezing occurs below the half linewidth of the

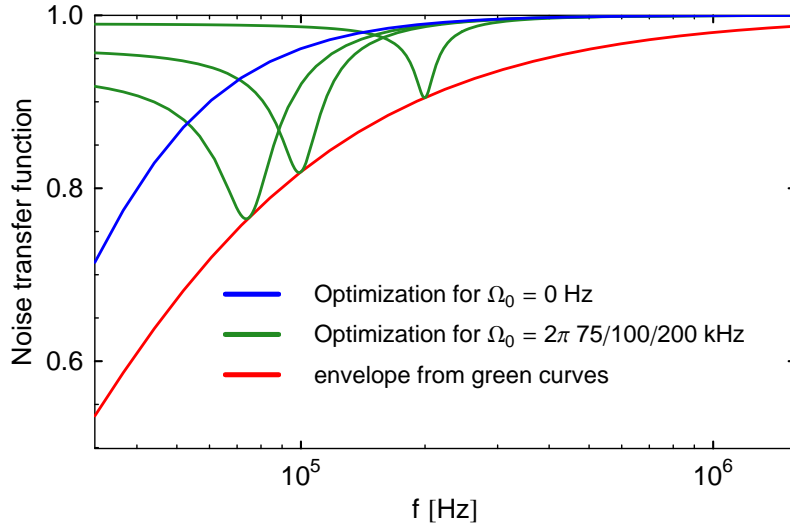


Figure 4.32.: Noise transfer function for differently optimized configurations. By adjusting the detuning according to Eq. (4.128) we can optimize the squeezing factor for frequencies within the half linewidth of the cavity. Here we use $\tilde{\mathcal{K}}_{\text{op}} = 2\epsilon$, i.e. infinite squeezing is achievable for $\Omega = 0$, and $\epsilon = 2\pi \cdot 10$ kHz as in Fig. 4.31.

cavity under consideration, while the spectrum tends to unity for high frequencies. In terms of classical dynamics, this state corresponds to the critical state where an infinite slope occurs for a certain detuning, as discussed in the beginning of Sec. 4.4.2. For a rigorous treatment of the squeezing near zero sideband frequencies, it is necessary to go beyond the linearized formalism used here (cf. Ref. [64]), since the assumption that the quantum fluctuations are small compared to the expectation value of the field is no longer valid. (iii) If the nonlinear coupling constant is further increased, i.e. $|\tilde{\mathcal{K}}_{\text{op}}| > 2\epsilon$, one enters a regime corresponding to a multi-stable state of the system. Similarly to the critical state, the linearized formalism also breaks down within this domain. But it was shown in Ref. [63] that a semi-classical description near and beyond the critical point still provides accurate predictions. It follows that no Schrödinger-cat-like behavior occurs, which could not be treated within a semi-classical theory. This is to be seen as a hint that any physical system which is coupled to the outside world hardly shows a violation of the hidden-variable theory. However, this statement is still in accordance with the results presented in Ref. [109] where a *crescent*-shaped squeezed state was predicted. These authors considered only the interaction of single photons with a Kerr medium, without taking an external heat bath into account. In Ref. [107] a *weakly* coupled nonlinear cavity was investigated, which shows various effects which cannot be treated within a semi-classical formalism.

Any real experimental set-up suffers from classical noise, which imposes an additional contribution to the total noise spectral density. In the case of the critical state, i.e. $|\tilde{\mathcal{K}}_{\text{op}}| = 2\epsilon$, we obtain for classical noise in the amplitude quadrature:

$$S^{\text{cl}}(\Omega) = \frac{m\epsilon\theta^2}{4(4\epsilon^2 + \Omega^2)\hbar} S_x. \quad (4.127)$$

We find minimal classical noise in the amplitude quadrature which coincides with the

optimally squeezed quadrature. The squeezed vacuum fluctuations are not completely masked by classical noise since it is minimal in the amplitude quadrature, which coincides with the optimally squeezed quadrature.

The noise spectrum given in Eq. (4.126) is not the overall minimum, achievable for a certain frequency. By minimizing $|M|^2$ for a chosen frequency Ω_0 one obtains for the optimal detuning

$$\lambda = \Re \left[\frac{1}{2} \left(-\tilde{\mathcal{K}}_{\text{op}} \pm \sqrt{\tilde{\mathcal{K}}_{\text{op}}^2 - 4(\epsilon^2 - \Omega_0^2)} \right) \right]. \quad (4.128)$$

For the critical value of the Kerr coupling constant, i.e. $\tilde{\mathcal{K}}_{\text{op}} = 2\epsilon$, the spectrum optimized for different frequencies as well as the corresponding envelope are shown in Fig. 4.32. The envelope is given by

$$S_{\text{min}}^{\text{env}}(\Omega) = \frac{\Omega^2 + 2\epsilon \left(\epsilon - \sqrt{\epsilon^2 + \Omega^2} \right)}{\Omega^2}. \quad (4.129)$$

Finally it should be mentioned that it is also possible to shift infinite squeezing from zero sideband frequency to higher frequencies. Two coupled resonators can be so arranged that the system exhibits a high bandwidth for certain sideband frequencies (cf. Refs. [135, 153]). This allows us to extract highly squeezed states at these particular frequencies, but the underlying effect is the same as in the previously discussed simple set-up.

5. Towards the preparation of macroscopic quantum states

Quantum theory is essential in order to interpret the behavior of systems at atomic length scales and below. Within this range, predictions of quantum mechanics have been verified experimentally to a very high degree of accuracy, including the Heisenberg uncertainty relation and the quantization of energy eigenstates. This chapter deals with the preparation, manipulation and observation of non-classical states of kilogram-scale objects. The goal is to provide a theoretical basis for testing quantum mechanics in the macroscopic world for the first time. For this purpose we introduce a general theoretical formalism which applies to any linear quantum measurement device [27]. However, in this thesis the suspended mirrors of a Michelson-type interferometer are the macroscopic objects under consideration. We deem such an interferometer with homodyne detection of the outgoing field an appropriate fundament for the aspired demonstration. The most sensitive devices of this kind are gravitational wave detectors, which can actually be regarded as the most sensitive instruments ever invented [103].

Different techniques exist aiming at the preparation of particular quantum states. The first method relies on the implementation of a feedback control system. The probe, i.e. the macroscopic mechanical oscillator, is continuously measured and the classical measurement record is fed back in real time. The oscillator's position and momentum are actuated by applying an adequate force. Hence the system's Hamiltonian is so manipulated that the desired state is generated. A sophisticated review of this topic can be found in Ref. [157]. One has to distinguish between two different types of forces. First, the thermal motion of the oscillator is countered by applying a frictionless damping force (*cold damping*). Such a force reduces the amplitude of an oscillatory motion of the suspended mirror, while it also reduces its mechanical quality factor. Second, a frictionless restoring force can shift the mechanical resonance frequency of the oscillator upwards, which effectively increases the quality factor. Note that both forces can also be provided in an all-optical way: radiation pressure forces in a detuned cavity can either exhibit restoring (*optical trapping*) [52] or damping (*cavity cooling*) [140] features (cf. also Sec. 4.3). The second state preparation scheme does not rely on any particular control system. We simply exploit the fact that – in the ideal case – a projective measurement fixes the state of the system, which solely depends on the measurement result. Translated to a real experimental set-up, involving a Michelson interferometer, it works as follows: usually the differential mirror motion is continuously measured via homodyne detection of the modulation fields leaking out at the dark port. Such a quantum measurement [26] allows us to observe a certain trajectory of the differential motion. The (quantum) state of the measured degree of freedom needs to be conditioned upon the registered classical information, which follows the concept of *a posteriori* [12] states. In contrast to the feedback scheme, the differential mode still undergoes a random walk since there is no physical manipulation associated with the actual measurement [157]. The measurement just updates our knowledge of the probe's

state!

This chapter deals with the preparation of conditional and controlled non-classical states of macroscopic test masses. The exploitation of these two concepts enables us to prepare nearly Heisenberg-limited Gaussian quantum states of macroscopic oscillators, provided that the measurement device exhibits a sub-SQL sensitivity. Various quantum effects can be revealed and it is shown that the quantum state survives long enough to be probed with a second verification stage down to a sub-Heisenberg level. Within this scope it will be shown that it is possible to observe quantized energy eigenstates of the two suspended end mirrors of a Michelson interferometer, entangling them with an optical field or even with each other.

This chapter is organized as follows: in the first section recent experimental efforts in the field of macroscopic quantum state engineering are reviewed. In Sec. 5.2 the Michelson-type interferometer is introduced again in the context of quantum state preparation. In Sec. 5.3 properties of Gaussian states are discussed in order to provide a basis for the formulation of a "measure of quantumness" in Sec. 5.4 and a "measure of entanglement" in the subsequent section. Then we start to formulate a general theoretical description for the conditional and controlled state preparation techniques. A brief introduction to the concept of conditional states is given by means of the stochastic master equation approach in Sec. 5.6.1. Then we propose an alternative concept, namely the quantum Wiener filter method, in Sec. 5.6.2. In Sec. 5.7 the preparation of a quantum state using classical control is investigated. These theoretical tools come into operation in Sec. 5.8, where we investigate the preparation of non-classical states and optomechanical entanglement in the presence of non-Markovian noise. In the following section, it is shown that entanglement between two macroscopic objects is feasible even in the presence of realistic decoherence processes. In Sec. 5.10 the relevance of non-classical macroscopic states in the context of quantum mechanics is discussed.

5.1. Review of recent experimental results

Ongoing experiments involving test masses ranging from 10^{-11} to 1000 kg (cf. e.g. Refs. [110, 122, 132]) have demonstrated that linear feedback control is an indispensable tool for quantum state preparation. An outstanding experimental effort has been made by the LIGO Scientific Collaboration: the LIGO detectors are currently operating at a factor of ~ 10 (in amplitude) away from the SQL in their most sensitive band. The dominant noise sources have classical origin [84]. Such a low classical noise budget gave the opportunity to create a 2.7 kg oscillator with an eigenfrequency of around 150 Hz (up shifted from the pendulum frequency of 1 Hz), and with an occupation number ~ 200 (cf. Ref. [6]). This was achieved by simply damping the oscillator by appropriately adjusting the feedback control. Note that in this case the feedback control system provides a restoring as well as a damping force. It should be emphasized that they employed a constant feedback as proposed in Refs. [49, 115, 163]. But as soon as one comes closer to a pure quantum state, i.e. the occupation number approaches and eventually goes below unity, the optimal control becomes crucial, which is discussed in detail in our Ref. [58] and Sec. 5.7.

Another approach is investigated in our Ref. [52] where we consider a stable all-optical trap for a gram-scale mirror. The experimentally realized scheme is based upon the dou-

ble optical spring technique proposed in Sec. 4.3. A detuned cavity composed of a fix input mirror and a moveable 1 gram end mirror is driven by two carrier fields with a total power of 3 W. These are separated in frequency by a free spectral range and effectively sense different detunings of the resonator. By appropriately adjusting the detunings we can create simultaneously an optical restoring force and a viscous optical damping force (cf. also Fig. 4.14). More precisely, the first carrier is detuned to higher frequencies (blue detuning) and therefore provides an anti-damping and a restoring force, shifting the mechanical eigenfrequency from $\omega_m = 2\pi \cdot 172$ Hz up to $\omega_{\text{eff}} = 2\pi \cdot 2178$ Hz. About 5% of the light is used for the second carrier, which is detuned to lower frequencies (red detuning). This introduces a damping as well as an anti-restoring force and hence the effective mechanical eigenfrequency is slightly shifted back to lower frequencies. The damping force can be increased by further red shifting the second carrier and the mechanical resonator's effective temperature is reduced. The anti-restoring force associated with the second carrier also changes when varying the detuning. This implies that the detuning corresponding to the first carrier has to be readjusted accordingly, in order to maintain a constant effective mechanical eigenfrequency. The advantage of such an all-optical scheme is that no additional thermal noise is introduced. The combination of both effects (i.e. the presence of a restoring and damping force) allows us to reach much lower temperatures than attainable by cold damping alone. It has been demonstrated that the system is stable and that an effective temperature of 0.8 K of the optically trapped and cooled test mass has been reached.

5.2. State preparation with a Michelson interferometer

A simple Michelson interferometer already meets all the requirements essential for preparing the differential mode of its suspended macroscopic end mirrors into a quantum state. It accomplishes a high precision measurement of the test mass mirrors' differential displacement with laser light and a preeminent isolation from environmental influences has already been realized – a constitutive feature of all operating and planned gravitational wave detectors. However, the theoretical treatment introduced in Sec. 2.3.4 and Chap. 4 needs to be modified slightly. Remember that the detection of gravitational waves is obstructed by different classical noise contributions which simply add up to a total classical noise budget. Whereas in the context of quantum state preparation we have to differentiate between two types of noise sources contaminating the measurement: *force noise* $\hat{\mathcal{F}}$ and *sensing noise* $\hat{\mathcal{Z}}$, where both contain quantum *and* classical components. The quantum noise is dominated at high frequencies by shot noise (sensing noise) and at low frequencies by radiation pressure noise (force noise). The classical noise sources have to be distinguished in the same way: classical force noise acts directly on the center of mass of the measured object, and in real experiments it is due to e.g. seismic noise or thermal noise in the suspension of the mirrors. The classical sensing noise accounts for a "pseudo" motion of the measured object. This corresponds to fluctuations in the relative distance between the mirror's center of mass and the averaged location of its surface. Possible contributions arise from thermal fluctuations in the mirror's substrate and coating. The previous investigation of gravitational wave detectors did not require such a distinction, since one is only interested in a signal which is masked by both kinds of noise contributions in the same manner.

In this chapter different configurations are used for state preparation purposes. They are briefly introduced in the following section, in order to predefine several notational issues.

5.2.1. Markovian quantum noise

First we consider a simple Michelson interferometer without arm cavities and end mirrors suspended as pendulums with angular eigenfrequency ω_m and damping rate γ_m . The corresponding equations of motion in frequency domain for the output field \hat{y} and the position (momentum) observable \hat{x} (\hat{p}) are given by [cf. Eqs. (2.87)-(2.88)]:

$$\hat{x}(\Omega) = -\frac{1}{m(\Omega^2 + i\gamma_m\Omega - \omega_m^2)} \left[\alpha\hat{a}_1 + \hat{\xi}_F \right], \quad \hat{p}(\Omega) = -im\Omega\hat{x}(\Omega), \quad (5.1)$$

$$\hat{y}(\Omega) = \hat{a}_1 \sin \zeta + \cos \zeta [\hat{a}_2 + \alpha/\hbar(\hat{x}(\Omega) + \hat{\xi}_x)], \quad (5.2)$$

where $\hat{a}_{1,2}$ are the input quadrature fields, α is the measurement strength and ζ the homodyne detection angle. The operators $\hat{\xi}_F$ and $\hat{\xi}_x$ account for the classical force and sensing noise, respectively. The residual quantities have already been defined in Sec. 2.3. In the ideal case monitoring the differential motion of the Michelson interferometer's two end mirrors is equivalent to measuring the motion of a single mirror. One has to adjust the mirror mass m and the measurement strength α appropriately [cf. Eqs. (2.88) and (2.212)]:

	single mirror	simple Michelson	signal-recycled Michelson	
α	$\sqrt{8\hbar\omega_0 P}/c$	$\sqrt{4\hbar\omega_0 P}/c$	$2/\tau\sqrt{4\hbar\omega_0 P}/c$	(5.3)
m	m'	$m'/2$	$m'/2$	

where τ is the transmissivity of an additional mirror placed behind the interferometer's output port, forming a low finesse cavity together with the end mirrors. Further on m' is the mass of a single (end) mirror and P is the optical power impinging on it. From Eqs. (5.1)-(5.2) one can directly infer that the total force and sensing noise are given by

$$\hat{\mathcal{F}} = \alpha\hat{a}_1 + \hat{\xi}_F, \quad \hat{\mathcal{Z}} = \hat{\xi}_x + \frac{\hat{a}_1 \sin \zeta + \hat{a}_2 \cos \zeta}{\alpha/\hbar \cos \zeta}, \quad (5.4)$$

which is consistent with Eq. (2.150). The corresponding noise spectral densities can be deduced by means of Eq. (2.155). In this simple case the quantum noise naturally exhibits Markovian behavior which allows us to describe its noise spectral density by a single quantity, provided that the test masses can be considered as quasi free and the phase quadrature is detected. Here we choose the characteristic *measurement frequency*

$$\Omega_q \equiv \alpha/\sqrt{m\hbar}, \quad (5.5)$$

where the quantum noise spectral density touches the SQL. In general we have to deal with multiple colored classical noise sources. But if we assume that the classical noise contributions also have white spectra S_{ξ_F} and S_{ξ_x} , we can express them in terms of the characteristic frequencies Ω_F and Ω_x , respectively, where they intersect the SQL, i.e. we have

$$S_{\xi_F} = 2\hbar m \Omega_F^2 \quad \text{and} \quad S_{\xi_x} = 2\hbar/(m\Omega_x^2). \quad (5.6)$$

5.2.2. Non-Markovian quantum noise

As soon as the system under consideration comprises a finite bandwidth cavity we have to cope with non-Markovian dynamics. Remember that the equations of motion in the frequency domain for a detuned cavity with a suspended end mirror and a fixed input mirror can be written in the following form:

$$\hat{y}_1(\Omega) = \hat{Y}_1(\Omega) + R_{Y_1F}(\Omega)(\hat{x}(\Omega) + \hat{\xi}_x), \quad \hat{y}_2(\Omega) = \hat{Y}_2(\Omega) + R_{Y_2F}(\Omega)(\hat{x}(\Omega) + \hat{\xi}_x), \quad (5.7)$$

$$\hat{A}_1(\Omega) = \sqrt{\frac{1}{2\epsilon}}(\hat{y}_1(\Omega) + \hat{a}_1(\Omega)), \quad \hat{A}_2(\Omega) = \sqrt{\frac{1}{2\epsilon}}(\hat{y}_2(\Omega) + \hat{a}_2(\Omega)), \quad (5.8)$$

$$\hat{y}(\Omega) = \hat{y}_1(\Omega) \sin \zeta + \hat{y}_2(\Omega) \cos \zeta, \quad (5.9)$$

where $\hat{y}_{1,2}$ are the outgoing quadrature fields while $\hat{A}_{1,2}$ are the cavity mode operators [cf. Eq. (2.211)]. As in Sec. 5.2.1 the operators $\hat{\xi}_x$ and $\hat{\xi}_F$ account for the classical noise sources and the residual quantities are already defined in Sec. 2.3.4. Further on the position and momentum of the mirror obey the following equations:

$$\begin{aligned} \hat{x}(\Omega) &= R_{xx}(\Omega) \left[\hat{F}(\Omega) + R_{FF}(\Omega)(\hat{x}(\Omega) + \hat{\xi}_x) + K_{\text{ctrl}} \hat{y}(\Omega) \right] + \hat{\xi}_F, \\ \hat{p}(\Omega) &= -im\Omega \hat{x}(\Omega). \end{aligned} \quad (5.10)$$

These equations of motion are valid for a simple cavity and also for a Michelson interferometer with arm cavities comprising detuned signal-recycling and we can switch between these two configurations by means of the relations given in Eq. (2.142). Note that in the case of a detuned configuration the feedback control filter K_{ctrl} has to be chosen appropriately in order to guarantee stable dynamics.

A characteristic measurement frequency can also be defined by

$$\Omega_q^{\text{cav}} = \theta / \sqrt{2\epsilon}, \quad (5.11)$$

which corresponds to the frequency where the quantum noise spectral density of the associated adiabatically eliminated system (cf. Sec. 2.3.8) touches the SQL. If classical white noise sources come into play they can be described by the spectra given in Eq. (5.6) and the characteristic frequencies Ω_x and Ω_F refer to the adiabatically eliminated system.

5.2.3. Comment on measured degree of freedom

In the following investigations we aim at preparing a quantum state of the center of mass motion of the mirrors under consideration. More precisely, we refer solely to a single degree of freedom which is defined by the direction of the incident laser beam. The residual degrees of freedom are not affected by the proposed state preparation scheme.

In order to evade the influence of the sensing noise one might naively think that it is also possible to apply the state preparation apparatus to the mirrors' surface observables. This would turn the "pseudo" motion induced by the sensing noise into a real one. But in general, the sensing noise contributions fall off slower than the force noise contributions, e.g. for the thermoelastic noise we have $\sim 1/f$ and for the internal thermal noise we assume $\sim 1/\sqrt{f}$ (cf. also Fig. 5.12). Consequently we obtain for the spectral densities

of the position and momentum observables the following relations, if we just consider thermoelastic noise:

$$S_{xx} \sim 1/f^2 \Rightarrow S_{pp} = m^2(2\pi f)^2 S_{xx} \rightarrow \text{const.} \neq 0 \quad \text{for } f \rightarrow \infty, \quad (5.12)$$

i.e. the momentum's spectral density $S_{pp}(\Omega)$ does not vanish in the high frequency regime. Accordingly, the unconditional momentum variance diverges as one can directly deduce from Eq. (2.159). This divergence cannot be cured by employing a conditional measurement process, since a realistic detection scheme exhibits a limited bandwidth and therefore the high frequency noise is not accessible. Nevertheless, a careful calculation reveals that the position variance can still be finite, but it is almost impossible to penetrate into the quantum regime due to the presence of internal thermal noise.

5.3. Gaussian states

The systems discussed in this chapter are quantum systems with N canonical degrees of freedom. They are characterized by N pairs of canonical operators, which we combine into a vector:

$$\hat{\boldsymbol{\xi}}^T \equiv (\hat{x}_1, \hat{p}_1, \dots, \hat{x}_N, \hat{p}_N). \quad (5.13)$$

Up to a normalization the operators \hat{x}_i (\hat{p}_i) correspond to the real (imaginary) parts of the familiar bosonic annihilation operators \hat{a}_i . For the following general discussion we prefer to choose the normalization in such a way that the canonical operators are dimensionless, i.e. $\hat{a}_i = 1/\sqrt{2}(\hat{x}_i + i\hat{p}_i)$ with $[\hat{a}_i, \hat{a}_j^\dagger] = \delta_{ij}$. This has to be adjusted, depending on the physical system under consideration (mechanical oscillator, electromagnetic field, etc.). The commutation relations can be expressed in the following compact form:

$$[\hat{\xi}_i, \hat{\xi}_j] = i\Omega_{ij} \quad \text{with} \quad \boldsymbol{\Omega} = \bigoplus_{j=1}^N \begin{pmatrix} 0 & 1 \\ -1 & 0 \end{pmatrix}. \quad (5.14)$$

For an arbitrary density operator $\hat{\rho}$ of the system we define a vector of mean values (first-order moments) and the covariance matrix \mathbf{V} with the second-order moments as its components:

$$\langle \hat{\xi}_i \rangle \equiv \text{tr}[\hat{\rho}\hat{\xi}_i], \quad (5.15)$$

$$V_{ij} \equiv \frac{1}{2}\text{tr}[\rho\{\hat{\xi}_i - \langle \hat{\xi}_i \rangle, \hat{\xi}_j - \langle \hat{\xi}_j \rangle\}_+] = \frac{1}{2}\langle \hat{\xi}_i \hat{\xi}_j + \hat{\xi}_j \hat{\xi}_i \rangle - \langle \hat{\xi}_i \rangle \langle \hat{\xi}_j \rangle, \quad (5.16)$$

where $\{\dots\}_+$ denotes the plus commutator. A density operator $\hat{\rho}$ completely describes the statistical state of an arbitrary quantum system and it corresponds to a density matrix under some orthonormal basis. It is a hermitian and positive semidefinite operator of trace one, defined on a certain Hilbert space \mathcal{H} . There exist various methods of expressing the density operator in terms of a c-number function. Here we use a quasiprobability distribution introduced by Wigner [168] which is given by

$$W(\mathbf{x}, \mathbf{p}) = \frac{1}{\pi^N} \int d\mathbf{x}' \langle \mathbf{x} - \mathbf{x}' | \hat{\rho} | \mathbf{x} + \mathbf{x}' \rangle \exp [2i(\mathbf{x}')^T \cdot \mathbf{p}] \quad (5.17)$$

$$= \frac{1}{(2\pi)^{2N}} \int d\boldsymbol{\lambda} \chi(\boldsymbol{\lambda}) \exp [-i\boldsymbol{\lambda}^T \cdot \boldsymbol{\xi}], \quad (5.18)$$

with $\mathbf{x}^T = (x_1, \dots, x_N)$, $\mathbf{p}^T = (p_1, \dots, p_N)$ and $\hat{\boldsymbol{\xi}}^T \equiv (x_1, p_1, \dots, x_N, p_N)$. The relation between these two representations given in Eqs. (5.17)-(5.18) is clarified e.g. in Ref. [81]. In Eq. (5.18) we have used the well-known characteristic function [166] defined as:

$$\chi(\boldsymbol{\lambda}) = \text{tr} \left[\hat{\rho} \exp \left[i \boldsymbol{\lambda}^T \cdot \hat{\boldsymbol{\xi}} \right] \right]. \quad (5.19)$$

This is the Fourier transform of the Wigner function and therefore completely specifies the quantum state. A quantum state is Gaussian if its characteristic function is most quadratic in its canonical variables, i.e. if it assumes the form:

$$\chi(\boldsymbol{\lambda}) = \exp \left[-\frac{1}{4} \boldsymbol{\lambda}^T \cdot \mathbf{V} \cdot \boldsymbol{\lambda} + i \langle \hat{\boldsymbol{\xi}}^T \rangle \cdot \boldsymbol{\lambda} \right]. \quad (5.20)$$

Gaussian states are therefore completely characterized by their first- and second-order moments. This allows us to translate properties of Gaussian states into properties of finite-dimensional matrices, which will be used e.g. for the definition of entanglement criteria. In the following we consider w.l.o.g. Gaussian states with zero mean ($\langle \hat{\boldsymbol{\xi}} \rangle = \mathbf{0}$). Hence we can express the Wigner function given in Eq. (5.17) solely in terms of the covariance matrix \mathbf{V} :

$$W(\boldsymbol{\xi}) = \frac{1}{\pi^N \sqrt{\det \mathbf{V}}} e^{-\boldsymbol{\xi}^T \cdot \mathbf{V}^{-1} \cdot \boldsymbol{\xi}}. \quad (5.21)$$

By using the definition of the covariance matrix and the commutation relations provided in Eq. (5.14) one obtains (cf. Ref. [146])

$$\langle \hat{\xi}_i \hat{\xi}_j \rangle = \text{tr} \left[\hat{\rho} \hat{\xi}_i \hat{\xi}_j \right] = V_{ij} + \frac{i}{2} \Omega_{ij}, \quad (5.22)$$

which implies that the density operator is positive semidefinite if and only if the matrix $\mathbf{V} + i\boldsymbol{\Omega}/2$ is positive semidefinite, i.e.

$$\mathbf{V} + i\boldsymbol{\Omega}/2 \geq 0. \quad (5.23)$$

Gaussian states can be transformed into each other by transforming the corresponding covariance matrix as $\mathbf{V} \rightarrow \mathbf{V}' = \mathbf{S} \cdot \mathbf{V} \cdot \mathbf{S}^T$ where we have to require that the canonical commutation relations given in Eq. (5.14) are preserved, i.e. $\mathbf{S} \cdot \boldsymbol{\Omega} \cdot \mathbf{S}^T = \boldsymbol{\Omega}$. Real matrices satisfying this condition form the so-called symplectic group $\text{Sp}(2N, \mathbb{R})$ and its elements are called symplectic transformations. These transformations can be realized experimentally by means of optical elements such as beam splitters, phase shifts and squeezers, together with homodyne detections (cf. Ref. [72]). This can be deduced directly from the Euler decomposition, applicable to every $\mathbf{S} \in \text{Sp}(2N, \mathbb{R})$: $\mathbf{S} = \mathbf{R}_1 \cdot \mathbf{D} \cdot \mathbf{R}_2$, where \mathbf{D} is a diagonal squeezing matrix, while \mathbf{R}_i generate N -mode rotations. Note that there exists a unitary operator $\hat{U}(\mathbf{S})$ corresponding to $\mathbf{S} \in \text{Sp}(2N, \mathbb{R})$, which transforms the density operator as $\hat{\rho} \rightarrow \hat{\rho}' = \hat{U}(\mathbf{S}) \hat{\rho} \hat{U}^\dagger(\mathbf{S})$.

Finally it should be emphasized that physical states deviate from an exact Gaussian form and their precise nature generally remains unknown. Nevertheless Gaussian states play a key role in various fields of theoretical physics since they can be handled easily and provide a good approximation in various situations.

5.4. Measure of quantumness

For the investigation of the transition from classical to quantum behavior, it is necessary to assess the non-classical character of a prepared state. A widely used definition was formulated by Titulaer and Glauber in Ref. [154] where they pointed out that a quantum state with a positive definite P function [82, 150] possess a classical analog. Remember that the P function is the Fourier transform of the normally ordered characteristic function given by

$$\chi_N(\boldsymbol{\lambda}) \equiv \chi(\boldsymbol{\lambda}) e^{\frac{1}{8}|\boldsymbol{\lambda}|^2}. \quad (5.24)$$

In the case of Gaussian states we can so redefine the phase space variables that the covariance matrix assumes a diagonal form with entries V'_{ii} . Then the normally ordered characteristic function reads:

$$\chi_N(\boldsymbol{\lambda}) = \exp \left[-\frac{1}{4} \sum_{i=1}^N \lambda_i^2 (V'_{ii} - 1/2) \right] \quad (5.25)$$

and it has a properly defined Fourier transform if and only if $V'_{ii} \geq 1/2$ for all $i \in [1, N]$, which can be expressed in the compact form:

$$\mathbf{V} - 1/2 \geq 0. \quad (5.26)$$

It was shown in Ref. [164] that a quantum state has no classical counterpart if and only if this condition is violated. A detailed review can be found in Ref. [15].

The relation given in Eq. (5.26) is based on the full information of the Gaussian state. Another less stringent measure of quantumness follows directly from the generalized Heisenberg uncertainty relation provided in Eq. (5.23). It is motivated by the assumption that an oscillator obeys a non-classical behavior if its fluctuations are close to the limit set by the Heisenberg uncertainty, which can be quantified by

$$U \equiv 2^{2N} \sqrt{\det \mathbf{V}} \geq 1. \quad (5.27)$$

The dimensionless quantity U indicates the *purity* of Gaussian states and it corresponds to the state's "area" in the N -dimensional phase space. The degree of purity of a state can also be characterized by other quantities besides U . The most prominent of these is the ubiquitous quantum (von Neumann) entropy [98, 174] which is directly related to the purity defined in Eq. (5.27):

$$S = \frac{U+1}{2} \log(U+1) - \frac{U-1}{2} \log(U-1) - \log(2). \quad (5.28)$$

The von Neumann entropy measures the amount of information missing for a complete characterization of a state, i.e. it quantifies to what extent a certain state has been determined. In the case of pure quantum states, an observer has maximal knowledge about the system and the entropy is equal to zero.

In previous publications, e.g. Refs. [49, 115, 163], a single mechanical oscillator was considered and its non-classicality was assessed by consulting the occupation number. This may not be the best figure of merit – for instance a squeezed state has to be regarded as highly non-classical, even though it could have high occupation numbers. Furthermore,

the definition of an occupation number requires a well-defined real valued eigenfrequency, which can be ambiguous for two reasons: *(i)* a feedback control system can modify the oscillator's original eigenfrequency and *(ii)* in the case of a finite quality factor Q_{eff} the choice for an effective real eigenfrequency Ω_{eff} would be ambiguous by $\sim \Omega_{\text{eff}}/Q_{\text{eff}}$. But in the case of vanishing cross-correlations of a single mode system it is possible to convert U given in Eq. (5.27) into an effective (mean) occupation number given by

$$N_{\text{eff}} = \frac{U}{2} - \frac{1}{2}. \quad (5.29)$$

This corresponds to the minimum occupation number achievable by putting the same test mass into a quadratic potential well with an arbitrary real eigenfrequency Ω_* , i.e.

$$N_{\text{eff}} = \min_{\Omega_*} \left[\frac{\frac{1}{2}mV_{pp} + \frac{1}{2}m\Omega_*^2V_{xx}}{\hbar\Omega_*} \right]. \quad (5.30)$$

The new eigenfrequency Ω_* can differ from the original mechanical eigenfrequency ω_m of the oscillator and the resulting quantum state tends to be position squeezed if $\Omega_* > \omega_m$ and momentum squeezed if $\Omega_* < \omega_m$. The definition of N_{eff} does not depend on a specific choice of the oscillator's eigenfrequency and it maintains a physical interpretation of an occupation number.

5.5. Measure of entanglement

The notion of entanglement was introduced by Erwin Schrödinger in 1935 [141]. His publication was a reply to the famous paper "Can Quantum-Mechanical Description of Physical Reality Be Considered Complete?" by Albert Einstein, Boris Podolsky and Nathan Rosen (EPR) [71]. These authors considered a pure unfactorizable state of two systems and remarked that such a bipartite state can be expanded in terms of different orthonormal bases ($\{|A_n\rangle\}$ or $\{|\mathcal{Y}_n\rangle\}$) of the first subsystem. By adopting the notation introduced in Ref. [172] we can formulate this mathematically as follows:

$$|\Psi\rangle = \sum_{n=1}^{\infty} c_n |A_n\rangle |\phi_n\rangle = \sum_{n=1}^{\infty} d_n |\mathcal{Y}_n\rangle |\varphi_n\rangle, \quad (5.31)$$

which is also called "Schmidt decomposition". If both expansions exist we have the opportunity to perform a measurement on the first subsystem either in the $\{|A_n\rangle\}$ or the $\{|\mathcal{Y}_n\rangle\}$ bases. Depending on our decision, the second subsystem collapses instantaneously into one of the states $|\phi_n\rangle$ or $|\varphi_n\rangle$. Even though the two subsystems under consideration might be separated by a long distance (which precludes any interaction) we can steer the second subsystem into different ensembles [172] by performing a certain measurement on the first one. This was problematic for EPR, since they demanded from any "reasonable" theory that it should be local and realistic, which means: *(i)* If one can predict with certainty the outcome of a measurement on a system localized in space-time, there must be a pre-existing value carried along by that system (physical reality). *(ii)* In order to maintain causality, a system cannot be influenced instantaneously by a spacelike separated event (locality). Hence the thought experiment can only be explained by abandoning one

of the assumptions which led EPR (wrongly) to the conclusion that quantum mechanics cannot be a complete theory.

In 1964 John Bell showed that local realism leads to certain constraints on the statistics of physically separated systems [13] that are not present in quantum mechanics. He condensed this in the Bell inequalities, which can be tested experientially [10, 127]. Gradually improved experiments have shown that the concept of local realism cannot be maintained even if quantum mechanics is complemented by local hidden variables. It should be emphasized that one only has to drop the concept of locality *or* reality. Note that the widely accepted Copenhagen interpretation of quantum mechanics abandons both concepts.

EPR also considered the following example in Ref. [71]: a pair of particles moving in opposite directions is considered, which are prepared in such a way that their total momentum is zero. Therefore measuring the momentum of the first particle also determines the momentum of the distant second one without directly measuring it. According to EPR there must be a predetermined momentum of the second particle. The same argument applies to a measurement of the position. But the Heisenberg uncertainty relation does not allow states of definite position *and* momentum. In this particular case it is not necessary to help oneself with the non-locality argument. This thought experiment is therefore not suitable for proving the non-locality of quantum mechanics. Nevertheless an apparent violation of the Heisenberg uncertainty relation occurs, known as the "EPR paradox". Entangled states showing this feature are called in the following *EPR-entangled*. It has been shown that a non-negative Wigner distribution always admits a local realistic hidden-variables model [14], since it can serve as a classical probability distribution for the hidden variables. The investigations carried out in the following are restricted to continuous variable Gaussian states (which always have a positive Wigner distribution) and therefore it is not possible to violate any Bell inequality. But in principle it is also possible to reveal the non-locality of Gaussian states by performing non-Gaussian measurements. Such a detection scheme cannot be based upon homodyne detection.

It has been discussed in detail in Refs. [102, 172] that Bell-non-local states are a subset of EPR-entangled states, which are in turn a subset of the usual entangled states. For the latter case a well-known criterion is re-derived in Sec. 5.5.1 which is applicable to two-mode Gaussian states. It simply relies on the fact that the transpose operation, applied to one part of a separable bipartite system, does not affect the positive definiteness of the density operator of the total system. Such an operation is called partial transposition. When applying it to a non-separable system, there is no guarantee that one obtains a positive density operator of the total system, i.e. a physical state.

In Sec. 5.5.2 a criterion for EPR-entanglement is derived, again for two-mode Gaussian states. This is accomplished by considering one subsystem conditioned upon the other, i.e. by performing a measurement on one subsystem one can *infer* the second-order moments of the other subsystem [138]. If the inferred second-order moments violate the Heisenberg uncertainty relation, one deals with EPR-entangled states. It is evident that the usual entanglement is symmetric between the two parties. This is not necessarily true for EPR-entangled states. The experimenter has to decide which subsystem should be subject to the measurement process. It can depend upon this decision whether he succeeds in demonstrating the presence of EPR-entanglement or not!

The inseparability of pure states is well understood and there is a simple criterion for its quantification in the case of a bipartite system (for continuous as well as discrete

variables): a unique measure is given by the partial von Neumann entropy, i.e. the von Neumann entropy of each subsystem quantifies the amount of entanglement. Note that any pure bipartite state is entangled if and only if (for suitably chosen observables) it yields a violation of a Bell inequality.

5.5.1. Non-separability

In the following the transposed density operator $\hat{\rho}^T$ is of particular importance. The hermiticity of the density operator implies that the transpose operation corresponds to a complex conjugation. This can either be interpreted as a time reversal or, in terms of continuous variables, as a sign change of the momentum variable [145], i.e. [cf. Eq. (5.17)]:

$$\hat{\rho} \rightarrow \hat{\rho}^T \iff W(\mathbf{x}, \mathbf{p}) \rightarrow W(\mathbf{x}, -\mathbf{p}). \quad (5.32)$$

This implies that the general properties of a density operator are preserved under the transpose operation and $\hat{\rho}^T$ should also describe a physical system. Now we consider a Hilbert space $\mathcal{H} = \mathcal{H}_A \otimes \mathcal{H}_B$ and the states $\hat{\rho}_j^{(A)}$ and $\hat{\rho}_j^{(B)}$ on \mathcal{H}_A and \mathcal{H}_B , respectively, each described by a single mode. A mixed state $\hat{\rho}$ on \mathcal{H} is by definition separable if and only if it can be written as

$$\hat{\rho} = \sum_j p_j \hat{\rho}_j^{(A)} \otimes \hat{\rho}_j^{(B)}, \quad (5.33)$$

with $p_j \geq 0$ and $\sum_j p_j = 1$. The application of the partial transpose operation to the second Hilbert space, i.e.

$$\hat{\rho} \rightarrow \hat{\rho}^{TB} = \sum_j p_j \hat{\rho}_j^{(A)} \otimes (\hat{\rho}_j^{(B)})^T \iff W(x_1, x_2, p_1, p_2) \rightarrow W(x_1, x_2, p_1, -p_2) \quad (5.34)$$

necessarily takes a separable density operator into another separable *bona fide* density operator. Demanding that $\hat{\rho}^{TB}$ is a bona fide density operator is only a necessary condition for separability. There exist non-separable states with a proper partially transposed density operator. However, the following considerations are restricted to bipartite two-mode Gaussian states which implies that the criterion can be regarded as necessary *and* sufficient [94, 130, 145]. Since in any case hermiticity and trace are not affected by the partial transpose operation, one has to test $\hat{\rho}^{TB}$ for positive semidefiniteness in order to identify non-separable states. Due to the fact that Gaussian states are completely characterized by their first- and second-order moments it must be possible to so translate the separability criterion that it is directly applicable to the covariance matrix \mathbf{V} [cf. Eq. (5.15)].

For the sake of simplicity, we recast the covariance matrix into the following form, known as the "Standard Form I" (cf. Ref. [65]):

$$\mathbf{V} = \begin{pmatrix} a & 0 & c & 0 \\ 0 & a & 0 & d \\ c & 0 & b & 0 \\ 0 & d & 0 & b \end{pmatrix} \equiv \begin{pmatrix} \boldsymbol{\alpha} & \boldsymbol{\gamma} \\ \boldsymbol{\gamma}^T & \boldsymbol{\beta} \end{pmatrix}. \quad (5.35)$$

This can be obtained by applying appropriate local symplectic transformations $\text{Sp}(2, \mathbb{R}) \otimes \text{Sp}(2, \mathbb{R})$ which belong to a subgroup of the real symplectic group $\text{Sp}(4, \mathbb{R})$.

A matrix is positive semidefinite if and only if all its principal minors are non-negative (Sylvester criterion) and therefore Eq. (5.23) splits into four conditions, namely:

$$a \geq 0 \wedge \det \boldsymbol{\alpha} \geq \frac{1}{4} \wedge a^2 - ac^2/b \geq \frac{1}{4} \wedge \frac{1}{4} + \det \mathbf{V} \geq \underbrace{(\det \boldsymbol{\alpha} + \det \boldsymbol{\beta} + 2 \det \boldsymbol{\gamma})}_{\equiv \Delta}, \quad (5.36)$$

where the Standard Form I [cf. Eq. (5.35)] has been used. All conditions have to be satisfied in order to ensure that the Heisenberg uncertainty relation is not violated. Nevertheless the first three conditions are commonly disregarded in the literature.

The next step is to rewrite Eq. (5.36) for the partially transposed system. From Eq. (5.21) one can directly infer that the partial transpose operation affects the covariance matrix in the following way:

$$\hat{\rho} \rightarrow \hat{\rho}^{TB} \iff W(x_1, x_2, p_1, p_2) \rightarrow W(x_1, x_2, p_1, -p_2) \iff \mathbf{V} \rightarrow \mathbf{A} \cdot \mathbf{V} \cdot \mathbf{A}, \quad (5.37)$$

with $\mathbf{A} = \text{diag}(1, 1, 1, -1)$. It can be easily verified that the first three conditions given in Eq. (5.36) are left unchanged, while the fourth condition changes in the following way:

$$\frac{1}{4} + 4 \det \mathbf{V} \geq \tilde{\Delta} \quad \text{with} \quad \tilde{\Delta} \equiv \Delta - 4 \det \boldsymbol{\gamma}. \quad (5.38)$$

We can immediately conclude that a bipartite Gaussian state is separable if and only if

$$\frac{1}{4} + 4 \det \mathbf{V} \geq \tilde{\Delta} \quad (5.39)$$

is satisfied, which agrees exactly with the criterion found by Simon in Ref. [145]. Since Δ , $\tilde{\Delta}$ and $\det \mathbf{V}$ are invariant under symplectic transformations, Eq. (5.39) already provides a general criterion for any covariance matrix, i.e. it is not necessary to switch to the Standard Form I.

An appropriate symplectic transformation $\mathbf{S} \in \text{Sp}(4, \mathbb{R})$ allows us to so transform the covariance matrix that it is diagonal, i.e. $\mathbf{V} = \text{diag}(n_-, n_-, n_+, n_+)$, and completely determined by the $\text{Sp}(4, \mathbb{R})$ invariants

$$n_{\pm}^2 = \frac{1}{2} \left(\Delta \pm \sqrt{\Delta^2 - 4 \det \mathbf{V}} \right). \quad (5.40)$$

Inserting the diagonal covariance matrix into Eq. (5.36) simplifies the last condition to $n_- \geq 1/2$. The symplectic invariants \tilde{n}_{\pm} of the partially transposed system can be obtained by substituting $\Delta \rightarrow \tilde{\Delta}$ in Eq. (5.40). Hence one can conclude that a state is separable if and only if

$$\tilde{n}_- = \sqrt{\frac{1}{2} \left(\tilde{\Delta} - \sqrt{\tilde{\Delta}^2 - 4 \det \mathbf{V}} \right)} \geq \frac{1}{2} \quad \text{with} \quad \tilde{\Delta} = \det \boldsymbol{\alpha} + \det \boldsymbol{\beta} - 2 \det \boldsymbol{\gamma}, \quad (5.41)$$

which again is a general criterion due to the invariance of $\tilde{\Delta}$ and $\det \mathbf{V}$ under $\text{Sp}(4, \mathbb{R})$ transformations.

As stated e.g. in Ref. [7], a proper measure of entanglement for bipartite Gaussian states should be a monotonically decreasing function of \tilde{n}_- since the violation of the condition given in Eq. (5.41) should be quantified. In Ref. [160]

$$E_{\mathcal{N}} = \max[0, -\log_2 2\tilde{n}_-] \quad (5.42)$$

was chosen, which is widely known as the *logarithmic negativity*.

5.5.2. Einstein-Podolsky-Rosen-entanglement

Here we consider the EPR-paradox associated with a bipartite entangled state with correlations in position and momentum. As stated in the beginning, this can lead to an apparent violation of the Heisenberg uncertainty relation. In order to formulate the problem mathematically, we think of it in the following way: we perform measurements on one subsystem of an ensemble of identically prepared states (quantum tomography). Then we can ask for the *inferred* Heisenberg uncertainty of the other subsystem. If and only if the Heisenberg uncertainty principle is violated for this subsystem, the EPR-paradox is demonstrated. Here we consider the special case of two-mode Gaussian states which are completely determined by the covariance matrix of their second-order moments. By adopting the notation of the covariance matrix introduced in Eq. (5.35) we can write the covariance matrix of subsystem β , conditioned on measurements on subsystem α , in the following way:

$$\mathbf{V}(\beta|\alpha) = \beta - \gamma\alpha^{-1}\gamma^T. \quad (5.43)$$

Here we employ the Schur complement widely used in probability theory and statistics. The inferred uncertainty is given by

$$\det \mathbf{V}(\beta|\alpha) = \left(b - \frac{c^2}{a}\right) \left(b - \frac{d^2}{a}\right) = \frac{\det \mathbf{V}}{\det \alpha}, \quad (5.44)$$

which implies that the EPR-paradox occurs if and only if

$$\frac{\det \mathbf{V}}{\det \alpha} < \frac{1}{4}. \quad (5.45)$$

This again is a general criterion for the covariance matrix of a two-mode Gaussian system, since $\det \mathbf{V}$ and $\det \alpha$ are invariant under $\text{Sp}(2, \mathbb{R}) \otimes \text{Sp}(2, \mathbb{R})$ operations. The inferred uncertainty expressed in terms of Standard Form I quantities was first obtained by Reid in Ref. [138]. An alternative, more general derivation can be found in Refs. [102, 172]. In contrast to the logarithmic negativity, the criterion for EPR entanglement can only be expressed in terms of $\text{Sp}(2, \mathbb{R}) \otimes \text{Sp}(2, \mathbb{R})$ invariants. This is due to the fact that non-separability is symmetric between both systems while the EPR-entanglement is inherently asymmetric. Note that the EPR-criterion is strictly stronger than the non-separability criterion introduced in the previous section. In other words, the EPR-entanglement criterion is a sufficient but not necessary criterion for entanglement. In the following we quantify the amount of EPR-entanglement by

$$E_{\text{EPR}} = \max \left[0, -\log_2 [2\sqrt{\det \mathbf{V} / \det \alpha}] \right]. \quad (5.46)$$

It should be emphasized that the criterion given in Eq. (5.45) also exploits the correlations between position and momentum. This is a kind of generalization of the original thought experiment of EPR. These correlations can occur when using the conditional state preparation method, while in the case of controlled systems they vanish anyway. Aesthetical motives might incite the experimenter to restrict himself to the inferred uncertainties of position and momentum, which preserves the original flavor of the EPR-paradox. This can be accomplished by simply setting the entries in the measured covariance matrix corresponding to the correlations between position and momentum to zero. This would open out into the traditional EPR-criterion [71] which is reviewed in detail e.g. in Ref. [31]. In this case it is obviously even more challenging to demonstrate the EPR-paradox.

5.6. Conditional states

The following investigations are based on the well-established concept of conditional states, which should first be clarified by means of a simple example. We consider a system described at time t by the normalized state vector $|\Psi\rangle$ belonging to the Hilbert space \mathcal{H} . The corresponding density operator is given by

$$\hat{\rho}(t) = |\Psi\rangle\langle\Psi|, \quad (5.47)$$

which clearly describes a pure system. Now an observable \hat{A} is introduced which has discrete eigenvalues a_1, a_2, a_3, \dots corresponding to the eigenstates $|A_1\rangle, |A_2\rangle, |A_3\rangle, \dots$ of the system. By defining the projection operator $P_{j,A} = |A_j\rangle\langle A_j|$, the probability of obtaining the i th measurement result (i.e. the particular value a_i) can be written as:

$$\mathcal{P}(i, \hat{A}, \hat{\rho}(t)) = \text{tr}[\hat{\rho}(t)\hat{P}_{i,A}]. \quad (5.48)$$

After the measurement at time $t + \Delta t$, the new state of the system conditioned on the measurement result a_i is given by

$$\hat{\rho}(t + \Delta t | \hat{A} = a_i) = \frac{P_{i,A}\hat{\rho}(t)P_{i,A}}{\mathcal{P}(i, \hat{A}, \hat{\rho}(t))}. \quad (5.49)$$

It can be easily verified that the system's purity is maintained. If a careless experimenter loses the result of his measurement the final state is a mixture of all possible outcomes weighted by the associated probabilities:

$$\hat{\rho}(t + \Delta t) = \sum_i \mathcal{P}(i, \hat{A}, \hat{\rho}(t))\hat{\rho}(t + \Delta t | \hat{A} = a_i), \quad (5.50)$$

i.e. the system is not in a pure state anymore. This simple example already illustrates that past measurement results have to be taken into account in order to unravel a quantum state in an optimal way.

Now we turn over to a continuous measurement process, i.e. where information about a certain observable $\hat{x}(t)$ is continuously extracted from the system. For example a mirror is illuminated with light in order to track its motion continuously. The conditional state must depend on the entire history of the observation up to a given time [118] and therefore it is also called an *a posteriori* [12] state. In contrast to the simple example above, the measurement only extracts partial information about the observable. The conventional way of describing such a process is to construct a stochastic master equation [61, 81, 93, 118] which can also cope with mixed initial states, inefficient detections and the presence of unmeasured couplings to the environment, i.e. thermal noise. This concept is briefly reviewed in Sec. 5.6.1. Note that the following discussion is restricted to initial Gaussian states. It was shown in Ref. [100] that the conditional state remains Gaussian under the usual stochastic master equation considered here. In general a Gaussian state is completely characterized by its first- and second-order moments. The mean values, i.e. the first-order moments, change in a random way determined by the stochastic variables. During measurement, a certain trajectory (cf. Fig. 5.1) of the measured observable is mapped out and the system is conditioned upon this information. The second-order moments depend on the measurement time and the initial state, while they are independent

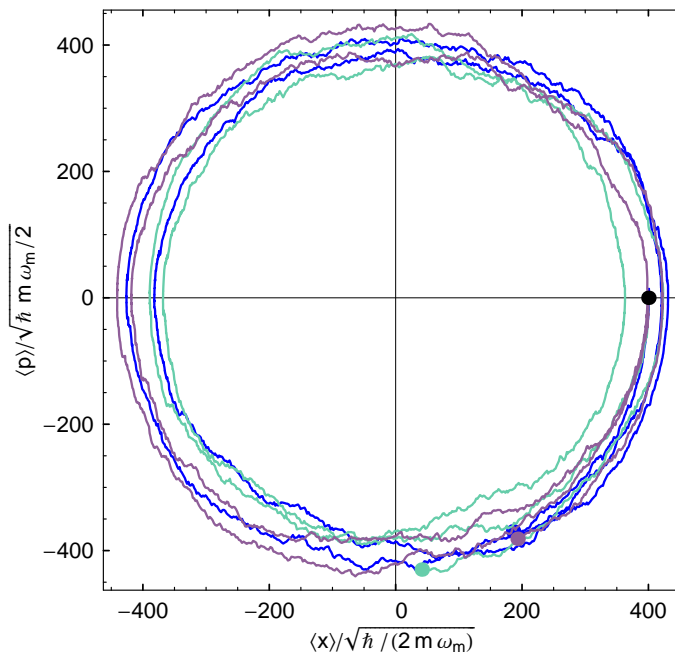


Figure 5.1.: Simulation of three random walks of a suspended mirror undergoing a continuous conditional position measurement. The measurement is realized by shining a laser beam onto the mirror and detecting the phase quadrature of the reflected light. Each point in phase space corresponds to a particular normalized position and momentum of the mirror. Parameters: measurement strength $\Omega_q = 2\pi \cdot 30$ Hz, mechanical eigenfrequency $\omega_m = 2\pi \cdot 1$ Hz. Duration of measurement: 2.2 sec. Black dot marks common starting point in phase space. No classical noise is taken into account.

of the actual trajectory. They approach their steady state values, which are independent of the initial purity of the system.

If one is only interested in steady state second-order moments, a much simpler approach can be used. Introducing the Wiener filtering method [167] in the context of quantum systems allows us to determine the conditional steady states directly from the experimentally accessible spectral densities [48]. This concept is presented in detail in Sec. 5.6.2 and is primarily used in this chapter.

5.6.1. Stochastic master equation

The stochastic master equation is a set of stochastic differential equations that simulates the joint evolution of the system's conditional density matrix $\hat{\rho}$ and measurement output $\hat{y}(t)$. The concept was successfully applied to various configurations, including simple two level systems [83] and nanomechanical resonators [61, 93]. In the latter case a single-electron transistor [85, 111, 143] continuously monitored the resonator's position. In this section we re-derive the stochastic master equation for a different experimental set-up, namely the position of a single suspended mirror should be tracked by using a laser beam. The light constitutes an auxiliary Markovian measurement system (one that has uncorrelated measurement noise at different times and constant measurement strength) which interacts unitarily with the probe, i.e. the suspended mirror. Therefore the elec-

tromagnetic field becomes entangled with the probe and we can consecutively perform a projective measurement by employing a homodyne detector. The intrinsic relation between the probe and the auxiliary detection scheme is discussed in detail by Jacobs et al. in Ref. [101], where they pointed out that a chain of quantum measurement devices does not affect the treatment in terms of the stochastic master equation fundamentally.

In order to develop a theoretical formulation, we divide the whole observation period into short time intervals of length Δt . Each time a measurement record is generated which is proportional to the output field's phase quadrature \hat{y} (Eq. (5.2) with $\zeta = 0$) integrated over Δt , i.e.

$$\hat{B} \equiv \int_t^{t+\Delta t} \hat{y}(t') dt'. \quad (5.51)$$

It can be verified easily that

$$\langle \hat{B} \rangle = \frac{\alpha}{\hbar} \langle \hat{x} \rangle \Delta t \quad \text{and} \quad \langle \hat{B}^2 \rangle = \frac{1}{2} \Delta t + \mathcal{O}(\Delta t^2), \quad (5.52)$$

where we adopted the notation introduced in Sec. 5.2.1. From this we can infer that the position of the mirror is determined with an accuracy of

$$\langle (\Delta \hat{x})^2 \rangle = \frac{1}{2} \frac{\hbar^2}{\alpha^2} \frac{1}{\Delta t}. \quad (5.53)$$

Now we need to construct an appropriate projection operator which describes such a measurement. Remember that the position operator \hat{x} has a continuous spectrum of eigenvalues x corresponding to eigenstates $|x\rangle$. But we cannot project onto a single eigenstate as in our simple example, since we have only gained partial knowledge by the measurement. Hence the measurement needs to be described by a sum of Gaussian weighted projection operators onto eigenstates of \hat{x} :

$$\hat{P}(\tilde{x}) = \left(\frac{1}{\sqrt{\langle (\Delta \hat{x})^2 \rangle} \sqrt{2\pi}} \right)^{1/2} \int_{-\infty}^{+\infty} dx \exp \left[-\frac{1}{4} \left(\frac{x - \tilde{x}}{\sqrt{\langle (\Delta \hat{x})^2 \rangle}} \right)^2 \right] |x\rangle \langle x| \quad (5.54)$$

$$= \left(\frac{\alpha}{\hbar} \sqrt{\Delta t / \pi} \right)^{1/2} \exp \left[-\frac{1}{2} \frac{\alpha^2}{\hbar^2} \Delta t (\hat{x} - \tilde{x})^2 \right], \quad (5.55)$$

where the continuous variable \tilde{x} corresponds to the result of the single measurement. The operator \hat{P} is widely known as the Krauss projection operator (cf. e.g. Ref. [101]). It projects the joint probe-system quantum state into the sub-space in which the readout observable has definite values of $\hat{y} = y(t') \propto \tilde{x}(t')$, $0 < t' < t$. It is obvious that increasing the measurement strength α shrinks the width of the Gaussian distribution. Engineering a more precise measurement apparatus confines the mirror within a smaller region around its mean position. For an infinite measurement strength the associated operator $\hat{F}(\tilde{x}) = \hat{P}(\tilde{x})\hat{P}(\tilde{x})$ even becomes a delta function.

The measurement result \tilde{x} can be regarded as a stochastic quantity, i.e.

$$\tilde{x} = \langle \hat{x} \rangle + \frac{\hbar}{\sqrt{2\alpha}\Delta t} \Delta W, \quad (5.56)$$

where $\Delta W = W(t + \Delta t) - W(t)$ is the Wiener increment (cf. eg. Ref. [149]). It is a random variable with zero mean, variance Δt and it is normally distributed. Now we

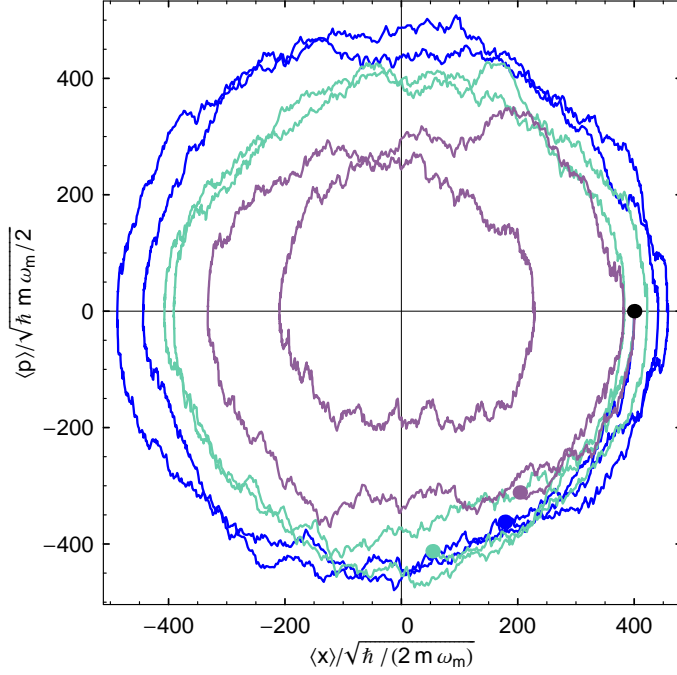


Figure 5.2.: Simulation of three random walks for parameters as in Fig. 5.1, but additionally force noise is taken into account with $\Omega_F = 2\pi \cdot 40$ Hz.

expand the projection operator \hat{P} in terms of Δt and take the limit $\Delta t \rightarrow 0$, i.e. we set $\Delta t = dt$, $\Delta W = dW$ and $(\Delta W)^2 = dt$, where the latter relation follows from the Itô calculus rules. Then the expansion up to first order in dt reads:

$$\hat{P} \propto 1 + \frac{\alpha^2}{2\hbar^2} \left(2\langle \hat{x} \rangle \hat{x} - \frac{1}{2} \hat{x}^2 \right) dt + \frac{\alpha}{\sqrt{2\hbar}} \hat{x} dW. \quad (5.57)$$

Now we can apply this projection operator to the initial density matrix $\hat{\rho}$ of the probe system – just as in the simple example – and obtain

$$\hat{\rho}(t + dt) \propto \hat{P} \hat{\rho}(t) \hat{P} \quad (5.58)$$

$$\propto \hat{\rho}(t) - \frac{\alpha^2}{2\hbar^2} \left(2\langle \hat{x} \rangle \{ \hat{x}, \hat{\rho}(t) \}_+ - \frac{1}{2} \{ \hat{x}^2, \hat{\rho}(t) \}_+ \right) dt - \frac{\alpha}{\sqrt{2\hbar}} \{ \hat{x}, \hat{\rho}(t) \}_+ dW. \quad (5.59)$$

Normalizing the density operator and expanding it in powers of dt yields the stochastic master equation in its Itô form for the conditional evolution of the probe's density operator:

$$\hat{\rho}(t + dt) = \hat{\rho}(t) + \frac{\alpha^2}{4\hbar^2} [\hat{x}, [\hat{x}, \hat{\rho}(t)]] dt - \frac{\alpha}{\sqrt{2\hbar}} (\{ \hat{x}, \hat{\rho}(t) \}_+ - 2\langle \hat{x} \rangle \hat{\rho}(t)) dW, \quad (5.60)$$

which agrees with Eq. (2.1) in Ref. [61], apart from the definition of measurement strength α . We can interpret the terms constituting the stochastic differential equation as follows: the second term in Eq. (5.60) accounts for the backaction of the measurement, while the last represents the information obtained by the measurement. More precisely, the Wiener

increment dW describes a stochastic process that simultaneously drives the conditional quantum state and the measurement data – both of which are stochastic processes. Different realizations of dW correspond to different possible scenarios that could take place in reality. Note that the backaction term occurs even if one disregards the measurement record.

We can easily extend the stochastic master equation: first we take the probe's free evolution into account, which gives rise to the additional term $-\frac{i}{\hbar}[\hat{H}_{\mathcal{P}}, \hat{\rho}]$. A white force noise acting on the mirror disturbs the measurement in almost the same manner as the unavoidable backaction. Consequently we can include such a noise source by inserting the term $S_F/(4\hbar^2)[\hat{x}, [\hat{x}, \hat{\rho}(t)]]dt$. The presence of sensing noise can be incorporated into the formalism by modifying Eq. (5.56) appropriately:

$$\tilde{x} = \langle \hat{x} \rangle + \sqrt{1 + \alpha^2 S_{\xi_x}/\hbar^2} \frac{\hbar}{\sqrt{2}\alpha\Delta t} \Delta W. \quad (5.61)$$

This is due to the fact that sensing noise and shot noise affect the measurement in a similar way. The total stochastic master equation therefore reads:

$$\begin{aligned} \hat{\rho}(t + dt) = & \hat{\rho}(t) - \frac{i}{\hbar}[\hat{H}_{\mathcal{P}}, \hat{\rho}] + \frac{\alpha^2}{4\hbar^2}[\hat{x}, [\hat{x}, \hat{\rho}(t)]]dt + \frac{S_{\xi_F}}{4\hbar^2}[\hat{x}, [\hat{x}, \hat{\rho}(t)]]dt \\ & - \frac{\alpha}{\sqrt{2}\hbar} \frac{1}{\sqrt{1 + \alpha^2 S_{\xi_x}/\hbar^2}} (\{\hat{x}, \hat{\rho}(t)\}_+ - 2\langle \hat{x} \rangle \hat{\rho}(t)) dW. \end{aligned} \quad (5.62)$$

The probe's Hamiltonian is given by

$$\hat{H}_{\mathcal{P}} = \frac{\hat{p}^2}{2m} + \frac{1}{2}m\omega_m^2 \hat{x}^2, \quad (5.63)$$

which describes a mirror with mass m and mechanical eigenfrequency ω_m . We can infer from Eq. (5.62) that increasing the sensing noise devaluates the measurement record. In the case of an infinite sensing noise level we end up with the unconditional evolution. If the force noise term dominates, the position of the mirror is randomized and one can only acquire information by increasing the measurement strength. Note that Eq. (5.62) allows us to study the full time evolution of the configuration we proposed in our Ref. [125].

By using $d\langle \hat{O} \rangle = \text{tr}(\hat{O}d\rho)$ with $d\rho = \hat{\rho}(t + dt) - \hat{\rho}(t)$, a stochastic differential equation can be derived for the first-order moments and a conventional one for the second-order moments. Their solution can be obtained as outlined in Ref. [61]. The solution of the stochastic differential equation is depicted in Figs. 5.1 and 5.2 which show that the suspended mirror undergoes a random walk in phase space. The second-order moments satisfy a Riccati matrix differential equation which can be solved with a standard method [139]. The solution is illustrated in Fig. 5.3, where the second-order moments approach a steady state in a time much shorter than an oscillator period. The expression for the second-order moments are cumbersome and therefore only the state's purity [cf. Eq. (5.27)] in the case of no classical noise is given explicitly:

$$U^2(t) = 1 + \frac{2(2c^2 - 1)(V_0^2 - 1)}{2V_0c^3 \sinh 2bt_m + (V_0^2 + 1)c^2 \cosh 2bt_m - (2c^2 - 1)(V_0^2 - 1) + (c^2 - 1)(V_0^2 + 1) \cos 2ct_m + 2bV_0 \sin 2ct_m} \quad (5.64)$$

with

$$t_m = \omega_m t, \quad b = \frac{1}{\sqrt{2}} \sqrt{\sqrt{1 + \frac{4}{r^2}} - 1}, \quad c = \frac{1}{\sqrt{2}} \sqrt{\sqrt{1 + \frac{4}{r^2}} + 1}, \quad r = \frac{2m\omega_m^2 \hbar}{\alpha^2}. \quad (5.65)$$

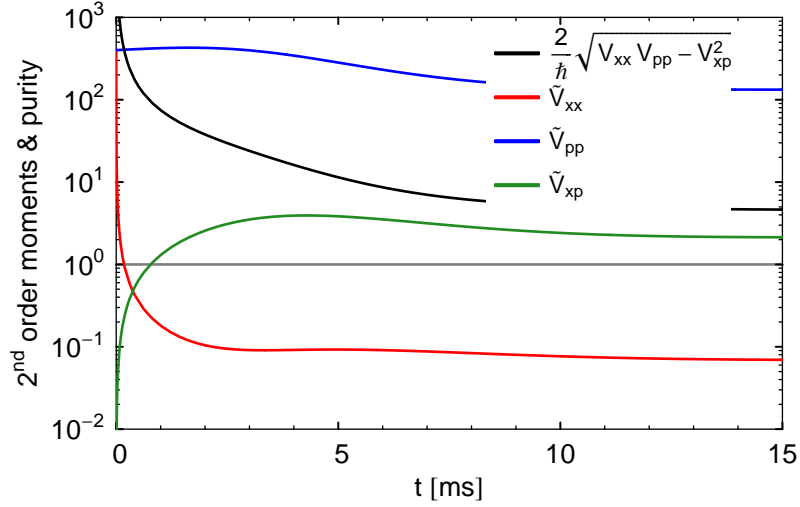


Figure 5.3.: Time evolution of second-order moments (normalized to the ground state of a harmonic oscillator) and purity for parameters as considered in Fig. 5.1. Quantum state progressively collapses due to the measurement.

From Eq. (5.64) one can infer that the system is close to a pure state when $t \gg 1/(2b\omega_m)$, regardless of the initial purity V_0 .

Fig. 5.4 shows the time evolution of both first-order moments. The oscillator's position reaches a squeezed state which gives rise to a relatively clean sinusoidal oscillation compared to the momentum which is anti-squeezed.

5.6.2. Quantum Wiener filter

If the measurement process has been started for a long enough time [much longer than the time constant of transients, cf. Eq. (5.65)], then the second-order moments are stationary. This can be accomplished within a time interval much shorter than a period of the mechanical oscillator under consideration. Therefore the evaluation of the steady state second-order moments is sufficient for various applications. These moments can either be obtained by means of the stochastic master equation or in a relatively simple way by employing the Wiener filter method [167] in the context of quantum systems [48]. This method is widely-used in engineering, where the evaluation of the conditional expectation value of a system variable, based on a stretch of data, is a common problem. This approach applies to stable linear systems with Gaussian noise.

In our case, the data are obtained by sensing a certain quadrature of the detector's output observable which is described by the Heisenberg operator $\hat{y}(t)$. The goal is to acquire information about the probe's observables \hat{x}_l with $l = 1, 2, \dots, n$, e.g. the position $\hat{x}(t)$ or momentum $\hat{p}(t) = m\partial_t\hat{x}(t)$. At any instant, values of $\langle\hat{x}_l\rangle$ are determined by measurement results in the past. This requires that the commutation relations

$$[\hat{y}(t), \hat{y}(t')] = 0 \quad \forall t, t' \quad \text{and} \quad (5.66)$$

$$[\hat{x}_l(t), \hat{y}(t')] = 0 \quad \forall t > t' \quad (5.67)$$

are satisfied. The first relation was already introduced in Eq. (2.133) and it ensures that any sample of data can be stored as a classical piece of data [37], which is indispensable

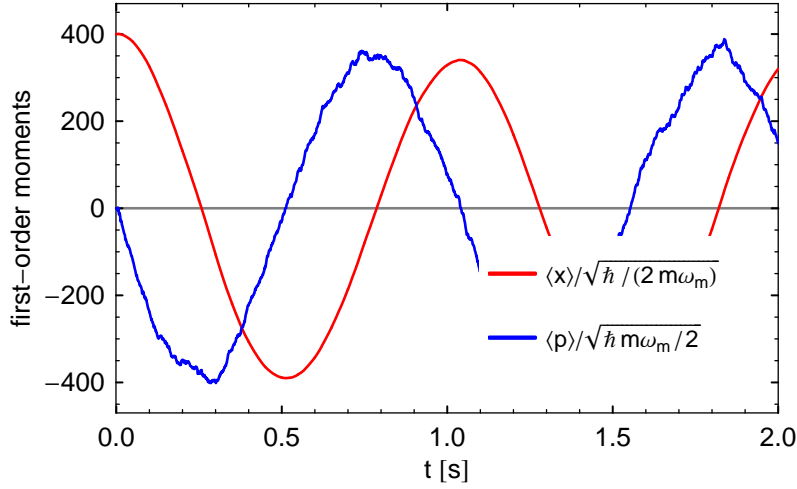


Figure 5.4.: Time evolution of first-order moments for parameters as considered in Fig. 5.1. The curve representing the momentum is less smooth, which is due to anti-squeezing as one can infer from Fig. 5.3.

for applying the Wiener filter method. The second relation has to be satisfied due to causality, i.e. the detector's output should not influence any future probe observable.

The following considerations are valid for arbitrary probe observables \hat{x}_l where we assume that all linear observables have a zero (unconditional) expectation value. Suppose we have recorded a certain set of data, namely $\mathcal{Y}(t) = \{y(t') : -\infty < t' < t\}$, and $\hat{x}_l(t+a)$ should be estimated. One has to distinguish between three different scenarios [133]: (i) $a = 0$ corresponds to the *filtering* problem where one wishes to estimate the current state of the probe observables based on historical data. (ii) $a > 0$ is related to the *prediction* problem where one is interested in estimating the state a time units in the future, by using $\mathcal{Y}(t)$. (iii) It is also possible to estimate past states of the probe's observables by choosing $a < 0$, which is called the *smoothing* problem. Here we are primarily interested in the filtering and prediction problem, which can be implemented in real-time since they are causal, while the soothing problem is essentially non-causal.

The probe observable \hat{x}_l can be decomposed at time $t + a$ in the following way:

$$\hat{x}_l(t+a) = \int_{-\infty}^t dt' K_l(t-t') \hat{y}(t') + \hat{R}_l(t), \quad (5.68)$$

where the first term accounts for the known part which can be extracted from the historical data, while the second term represents the estimation error. This error must be uncorrelated with the data used to generate the estimate, i.e.

$$\langle \hat{R}_l(t) \hat{y}(t') \rangle_{\text{sym}} = 0 \quad \forall t' \leq t \quad (5.69)$$

should be satisfied, which already provides the necessary and sufficient condition for the optimal filter function K_l . Plugging Eq. (5.68) into Eq. (5.69) yields

$$Q_{x_l y}(t+a-t'') - \int_{-\infty}^t dt' K_l(t-t') Q_{y y}(t'-t'') = 0, \quad \forall t'' \leq t, \quad (5.70)$$

where the first-order correlation function introduced in Eq. (2.154) has been used. Remember that the first-order correlation function is the Fourier transform of the corresponding noise spectral density [cf. Eq. (2.155)]. We can rewrite Eq. (5.70) in the following way:

$$Q_{xly}(\tau + a) - \int_{-\infty}^{\infty} d\tau' K_l(\tau') Q_{yy}(\tau - \tau') = 0, \quad \forall \tau \geq 0, \quad (5.71)$$

where we have used $K_l(\tau') = 0$ for $\tau' < 0$, which is required by causality. This integral equation is the continuous-time version of the Wiener-Hopf equation, which in turn is a Fredholm equation of the first kind. In the case of a white-noise process exhibiting a constant spectral density, i.e. $S_{yy}(\Omega) = 1$ or equivalently $Q_{yy}(\tau - \tau') = \delta(\tau - \tau')/2$, this can easily be solved:

$$Q_{xly}(\tau + a) = \int_{-\infty}^{\infty} d\tau' K_l(\tau') \delta(\tau - \tau')/2 = K_l(\tau)/2, \quad \forall \tau \geq 0, \quad (5.72)$$

and therefore

$$K_l(\tau) = \begin{cases} 2Q_{xly}(\tau + a) & \tau \geq 0 \\ 0 & \tau < 0. \end{cases} \quad (5.73)$$

By using the definition of the single-sided noise spectral density given in Eq. (2.155), one obtains for the Fourier transform of Eq. (5.73) the expression

$$\tilde{K}_l(\Omega) = [S_{xly}(\Omega)e^{-i\Omega a}]_+, \quad (5.74)$$

where we introduced the notation $[F(\Omega)]_+$. This stands for taking the component of the function $F(\Omega)$ whose inverse Fourier transform has only support for positive times. Operationally, this could be obtained by either decomposing $F(\Omega)$ into

$$F(\Omega) = \sum_k \frac{\alpha_k}{\Omega - \Omega_k} \quad (5.75)$$

and only keeping terms with $\Im[\Omega_k] < 0$, or by switching to the time domain, eliminating the positive-time components of $F(t)$ and returning to the Fourier domain. Both approaches will become ambiguous when $F(\Omega)$ does not approach zero for $\Omega \rightarrow \infty$.

The Wiener filter in the case of colored noise can be obtained by "pre-whitening" the observed data and then applying the trivial Wiener filter given in Eq. (5.74) to the whitened data. We assume that the outgoing field has a spectral density $S_{yy}(\Omega)$, which can be written as

$$S_{yy}(\Omega) = \phi_{yy}^+(\Omega)\phi_{yy}^-(\Omega), \quad (5.76)$$

where $\phi_{yy}^+(\Omega)$ has only poles and zeros in the lower half complex plane, while $\phi_{yy}^-(\Omega)$ has only poles and zeros in the upper-half complex plane, i.e. the spectral density can be so factorized that

$$\phi_{yy}^+(\Omega) = \frac{\prod_{i=1}^m (\Omega - z_i)}{\prod_{i=1}^n (\Omega - p_i)} \quad \text{and} \quad \phi_{yy}^-(\Omega) = \phi_{yy}^+(-\Omega) = [\phi_{yy}^+(\Omega)]^*, \quad (5.77)$$

where $\{z_i\}$ ($\{p_i\}$) are the zeros (poles) of $S_{yy}(\Omega)$ in the lower half complex plane. Functions that have both, poles and zeros, exclusively in the lower half complex plane can

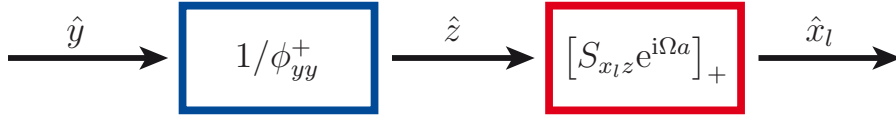


Figure 5.5.: Cascaded filtering process: output observable \hat{y} is transformed into a white noise process \hat{z} without loss of information. Then the Wiener filter is applied to \hat{z} in order to obtain an optimal estimate for \hat{x}_l .

be regarded as transfer functions of causal systems, which also exhibit an inverse causal transfer function given by $1/\phi_{yy}^+(\Omega)$. Therefore we can define

$$\hat{z}(\Omega) \equiv \hat{y}(\Omega)/\phi_{yy}^+(\Omega), \quad (5.78)$$

which contains exactly the same information as \hat{y} due to the causality of $\phi_{yy}^+(\Omega)$. It can be easily verified that

$$S_{zz}(\Omega) = 1, \quad (5.79)$$

which means that \hat{z} contains independent information at different times, i.e. it describes a white noise process. Hence the solution given in Eq. (5.73) applies directly. The cascaded filtering process is depicted in Fig. 5.5 where the outgoing field first passes the whitening filter and then the trivial Wiener filter given in Eq. (5.74). Mathematically, this can be formulated in the following way

$$\tilde{K}_l(\Omega) = \frac{1}{\phi_{yy}^+(\Omega)} [S_{x_l z}(\Omega)e^{-i\Omega a}]_+ = \frac{1}{\phi_{yy}^+(\Omega)} \left[\frac{S_{x_l y}(\Omega)e^{-i\Omega a}}{\phi_{yy}^-(\Omega)} \right]_+, \quad (5.80)$$

and Fourier transform of this combined filter function can be written as

$$K_l(t) = \int_{-\infty}^{\infty} \frac{d\Omega}{2\pi} \frac{1}{\phi_{yy}^+(\Omega)} \left[\frac{S_{x_l y}(\Omega)e^{-i\Omega a}}{\phi_{yy}^-(\Omega)} \right]_+ e^{-i\Omega t}. \quad (5.81)$$

Finally the conditional first-order moments are given by

$$\langle \hat{x}_l(t+a) \rangle_c = \int_{-\infty}^0 dt' K_l(t-t') \hat{y}(t'), \quad (5.82)$$

while we obtain for the second-order moments:

$$\begin{aligned} V_{lm}^c[a] &= \langle \hat{R}_l(t) \hat{R}_m(t) \rangle_{\text{sym}} \quad (5.83) \\ &= \left\langle \left[\hat{x}_l(t+a) - \int_{-\infty}^t dt' K_l(t-t') \hat{y}(t') \right] \left[\hat{x}_m(t+a) - \int_{-\infty}^t dt' K_m(t-t') \hat{y}(t') \right] \right\rangle_{\text{sym}} \\ &= \int_0^{\infty} \frac{d\Omega}{2\pi} \Re \left[S_{x_l x_m}(\Omega) - \left[\frac{S_{x_l y}(\Omega)e^{-i\Omega a}}{\phi_{yy}^-(\Omega)} \right]_+ \left[\frac{S_{x_m y}(\Omega)e^{-i\Omega a}}{\phi_{yy}^-(\Omega)} \right]_+^* \right] \\ &= V_{lm}^{\text{uc}} - \frac{1}{2} \int_0^{\infty} dt G_{x_l}(t) G_{x_m}(t) + \frac{1}{2} \int_0^a dt G_{x_l}(t) G_{x_m}(t) \\ &= V_{lm}^c[0] + \frac{1}{2} \int_0^a dt G_{x_l}(t) G_{x_m}(t), \quad (5.84) \end{aligned}$$

where V_{lm}^{uc} accounts for the unconditional variance which was already introduced in Eq. (2.159) and the function G_{x_l} is given by

$$G_{x_l}(\Omega) \equiv \left[\frac{S_{xly}(\Omega)}{\phi_{yy}^-(\Omega)} \right]_+ \quad (5.85)$$

One can infer from Eq. (5.84) that the conditional variance in the case of $a = 0$, i.e. $V_{lm}^c[0]$, is always lower than the unconditional. Furthermore it can be deduced that the predicted variance increases to the distant future, which is also quite intuitive.

Two-Channel wiener filter

In the previous section the Wiener filtering method in the case of a single output channel was derived. But some measurement devices, e.g. a double optical spring set-up (cf. Sec. 4.3), provide two output channels (\hat{y}_1 and \hat{y}_2) giving information about the same probe observables. There exists an extended Wiener filter which takes both measurement outputs into account in order to obtain an optimal estimate for these observables. The derivation of this procedure can be accomplished by recapitulating each step of the previous derivation for vector-valued functions. The modus operandi is outlined in the following: we combine the probe observables into a vector $\hat{\mathbf{x}}^T(t) = (\hat{x}_1, \dots, \hat{x}_n)$, whose decomposition can be written as

$$\hat{\mathbf{x}}(t+a) = \int_{-\infty}^t dt' \mathbf{K}(t-t') \cdot \hat{\mathbf{y}}(t') + \hat{\mathbf{R}}(t), \quad (5.86)$$

where the measurement outputs are represented by the vector $\hat{\mathbf{y}}^T(t) = (\hat{y}_1(t), \hat{y}_2(t))$. Each component accounts for a certain quadrature of an individual output field. The vector $\hat{\mathbf{R}}(t)$ has n components and it denotes the estimation-error. Again we must require that the error is perpendicular to the data used to generate the estimate, i.e.

$$\langle \hat{\mathbf{R}}(t) \cdot \hat{\mathbf{y}}^T(t') \rangle_{\text{sym}} = 0 \quad \forall t' \leq t. \quad (5.87)$$

Defining the first-order correlation function as $\mathbf{Q}_{ab}(t-t') = \langle \hat{\mathbf{a}}(t) \cdot \hat{\mathbf{b}}^T(t') \rangle_{\text{sym}}$ allows us to rewrite the Wiener-Hopf equation in the following way:

$$\mathbf{Q}_{xy}(\tau+a) - \int_{-\infty}^{\infty} d\tau' \mathbf{K}(\tau') \cdot \mathbf{Q}_{yy}(\tau-\tau') = 0, \quad \forall \tau \geq 0. \quad (5.88)$$

Solving the equation for a trivial white noise process and then applying the result to a pre-whitened output vector $\hat{\mathbf{y}}$ reveals for the optimal filter function:

$$\tilde{\mathbf{K}}(\Omega) = [e^{-i\Omega a} \mathbf{S}_{xy}(\Omega) \cdot (\phi_{yy}^-(\Omega))^{-1}]_+ \cdot (\phi_{yy}^+(\Omega))^{-1}, \quad (5.89)$$

which requires the factorization of the spectral density matrix:

$$\mathbf{S}_{yy}(\Omega) = \phi_{yy}^+(\Omega) \cdot \phi_{yy}^-(\Omega). \quad (5.90)$$

An appropriate general factoring procedure for rational matrices is presented in Ref. [59]. Note that the matrix elements of $\phi_{yy}^+(\Omega)$ and $(\phi_{yy}^+(\Omega))^{-1}$ should be analytic in the upper half complex plane while those of $\phi_{yy}^-(\Omega)$ and $(\phi_{yy}^-(\Omega))^{-1}$ should be analytic in the lower

half complex plane and the notation $[\dots]_+$ stands for taking the component of each matrix element whose inverse Fourier transform has only support for positive times. Finally one obtains

$$\begin{aligned} \mathbf{V}^c[a] &= \int_0^\infty \frac{d\Omega}{2\pi} \left[\mathbf{S}_{xx}(\Omega) - [e^{-i\Omega a} \mathbf{S}_{xy}(\Omega) \cdot (\phi_{yy}^-(\Omega))^{-1}]_+ \cdot [e^{-i\Omega a} \mathbf{S}_{xy}(\Omega) \cdot (\phi_{yy}^-(\Omega))^{-1}]_+^\dagger \right] \\ &= \mathbf{V}^{\text{uc}} - \frac{1}{2} \int_0^\infty dt \mathbf{G}_{xy}(t) \cdot \mathbf{G}_{xy}^T(t) + \frac{1}{2} \int_0^a dt \mathbf{G}_{xy}(t) \cdot \mathbf{G}_{xy}^T(t) \\ &= \mathbf{V}^c[0] + \frac{1}{2} \int_0^a dt \mathbf{G}_{xy}(t) \cdot \mathbf{G}_{xy}^T(t), \end{aligned} \quad (5.91)$$

with

$$\mathbf{G}_{xy}(\Omega) \equiv [\mathbf{S}_{xy}(\Omega) \cdot (\phi_{yy}^-(\Omega))^{-1}]_+. \quad (5.92)$$

5.6.3. State preparation in presence of Markovian noise

In this section we specialize to Markovian measurement systems, i.e. systems comprising only Gaussian white noise, which allows an analytical derivation of the conditional second-order moments.

A general Markovian quantum measurement on a harmonic oscillator can be written in the following way:

$$\hat{\mathcal{O}}(\Omega) = \hat{\mathcal{Z}}(\Omega) + \hat{x}(\Omega), \quad \hat{x}(\Omega) = R_{xx}(\Omega) \hat{\mathcal{F}}(\Omega), \quad (5.93)$$

where $\hat{\mathcal{O}}$ is the outgoing field. The form of Eq. (5.93) is consistent with Eq. (2.150) where a non-Markovian measurement has been considered, since the dynamics of finite bandwidth arm-cavities were taken into account. The real and constant (cross-) spectral densities S_{ZZ} , S_{ZF} and S_{FF} characterize $\hat{\mathcal{F}}$ and $\hat{\mathcal{Z}}$ and they are constrained by the Heisenberg uncertainty relation [27]:

$$\sqrt{S_{ZZ} S_{FF} - S_{ZF}^2} \equiv (1 + \mu)^{1/2} \hbar \geq \hbar. \quad (5.94)$$

It can easily be verified that the explicit expressions given in Eq. (5.4) are already sufficient for spanning all possible regimes of Markovian quantum measurements. If the measurement strength and homodyne detection angle are variable (but frequency independent), it is not possible to improve the second-order moments further by e.g. the injection of frequency-independent squeezed light. Nevertheless this last method might be eligible due to the practical convenience of lowering the circulating or pumping power.

By assuming $\omega_m \gg \gamma_m$, the noise spectral density of the output observable $\hat{\mathcal{O}}$ can be written as

$$\begin{aligned} S_{\mathcal{O}\mathcal{O}} &= S_{ZZ} + 2\Re[R_{xx}] S_{ZF} + S_{FF} |R_{xx}|^2 \\ &= S_{ZZ} Q Q^* / (P P^*) \end{aligned} \quad (5.95)$$

with $P \equiv -1/R_{xx}$ and $Q Q^* \equiv m^2(\Omega^4 - 2A\omega_m^2\Omega^2 + B^2\omega_m^4)$ and

$$A \equiv 1 + \frac{1}{m\omega_m^2} \frac{S_{ZF}}{S_{ZZ}}, \quad B^2 \equiv 1 + \frac{2}{m\omega_m^2} \frac{S_{ZF}}{S_{ZZ}} + \frac{1}{m^2\omega_m^4} \frac{S_{FF}}{S_{ZZ}}. \quad (5.96)$$

Furthermore one obtains

$$S_{xx} = S_{\mathcal{FF}}/(PP^*), \quad S_{x\mathcal{O}} = (S_{\mathcal{FF}} - P^*S_{\mathcal{ZF}})/(PP^*). \quad (5.97)$$

In calculating the conditional states it is crucial to spectral factorize $S_{\mathcal{OO}}$. However, in this case it can be easily accomplished by using Eq. (5.95) since the zeros of $S_{\mathcal{OO}}$ are simply given by $\sqrt{m}\omega_m(\pm\sqrt{(A+B)/2} \pm i\sqrt{(-A+B)/2})$ and the poles can be read off Eq. (2.118). Hence it is straightforward to determine the conditional covariance matrix in terms of (A, B, μ) by means of the formalism introduced in Sec. 5.6.2. We use $\hat{p} = -im\Omega\hat{x}$ and obtain:

$$\mathbf{V} \equiv \begin{pmatrix} V_{xx}^c & V_{xp}^c \\ V_{xp}^c & V_{pp}^c \end{pmatrix} = \frac{\hbar(1+\mu)^{1/2}}{2} \begin{pmatrix} \frac{1}{m\omega_m} \sqrt{\frac{2}{B+A}} & \sqrt{\frac{B-A}{B+A}} \\ \sqrt{\frac{B-A}{B+A}} & m\omega_m \sqrt{\frac{2B^2}{B+A}} \end{pmatrix}. \quad (5.98)$$

The conditional purity is given by

$$U = \frac{2}{\hbar} \sqrt{\det(\mathbf{V})} = (1+\mu)^{1/2}, \quad (5.99)$$

which is identical to the "purity" of the measurement process [cf. Eq. (5.94)], except for a factor of 1/2. Note that they exactly coincide when switching to double-sided noise spectral densities. In the absence of classical noise ($\mu = 0$), the conditional quantum state of the oscillator is always pure.

5.7. Classical control

5.7.1. Conditioning and feedback control

Complex optical configurations, such as detuned SR interferometers, can exhibit instabilities which have to be cured by an appropriate feedback control system (cf. also Chap. 4). It was shown in Ref. [37] that the instabilities can be suppressed without altering the noise curves of the uncontrolled configuration. Since the Wiener filtering method only applies to stable systems, one has to ensure that the conditional second-order moments also do not depend on a certain realization of the feedback system. It is intuitive that applying a noise-free classical controller does not change the conditional variances from the uncontrolled case. Feeding back known information into a known system should not affect fluctuations that are independent of one's knowledge, i.e. $\hat{R}(t)$ [cf. Eq. (5.68)].

5.7.2. Controlled states

The implementation of a feedback control system can also be motivated by the following issue: as discussed in Sec. 5.6.1, the conditional first-order moments (e.g. $\langle \hat{x} \rangle_c$ and $\langle \hat{p} \rangle_c$) are stochastic, i.e. they undergo a random walk – although the second-order moments converge to constants at a rate depending on the measurement strength and on the system dynamics. For many applications it is desirable to prepare a stationary quantum state with fixed first-order moments. This can be accomplished by collecting information via a continuous measurement which is fed back in real time in order to modify the system's Hamiltonian and obtain the desired behavior. The question arises whether an appropriate realization of a feedback control system is able to fix the first-order moments while

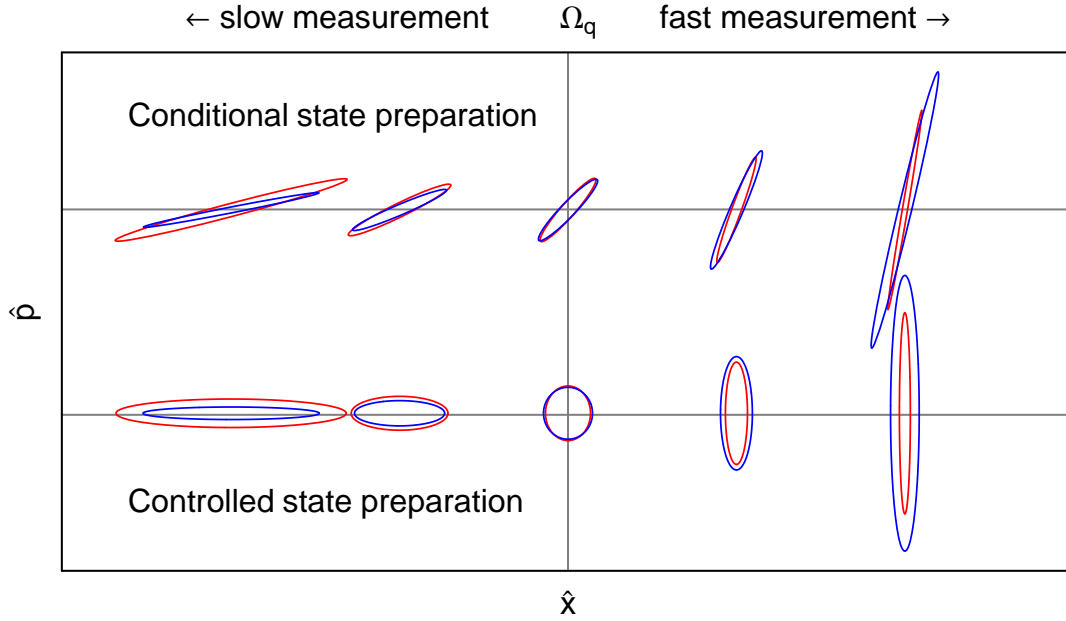


Figure 5.6.: Squeezing ellipses of mechanical degree of freedom for different touching frequencies Ω_q of the quantum noise spectral density (cf. also Fig. 5.19). The blue (red) ellipses are generated in the presence of white sensing (force) noise. The two central ellipses corresponds to a touching frequency of $\sqrt{\Omega_x \Omega_F}$ [cf. Eq. (5.6)]. For this frequency the total classical noise is minimal and the purity of the quantum state is optimal (cf. Fig. 5.21). The cross correlations vanish in the case of a controlled system (lower series) and hence the ellipses can only assume two perpendicular orientations.

maintaining the conditional second-order moments. Unfortunately this can be ruled out right from the beginning because of the following argument: measuring the unconditional variances of the controlled system would result in $V_{xp}^{\text{ctrl}} = 0$, which would require that $V_{xx}^{\text{ctrl}} V_{pp}^{\text{ctrl}} < V_{xx}^c V_{pp}^c$ in order to at least maintain the purity of the state. But this is impossible, since it was shown in Sec. 5.6.2 that V_{xx}^c and V_{pp}^c are already optimal. It follows that the controlled state always differs from a pure state, unless $V_{xp}^c = 0$, even in the absence of classical noise. Nevertheless a slightly unconventional measurement strategy (frequency-independent input squeezing or homodyne detection at a non-phase quadrature) still allows the controlled states to approach a minimum Heisenberg uncertainty state [58].

Only a unique controller can make the most of the situation and minimize the quantum state's purity. This general optimal control kernel K_{ctrl} is derived in the following. The closed-loop position and momentum of the oscillator read

$$\hat{x}_{\text{ctrl}}(\Omega) = \hat{x}_0(\Omega) - K_{\text{ctrl}}(\Omega)\hat{y}_0(\Omega), \quad \hat{p}_{\text{ctrl}}(\Omega) = \hat{p}_0(\Omega) + im\Omega K_{\text{ctrl}}(\Omega)\hat{y}_0(\Omega), \quad (5.100)$$

where \hat{x}_0 and \hat{p}_0 are the corresponding open-loop quantities and \hat{y}_0 is the open-loop outgoing field that we measure. The closed-loop dynamics are stable and the feedback control is proper if and only if K_{ctrl} is causal (i.e. no poles in the upper-half complex plane occur) and $\lim_{\Omega \rightarrow \infty} \Omega K_{\text{ctrl}}(\Omega) = 0$ (which, together with causality, implies $K_{\text{ctrl}}(t = 0) = 0$ in the time domain). In order to relate the controlled with the conditioned second-order

moments, we switch to the time domain and replace \hat{x}_0 and \hat{p}_0 in Eq. (5.100) with the decomposition introduced in Eq. (5.68). A straightforward calculation reveals that

$$V_{xx}^{\text{ctrl}} = V_{xx}^c + \Delta_x \quad \text{and} \quad V_{pp}^{\text{ctrl}} = V_{pp}^c + \Delta_p, \quad (5.101)$$

with

$$\begin{bmatrix} \Delta_x \\ \Delta_p \end{bmatrix} \equiv \frac{1}{2} \int_0^{+\infty} dt \begin{bmatrix} [G_x(t) - f(t)]^2 \\ [G_p(t) - mf(t)]^2 \end{bmatrix} \quad \text{and} \quad f(t) \equiv \int_0^t \phi_+(t-t') K_{\text{ctrl}}(t') dt'. \quad (5.102)$$

Here we have used $G_p(t) = m\dot{G}_x(t)$ (for $t > 0$), which implies that $V_{xp}^c = mG_x^2(t=0)/4 > 0$. Due to the fact that cross-correlations vanish ($V_{xp}^{\text{ctrl}} = 0$), we only have to minimize $(V_{xx}^{\text{ctrl}} V_{pp}^{\text{ctrl}})^{1/2}$ over all f with the constraint that $f(t=0) = 0$. Here one might wonder about setting $\Delta_x = \Delta_p = 0$ by choosing $f(t) = G_x(t)$, since $G_p(t) = m\dot{G}_x(t)$. However, this is not possible unless $G_x(t=0) = 0$, because we have required $f(t=0) = 0$ – which is essential, because otherwise we would have a term $\delta_+(t)f(t=0)$ added to $\dot{f}(t)$ in the definition of Δ_p , which would make Δ_p infinite. Keeping this condition at the back of our mind, we obtain

$$\hbar U_{\text{opt}}/2 \equiv \min_f \sqrt{V_{xx}^{\text{ctrl}} V_{pp}^{\text{ctrl}}} = \sqrt{V_{xx}^c V_{pp}^c + V_{xp}^c}, \quad (5.103)$$

which is achievable by a unique controller with

$$\phi_+(\Omega) K_{\text{ctrl}}(\Omega) = G_x(\Omega) - G_x(t=0)/(\rho - i\Omega), \quad \rho = \sqrt{V_{pp}^c/(m^2 V_{xx}^c)}. \quad (5.104)$$

Then the second-order moments are given by

$$\mathbf{V}^{\text{ctrl}} \equiv \begin{pmatrix} V_{xx}^{\text{ctrl}} & V_{xp}^{\text{ctrl}} \\ V_{xp}^{\text{ctrl}} & V_{pp}^{\text{ctrl}} \end{pmatrix} = \begin{pmatrix} V_{xx}^c + V_{xp}^c/\sqrt{V_{pp}^c/V_{xx}^c} & 0 \\ 0 & V_{pp}^c + V_{xp}^c\sqrt{V_{pp}^c/V_{xx}^c} \end{pmatrix}. \quad (5.105)$$

5.8. State Preparation in presence of non-Markovian noise

In Sec. 5.6.3 we found that the conditional second-order moments associated with the macroscopic object under consideration can be obtained analytically in the case of a general Markovian measurement process. In fact, for realistic systems with multiple colored noise sources and non-Markovian dynamics (e.g., finite-bandwidth cavities), it is no longer possible to derive such compact analytic expressions for the conditional covariance matrix. This is mainly due to the fact that no general solution exists for the roots of polynomials of degree five or higher, as stated by the Abel-Ruffini theorem. Fortunately, the derivation of the quantum Wiener filter in Sec. 5.6.2 already provides a recipe for the implementation of a numerical routine (cf. App. A). Such a simulation tool allows us to extend our investigations to various systems including current and future gravitational wave detectors and planned small scale experimental set-ups. At the end of this section an example configuration is discussed in detail.

In the special case of a tuned cavity without classical noise there still exists a general analytic solution for the second-order moments which can be obtained by employing complex analysis. Such a model configuration provides some interesting insight into the behavior of finite-bandwidth systems.

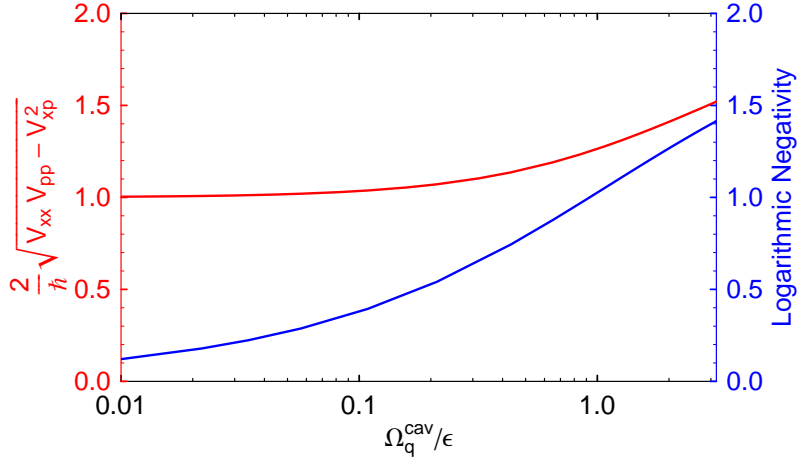


Figure 5.7.: Purity of test mass's quantum state (red line) compared to entanglement between test mass and cavity mode (blue line), both versus the dimensionless ratio $\Omega_q^{\text{cav}}/\epsilon$. Since the free mass limit, i.e. $\omega_m = 0$, is considered here, the purity and entanglement only depend upon this ratio, as one can infer from Eq. (5.108). The cavity mode's purity exactly agrees with that of the test mass. No classical noise is taken into account and the phase quadrature is detected. Note that the uncertainty as well as the logarithmic negativity do not diverge: $\Omega_q^{\text{cav}}/\epsilon \rightarrow \infty \Rightarrow U \rightarrow 1 + \sqrt{2}$

5.8.1. Tuned cavity

We consider a simple tuned cavity of length L with a finite bandwidth ϵ . The input mirror is fixed, while the end-mirror is suspended as a pendulum with mechanical eigenfrequency ω_m and damping γ_m . The Heisenberg equations of motion in the frequency domain can be obtained directly from the relations given in Sec. 5.2.2 by setting the detuning to zero. If the phase quadrature of the outgoing light ($\zeta = 0$) is detected, the eight zeros of its spectral density S_{yy} are given by $\pm a_1 \pm ib_1$ and $\pm a_2 \pm ib_2$ with (for simplicity for a vanishing mechanical damping, i.e. $\gamma_m = 0$):

$$a_{1,2} = \frac{1}{2} \sqrt{\sqrt{\frac{\omega_m^2}{\epsilon^2} (-4 \pm \sqrt{2}r) + r^2 \mp \sqrt{2}r + \frac{\omega_m^2}{\epsilon^2} \pm \frac{r}{\sqrt{2}}} - 1}, \quad (5.106)$$

$$b_{1,2} = \frac{1}{2} \sqrt{\sqrt{\frac{\omega_m^2}{\epsilon^2} (-4 \mp \sqrt{2}r) + r^2 \pm \sqrt{2}r - \frac{\omega_m^2}{\epsilon^2} \pm \frac{r}{\sqrt{2}}} + 1}, \quad (5.107)$$

where

$$r = \sqrt{\sqrt{\left[2 \frac{\Omega_q^{\text{cav}}}{\epsilon}\right]^4 + \left[\frac{\omega_m^2}{\epsilon^2} + 1\right]^4} + \left[\frac{\omega_m^2}{\epsilon^2} + 1\right]^4}. \quad (5.108)$$

The zeros are required for the spectral decomposition introduced in Eq. (5.76). After going through the whole Wiener filtering procedure, one ends up with the following conditional

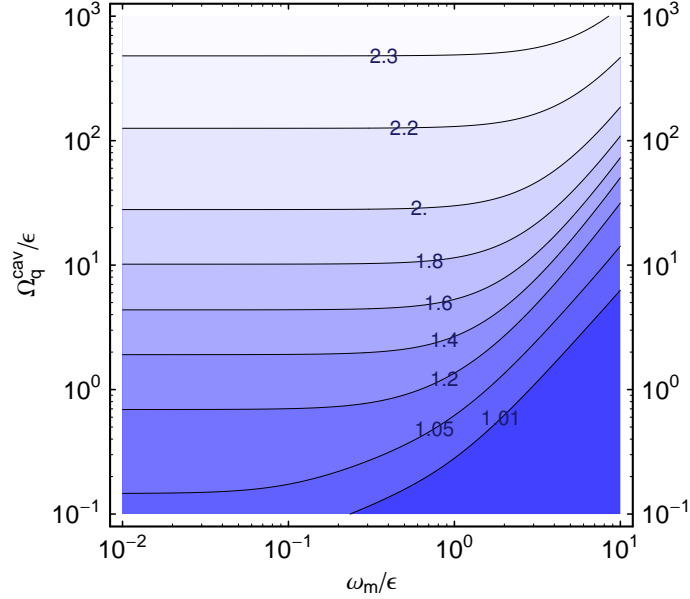


Figure 5.8.: Contour plot of the test mass state's purity versus the dimensionless ratios $\Omega_q^{\text{cav}}/\epsilon$ and ω_m/ϵ . In contrast to Fig. 5.7, we also comprise a non-zero mechanical eigenfrequency ω_m and therefore the purity is completely determined by these two ratios [cf. Eq. (5.108)]. Again, the phase quadrature is detected and no classical noise is present.

second-order moments:

$$V_{xx}^c = \frac{\hbar\epsilon}{6m(\Omega_q^{\text{cav}})^2} (c_1^3 + 3c_1^2 + 3c_1 + c_3), \quad (5.109)$$

$$V_{pp}^c = \frac{\hbar m \epsilon^3}{120(\Omega_q^{\text{cav}})^2} (3c_1^5 + 15c_1^4 + 20c_1^3 + 60c_3 + 60c_5), \quad (5.110)$$

$$V_{xp}^c = \frac{\hbar\epsilon^2}{16(\Omega_q^{\text{cav}})^2} c_1^2 (c_1 + 2)^2. \quad (5.111)$$

where the coefficients are given by

$$c_k = \frac{2}{k} \Im \left[(a_1 + ib_1)^k + (a_2 + ib_2)^k - i^k \right]. \quad (5.112)$$

The conditional variances given in Eqs. (5.109)-(5.111) are already cumbersome expressions, which indicates that an analytic treatment of even more sophisticated configurations is no longer possible. However, we can still draw some important conclusions from these second-order moments. By expanding the purity U in terms of $\Omega_q^{\text{cav}}/\epsilon$, we obtain

$$U = \frac{2}{\hbar} \sqrt{V_{xx}^c V_{pp}^c - (V_{xp}^c)^2} = 1 + \frac{1}{2\sqrt{2}} \frac{\Omega_q^{\text{cav}}}{\epsilon} + \mathcal{O}((\Omega_q^{\text{cav}}/\epsilon)^2), \quad (5.113)$$

which reveals that, even in the quantum noise limited case, the conditional state of the test mass cannot be pure as long as $\Omega_q^{\text{cav}}/\epsilon > 0$. This behavior is additionally illustrated

by Fig. 5.7. It should be emphasized that this is in contrast to the Markovian limit, i.e. $\epsilon \rightarrow \infty$, where the conditional state is always pure in the absence of classical noise, as one can infer from Eq. (5.99). This difference can be explained as follows: in the case of a finite-bandwidth cavity, the light is stored inside the resonator for a certain amount of time. The information carried by the light concerning the test mass's state cannot leave the cavity instantaneously and hence is not accessible for the conditioning process. Consequently, the intra-cavity mode needs to be taken into account for a complete characterization of the system. It forms, together with the test mass, a two-mode Gaussian system. The residual second-order moments required for completing the corresponding 4×4 conditional covariance matrix can be obtained in the same way as Eqs. (5.109)-(5.111). It turns out that the composite system is indeed a pure one, i.e. limited by the Heisenberg uncertainty, even though each individual system resides in a mixed state. This already proves the presence of entanglement between the test mass and the cavity mode as clarified in Sec. 5.5. The close relation between the system's inseparability and the test mass state's purity is illustrated by Fig. 5.7. The entanglement, quantified by the logarithmic negativity, increases with smaller bandwidth ϵ and with higher measurement frequency Ω_q^{cav} , while the test mass state's purity deteriorates. As long as $\Omega_q^{\text{cav}} \ll \epsilon$, this effect is negligible and an adiabatically eliminated cavity mode provides a good approximation. The purity of the cavity mode agrees exactly with that of the test mass. This is due to the fact that, in the absence of classical noise, our lack of information is solely attributed to the inherent storage time of the resonator, which equally affects both systems. Note that the uncertainty does not diverge for a small bandwidth or high measurement frequency, instead we obtain $U \rightarrow 1 + \sqrt{2}$ for $\Omega_q^{\text{cav}}/\epsilon \rightarrow \infty$.

In Fig. 5.8 we consider a configuration with a non-zero mechanical eigenfrequency ω_m . It turns out that the test mass state's purity can be improved by increasing ω_m . This phenomenon may be explained by the following hand-waving argument: by increasing ω_m , the mechanical oscillator and the optical oscillator, which would naturally resonate at zero modulation-frequency, become more separated in the frequency space and therefore their entanglement decreases. This implies that the test mass state becomes more pure. But the regime with such high mechanical resonance frequencies is usually not accessible by current gravitational wave detectors. But the result suggests that it might be advantageous to shift the mechanical eigenfrequency to higher frequencies by exploiting a restoring optical spring (cf. Ref [37] or Sec. 4.3).

Now we return to the free mass limit and introduce two simple classical noise sources, namely classical force and sensing noise, both inherently white. The spectral density of the force (sensing) noise [cf. Eq. (5.6)] intersects the SQL at Ω_F (Ω_x), as depicted in Fig. 5.19. Recall that the classical force noise increases with higher Ω_F , while the classical sensing noise increases with lower Ω_x . In order to obtain the conditional second-order moments, we need to switch to a numerical simulation of the system. The result is shown in Fig. 5.9 where each noise source is treated individually and, as expected, the conditional state becomes more and more mixed with an increasing classical noise level. The state's purity also crucially depends on the ratio between the measurement frequency and the optical bandwidth. The dashed line is associated with a Markovian system which exhibits an infinite bandwidth, i.e. $\epsilon \rightarrow \infty$. In the case of a low classical noise level, i.e. $\Omega_q^{\text{cav}} \ll \Omega_x$ and $\Omega_F \ll \Omega_q^{\text{cav}}$, respectively, the finite-bandwidth configuration encounters its fundamental limit, which depends on the resonator's storage time and measurement

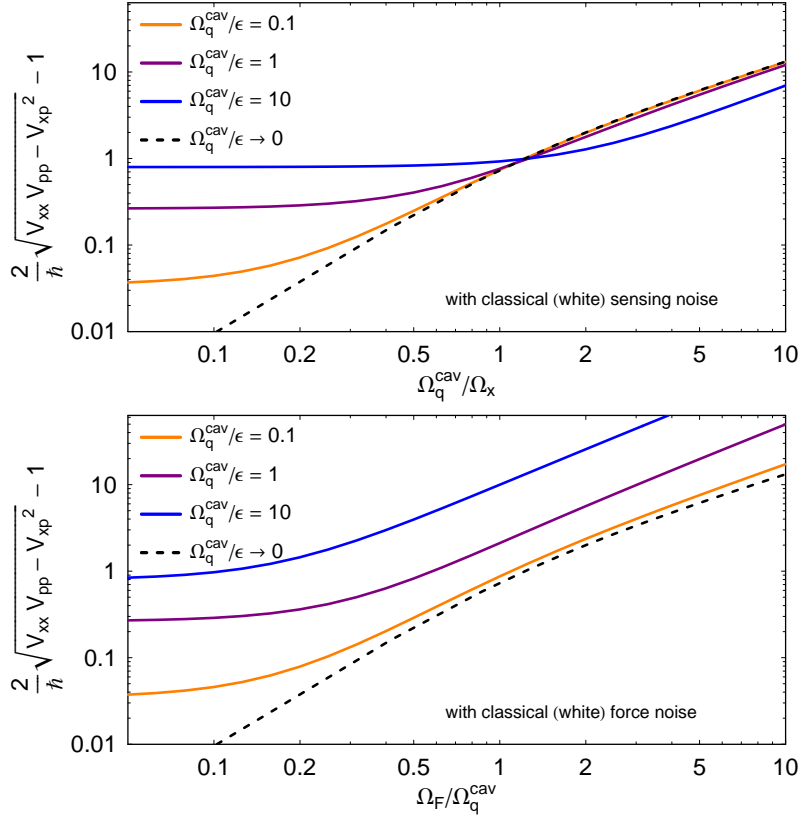


Figure 5.9.: Test mass state's purity versus classical sensing noise and without classical force noise (upper panel) as well as classical force noise and without sensing noise (lower panel), both for different examples of ratios between measurement frequency and bandwidth. The dashed curve represents the infinite-bandwidth limit. The free mass limit is used, i.e. $\omega_m = 0$ and the phase quadrature is detected.

frequency (cf. Fig. 5.7). If we only take sensing noise into account we know for sure that the motion of the test mass is solely driven by quantum backaction noise. A high sensing noise level randomizes the measurement record and hence the delimited accessibility of the intra-cavity field due to the finite bandwidth is insignificant. Consequently all curves roughly coincide for $\Omega_q^{\text{cav}} \gtrsim \Omega_x$ in the upper panel of Fig. 5.9. The lower panel illustrates that the finite-bandwidth configuration is fairly susceptible to classical force noise which is again due to the lack of information regarding the test mass's motion induced by the force noise. These results suggest that a state preparation scheme which employs finite bandwidth cavities might perform comparably to an adiabatically eliminable system in the presence of a certain classical noise budget, even though performing suboptimally in the quantum noise limited case. For practical reasons (e.g. lowering the input power) the implementation of finite-bandwidth cavities should be taken into consideration for experimental set-ups aiming at macroscopic quantum state preparation.

Fig. 5.10 illustrates the dependance of the second-order moments and the state's purity on the measurement frequency in the case of fixed characteristic frequencies of the classical noise sources. In contrast to a Markovian measurement process (cf. Fig. 5.21), the

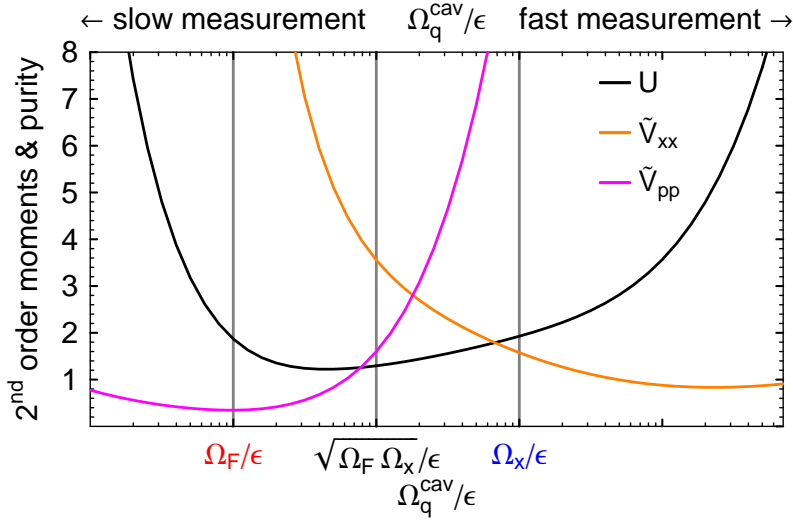


Figure 5.10.: Conditional second-order moments and purity versus the ratio of measurement frequency and bandwidth. This plot is related to Fig. 5.21, where a Markovian measurement process is considered. In this case the purity increases faster for low measurement frequencies. This is due to the increased susceptibility to classical force noise (cf. Fig. 5.9). The free mass limit is used and the second-order moments are normalized to the ground state of a harmonic oscillator with eigenfrequency $\sqrt{\Omega_F \Omega_x}$.

uncertainty increases faster for low measurement frequencies. This is due to the fact that the finite-bandwidth system is more susceptible to classical force noise compared to an infinite-bandwidth configuration.

Note that in the case of Advanced LIGO [1], the measurement frequency Ω_q^{cav} is planned to roughly coincide with the half cavity's bandwidth ($\epsilon/(2\pi) \sim 100$ Hz) which corresponds to the purple lines in Fig. 5.9. Furthermore, it is expected that the suspension thermal noise is associated with an intersecting frequency $\Omega_F/(2\pi) \sim 30 - 40$ Hz - that would be less than $\Omega_q^{cav}/2$ - but the coating thermal noise may provide an Ω_x that coincides with Ω_F or is just marginally higher.

5.8.2. Detuned cavity

In upcoming GW detectors, e.g. Advanced LIGO [1], a restoring optical spring shifts the mechanical eigenfrequency up into the detection band. This motivates the analysis of a detuned configuration in the context of macroscopic quantum state preparation. The circulating power and thus the radiation pressure force exerted on a mirror inside a detuned cavity depends linearly on the length of the cavity. This gives rise to an optical spring or anti-spring (cf. Ref. [37] or Sec. 4.3), both shifting the (free) mechanical and (free) optical resonance frequencies in the complex plane. Recall that such a system is unstable due to the presence of an anti-damping or anti-restoring optical force and hence an appropriate linear feedback system needs to be implemented. In the ideal case, however, such a control system does not affect the conditional second-order moments, as pointed out in Sec. 5.7.

The Heisenberg equations of motion for a detuned cavity (which is completely equivalent

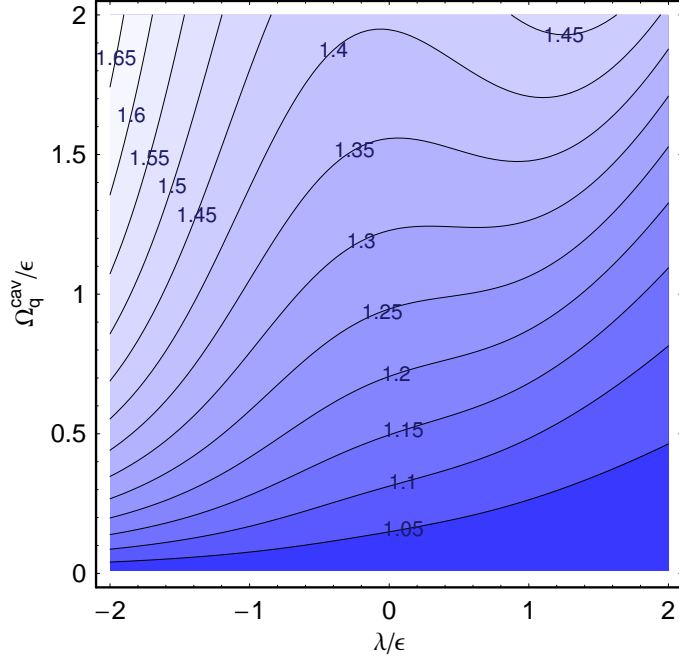


Figure 5.11.: Contour plot of test mass state's purity versus the ratios λ/ϵ and $\Omega_q^{\text{cav}}/\epsilon$. Free mass limit is used, i.e. $\omega_m = 0$, the phase quadrature is detected and only quantum noise is taken into account.

to a detuned SR interferometer) can be found in Sec. 5.2.2. For such a system it is also not expedient to seek an analytical expression of the covariance matrix, so that we are confined to numerical results. Fig. 5.11 reveals that detuning the cavity can lead to an improved test mass state's purity compared to a non-detuned configuration. In the case of a blue detuned cavity ($\lambda > 0$) and for $\Omega_q^{\text{cav}} < \epsilon$ Fig. 5.11 resembles Fig. 5.8. This is due to the fact that increasing the detuning while holding the measurement frequency fixed pushes the optical resonance to higher frequencies, while the mechanical resonance is shifted to a lesser extent. Consequently the separation of the two oscillators increases in frequency space and the entanglement between them decreases.

Note that for high measurement frequencies, i.e. $\Omega_q^{\text{cav}} > \epsilon$, the state of the test mass could locally become purer in the case of a small red detuning ($\lambda \lesssim 0$), which produces an anti-spring. The uncertainty diverges for an infinitely red detuned cavity ($\lambda \rightarrow -\infty$).

5.8.3. Example configuration

In this section we consider more realistic configurations involving multiple colored noise sources. First we restrict ourselves to a pseudo noise budget of an advanced interferometric gravitational wave detector, shown in the left panel of Fig. 5.12. It illustrates the fact that all noise contributions tend to rise fast towards low frequencies, which is ignored by a simple Markovian noise model. Especially seismic noise dominates the entire spectrum below 10 Hz. In order to apply the numerical Wiener filter procedure (cf. App. A), all classical noise spectra need to be approximated by even rational functions. This is exemplified by Fig. 5.12 (right panel) where the seismic noise spectral density, pre-

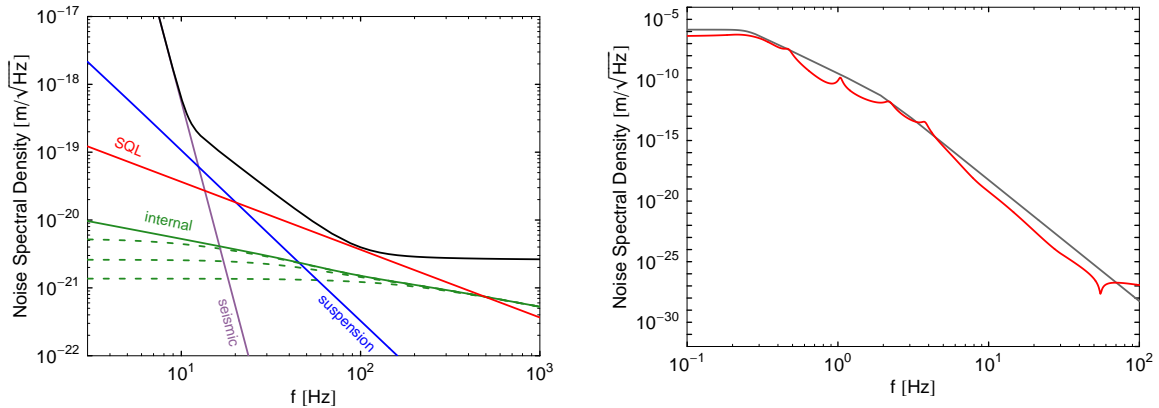


Figure 5.12.: *Left panel:* possible (colored) noise budget of an advanced interferometric gravitational wave detector. Seismic (violet), suspension thermal (blue, follows $\sim 1/f^{5/2}$) and internal thermal (green, follows $\sim 1/f^{1/2}$) noise spectra are shown as well as the total noise (black) – including Markovian quantum noise with phase quadrature readout. For the thermal noise sources we employed the Padé approximation which entails valid spectra between 0.1 Hz and 2 kHz. *Right panel:* seismic noise pre-estimated by the simulation tool *Bench* [2] (red) and a fit by rational function (gray)

estimated by the simulation tool *Bench* [2], is approximated accordingly. The seismic noise spectrum is constant below 0.25 Hz, then it drops as $\sim 1/f^6$ between 0.25 Hz and 2 Hz and finally it drops as $\sim 1/f^{10}$ above 2 Hz. The suspension thermal noise constitutes a second force noise contribution which drops as $\sim 1/f^{5/2}$ above the pendulum eigenfrequency and it intersects the SQL at 20 Hz. Such a frequency dependance presumes structural damping. The internal thermal noise follows $\sim 1/f^{1/2}$ and it intersects the SQL at 500 Hz. Additionally we assume that the gravity gradient noise can be suppressed completely through monitoring the ground's motion. Note that we need to employ the Padé approximation in the case of the suspension and internal thermal noise, in order to guarantee even rational functions in f .

It should be emphasized that the conditional second-order moments can diverge, if the sensing noise rises towards low frequencies, and therefore a cut-off frequency must be chosen carefully. This issue is illustrated by Figs. 5.13 (upper left panel) where the cut-off frequency of the sensing noise is varied, while the classical force noise contributions are held fixed. The divergence we face means physically that our system will be noisy if observed for a long time, but it can still appear quiet with regard to short time scales. The preparation stage only lasts for a finite amount of time τ_{prep} , which naturally gives rise to a cut-off frequency at $\sim 1/\tau_{\text{prep}}$. Further on it will be shown in an forthcoming paper [46] that the low frequency noise will be canceled out in a subsequent verification stage. Interestingly, an artificial suppression of the force noise cures the divergence, since we know for sure that the motion of the test masses is not driven by classical noise at low frequencies. Consequently it must be tolerable if we disregard the low frequency measurement record contaminated by sensing noise.

The preparation stage may be followed by a certain period of free evolution before an independent verification stage starts. During the evolution stage, the conditional quantum

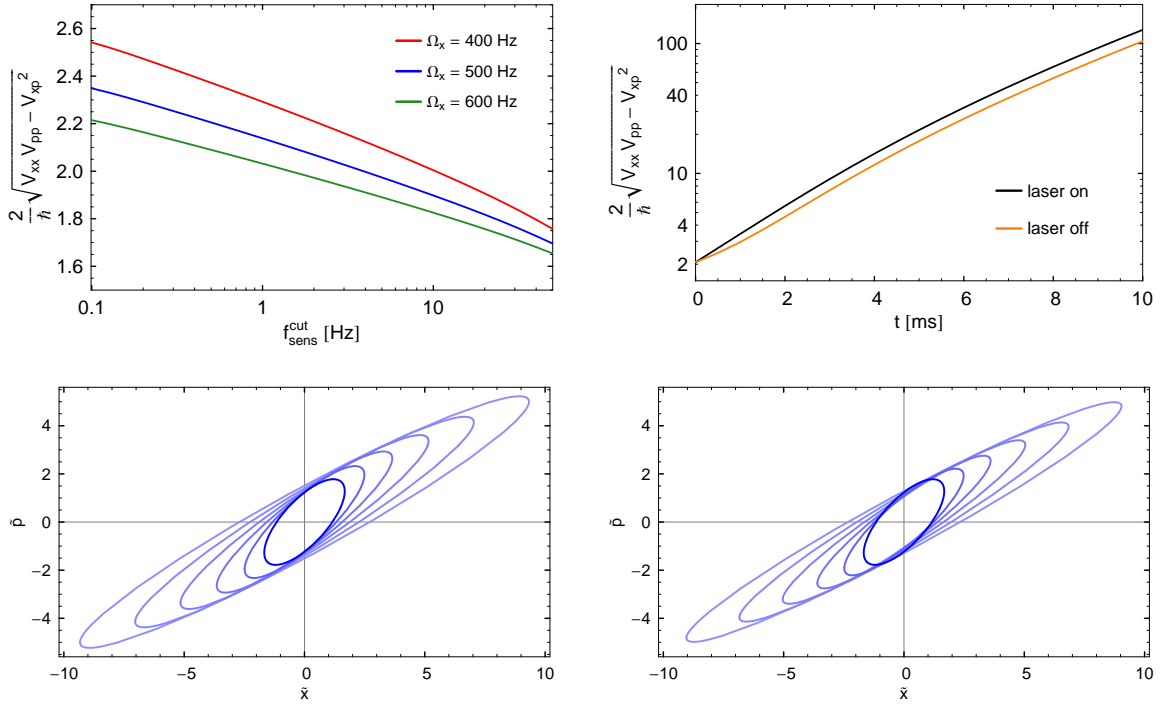


Figure 5.13.: *Upper left panel:* purity of conditional state versus sensing noise cut-off frequency for three different sensing noise levels. Force noise contributions are the same as in Fig. 5.12. The second-order moments formally diverge when downshifting the cut-off frequency. For subsequent plots we use $\Omega_x = 2\pi 500$ Hz and cut off the sensing noise around $2\pi 1$ Hz. *Upper right panel:* purity of conditional state versus free evolution time. The state’s survival time is extended when switching off the measurement device, which is due to the absence of radiation pressure induced decoherence. *Lower left panel:* squeezing ellipses of the mechanical mode, where second-order moments are normalized to ground state of harmonic oscillator at frequency Ω_q , i.e. the quantum noise touching. Measurement device is turned on. *Lower right panel:* squeezing ellipses when measurement device is turned off. Elapsed time for both cases: $t = 0, 0.8, 1.6, 2.4, 3.2, 4$ ms (from inner to outer ellipse).

state undergoes a thermal decoherence, i.e. additional fluctuations are introduced. If the evolution time is comparable to the timescale set by the measurement frequency, i.e. $\lesssim 1/\Omega_q$, the state remains reasonably pure. This is illustrated by Fig. 5.13 (upper right panel), where we distinguish between two different scenarios: (i) the measurement device, i.e. the laser, is still in operation after finishing the preparation stage but the measurement record is no longer used for constructing the conditional quantum state. The test masses are constantly exposed to radiation pressure forces, which gives rise to an additional decoherence process. In the second case (ii) the measurement device, and hence radiation pressure noise, is cut off instantaneously right after the preparation stage. This can be put into practice by applying the backaction evasion technique discussed at the end of Sec. 2.3.2. In order to obtain the ”off” conditional second-order moments, one has to subtract the effects induced by radiation pressure fluctuations from the results $V_{lm}^c[a]$ generated by the usual predictive Wiener filter procedure introduced in Sec. 5.6.2.

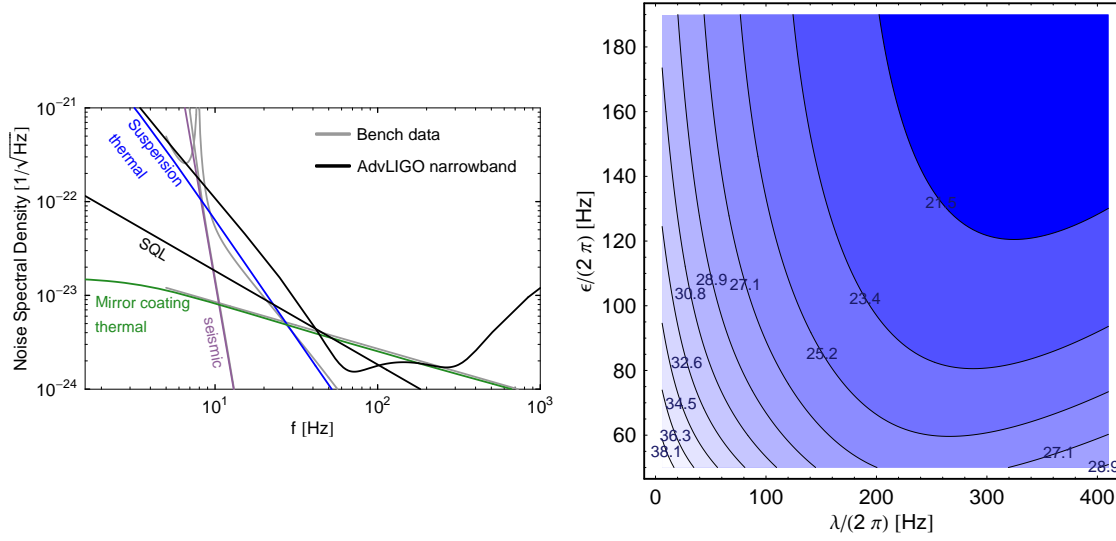


Figure 5.14.: *Left panel:* spectral densities of main noise sources present in Advanced LIGO gravitational wave detector: seismic (violet), suspension thermal (blue) and internal thermal (green) noise, as well as the quantum noise (black) of the Advanced LIGO narrowband configuration (cf. Tab. 2.1). We assume that gravity gradient noise can be suppressed through monitoring of the ground’s motion. Pre-estimated classical non-Markovian noise budget is fitted by rational functions with characteristic spectra as in Fig. 5.12. *Right panel:* purity of conditional state (of the differential mode) versus detuning λ and bandwidth ϵ . Most pure state occurs for slightly blue-shifted detuning. Lowering bandwidth always improves purity.

This can be easily accomplished as long as the radiation pressure fluctuations exhibit a white spectrum:

$$V_{lm}^{\text{off}}[a] = V_{lm}^c[a] - \frac{1}{2} \int_t^{t+a} dt' C_l(t+a-t') C_m(t+a-t') S_{F_{\text{rad}}}, \quad (5.114)$$

where C_l accounts for the time domain susceptibility of the observable x_l to external classical forces [cf. Eq. (2.115)]. The spectral density of the radiation pressure noise is simply given by $S_{F_{\text{rad}}} = \alpha^2$ as one can infer from Eq. 5.1.

Advanced LIGO

The classical noise budget of the forthcoming Advanced LIGO gravitational wave detector [1] was pre-estimated by the simulation tool *Bench* [2]. The classical noise contributions are highly non-Markovian and they tend to rise fast in the low frequency regime. We choose the same characteristic spectra as in the previous example and adjust the parameters so that the predicted Advanced LIGO classical noise budget is well approximated. A comparison between the *Bench* data and the approximating rational functions is shown in Fig. 5.14. Again we assume that the gravity gradient noise can be suppressed completely. In contrast to the previous example, Advanced LIGO comprises finite bandwidth cavities, which gives rise to non-Markovian dynamics.

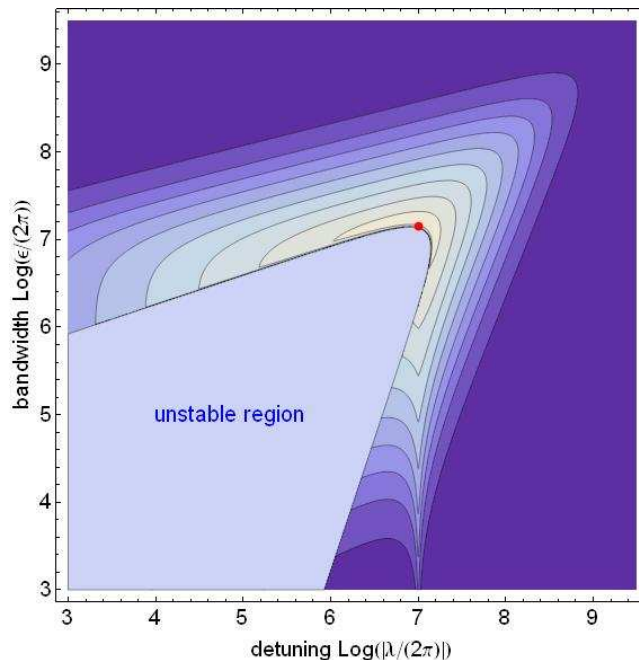


Figure 5.15.: Stable region versus optical detuning λ and bandwidth ϵ for the configuration (cf. Tab. 5.1) investigated by Vitali et al. in Ref. [161]. A lighter blue shading indicates higher damping. The red dot corresponds to the configuration exhibiting both, maximal mechanical damping and maximal optomechanical entanglement.

We have carried out a full parameter search in order to optimize the configuration with respect to the purity of the conditional state. Remember that we aim at preparing a conditional state of the differential mode of the four movable arm cavity mirrors. This is equivalent to considering a stand-alone oscillator with one-fourth the mass of a single arm cavity mirror. The result of the optimization is shown in the right panel of Fig. 5.14, which depicts the purity versus detuning λ and bandwidth ϵ . It clearly shows that the purity of the conditional state benefits from a restoring optical spring, i.e. a positive detuning facilitates the preparation of macroscopic quantum states. Note that increasing the bandwidth ϵ always gives rise to an additional improvement, which has been clarified in Sec. 5.8.1.

Aside from the currently estimated classical noise budget, a more optimistic scenario is investigated, in which the seismic and suspension thermal noise are reduced by a factor of ten, while the coating thermal noise is lowered by a factor of three (in amplitude). A rough optimization revealed that the minimal achievable uncertainty drops down to $U \approx 10$.

5.8.4. Optomechanical entanglement

The last section aimed at preparing a conditional state of macroscopic test masses, which is as pure as possible in order to penetrate into the quantum regime. It has also been shown that employing finite bandwidth cavities gives rise to entanglement between the cavity mode and the macroscopic test mass, which prevents both states from being pure,

symbol	physical meaning	value
P_{in}	input power	50 mW
L	cavity length	10^{-3} m
$2\pi c/\omega_0$	laser wavelength	810 nm
ϵ	half bandwidth	$2\pi \cdot 1.4 \cdot 10^7$ Hz
λ	detuning	$2\pi \cdot 10^7$ Hz
ω_m	mechanical eigenfrequency	$2\pi \cdot 10$ MHz
γ_m	mechanical damping	$2\pi \cdot 100$ Hz
m	effective mass of mechanical mode	$5 \cdot 10^{-12}$ kg
T	temperature	$4 \cdot 10^{-11}$ K

Table 5.1.: Parameter values used by Vitali et al. in Ref. [161]. The given values for ϵ and λ correspond to the red dot in Fig. 5.15. This choice guarantees maximal mechanical damping which is related to the presence of optomechanical entanglement.

even in the absence of classical noise. Nevertheless, it is a serious task to demonstrate this optomechanical entanglement, since it involves at least one macroscopic part. This would be a first step towards generating entanglement between two distinct macroscopic objects (cf. Sec. 5.9). The so-called "ponderomotive entanglement" was discussed extensively in the literature, cf. e.g. Refs. [161, 171], and a common underlying notion can be distilled easily: the restriction to an unconditional approach requires that the mechanical degree of freedom is strongly damped, in order to ensure that the influence of the thermal environment becomes negligible in comparison with optical forces. If the test mass is so cooled that it resides near its quantum ground state, entanglement with the fluctuating optical field comes into reach. By using the formalism introduced in this thesis, we can easily recover previous results. Again a simple cavity with a suspended end-mirror and a fixed input mirror is considered. The corresponding equations of motion in the frequency domain can be found in Sec. 5.2.2. These describe a single optical spring system, which can also exhibit stable dynamics, (without employing a feedback control system) as pointed out in Refs. [140, 170]. In order to reach this special regime, the optical frequency scales must be comparable with the mechanical oscillator's eigenfrequency. Vitali et al. considered in their Ref. [161] a mechanical oscillator with an eigenfrequency of $\omega_m = 2\pi \cdot 10$ MHz which permits penetration into the above-mentioned regime. Whereas in Ref. [171] a mechanical oscillator with resonance frequency $\omega_m = 2\pi \cdot 1$ Hz was considered, which was stabilized by the implementation of our proposed double optical spring technique (cf. Sec. 4.3).

But first we take a closer look at the configuration proposed by Vitali et al. [161]. They considered a certain degree of freedom of the mirror, with parameters given in Tab. 5.1. In Fig. 5.15 the stable regime of this configuration is explored in a similar manner to Fig. 4.16, but here the contour lines indicate the amount of mechanical damping. This plot justifies Vitali et al.'s [161] choice of parameters, marked by the red dot close to the edge of the stable region. This configuration exhibits maximal mechanical damping, which is essential for the preparation of optomechanical entanglement. The unconditional second-order moments can be derived easily via Eq. (2.159) – we just need to calculate the (cross-) spectral densities S_{ab} with $a, b \in \{\hat{A}_1, \hat{A}_2, \hat{x}, \hat{p}\}$. The variances are the constituents

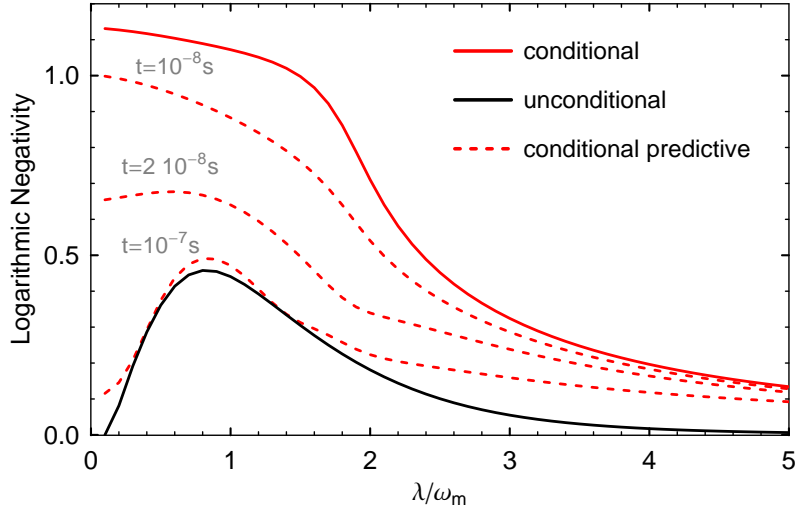


Figure 5.16.: Comparison between conditionally (solid red) and unconditionally (solid black) prepared optomechanical entanglement. The solid black curve reproduces the result obtained by Vitali et al. in Ref. [161] (cf. their Fig. 1). If the system undergoes a conditional measurement, the logarithmic negativity increases. After finishing the conditional state preparation process, the amount of entanglement evolves pursuant to the dashed red curves if the laser is still in operation. Within a time period $\tau \sim 1/\epsilon$, the conditionally generated entanglement falls back to the unconditional scenario.

of the 4×4 covariance matrix, which can be tested for entanglement by means of the criteria formulated in Sec. 5.5. The result is shown in Fig. 5.16, where the solid black curve agrees with that presented by Vitali et al. in Fig. 1 of their Ref. [161]. In order to verify the presence of entanglement experimentally, one has to detect the outgoing field, while the mechanical degree of freedom has to be observed independently. Then all entries of the covariance matrix are accessible by an appropriate state tomography as proposed in Vitali et al. [161]. In this manner one can test the non-separability of the optomechanically coupled system. Note that these authors have only taken into account Markovian force noise at a very low level (cf. Tab. 5.1).

Now we switch to a conditional state-preparation scheme which requires a homodyne detection of the outgoing field right from the beginning. The amplitude and phase quadrature of the intra-cavity mode as well as the position and momentum of the mirror are conditioned upon the information obtained by the readout. Mathematically, one has to apply the Wiener filter method introduced in Sec. 5.6.2 to all the experimentally accessible spectral densities S_{ab} . The conditioning process aims at purifying the states of both constituents of the bipartite system. In the quantum noise limited regime this might cause a diminished amount of entanglement. But unconditionally prepared entanglement can vanish swiftly when introducing realistic decoherence processes since both systems become mixed. This can be counteracted by employing a conditional state preparation scheme, i.e. the robustness of the entangled state can be improved. This is illustrated by Fig. 5.16 where the conditionally prepared entanglement (solid red curve) exceeds its unconditional counterpart (solid black curve) significantly. It is also possible to introduce an independent verification stage in the case of the conditional state preparation scheme.

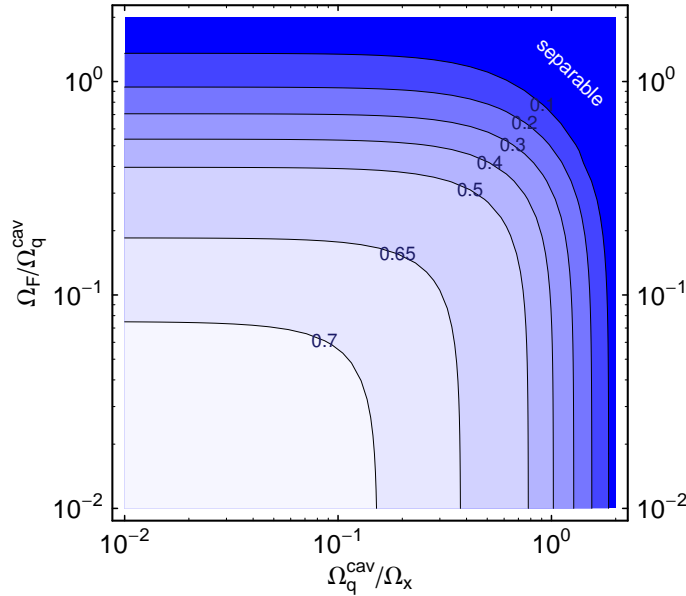


Figure 5.17.: Contour plot of logarithmic negativity versus the ratios $\Omega_q^{\text{cav}}/\Omega_x$ and $\Omega_F/\Omega_q^{\text{cav}}$, where the bandwidth of the cavity was so chosen such it coincides with the measurement frequency, e.g. $\epsilon = \Omega_q^{\text{cav}}$.

This is crucial, since the outgoing light is already used for the preparation stage. But if the entanglement persists for a sufficient long time, it is possible to switch to a different detection scheme, enabling the experimenter to verify the generated conditional quantum state in an independent manner. The set-up proposed by Vitali et al. [161] (cf. Tab. 5.1) involves a low finesse cavity, which implies that the conditionally prepared entanglement vanishes within a short time $\tau \sim 1/\epsilon \sim 10^{-7}$ sec. This is also illustrated in Fig. 5.16 by the dashed red lines which were obtained by using the predictive Wiener filtering method (cf. Sec. 5.6.2). It can be seen that we fall back onto the simple unconditional scenario.

The previous example has been chosen in order to illustrate the difference between conditional and an unconditional state preparation strategies. It should be emphasized that the advantage of the conditional state preparation scheme does not fully come into play for the parameter regime studied by Vitali et al. [161] These authors confined themselves to configurations where the mechanical degree of freedom is strongly damped. The conditional state preparation technique permits the treatment of more realistic systems, e.g. current or planned gravitational wave detectors with quasi free test masses. In Fig. 5.17 a simple tuned cavity with a quasi free movable end mirror is considered in the presence of Markovian force and sensing noise. It turns out that optomechanical entanglement can persist, even if the characteristic frequencies of both classical noise contributions are comparable with the measurement frequency (cf. also Fig. 5.19). This means that entanglement can survive regardless of a total classical noise budget being above the SQL for all frequencies.

5.9. Entanglement of macroscopic test masses

In this section we investigate the generation of entanglement between two macroscopic objects. It is shown that a non-separable state can persist even in presence of realistic decoherence processes. A simple Michelson interferometer with suspended mirrors and simultaneous homodyne readouts at both output ports forms the basis of the feasibility study (cf. Fig. 5.18). We aim at entangling the position and momentum of the two suspended end mirrors, which strongly resembles the original Einstein-Podolsky-Rosen thought experiment [71] discussed in detail in Sec. 5.5. In order to achieve this ambitious goal, the two mirrors under consideration need to be prepared in carefully chosen quantum states. The two measurement outputs, belonging to completely decoupled systems, provide an indirect access to the observables of each individual mirror, namely the position and momentum of the north (\hat{x}^n, \hat{p}^n) and the east (\hat{x}^e, \hat{p}^e) mirror. They are related to the position and momentum observables of the common (\hat{x}^c, \hat{p}^c) and the differential (\hat{x}^d, \hat{p}^d) mode as follows:

$$\mathbf{x} \equiv \begin{pmatrix} \hat{x}^d \\ \hat{p}^d \\ \hat{x}^c \\ \hat{p}^c \end{pmatrix} = \begin{pmatrix} \hat{x}^e - \hat{x}^n \\ \hat{p}^e - \hat{p}^n \\ \hat{x}^e + \hat{x}^n \\ \hat{p}^e + \hat{p}^n \end{pmatrix}, \quad (5.115)$$

where the elements of the vector \mathbf{x} satisfy the commutation relation given in Eq. (5.14), i.e. $[\hat{x}^{c,d}, \hat{p}^{c,d}] = i\hbar$. The following investigations are restricted to a subclass of states with Gaussian statistics. Hence the state of the bipartite system is completely characterized by its second-order moments. By using Eq. (5.15) we obtain the 4×4 covariance matrix

$$\mathbf{V} = \begin{pmatrix} \mathbf{V}_{ee} & \mathbf{V}_{en} \\ \mathbf{V}_{ne} & \mathbf{V}_{nn} \end{pmatrix} \quad (5.116)$$

with

$$\mathbf{V}_{ee} = \begin{pmatrix} (V_{xx}^c + V_{xx}^d)/4 & (V_{xp}^c + V_{xp}^d)/2 \\ (V_{xp}^c + V_{xp}^d)/2 & V_{pp}^c + V_{pp}^d \end{pmatrix}, \quad \mathbf{V}_{en} = \begin{pmatrix} (V_{xx}^c - V_{xx}^d)/4 & (V_{xp}^c - V_{xp}^d)/2 \\ (V_{xp}^c - V_{xp}^d)/2 & V_{pp}^c - V_{pp}^d \end{pmatrix} \quad (5.117)$$

and $\mathbf{V}_{nn} = \mathbf{V}_{ee}$ as well as $\mathbf{V}_{ne} = \mathbf{V}_{en}$. A covariance matrix of the same form emerges from the investigation of two light beams overlapped on a beam splitter. In the case of differently squeezed beams, continuous-variable entanglement between the amplitude and phase-quadratures of the outgoing pair of light beams can be generated [21, 78].

The presence of entanglement imposes certain requirements on the classical noise level which are discussed in the following for different configurations. All scenarios can be examined with regard to the usual entanglement (cf. Sec. 5.5.1) and the stronger EPR-entanglement (Sec. 5.5.2). Here we restrict the discussion to the former case, while a detailed study of EPR-entanglement can be found in Ref. [123].

Configuration

To begin, we consider a simple Michelson interferometer without arm cavities (cf. also Sec. 5.2.1) as shown in Fig. 5.18. A power-recycling mirror (PR) is positioned behind

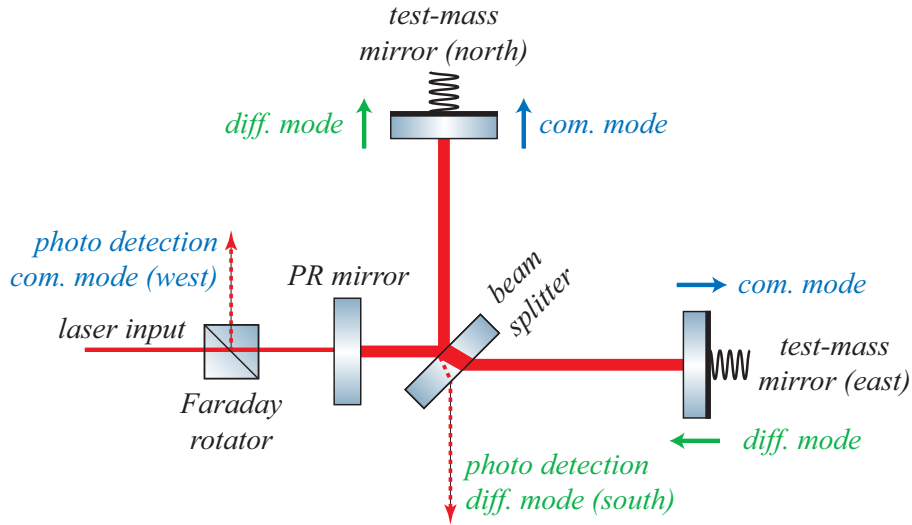


Figure 5.18.: Schematic plot of a power-recycled (PR) Michelson interferometer. Suspended end-mirrors are much lighter than other suspended optics. A differential motion of test mass mirrors is detected at the dark (south) port and a common motion at the bright (west) port. A frequency-independent homodyne detection is performed at each port. A Faraday rotator might be used to separate the back reflected light from the ingoing light.

the interferometer’s dark port in a way that it forms a resonant low-finesse cavity together with the end mirrors. Both output ports are equipped with homodyne readout schemes which are able to detect a certain frequency-independent quadrature phase (see Sec. 2.3.5). Such an experimental set-up is susceptible to classical laser noise, which complicates the common mode’s state preparation procedure. Laser amplitude noise gives rise to additional force noise, while phase fluctuations contribute to the total sensing noise. Moreover an efficient photo-detection of a high-power optical field has to be managed. Due to these issues, in principle an asymmetric treatment of the common and differential mode is required, which is discussed in Ref. [123].

5.9.1. Relation between entanglement and SQL

In our Ref. [125] we provided a simple criterion for the presence of entanglement in the case of a Markovian measurement process: it is necessary that the total classical (white) noise resides below the SQL in a certain frequency window. There exists such a window if and only if $\Omega_x/\Omega_F > 2$, where Ω_F (Ω_x) corresponds to the frequency where the force (sensing) noise intersects the SQL, as shown schematically in Fig. 5.19. A sufficient condition concerning the size of the window, depends crucially on the implemented measurement scheme and the type of entanglement (entanglement in general or EPR-entanglement) one is aiming at.

It is instructive to look for entanglement in the case of the most general Markovian measurement process (i.e. variable homodyne detection angle and measurement strength, cf. Sec. 5.6.3) since this permits the derivation of an ultimate limit on the classical (white) noise level. The far left curve in Fig. 5.20 accounts for such a scheme and it illustrates

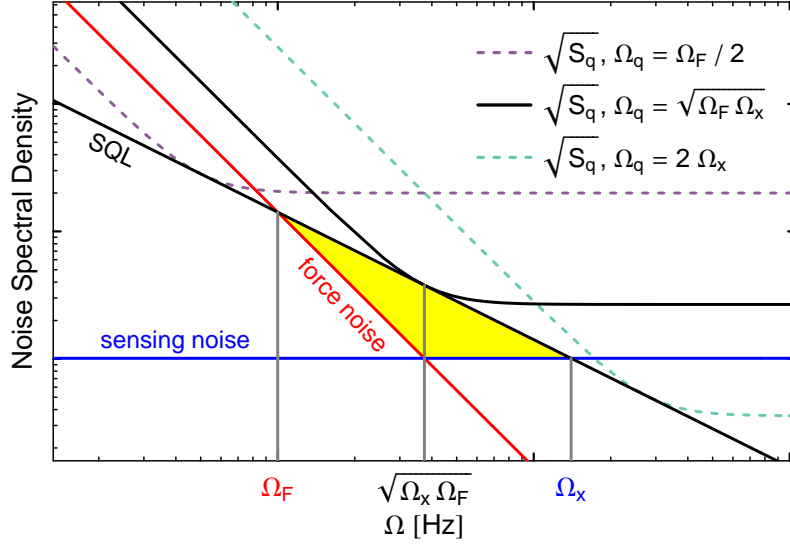


Figure 5.19.: Noise spectral densities in arbitrary units for Markovian quantum and classical noise. The classical force (sensing) noise spectrum intersects the SQL at Ω_F (Ω_x). The total classical noise is minimal at $\sqrt{\Omega_F \Omega_x}$. The dashed curves can be interpreted as the noise spectral densities of common and differential mode, respectively. Further, this example configuration exhibits entanglement in general ($E_{\mathcal{N}} = 0.99$) as well as EPR-entanglement ($E_{\text{EPR}} = 0.03$).

the realizable amount of entanglement in terms of the logarithmic negativity. This result is primarily of a theoretical nature since the measurement strength, which is proportional to the circulating power, must be very high. Furthermore a detection near the amplitude quadrature is required which might not be feasible in a real experimental set-up. However, we can conclude that it is not possible to generate any entanglement between the two test masses if $\Omega_x/\Omega_F \lesssim 2.8$.

When the two homodyne readouts are confined to a detection of the phase quadrature, only a subclass of Markovian measurement processes is covered. This implies that the requirements for the generation of an entangled state must increase, as confirmed by Fig. 5.20. The second left curve always resides below the curve corresponding to the most general measurement process and the ratio Ω_x/Ω_F needs to be enlarged to ~ 3.8 . The labels indicate that the common mode's measurement frequency (Ω_q^c) is close to Ω_x , while that of the differential mode (Ω_q^d) is close to Ω_F . Such an arrangement can be explained as follows: a high measurement frequency corresponds to a fast measurement which allows a determination of the position with high precision, whereas the momentum uncertainty becomes small in the case of a slow measurement. This is explained e.g. in Ref. [27] (see Chap. 1.4) by means of the "Heisenberg microscope". We cannot arbitrarily enhance the position measurement accuracy since a measurement with $\Omega_q \gg \Omega_x$ would be contaminated by classical sensing noise. The same is true for a momentum measurement which suffers from the classical force noise at low frequencies. It turns out that the position (momentum) uncertainty becomes minimal if the quantum noise touching frequency coincides with Ω_x (Ω_F) which is illustrated by Fig. 5.21. Choosing the measurement frequencies around Ω_x and Ω_F , respectively, ensures that the squeezing ellipses

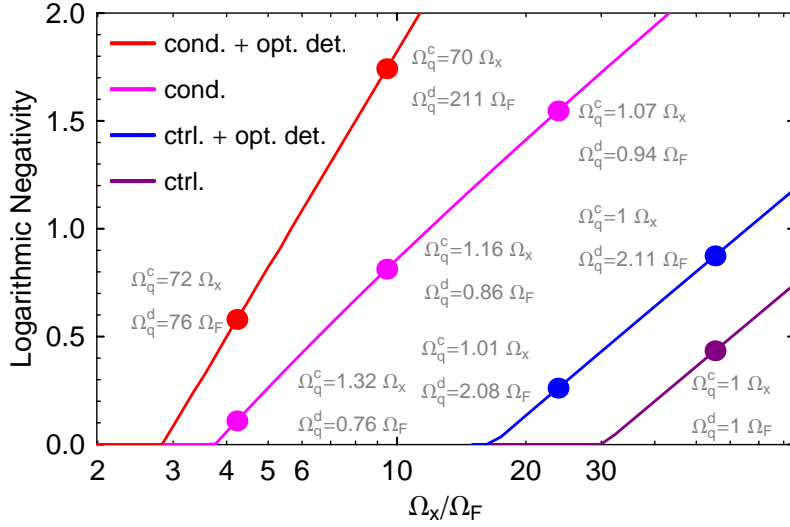


Figure 5.20.: Logarithmic negativity versus the ratio Ω_x/Ω_F for different configurations: conditional state preparation scheme with variable homodyne readouts (red) and phase quadrature detection (magenta). Controlled state preparation with variable homodyne readouts (blue) and phase quadrature detection (violet). Amount of entanglement was maximized with respect to the measurement strength (Ω_q^c, Ω_q^d) and, where relevant, with respect to the two homodyne detection angles.

of the common and differential mode are arranged almost perpendicularly. This is closely related to the generation of optical entanglement, where one also tries to overlap beams which are squeezed in orthogonal quadratures. In our case, it is not possible to obtain exactly orthogonal squeezing ellipses due to the presence of cross-correlations. The orientation of the squeezing ellipse versus the measurement frequency is shown in Fig. 5.6. Note that in the absence of classical noise there is always entanglement, except for the case where both modes are prepared in the same way.

As mentioned in the beginning it is also possible to generate entanglement by employing a feedback control scheme which fixes the first-order moments of common and differential mode in phase space. It is shown in Fig. 5.20 that a ratio of $\Omega_x/\Omega_F \gtrsim 26$ with and $\Omega_x/\Omega_F \gtrsim 30$ without a variable homodyne readout allows the preparation of an entangled state. The inherent drawback of such a scheme is also illustrated by Fig. 5.21, which shows the purity and the second-order moments for the controlled state. These always reside above their conditional state counterparts while they have an assimilable shape. For the controlled configuration with phase quadrature readout, the optimal entanglement always occurs when the quantum noise touching frequencies exactly agree with Ω_x and Ω_F , respectively. This is due to the fact that for those frequencies the position or momentum uncertainty is minimal and the cross correlations vanish anyway (cf. Fig. 5.6).

5.9.2. Time evolution

In the previous section, we investigated the steady state entanglement between two test masses of a Michelson interferometer for a Markovian measurement process. The measurement time-scales set by the touching frequencies of the quantum noise already provide

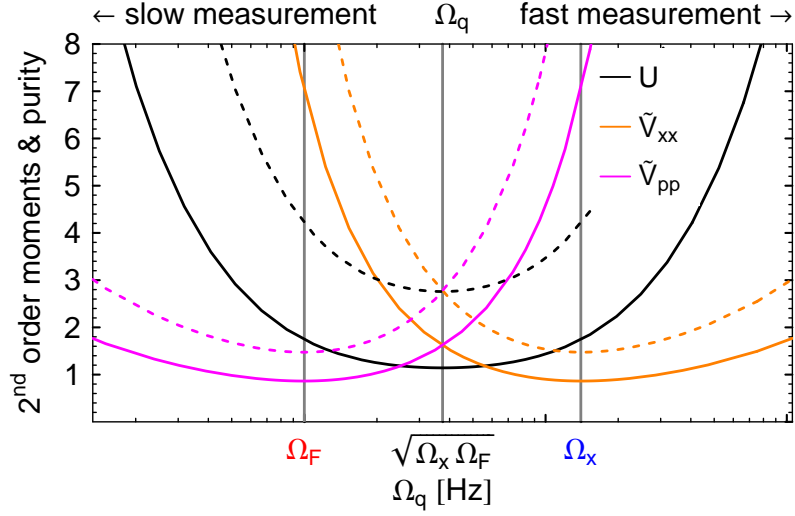


Figure 5.21.: Conditional (solid) and controlled (dashed) variances and purity versus touching frequency of quantum noise spectral density. A high touching frequency (fast measurement) improves accuracy for the position, while a low touching frequency (slow measurement) improves accuracy for the inferred momentum. The minimum of the mechanical mode’s purity coincides with the minimal classical noise at $\sqrt{\Omega_x \Omega_F}$. Variances normalized to the ground state of a harmonic oscillator with eigenfrequency $\sqrt{\Omega_x \Omega_F}$.

an indicator for the time required for building up an entangled state. This issue has to be investigated rigorously, since the time evolution might be crucial for the design of a realistic experimental set-up. In order to prevent low frequency classical noise from disturbing the experiment one has to complete the preparation stage within a sufficiently short time. A time domain study therefore motivates a cut-off frequency which needs to be introduced in the case of a non-Markovian classical noise budget.

Any general Markovian measurement process can be treated by the stochastic master equation formalism discussed in Sec. 5.6.1. This allows us to study in an exemplary way the time evolution of a given configuration obtained within the framework of the optimization carried out for Fig. 5.20. It turns out that the entanglement can even appear long before the final steady state is reached, as illustrated by Fig. 5.22. This is especially true for a pre-cooled oscillator, where the entanglement can be even stronger during the time evolution before reaching the steady state. This is due to the fact that the oscillator’s initial mixed state can have a momentum uncertainty much smaller than the final steady state, which might be momentum anti-squeezed. The reduction of the position uncertainty is very fast, while the momentum variance changes relatively slowly. This allows us to generate a state which is purer than the final steady state. The steady state can be reached within a time period defined by

$$1/(2\omega_m t) \gg \sqrt{2} \sqrt{\sqrt{\frac{2(\Omega_F/\Omega_q)^2 + 1}{(2(\Omega_q/\Omega_x)^2 + 1)(\omega_m/\Omega_q)^4} + 1} - 1}. \quad (5.118)$$

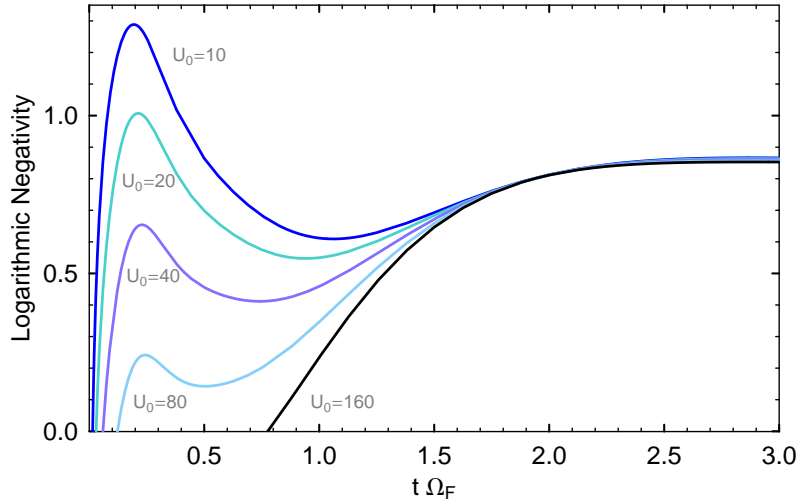


Figure 5.22.: Time evolution of the entanglement during preparation stage for a configuration with phase quadrature readout and parameters $\Omega_q^c = 1.16\Omega_x$, $\Omega_q^d = 0.86\Omega_F$, $\Omega_x/\Omega_F = 10$ and $\omega_m = \Omega_F/20$. This configuration is also marked in Fig. 5.20. Equal initial purities are assumed for common and differential mode. Each curve corresponds to an indicated initial purity.

5.9.3. Non-Markovian noise

A simple Markovian noise budget captures the main features of noise sources present in a gravitational wave detector. Such a simplification allows us to make order-of-magnitude estimations and results carry over directly to systems of different sizes. Note that the Markovian assumption applies more accurately to small-scale devices which operate at high frequencies. A large-scale advanced interferometric gravitational wave detector is more accurately described by the pseudo classical noise budget introduced in Fig. 5.12. This illustrates the fact that classical noise sources tend to rise fast in the low frequency regime, which complicates the generation of entanglement between the two end mirrors. The pseudo noise budget in Fig. 5.12 exhibits a ratio of $\Omega_x/\Omega_F \sim 25$, which would allow the generation of entanglement in the case of white classical noise (cf. Fig. 5.20). But here we have to deal with non-Markovian noise sources and a numerical exploration revealed that the given noise level does not allow any entanglement between the two test masses, if we assume that the sensing noise is cut off around 2π 1 Hz. In the case of a reduced sensing noise level with $\Omega_x = 2\pi$ 1000 Hz, which corresponds to a ratio of $\Omega_x/\Omega_F \sim 50$, it is possible to prepare an entangled state. After the preparation stage, the measurement device can be switched off, or alternatively one simply disregards the measurement record. The time evolution of the entangled state is illustrated by Fig. 5.23 for both scenarios.

5.10. Outlook

We have shown that a gravitational wave detector is suitable for studying quantum mechanical states of its macroscopic test mass mirrors. Even though the test masses in currently operating gravitational wave detectors are still far from a true minimum Heisen-

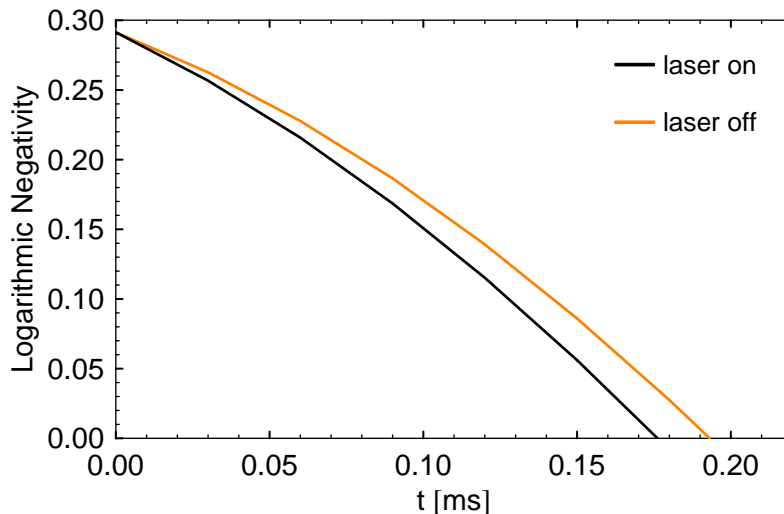


Figure 5.23.: Logarithmic negativity versus free evolution time after preparation stage for the classical noise budget introduced in Fig. 5.12 but with $\Omega_x = 2\pi$ 1000 Hz (i.e. $\Omega_x/\Omega_F = 50$) and a sensing noise cut-off around 2π 1 Hz. Measurement frequencies associated with common and differential mode: $\Omega_q^c = 2\pi$ 1550 and $\Omega_q^d = 2\pi$ 55.

berg uncertainty state and from being entangled, we are confident in the success of our proposed project because of the advance of experimental techniques: in large-scale prototypes the reduction of thermal noise is investigated by cooling down the test mass mirrors to some tenth of Kelvin [121] and there is an auspicious progress in the design of new test mass mirrors with better thermal properties [33, 34, 35, 18, 126].

Within the framework of this chapter, a complete experiment has been outlined which has three stages: preparation, evolution and verification. We have investigated the first two stages extensively: we have shown that a sub-SQL sensitivity allows us to engineer nearly pure Gaussian states of test masses with regard to a single mechanical degree of freedom. Additionally, we have extended the scope to entangled states, involving either a macroscopic and an optical part or even two macroscopic parts. The respective non-classical state survives long enough to be probed with a subsequent verification stage. This last stage, which requires a sub-Heisenberg resolution, needs to be investigated further. Such an independent stage serves as a validation for the chosen filter functions and unconditional variances, which crucially influence the outcome of the Wiener filtering procedure.

A verifiable EPR-entangled state of macroscopic test masses allows us to venture out into the speculative theory of gravity decoherence. According to Diósi's and Penrose's proposals [60, 129], the time scale beyond which quantum superpositions may become unstable is given by \hbar/E_G . According to Penrose, E_G corresponds to the mechanical work required for separating two components of the quantum superposition from each other, under the assumption that gravitation acts between them. An order-of-magnitude estimation has revealed that the Diósi-Penrose hypothesis of gravity-induced quantum state reduction is experimentally testable by means of our proposed macroscopic entanglement scheme.

6. Summary and outlook

Within the scope of this thesis two subject areas have been covered – the investigation of novel designs of interferometric gravitational wave detectors and the preparation of macroscopic quantum states. Initially, these subjects seem to be rather disjunct, but they are surprisingly related in the sense that a concrete experimental implementation involves the same device, namely a Michelson-type interferometer. Therefore a common formalism is required for an appropriate theoretical treatment, i.e. the transformation of quantum fields due to the interaction with optical components needs to be formulated. Complex optical systems can be handled by identifying interconnected elementary subsystems with well-known transfer functions. An appropriate mathematical framework is provided by Corbitt et al. in Ref. [54]. A minor extension to this formalism was introduced in Chap. 2, where a recipe for the treatment of experimental set-ups comprising three dimensions was proposed.

In Chap. 3 the optimization of gravitational wave detectors towards the detection of compact-binary inspirals was reviewed. Besides the criterion for such a narrowband optimization, a procedure was proposed which allows us to launch a more broadband operational mode. This renders the possibility of building a detector sensitive to more speculative (yet in some sense astrophysically more interesting) intermediate-mass black-hole binaries with a broad frequency range, without sacrificing sensitivity for low-mass systems, which are more certain to exist.

In Sec. 4.1 a novel class of laser interferometric gravitational wave detectors was introduced based on the injection of multiple carrier fields. A general framework was formulated, which allows us to treat a Michelson-type interferometer operated by an arbitrary number of carrier lights. This concept provides exceeding flexibility in reshaping the detector’s noise spectral density and optimizing towards specific gravitational wave sources. The ingoing carrier lights must differ at least in frequency or polarization, which allows us to separate the corresponding outgoing sideband fields at the dark port and therefore sense each one independently by a homodyne detection scheme. The output channels need to be combined in an optimal way by the implementation of an appropriate filtering procedure, derived in Sec. 4.1.

We have applied the general formalism to two different schemes, both involving two carrier lights injected into the bright port of a signal-recycling interferometer. First the *local readout* configuration (cf. Sec. 4.2) was considered, which unifies the optical-bar and the detuned signal-recycling technique. It is well-known that a rigid optical spring – present in a (blue) detuned signal-recycling interferometer – deteriorates sensitivity at frequencies below the optomechanical resonance. We have shown that sensing the central Michelson degree of freedom allows us to recover the sensitivity at low frequencies. This is based on the fact that a gravitational wave induced motion of the rigidly connected arm cavity mirrors is monitored by means of the secondary carrier light. The inherent instability of such a single optical spring system can be cured by a linear feedback control

system. We have demonstrated that the combined output is invariant with respect to the implementation of such a control scheme.

In the case of the second configuration, investigated in Sec. 4.3, the implementation of the aforementioned control system becomes obsolete. The so-called *double optical spring* scheme comprises two optical springs where each individual one, acting alone, would induce unstable dynamics. An appropriate arrangement allows us to establish an all-optical stabilization scheme. The test masses are trapped by a stable ponderomotive potential well provided by two carrier light fields whose detunings have opposite signs. Additionally, sensitivity can be significantly improved due to the increased number of degrees of freedom. For instance, the first carrier furnishes a good sensitivity in the low-frequency regime while the other gives the main contribution at high frequencies.

The sensitivity of the planned Advanced LIGO detector can be increased dramatically and without much effort by the implementation of the suggested concepts. In addition, we have proved the sustainability of the proposals by investigating them in the presence of a reduced classical noise budget. We have demonstrated that a multi-carrier configuration is much more capable than single optical spring interferometers of taking advantage of a potential future noise level. Furthermore we have verified the compatibility of the proposed schemes with other quantum non-demolition techniques, i.e. the injection of squeezed vacuum states into the dark port [39, 86, 117, 159, 158] and a variational homodyne detection scheme [39, 108, 134] were considered in Sec. 4.2.4. These explorations suggest that the presented concepts can also be regarded as candidate designs for third generation detectors. It will be important to conduct further investigations focusing in particular on implementation issues. Moreover, it should be emphasized that the employed numerical optimization routine (cf. App. A) is not suitable for detectors comprising three or even more carrier lights. The associated high dimensional parameter spaces should be explored by advanced computational tools.

In Sec. 4.4 a linear transfer function for a third-order nonlinear medium was derived rigorously within the framework of the two-photon formalism [44]. The result has been used for the investigation of a detuned signal-recycling interferometer comprising Kerr-nonlinear arm-cavities. A minor improvement in sensitivity can be achieved, but practical reasons might support the implementation of such a scheme. For instance, it is possible to mimic the noise spectral density of a detuned configuration by means of a nonlinear tuned set-up. Furthermore we have investigated a continuous wave squeezed light source realized by a monolithic Kerr-nonlinear cavity. An arbitrary amount of squeezing has been predicted for zero sideband frequency.

The long-baseline laser interferometric gravitational wave detectors can also be used to study quantum mechanical states of truly macroscopic test masses, which was investigated in Chap. 5 of this thesis. During the steady-state operation, the detector's differential mode undergoes a continuous measurement, which entails a continuous collapse of the corresponding quantum state. The recorded data can be used to construct the conditional position and momentum expectation values, which constitute the first-order moments of the Gaussian conditional quantum state. These, along with the associated second-order moments, completely characterize the conditional quantum state. For systems undergoing a continuous measurement, the evolution is conventionally described by a stochastic master equation. This well-known concept was specialized for a simple Michelson interferometer in Sec. 5.6.1. We have taken Markovian quantum noise, classical white force

and sensing noise into account. More complex systems can be treated within the framework of a new approach introduced in Sec. 5.6.2, namely the Wiener filtering method in the context of quantum mechanics. It allows us to directly determine the conditional steady-state from the experimentally accessible noise spectral densities and it can cope with multiple colored noise sources and non-Markovian dynamics. In addition to this concept an alternative state preparation scheme based upon feedback control was introduced in Sec. 5.7. An optimal feedback controller has been derived which minimizes the uncertainty for a general linear measurement process. Furthermore it has been shown that, even in the absence of classical noise, a pure quantum state is not always achievable via feedback.

In Sec. 5.8 we applied the aforementioned techniques to systems comprising non-Markovian noise. In the first instance we considered the conditional quantum state of a test mass inside a finite-bandwidth system in Sec. 5.8.1. It has been demonstrated that even a quantum noise limited configuration does not allow the preparation of a minimum Heisenberg uncertainty state. This is due to the fact that the cavity mode and the test mass form a composite two-mode Gaussian system which exhibits entanglement. It has been shown that this optomechanical entanglement can persist, even if the total classical noise level exceeds the standard quantum limit for all frequencies (cf. Sec. 5.8.4). After the preparation stage, this quantum state survives long enough to be probed in a subsequent verification stage. In addition, a comparison between unconditionally and conditionally generated optomechanical entanglement has been carried out, based on the detuned small-scale device investigated by Vitali et al. [161] in Ref. [161]. It has turned out that the conditional state preparation scheme allows us to increase the amount as well as the robustness of the entangled state.

In Sec. 5.8 we pointed out that the purity of a conditional quantum state of macroscopic test masses can benefit from introducing an optical (anti) spring. This has been verified numerically for the quantum noise limited regime. Furthermore we have optimized the uncertainty of the differential mode of the planned Advanced LIGO gravitational wave detector in the presence of pre-estimated realistic decoherence processes. It has been confirmed that only a moderately reduced classical noise budget allows us to prepare a nearly pure quantum state of the mechanical mode under consideration.

Entanglement can be regarded as the furthest and most radical departure of quantum mechanics from traditional classical physics. It is therefore of particular importance to demonstrate this aspect of quantum mechanics for bipartite systems comprising two macroscopic parts. We have proposed a Michelson interferometer with homodyne detections at both output ports as the basis of such a demonstration. In the first instance, we restricted ourselves to a Markovian measurement process which approves a time domain simulation by means of the stochastic master equation, as conducted in Sec. 5.9. Furthermore we have found a close relation between the generation of entanglement and the standard quantum limit for a free mass. In this respect, we note that our results for Markovian systems only depend on the ratio between the various noise contributions and the standard quantum limit, and therefore directly carry over to systems of different scales. Such a scaling law is not available in the case of a colored classical noise budget, considered at the end of Sec. 5.9. We have focused on a realistic classical noise floor of a future interferometric gravitational wave detector, for which we have investigated, *inter alia*, the survival time of an entangled state.

Further investigations should be carried out aiming at the development of refined experimental techniques which meet the specifications outlined within the framework of this thesis. From a theoretical point of view, it is demanding to bring other well-established quantum ambiguities into the macroscopic domain. For instance a framework for teleporting quantum states between two coherently operating interferometers should be elaborated.

The detection of gravitational waves and the preparation of macroscopic quantum states are auspicious and rapidly evolving fields of research. It would be a great privilege for me if this work were to contribute a small piece to the giant puzzle.

A. Program codes

Wiener Filter

The following MATHEMATICA v5.2 code represents a numerical implementation of the Wiener filtering method introduced in Sec. 5.6.2. The package calculates the second-order moments as well as the purity of the quantum state for a given set of numerical spectral densities.

```
1 (* ::Package:: *)
2
3 Cleaner::usage =
4 "Cleaner[z1,p1,n] compares lists z1, p1 and removes identical
5 elements, works with accuracy n"
6
7 rootlister::usage =
8 "rootlister[f,x,n] lists roots of function f, works with accuracy n"
9
10 multirootlister::usage =
11 "multirootlister[slist, x, n] lists roots of functions collected in
12 slist, works with accuracy n"
13
14 vuc::usage =
15 "vuc[sn,sd,sz,sp,spp,x] calculates unconditional second-order
16 moments; sn=numerator of SD, sd=denominator of SD,
17 sz=zeros of SD, sp=poles of SD, spp=poles of SD in LHP"
18
19 vinfo::usage =
20 "vinfo[s1overphimpp,s2overphimpp,coeff1overphimpp,coeff2overphimpp,x]
21 calculates conditional part of second-order moments"
22
23 VarGen::usage =
24 "VarGen[varlist,vallist,outlist,SYX,SXY,SPY,SXX,SPP,x,n,opt:
25 showout,opt:time,opt:saver]
26 prints conditional purity of quantum state
27  $(VXX*VPP-VXP^2)/(\hbar^2/4)$  and writes purity as well as
28 second-order moments into outlist.
29 SYX,SXY,SPY,SXX,SPP are numerical spectral densities
30 depending on x and variables summarized in
31 varlist. Values for variables in varlist are taken from
32 vallist. Options: output can be suppressed by showout=0;
33 predictive wiener filtering for non-zero time;
34 saves outlist in intervals specified by saver,
35 works with accuracy n"
36
37 Begin["WienerCalculator["]
38
```

```

39 (* Definition of auxiliary functions *)
40
41 Cleaner[z1_, p1_, n_] :=
42 Module[{is = {}, z = z1, p = p1},
43   While[True, {is =
44     Intersection[Ceiling[N[p, n] 10^(3 n/4)],
45       Ceiling[N[z, n] 10^(3 n/4)]]; If[is == {}, Break[]];
46     p = Drop[p, Position[Ceiling[N[p, n] 10^(3 n/4)],
47       is[[1]]][[1]]];
48     z = Drop[z, Position[Ceiling[N[z, n] 10^(3 n/4)],
49       is[[1]]][[1]]]};
50   Return[{z, p}]
51
52 rootlister[f_, x_, n_] :=
53 Module[{roots = NSolve[f == 0, x, n]},
54   Return[If[Length[Flatten[roots]] == 0, {}, x /. roots]]
55
56 multirootlister[slist_, x_, n_] :=
57 Module[{multilist = {}},
58   For[i = 1, i <= Length[slist], i++,
59     AppendTo[multilist, rootlister[slist[[i]], x, n]]];
60   Return[multilist]
61
62 vuc[sn_, sd_, sz_, sp_, spp_, x_] :=
63   Re[1/2 I CoefficientList[sn, x][[-1]]/CoefficientList[sd, x][[-1]]
64     Sum[Product[(spp[[i]] - sz)[[j]], {j, Length[sz]}]
65       /Product[(spp[[i]] - DeleteCases[sp, spp[[i]])][[j]]
66         , {j, Length[sp] - Count[sp, spp[[i]]}], {i, Length[spp]}]]
67
68 vinfo[s1overphimpp_, s2overphimpp_, coeff1overphimpp_,
69   coeff2overphimpp_, x_] :=
70   Re[1/2 I (Sum[Conjugate[coeff2overphimpp[[i]] coeff1overphimpp[[j]]
71     / (Conjugate[s2overphimpp[[i]] - s1overphimpp[[j]])]
72     , {i, Length[coeff2overphimpp]}, {j, Length[coeff1overphimpp]}])]
73
74 (* Wiener calculator *)
75
76 VarGen[varlist_, vallist_, outlist_, SY_, SXY_, SPY_, SXX_,
77   SPP_, x_, n_, showout_: 1, a_: 0, saver_: 0] :=
78 For[j = 1, j <= Length[vallist], {If[j == 1, values = {}];
79   varlist = vallist[[j]];
80   s2gether = Together[{SY_, SXY_, SPY_, SXX_, SPP}];
81   {SYn, SXYn, SPYn, SXXn, SPPn} = Numerator[s2gether];
82   {SYd, SXYd, SPYd, SXXd, SPPd} = Denominator[s2gether];
83   phimz = Select[rootlister[SYn, x, n], Im[Ceiling[# 10^n]] > 0 &];
84   phimp = Select[rootlister[SYd, x, n], Im[Ceiling[# 10^n]] > 0 &];
85   phicoeff = (CoefficientList[SYd, x][[-1]]/
86     CoefficientList[SYn, x][[-1]])^(1/2);
87   {SXYz, SPYz, SXXz, SPPz} =
88     multirootlister[{SXYn, SPYn, SXXn, SPPn}, x, n];
89   {SXYp, SPYp, SXXp, SPPp} =
90     multirootlister[{SXYd, SPYd, SXXd, SPPd}, x, n];

```

```

91  SXYoverphimz = Join[SXYz, phimp];
92  SXYoverphimp = Join[SXYp, phimz];
93  {SXYoverphimz, SXYoverphimp} =
94  Cleaner[SXYoverphimz, SXYoverphimp, 3 n/4];
95  SXYoverphimpp = Select[SXYoverphimp, Im[Ceiling[# 10^n]] < 0 &];
96  CoeffSXYoverphimpp =
97  phicoeff CoefficientList[SXYn, x][[-1]]
98  /CoefficientList[SXYd, x][[-1]]
99  Table[Exp[-I SXYoverphimpp[[i]] a] Product[(SXYoverphimpp[[i]]-
100  SXYoverphimz)[[j]], {j, Length[SXYoverphimz]}/
101  Product[(SXYoverphimpp[[i]] -
102  DeleteCases[SXYoverphimp, SXYoverphimpp[[i]]][[j]], {j,
103  Length[SXYoverphimp] - 1}], {i, Length[SXYoverphimpp]};
104  SPYoverphimz = Join[SPYz, phimp];
105  SPYoverphimp = Join[SPYp, phimz];
106  {SPYoverphimz, SPYoverphimp} =
107  Cleaner[SPYoverphimz, SPYoverphimp, 3 n/4];
108  SPYoverphimpp = Select[SPYoverphimp, Im[Ceiling[# 10^n]] < 0 &];
109  CoeffSPYoverphimpp =
110  phicoeff CoefficientList[SPYn, x][[-1]]/
111  CoefficientList[SPYd, x][[-1]]
112  Table[Exp[-I SPYoverphimpp[[i]] a] Product[(SPYoverphimpp[[i]]-
113  SPYoverphimz)[[j]], {j, Length[SPYoverphimz]}/
114  Product[(SPYoverphimpp[[i]] -
115  DeleteCases[SPYoverphimp, SPYoverphimpp[[i]]][[j]], {j,
116  Length[SPYoverphimp] - 1}], {i, Length[SPYoverphimpp]};
117  {SXXp, SXXz} = Cleaner[SXXp, SXXz, 3 n/4];
118  SXXpp = Select[SXXp, Im[Ceiling[# 10^n]] > 0 &];
119  {SPPp, SPPz} = Cleaner[SPPp, SPPz, 3 n/4];
120  SPPpp = Select[SPPp, Im[Ceiling[# 10^n]] > 0 &];
121  VXX=vuc[SXXn, SXXd, SXXz, SXXp, SXXpp, x]-vinfo[SXYoverphimpp,
122  SXYoverphimpp, CoeffSXYoverphimpp, CoeffSXYoverphimpp, x];
123  VPP=vuc[SPPn, SPPd, SPPz, SPPp, SPPpp, x]-vinfo[SPYoverphimpp,
124  SPYoverphimpp, CoeffSPYoverphimpp, CoeffSPYoverphimpp, x];
125  VXP=-vinfo[SXYoverphimpp, SPYoverphimpp, CoeffSXYoverphimpp, \
126  CoeffSPYoverphimpp, x];
127  If[showout == 1,
128  Print[Flatten[{varlist,
129  N[(VXX VPP - VXP^2)/((1.054572 10^-34)^2/4), 20]}]]];
130  AppendTo[values,
131  Flatten[{varlist, VXX VPP - VXP^2, VXX, VPP, VXP}]];
132  If[saver != 0 && Mod[j, saver] == 0, {Print[j],
133  Export["c:\\outlist" <> ToString[j] <> ".txt", N[values, 20],
134  "Table"], values = {}}];
135  If[j == Length[vallist], outlist = values]; j++
136
137 End[]

```

Interferometer optimization

The MATLAB simulation code furnishes a narrowband optimization (cf. Tab. 2.1) of the Advanced LIGO [1] gravitational wave detector. For each point in the bandwidth-detuning (λ, ϵ) plane we optimize the detection angle ζ and the result is stored in a file. The generated output has been used to obtain the contour plot shown in Fig. 3.1. The optimization of various interferometer designs can be accomplished in a similar manner. Note that the usual classical noise budget pre-estimated by the simulation tool *Bench* [2] is used.

```

1 %%%%%%%%%%%%%%%%%%%%%%%%%%%%%%%%%%%%%%%%%%%%%%%%%%%%%%%%%%%%%%%%%%%%%%%%%
2 %%%%%%%%%%%%%%%%%%%%%%%%%%%%%%%%%%%%%%%%%%%%%%%%%%%%%%%%%%%%%%%%%%%%%%%%% Optimization of Advanced LIGO %%%%%%%%%%%%%%%%%%%%%%%%%%%%%%%%%%%%%%%%%%%%%%%%%%%%%%%%%%%%%%%%%%%%%%%%%
3 %%%%%%%%%%%%%%%%%%%%%%%%%%%%%%%%%%%%%%%%%%%%%%%%%%%%%%%%%%%%%%%%%%%%%%%%%
4 clear;
5 format long g
6
7 %Specify output file
8 savefile1 = 'D:\matlab\advligodata.txt';
9
10 %Initialize the data vectors
11 datalist1=[];
12 datalist2=[];
13 maxdist=[];
14
15 %Initialize counter
16 counter=1;
17
18 %%%%%%%%%%%%%%%%%%%%%%%%%%%%%%%%%%%%%%%%%%%%%%%%%%%%%%%%%%%%%%%%%%%%%%%%%
19
20 %Planck constant
21 hbar=1.05457e-34;
22 %Speed of light
23 c=299792458;
24 %A distance of one million parsecs
25 Mpc=365.2422*24*60*60*299792458*3.26*10^6;
26 %Gravitational constant
27 G=6.6742e-11;
28 %solar mass
29 solarmass=1.9891e30;
30
31 %%%%%%%%%%%%%%%%%%%%%%%%%%%%%%%%%%%%%%%%%%%%%%%%%%%%%%%%%%%%%%%%%%%%%%%%%
32
33 %Integration starts at 7 Hz (seismic cut-off)
34 fmin=log10(7);
35 %Steps for integration
36 steps=500;
37
38 %%%%%%%%%%%%%%%%%%%%%%%%%%%%%%%%%%%%%%%%%%%%%%%%%%%%%%%%%%%%%%%%%%%%%%%%%
39
40 %Mass of single mirror
41 m=40;
42 %Arm length

```

```

95 %Total noise
96 SN=L.^2.*(coatB.^2+gra.^2+seisB.^2+suspB.^2);
97 %Measurement strength
98 thetaa=2.*sqrt(2).*sqrt(c.^(-1).*L.^(-1).*omega0.*Pa);
99
100 %%%%%%%%%%%%%%%%%%%%%%%%%%%%%%%%%%%%%%%%%%%%%%%%%%%%%%%%%%%%%%%%%%%%%%%%%
101
102 for epsilon1=4:stepsepsilon:320
103 for lambda1=0:stepslambda:600
104
105 epsilon=2.*pi.*epsilon1;
106 lambda=2.*pi.*lambda1;
107
108 %Mechanical susceptibility
109 RXX=(-1/2).*f.^(-2).*m.^(-1).*pi.^(-2);
110 %Optical transfer function amplitude quadrature
111 RY1Fa=2.^(-1/2).*lambda.*(sqrt(-1).*epsilon+(-1).*lambda...
112     +2.*f.*pi).^(-1).*sqrt(-1).*epsilon+lambda+2.*f.*pi)...
113     .^(-1).*sqrt(epsilon.*hbar.^(-1).*thetaa.^2);
114 %Optical transfer function phase quadrature
115 RY2Fa=(-1).*2.^(-1/2).*epsilon+(sqrt(-1)*(-2)).*f.*pi)...
116     .*(sqrt(-1).*epsilon+(-1).*lambda+2.*f.*pi).^(-1)...
117     .*(sqrt(-1).*epsilon+lambda+2.*f.*pi).^(-1)...
118     -1).*sqrt(epsilon.*hbar.^(-1).*thetaa.^2);
119 %Optical spring
120 RFFa=(1/4).*lambda.*(sqrt(-1).*epsilon+(-1).*lambda+...
121     2.*f.*pi).^(-1).*sqrt(-1).*epsilon+lambda+2.*f.*pi)...
122     .^(-1).*thetaa.^2;
123 %auxiliary function amplitude quadrature
124 y1a=(sqrt(-1).*epsilon+(-1).*lambda+2.*f.*pi).^(-1)...
125     .*(sqrt(-1).*epsilon+lambda+2.*f.*pi).^(-1)...
126     .*((-1).*epsilon.^2+lambda.^2+(-4).*f.^2.*...
127     pi.^2);
128 %auxiliary function phase quadrature
129 y2a=2.*epsilon.*lambda.*(sqrt(-1).*epsilon+(-1)...
130     .*lambda+2.*f.*pi).^(-1).*sqrt(-1).*epsilon...
131     +lambda+2.*f.*pi).^(-1);
132
133 for zetaa=0:stepszeta:1
134     zetaa=pi*zetaa;
135
136 %Transfer of amplitude quadrature
137 a2outa1=(2.*hbar.*RXX.*(1+(-2).*RFFa.*RXX).^(-1)...
138     .*RY2Fa.^2+(-1).*y2a).*cos(zetaa)+(2.*hbar...
139     .*RXX.*(1+(-2).*RFFa.*RXX).^(-1).*RY1Fa.*...
140     RY2Fa+y1a).*sin(zetaa);
141 %Transfer of phase quadrature
142 a2outa2=(2.*hbar.*RXX.*(1+(-2).*RFFa.*RXX).^(-1)...
143     .*RY1Fa.*RY2Fa+y1a).*cos(zetaa)+(2.*hbar.*RXX...
144     .*1+(-2).*RFFa.*RXX).^(-1).*RY1Fa.^2+y2a).*sin(zetaa);
145 %Transfer of classical noise
146 a2outN=(1+(-2).*RFFa.*RXX).^(-1).*RY2Fa.*cos(zetaa)...

```



```

147     +RY1Fa.*sin(zetaa));
148 %Transfer of signal
149 a2outh=(-1).*L.*((-1)+2.*RFFa.*RXX).^(-1).*(RY2Fa ...
150     .*cos(zetaa)+RY1Fa.*sin(zetaa));
151
152 %Spectral density: classical noise
153 Na=SN.*(a2outN.*conj(a2outN));
154
155 %Spectral density: quantum noise
156 na=a2outa1.*conj(a2outa1)+a2outa2.*conj(a2outa2);
157
158 %Spectral density: signal
159 sa=a2outh.*conj(a2outh);
160
161 %Final noise spectral density
162 Sopt=sa./(na+Na);
163
164 %%%%%%%%%%%%%%%%%%%%%%%%%%%%%%%%%%%%%%%%%%%%%%%%%%%%%%%%%%%%%%%%%%%%%%%%%
165
166 %Integration
167
168 intopt=0;
169
170 for n = npart:steps-1
171     intopt=intopt+(0.5*(Sopt(n+1)*(f(n+1))(-7/3)-Sopt(n)...
172         *(f(n))(-7/3))+Sopt(n)*(f(n))(-7/3)*(f(n+1)-f(n)));
173 end
174
175 intpart=intopt;
176
177 for n = 1:npart-1
178     intopt=intopt+(0.5*(Sopt(n+1)*(f(n+1))(-7/3)-Sopt(n)...
179         *(f(n))(-7/3))+Sopt(n)*(f(n))(-7/3)*(f(n+1)-f(n)));
180 end
181
182 distopt=grav*sqrt(intopt)/Mpc;
183 distpart=grav*sqrt(intpart)/Mpc;
184
185 %%%%%%%%%%%%%%%%%%%%%%%%%%%%%%%%%%%%%%%%%%%%%%%%%%%%%%%%%%%%%%%%%%%%%%%%%
186
187 %Store data
188 maxdist=[maxdist; [epsilon lambdaa zetaa distopt]];
189
190 %zeta end
191 end
192
193 %Sort list with respect to detectable distance
194 maxdist1=sortrows(maxdist,4);
195 %Select maximum
196 maximum1=maxdist1(length(maxdist1(:,4)),:);
197 %Reset data vector
198 maxdist=[];

```

```
199
200 %Collect Maxima
201 datalist1=[datalist1; maximum1];
202
203 %lambda end
204 end
205
206 datalist2=[datalist2; transpose(datalist1(:,4))];
207
208 %Create and save file
209 if exist(savefile1,'file')
210 save(savefile1,'datalist2','-append','-ASCII');
211 else
212 save(savefile1,'datalist2','-ASCII');
213 end
214
215 %Reset data vectors
216 datalist1=[];
217 datalist2=[];
218
219 %Counter
220 counter=counter+1;
221
222 %epsilon end
223 end
```

B. Promotion for conditional measurement

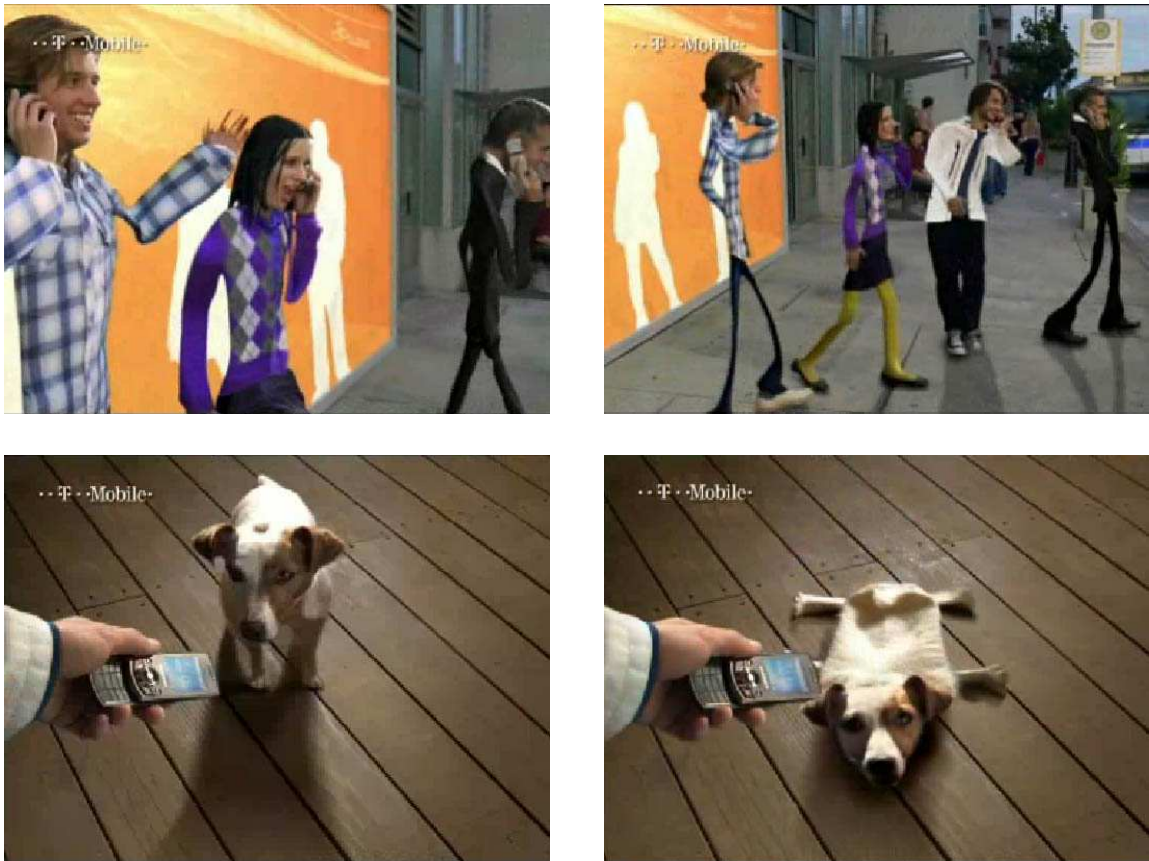


Figure B.1.: Human beings (upper panel) and dog (lower panel) undergoing a conditional measurement. (By courtesy of Telemaz Commercials GmbH)

Cellular wireless networks cover more than 200 countries worldwide and more than 80% of the world's population have access to this relatively new technology. Mobile phones are widely used in public and hence it can happen by accident that we listen to somebody (person A) answering a phone call. Usually the conversation begins with a statement regarding the actual location, e.g. "I'm close to the tram station Schneiderberg". Some highly advanced network may allow person A to submit a very accurate description of the position to a distant person B within a short amount of time. There is a certain information flow which entails a reduction of the entropy of the system under consideration, namely person A answering the phone call. Her or his wave function progressively collapses due to the measurement, which can result in a highly position squeezed state as illustrated by Fig. B.1. Note that people tend to focus on reporting their location while

they discard information about their actual speed. This gives reason to the observation of a position squeezed state. It is well-known that people move randomly, i.e. they perform a random walk, while using a mobile phone. Possible interactions with different people can entail a complex trajectory. Nevertheless, person A can update her or his position continuously, since mobile phone calls have become cheap over the last years. The observing person B can therefore continuously track the motion of person A. After some time, person B decides to hang up and hence the information flow suddenly stops. Person B is still able to predict the motion of person A, but the accuracy decays with time. During and after the phone call, person B uses certain properties of person A, e.g. her or his character, as well as known environmental influences for obtaining an optimal estimate of position and momentum. This is an essential feature of a conditional measurement scheme discussed in Sec. 5.6

It should be emphasized that the above consideration, i.e. App. B, is not part of the scientific content of this thesis.

Bibliography

- [1] <http://www.ligo.caltech.edu/advLIGO>.
- [2] <http://www.ligo.mit.edu/bench/bench.html>.
- [3] B. Abbott et al. First upper limits from LIGO on gravitational wave bursts. *Phys. Rev. D*, 69:102001, 2004.
- [4] B. Abbott et al. Upper limits from the LIGO and TAMA detectors on the rate of gravitational-wave bursts. *Phys. Rev. D*, 72:122004, 2005.
- [5] B. Abbott et al. Search for gravitational-wave bursts in LIGO data from the fourth science run. *Classical and Quantum Gravity*, 24:5343, 2007.
- [6] B. Abbott et al. Observation of a kilogram-scale oscillator near its quantum ground state. *submitted to Nature*, 2008.
- [7] G. Adesso, A. Serafini, and F. Illuminati. Determination of continuous variable entanglement by purity measurements. *Phys. Rev. Lett.*, 92:087901, 2004.
- [8] R. Adhikari. *private communication*, 2007.
- [9] M. Ando. Stable operation of a 300-m laser interferometer with sufficient sensitivity to detect gravitational-wave events within our galaxy.
- [10] A. Aspect, J. Dalibard, and G. Roger. Experimental test of Bell's inequalities using time-varying analyzers. *Phys. Rev. Lett.*, 49:1804, 1982.
- [11] P. Aufmuth and K. Danzmann. Gravitational wave detectors. *New J. Phys.*, 7:202, 2005.
- [12] A. Barchielli. Stochastic differential equations and a posteriori states in quantum mechanics. *Int. J. Theor. Phys.*, 32:2221, 1992.
- [13] J. S. Bell. On the Einstein-Podolsky-Rosen paradox. *Physics*, 1:195, 1964.
- [14] J. S. Bell. *Speakable and Unspeakable in Quantum Mechanics (Collected Papers on Quantum Philosophy)*. Cambridge University Press, 1988.
- [15] T. Beth and G. Leuchs, editors. *Quantum Information Processing*. Wiley-VCH, 2005.
- [16] D. G. Blair, editor. *The Detection of Gravitational Waves*. Cambridge University Press, 2005.
- [17] N. Bloembergen. *Nonlinear Optics*. World Scientific Publishing Company, 4th edition, 1996.

-
- [18] M. Bondarescu and K. S. Thorne. New family of light beams and mirror shapes for future LIGO interferometers. *Phys. Rev. D*, 74:082003, 2006.
- [19] R. S. Bondurant and J. H. Shapiro. Squeezed states in phase-sensing interferometers. *Phys. Rev. D*, 30:2548, 1984.
- [20] W. P. Bowen, R. Schnabel, P. K. Lam, and T. C. Ralph. Experimental investigation of criteria for continuous variable entanglement. *Phys. Rev. Lett.*, 90:043601, 2003.
- [21] W. P. Bowen, R. Schnabel, P. K. Lam, and T. C. Ralph. Experimental characterization of continuous-variable entanglement. *Phys. Rev. A*, 69:012304, 2004.
- [22] R. W. Boyd. *Nonlinear Optics, Third Edition*. Academic Press, 3rd edition, 2008.
- [23] V. B. Braginsky. *JETP*, 26:831, 1968.
- [24] V. B. Braginsky, M. L. Gorodetsky, F. Y. Khalili, A. B. Matsko, K. S. Thorne, and S. P. Vyatchanin. Noise in gravitational-wave detectors and other classical-force measurements is not influenced by test-mass quantization. *Phys. Rev. D*, 67:082001, 2003.
- [25] V. B. Braginsky, M. L. Gorodetsky, and F. Ya. Khalili. Optical bars in gravitational wave antennas. *Phys. Lett. A*, 232:340, 1997.
- [26] V. B. Braginsky and F. Y. Khalili. Low noise rigidity in quantum measurements. *Phys. Lett. A*, 257:241, 1999.
- [27] V. B. Braginsky and F. Y. Khalili. *Quantum Measurement*. Cambridge University Press, 1999.
- [28] V. B. Braginsky, S. E. Strigin, and S. P. Vyatchanin. Parametric oscillatory instability in Fabry-Perot interferometer. *Phys. Lett. A*, 287:331, 2001.
- [29] V. B. Braginsky, S. E. Strigin, and S. P. Vyatchanin. Analysis of parametric oscillatory instability in power recycled LIGO interferometer. *Phys. Lett. A*, 305:111, 2002.
- [30] S. L. Braunstein and H. J. Kimble. Teleportation of continuous quantum variables. *Phys. Rev. Lett.*, 80:869, 1998.
- [31] S. L. Braunstein and P. v. Loock. Quantum information with continuous variables. *Rev. Mod. Phys.*, 77:513, 2005.
- [32] O. P. Bruno and F. Reitich. Maxwell equations in a nonlinear Kerr medium. *Proceedings: Mathematical and Physical Sciences*, 447:65, 1994.
- [33] A. Bunkowski, O. Burmeister, P. Beyersdorf, K. Danzmann, R. Schnabel, T. Clausnitzer, E.-B. Kley, and A. Tünnermann. Low-loss grating for coupling to a high-finesse cavity. *Opt. Lett.*, 29(20):2342, 2004.
- [34] A. Bunkowski, O. Burmeister, K. Danzmann, and R. Schnabel. Input-output relations for a three-port grating coupled fabry-perot cavity. *Opt. Lett.*, 30(10):1183, 2005.

-
- [35] A. Bunkowski, O. Burmeister, D. Friedrich, K. Danzmann, and R. Schnabel. High reflectivity grating waveguide coatings for 1064 nm. *Class. Quantum Grav.*, 23:7297, 2006.
- [36] A. Buonanno and Y. Chen. Quantum noise in second generation, signal-recycled laser interferometric gravitational-wave detectors. *Phys. Rev. D*, 64:042006, 2001.
- [37] A. Buonanno and Y. Chen. Signal recycled laser-interferometer gravitational-wave detectors as optical springs. *Phys. Rev. D*, 65:042001, 2002.
- [38] A. Buonanno and Y. Chen. Scaling law in signal recycled laser-interferometer gravitational-wave detectors. *Phys. Rev. D*, 67:062002, 2003.
- [39] A. Buonanno and Y. Chen. Improving the sensitivity to gravitational-wave sources by modifying the input-output optics of advanced interferometers. *Phys. Rev. D*, 69:102004, 2004.
- [40] A. Buonanno, Y. Chen, and N. Mavalvala. Quantum noise in laser-interferometric gravitational-wave detectors with a heterodyne readout scheme. *Phys. Rev. D*, 67:122005, 2003.
- [41] A. Buonanno and T. Damour. Effective one-body approach to general relativistic two-body dynamics. *Phys. Rev. D*, 59:084006, 1999.
- [42] P. N. Butcher and D. Cotter. *The Elements of Nonlinear Optics*. Cambridge University Press, 1991.
- [43] C. M. Caves. Quantum-mechanical noise in an interferometer. *Phys. Rev. D*, 23:1693, 1981.
- [44] C. M. Caves and B. L. Schumaker. New formalism for two-photon quantum optics. *Phys. Rev. A*, 31:3068 & 3093, 1985.
- [45] C. M. Caves, K. S. Thorne, R. W. Drever, V. D. Sandberg, and M. Zimmermann. On the measurement of a weak classical force coupled to a quantum-mechanical oscillator: I. issues of principle. *Rev. Mod. Phys.*, 52:341, 1980.
- [46] Y. Chen. *et al., in preparation*, 2008.
- [47] Y. Chen and J. Harms. *private communication*, 2005.
- [48] Y. Chen, H. Mueller-Ebhardt, and K. Somiya. *private communication*, 2006.
- [49] P. F. Cohadon, A. Heidmann, and M. Pinard. Cooling of a mirror by radiation pressure. *Phys. Rev. Lett.*, 83:3174, 1999.
- [50] M. J. Collett and C. W. Gardiner. Squeezing of intracavity and traveling-wave light fields produced in parametric amplification. *Phys. Rev. A*, 30:1386, 1984.
- [51] M. J. Collett and D. F. Walls. Squeezing spectra for nonlinear optical systems. *Phys. Rev. A*, 32:2887, 1985.

-
- [52] T. Corbitt, Y. Chen, E. Innerhofer, H. Mueller-Ebhardt, D. Ottaway, H. Rehbein, D. Sigg, S. Whitcomb, C. Wipf, and N. Mavalvala. An all-optical trap for a gram-scale mirror. *Phys. Rev. Lett.*, 98:150802, 2007.
- [53] T. Corbitt, Y. Chen, F. Khalili, D. Ottaway, S. Vyatchanin, S. Whitcomb, and N. Mavalvala. Squeezed-state source using radiation-pressure-induced rigidity. *Phys. Rev. A*, 73:023801, 2006.
- [54] T. Corbitt, Y. Chen, and N. Mavalvala. Mathematical framework for simulation of quantum fields in complex interferometers using the two-photon formalism. *Phys. Rev. A*, 72:013818, 2005.
- [55] J.-M. Courty, A. Heidmann, and M. Pinarid. Back-action cancellation in interferometers by quantum locking. *Europhys. Lett.*, 63:226, 2003.
- [56] J. M. Courty, A. Heidmann, and M. Pinarid. Quantum locking of mirrors in interferometers. *Phys. Rev. Lett.*, 90:083601, 2003.
- [57] T. Damour, B. R. Iyer, and B. S. Sathyaprakash. Frequency-domain p-approximant filters for time-truncated inspiral gravitational wave signals from compact binaries. *Phys. Rev. D*, 62:084036, 2000.
- [58] S. L. Danilishin, H. Mueller-Ebhardt, H. Rehbein, K. Somiya, R. Schnabel, K. Danzmann, T. Corbitt, C. Wipf, N. Mavalvala, and Y. Chen. Creation of a quantum oscillator by classical control. *arXiv:0809.2024v1 [quant-ph]*, submitted to *Phys. Rev. Lett.*
- [59] M. Davis. Factoring the spectral matrix. *IEEE Trans. Autom. Control*, 8:296, 1963.
- [60] L. Diósi. Models for universal reduction of macroscopic quantum fluctuations. *Phys. Rev. A*, 40(3):1165, 1989.
- [61] A. C. Doherty, S. M. Tan, A. S. Parkins, and D. F. Walls. State determination in continuous measurement. *Phys. Rev. A*, 60:2380, 1999.
- [62] A. Dorsel, J. D. McCullen, P. Meystre, E. Vignes, and H. Walther. Optical bistability and mirror confinement induced by radiation pressure. *Phys. Rev. Lett.*, 51:1550, 1983.
- [63] P. D. Drummond, K. Dechoum, and S. Chaturvedi. Critical quantum fluctuations in the degenerate parametric oscillator. *Phys. Rev. A*, 65:033806, 2002.
- [64] P. D. Drummond and D. F. Walls. Quantum theory of optical bistability. I:nonlinear polarisability model. *J. Phys. A: Math. Gen.*, 13:725, 1980.
- [65] L.-M. Duan, G. Giedke, J. I. Cirac, and P. Zoller. Inseparability criterion for continuous variable systems. *Phys. Rev. Lett.*, 84:2722, 2000.
- [66] S. M. Dutra and G. Nienhuis. Derivation of a Hamiltonian for photon decay in a cavity. *J. Opt. B.*, 2:584, 2000.

-
- [67] S. M. Dutra and G. Nienhuis. Quantized mode of a leaky cavity. *Phys. Rev. A*, 62:063805, 2000.
- [68] A. Einstein. Die Grundlage der allgemeinen Relativitätstheorie. *Annalen der Physik*, 354:769, 1916.
- [69] A. Einstein. Näherungsweise Integration der Feldgleichungen der Gravitation. *Sitzungsber. Preuss. Akad. Wiss. Berlin*, page 688, 1916.
- [70] A. Einstein. Über Gravitationswellen. *Sitzungsber. Preuss. Akad. Wiss. Berlin*, page 154, 1918.
- [71] A. Einstein, B. Podolsky, and N. Rosen. Can quantum-mechanical description of physical reality be considered complete? *Phys. Rev.*, 47:777, 1935.
- [72] J. Eisert and M. B. Plenio. Introduction to the basics of entanglement theory in continuous-variable systems. *Int. J. Quant. Inf.*, 1:479, 2003.
- [73] L. Di Fiore. The present status of the VIRGO central interferometer. *and VIRGO collaboration, Class. Quant. Grav.*, 19:1421, 2002.
- [74] É. É. Flanagan and S. A. Hughes. Measuring gravitational waves from binary black hole coalescences. I. signal to noise for inspiral, merger, and ringdown. *Phys. Rev. D*, 57:4535, 1998.
- [75] É. É. Flanagan and S. A. Hughes. The basics of gravitational wave theory. *New J. Phys.*, 7:204, 2005.
- [76] A. G. Fox and T. Li. Resonant modes in an optical maser. *Proc. IRE*, 48:1904, 1960.
- [77] A. G. Fox and T. Li. Resonant modes in a maser interferometer. *Bell Sys. Tech. J.*, 40:453, 1961.
- [78] A. Furusawa, J. L. Sørensen, S. L. Braunstein, C. A. Fuchs, H. J. Kimble, and E. S. Polzik. Unconditional quantum teleportation. *Science*, 282:706, 1998.
- [79] C. W. Gardiner and M. J. Collett. Input and output in damped quantum systems: Quantum stochastic differential equations and the master equation. *Phys. Rev. A*, 31:3774, 1985.
- [80] C. W. Gardiner and M. J. Collett. Input and output in damped quantum systems: Quantum stochastic differential equations and the master equation. *Phys. Rev. A*, 31(6):3761, 1985.
- [81] C. W. Gardiner and P. Zoller. *Quantum noise*. Springer-Verlag, Berlin, 3rd edition, 2004.
- [82] R. J. Glauber. Coherent and incoherent states of the radiation field. *Phys. Rev.*, 131:2766, 1963.

-
- [83] H.-S. Goan and G.J. Milburn. Dynamics of a mesoscopic charge quantum bit under continuous quantum measurement. *Phys. Rev. B*, 64:235307, 2001.
- [84] E. Gustafson, D. Shoemaker, K. Strain, and R. Weiss. LSC white paper on detector research and development. *LIGO-T990080-00-D*, 1999.
- [85] U. Hanke, Y. M. Galperin, and K. A. Chao. Charge sensitivity of a single electron transistor. *Appl. Phys. Lett.*, 65, 1994.
- [86] J. Harms, Y. Chen, S. Chelkowski, A. Franzen, H. Vahlbruch, K. Danzmann, and R. Schnabel. Squeezed-input, optical-spring, signal-recycled gravitational-wave detectors. *Phys. Rev. D*, 68:042001, 2003.
- [87] J. Harms, R. Schnabel, and K. Danzmann. Finite mass beam splitter in high power interferometers. *Phys. Rev. D*, 70:102001, 2004.
- [88] S. W. Hawking, G. F. R. Ellis, P. V. Landshoff, D. R. Nelson, D. W. Sciama, and S. Weinberg. *The Large Scale Structure of Space-Time*. Cambridge University Press, 1975.
- [89] S. W. Hawking and W. Israel, editors. *Three Hundred Years of Gravitation*. Cambridge University Press, 1989.
- [90] A. Heidmann, J.-M. Courty, and M. Pinar. Quantum locking of mirrors in interferometric measurements. *Classical and Quantum Gravity*, 21:S1053, 2004.
- [91] G. Heinzel, A. Freise, H. Grote, K. Strain, and K. Danzmann. Dual recycling for GEO 600. *Class. Quantum Grav.*, 19:1547, 2002.
- [92] K.-S. Ho, S. H. Liu, and G. S. He. *Physics of Nonlinear Optics*. World Scientific Publishing Company, 1st edition, 2000.
- [93] A. Hopkins, K. Jacobs, S. Habib, and K. Schwab. Feedback cooling of nanomechanical resonator. *Phys. Rev. B*, 68:235328, 2003.
- [94] M. Horodecki, P. Horodecki, and R. Horodecki. Two-spin-1/2 mixtures and bell's inequalities. *Phys. Lett. A*, 210:223.
- [95] S. A. Hughes. Gravitational-wave physics. *Nuc. Phys. B*.
- [96] S. A. Hughes and K. S. Thorne. Seismic gravity-gradient noise in interferometric gravitational-wave detectors. *Phys. Rev. D*, 58:122002, 1998.
- [97] R. A. Hulse and J. H. Taylor. Discovery of a pulsar in a binary system. *Astrophys. J. Lett.*, 195:L51, 1975.
- [98] A. Isar. Uncertainty, entropy and decoherence of the damped harmonic oscillator in the lindblad theory of open quantum systems. *Fortschr. Phys.*, 47:855, 1999.
- [99] J. D. Jackson. *Classical Electrodynamics*. Wiley and Sons, 1999.
- [100] K. Jacobs and P. L. Knight. Linear quantum trajectories: Applications to continuous projection measurements. *Phys. Rev. A*, 57:2301, 1998.

-
- [101] K. Jacobs and D. A. Steck. A straightforward introduction to continuous quantum measurement. *Contemp. Phys.*, 47:279, 2006.
- [102] S. J. Jones, H. M. Wiseman, and A. C. Doherty. Entanglement, Einstein-Podolsky-Rosen correlations, Bell nonlocality, and steering. *Phys. Rev. A*, 76:052116, 2007.
- [103] L. Ju, D. G. Blair, and C. Zhao. Detection of gravitational waves. *Rep. Prog. Phys.*, 63:1317, 2000.
- [104] K. Kawabe (for the LIGO collaboration). Status of LIGO. *J. Phys.: Conference Series*, 120:032003, 2008.
- [105] S. Kawamura, O. Miyakawa, and K. Somiya. Reduction of radiation pressure noise using an auxiliary interferometer in a laser interferometric gravitational wave antenna. unpublished manuscript, 2001.
- [106] F. Khalili, I. S. Kondrashov, and D. A. Simakov. Optimization of laser interferometric gravitational wave detectors for multiple source types. *in preparation*, 2008.
- [107] K. V. Kheruntsyan. Wigner function for a driven anharmonic oscillator. *J. Opt. B*, 1:225, 1999.
- [108] H. J. Kimble, Y. Levin, A. B. Matsko, K. S. Thorne, and S. P. Vyatchanin. Conversion of conventional gravitational-wave interferometers into quantum nondemolition interferometers by modifying their input and/or output optics. *Phys. Rev. D*, 65:022002, 2001.
- [109] M. Kitagawa and Y. Yamamoto. Number-phase minimum-uncertainty state with reduced number uncertainty in a Kerr nonlinear interferometer. *Phys. Rev. A*, 34:3974, 1986.
- [110] D. Kleckner and D. Bouwmeester. Sub-kelvin optical cooling of a micromechanical resonator. *Nature*, 444:75, 2006.
- [111] A. N. Korotkov. Intrinsic noise of the single-electron transistor. *Phys. Rev. B*, 49:10381, 1994.
- [112] C. K. Law. Interaction between a moving mirror and radiation pressure: A Hamiltonian formulation. *Phys. Rev. A*, 51:2537, 1995.
- [113] R. Loudon. Quantum limit on the Michelson interferometer used for gravitational-wave detection. *Phys. Rev. Lett.*, 47:815, 1981.
- [114] R. Loudon. *The Quantum Theory of Light*. Oxford University Press, USA, 3rd edition, 2000.
- [115] S. Mancini, D. Vitali, and P. Tombesi. Optomechanical cooling of a macroscopic oscillator by homodyne feedback. *Phys. Rev. Lett.*, 80:688, 1998.
- [116] J. E. Mason and P. A. Willems. Signal extraction and optical design for an advanced gravitational-wave interferometer. *Appl. Opt.*, 42:1269, 2003.

-
- [117] K. McKenzie, N. Grosse, W. P. Bowen, S. E. Whitcomb, M. B. Gray, D. E. McClelland, and P. K. Lam. Squeezing in the audio gravitational-wave detection band. *Phys. Rev. Lett.*, 93:161105, 2004.
- [118] G. J. Milburn. Classical and quantum conditional statistical dynamics. *Quantum Semiclass. Opt.*, 8:269, 1996.
- [119] C. W. Misner, K. S. Thorne, and J. A. Wheeler. *Gravitation*. tobe found, 1973.
- [120] O. Miyakawa, R. Ward, R. Adhikari, M. Evans, B. Abbott, R. Bork, D. Busby, J. Heefner, A. Ivanov, M. Smith, R. Taylor, S. Vass, A. Weinstein, M. Varvella, S. Kawamura, F. Kawazoe, S. Sakata, and C. Mow-Lowry. Measurement of optical response of a detuned resonant sideband extraction gravitational wave detector. *Phys. Rev. D*, 74:022001, 2006.
- [121] S. Miyoki, T. Uchiyama, K. Yamamoto, H. Hayakawa, K. Kasahara, H. Ishitsuka, M. Ohashi, K. Kuroda, and D. Tatsumi. Status of the clio project. *Classical and Quantum Gravity*, 21:1173, 2004.
- [122] A. Morse, W. O. Hamilton, W. W. Johnson, E. Mauceli, and M. P. McHugh. Calibration and sensitivity of resonant-mass gravitational wave detectors. *Phys. Rev. D*, 59:062002, 1999.
- [123] H. Mueller-Ebhardt. PhD thesis, *in preparation* Leibniz Universität Hannover, 2008.
- [124] H. Mueller-Ebhardt, H. Rehbein, T. Corbitt, C. Wipf, N. Mavalvala, R. Schnabel, K. Danzmann, and Y. Chen. A double optical spring ponderomotive squeezer. *in preparation*, 2008.
- [125] H. Mueller-Ebhardt, H. Rehbein, R. Schnabel, K. Danzmann, and Y. Chen. Entanglement of macroscopic test masses and the standard quantum limit in laser interferometry. *Phys. Rev. Lett.*, 100:013601, 2008.
- [126] R. O’Shaughnessy. A note on coating thermal noise for arbitrary-shaped beams. *Class. Quantum Grav.*, 23:7627, 2006.
- [127] Z. Y. Ou and L. Mandel. Violation of bell’s inequality and classical probability in a two-photon correlation experiment. *Phys. Rev. Lett.*, 61:50, 1988.
- [128] A. F. Pace, M. J. Collett, and D. F. Walls. Quantum limits in interferometric detection of gravitational radiation. *Phys. Rev. A*, 47:3173, 1993.
- [129] R. Penrose. On gravity’s role in quantum state reduction. *Gen. Rel. Grav.*, 28:581, 1996.
- [130] A. Peres. Separability criterion for density matrices. *Phys. Rev. Lett.*, 77:1413, 1996.
- [131] K. Petermann. Calculated spontaneous emission factor for double-heterostructure injection lasers with gain-induced waveguiding. *IEEE J. Quantum Electronics*, 15(7):566, 1979.

-
- [132] M. Poggio, C. L. Degen, H. J. Mamin, and D. Rugar. Feedback cooling of a cantilever's fundamental mode below 5 mK. *Phys. Rev. Lett.*, 99:017201, 2007.
- [133] V. Poor. *An introduction to signal detection and estimation*. Springer-Verlag, 1994.
- [134] P. Purdue and Y. Chen. Practical speed meter designs for quantum nondemolition gravitational-wave interferometers. *Phys. Rev. D*, 66:122004, 2002.
- [135] H. Rehbein, J. Harms, R. Schnabel, and K. Danzmann. Optical transfer functions of Kerr nonlinear cavities and interferometers. *Phys. Rev. Lett.*, 95:193001, 2005.
- [136] H. Rehbein, H. Mueller-Ebhardt, K. Somiya, C. Li, R. Schnabel, K. Danzmann, and Y. Chen. Local readout enhancement for detuned signal-recycling interferometers. *Phys. Rev. D*, 76:062002, 2007.
- [137] H. Rehbein, H. Muller-Ebhardt, K. Somiya, S. L. Danilishin, R. Schnabel, K. Danzmann, and Y. Chen. Double optical spring enhancement for gravitational-wave detectors. *Phys. Rev. D*, 78:062003, 2008.
- [138] M. D. Reid. Demonstration of the Einstein-Podolsky-Rosen paradox using nondegenerate parametric amplification. *Phys. Rev. A*, 40:913, 1989.
- [139] W. T. Reid. *Riccati Differential Equations*. Academic Press, 1972.
- [140] A. Schliesser, P. Del'Haye, N. Nooshi, K. J. Vahala, and T. J. Kippenberg. Radiation pressure cooling of a micromechanical oscillator using dynamical backaction. *Phys. Rev. Lett.*, 97:243905, 2006.
- [141] E. Schrödinger. Die gegenwärtige Situation in der Quantenmechanik. *Naturwissenschaften*, 23:807, 1935.
- [142] I. R. Senitzky. Dissipation in quantum mechanics. the harmonic oscillator. *Phys. Rev.*, 119(2):670, 1960.
- [143] A. Shnirman and G. Schön. Quantum measurements performed with a single-electron transistor. *Phys. Rev. B*, 57.
- [144] D. Shoemaker. *and The LIGO Scientific Collaboration, Nucl. Inst. and Meth. A*, 517:154, 2004.
- [145] R. Simon. Peres-horodecki separability criterion for continuous variable systems. *Phys. Rev. Lett.*, 84:2726, 2000.
- [146] R. Simon, N. Mukunda, and B. Dutta. Quantum-noise matrix for multimode systems: $U(n)$ invariance, squeezing, and normal forms. *Phys. Rev. A*, 49:1567, 1994.
- [147] K. Somiya, P. Beyersdorf, K. Arai, S. Sato, S. Kawamura, O. Miyakawa, F. Kawazoe, S. Sakata, A. Sekido, and N. Mio. Development of a frequency-detuned interferometer as a prototype experiment for next-generation gravitational-wave detectors. *Appl. Opt.*, 44:3179, 2005.

-
- [148] K. Somiya, O. Miyakawa, P. Fritschel, and R. Adhikali. Length sensing and control of AdLIGO. *LIGO-T060272-00-I*, 2006.
- [149] H. Stark and J. W. Woods. *Probability and Random Processes with Applications to Signal Processing*. Prentice Hall, 3rd edition, 2001.
- [150] E. C. G. Sudarshan. Equivalence of semiclassical and quantum mechanical descriptions of statistical light beams. *Phys. Rev. Lett.*, 10:277–, 1963.
- [151] N. Takei, H. Yonezawa, T. Aoki, and A. Furusawa. High-fidelity teleportation beyond the no-cloning limit and entanglement swapping for continuous variables. *Physical Review Letters*, 94:220502, 2005.
- [152] K. S. Thorne, R. W. P. Drever, C. M. Caves, M. Zimmermann, and V. D. Sandberg. Quantum nondemolition measurements of harmonic oscillators. *Phys. Rev. Lett.*, 40:667, 1978.
- [153] A. Thüring, R. Schnabel, H. Lück, and K. Danzmann. Detuned twin-signal-recycling for ultrahigh-precision interferometers. *Opt. Lett.*, 32:985, 2007.
- [154] U. M. Titulaer and R. J. Glauber. Correlation functions for coherent fields. *Phys. Rev.*, 140:B676, 1965.
- [155] T. Uchiyama, D. Tatsumi, T. Tomaru, M. E. Tobar, K. Kuroda, T. Suzuki, N. Sato, A. Yamamoto, T. Haruyama, and T. Shintomi. Cryogenic cooling of a sapphire mirror-suspension for interferometric gravitational wave detectors. *Phys. Lett. A*, 242:211, 1998.
- [156] T. Uchiyama, T. Tomaru, M. E. Tobar, D. Tatsumi, S. Miyoki, M. Ohashi, K. Kuroda, T. Suzuki, N. Sato, T. Haruyama, A. Yamamoto, and T. Shintomi. Mechanical quality factor of a cryogenic sapphire test mass for gravitational wave detectors. *Phys. Lett. A*, 261:5, 1999.
- [157] R. v. Handel, J. K. Stockton, and H. Mabuchi. Modelling and feedback control design for quantum state preparation. *J. Opt. B*, 7:179, 2005.
- [158] H. Vahlbruch, S. Chelkowski, B. Hage, A. Franzen, K. Danzmann, and R. Schnabel. Demonstration of a squeezed-light-enhanced power- and signal-recycled Michelson interferometer. *Phys. Rev. Lett.*, 95:211102, 2005.
- [159] H. Vahlbruch, S. Chelkowski, B. Hage, A. Franzen, K. Danzmann, and R. Schnabel. Coherent control of vacuum squeezing in the gravitational-wave detection band. *Phys. Rev. Lett.*, 97:011101, 2006.
- [160] G. Vidal and R. F. Werner. Computable measure of entanglement. *Phys. Rev. A*, 65:032314, 2002.
- [161] D. Vitali, S. Gigan, A. Ferreira, H. R. Böhm, A. Guerreiro, V. Vedral, A. Zeilinger, and M. Aspelmeyer. Optomechanical entanglement between a movable mirror and a cavity field. *Phys. Rev. Lett*, 98:030405, 2007.

- [162] D. Vitali, S. Mancini, L. Ribichini, and P. Tombesi. Mirror quiescence and high-sensitivity position measurements with feedback. *Phys. Rev. A*, 65:063803, 2002.
- [163] D. Vitali, S. Mancini, L. Ribichini, and P. Tombesi. Macroscopic mechanical oscillators at the quantum limit through optomechanical cooling. *J. Opt. Soc. Am. B*, 20:1054, 2003.
- [164] W. Vogel. Nonclassical states: An observable criterion. *Phys. Rev. Lett.*, 84:1849, 2000.
- [165] S. P. Vyatchanin and E. A. Zubova. Quantum variation measurement of a force. *Phys. Lett. A*, 201:269, 1995.
- [166] D. F. Walls and G. J. Milburn. *Quantum Optics*. Springer-Verlag, Berlin, 2nd edition, 1995.
- [167] N. Wiener. *Extrapolation, Interpolation, and Smoothing of Stationary Time Series*. The MIT Press, 1949.
- [168] E. Wigner. On the quantum correction for thermodynamic equilibrium. *Phys. Rev.*, 40:749, 1932.
- [169] B. Willke. The GEO 600 gravitational wave detector. *et al.*, *Class. Quantum Grav.*, 19:1377, 2002.
- [170] I. Wilson-Rae, N. Nooshi, W. Zwerger, and T. J. Kippenberg. Theory of ground state cooling of a mechanical oscillator using dynamical backaction. *Phys. Rev. Lett.*, 99:093901, 2007.
- [171] C. Wipf, T. Corbitt, Y. Chen, and N. Mavalvala. A route to observing ponderomotive entanglement with optically trapped mirrors. *arXiv:0803.4001v1 [quant-ph]*, 2008.
- [172] H. M. Wiseman, S. J. Jones, and A. C. Doherty. Steering, entanglement, nonlocality, and the Einstein-Podolsky-Rosen paradox. *Phys. Rev. Lett.*, 98:140402, 2007.
- [173] B. Yurke. Wideband photon counting and homodyne detection. *Phys. Rev. A*, 32:311, 1985.
- [174] W. H. Zurek, S. Habib, and J. P. Paz. Coherent states via decoherence. *Phys. Rev. Lett.*, 70:1187, 1993.

Acknowledgements

It has been a great privilege for me to work as a Ph.D. student at the Albert-Einstein-Institut in Hannover. First of all I wish to express my sincere gratitude to Prof. Karsten Danzmann and Prof. Roman Schnabel, who gave me the opportunity to work on exciting subjects of research in an excellent academic environment.

I am deeply indebted to Prof. Roman Schnabel for his continuous support, patience and encouragement throughout this work. His overwhelming enthusiasm incited me to even greater efforts.

I am particularly grateful to Prof. Yanbei Chen for his readiness to discuss science and for sharing his enormous knowledge and experience with me. I have benefited from his deep insight, his invariably correct intuitions and his constant support. He introduced me to an exceptionally talented group of colleagues, whom I would like to thank: Kentaro Somiya for his helpfulness, a lecture in control theory and enlightening discussions about science and Germany's Next Topmodel, Stefan Danilishin and Haixing Miao for fruitful, very much appreciated discussions.

I especially wish to thank my colleague and friend Helge Müller-Ebhardt for his invaluable collaboration. He was a constant source of support and understanding. Sharing an office with him was always fun!

I thank Stefan Gossler, Harald Lück and Benno Wilke for stimulating discussions about "cool" LIGO matters.

The European Graduate College on Interference and Quantum Applications encouraged me to broaden my scientific horizon beyond my actual work. I thank Prof. Eberhard Tiemann for his courtesy and his support of the College.

I thank Jan Harms for a tutorial on general relativity and for rewarding discussions.

Special thanks go to Colin Black for proofreading my thesis.

My thanks to Nadine and the two Christians, who on many critical occasions gave me support and encouragement.

I would also like to thank my parents for their unconditional love and support.



Curriculum vitae

Henning Rehbein

Address

Lüderser Weg 21
30982 Pattensen
Germany
henning.rehbein@aei.mpg.de

Personal Details

Gender: Male
Date of birth: 24th of July, 1978
Place of birth: Hannover, Germany
Citizenship: German

University Studies

09/2004 – 12/2008 Doctoral studies in Physics, University of Hannover,
Max-Planck-Institut für Gravitationsphysik
(Albert-Einstein-Institut)
05/2004 Physik-Diplom, University of Hannover,
*Optische Bistabilität und gequetschtes Licht in einem
Kerr-Interferometer*
10/1999 – 05/2004 Diploma studies in Physics, University of Hannover

Military Service

07/1998 – 04/1999 Military service

Education

07/1998 General qualification for university entrance (Abitur),
Erich-Kästner-Gymnasium Laatzen
08/1991 – 07/1998 High School (Gymnasium), Erich-Kästner-Gymnasium Laatzen
08/1985 – 07/1991 Primary School (Grundschule, Orientierungsstufe), Pattensen

Publications

2008

- S. L. Danilishin, H. Mueller-Ebhardt, H. Rehbein, K. Somiya, R. Schnabel, K. Danzmann, T. Corbitt, C. Wipf, N. Mavalvala and Y. Chen: *Creation of a quantum oscillator by classical control*, arXiv: 0809.2024v1 [quant-ph], submitted to Phys. Rev. Lett., (2008)
- H. Rehbein, H. Mueller-Ebhardt, K. Somiya, S. L. Danilishin, R. Schnabel, K. Danzmann and Y. Chen: *Double optical spring enhancement for gravitational wave detectors*, Phys. Rev. D, **78**, 062003 (2008)
- R. Schnabel, H. Mueller-Ebhardt and H. Rehbein: *Verschränkte Spiegel. Ein realisierbares Gedankenexperiment*, Physik in unserer Zeit, **39**, 234 (2008)
- H. Mueller-Ebhardt, H. Rehbein, R. Schnabel, K. Danzmann and Y. Chen: *Entanglement of Macroscopic Test Masses and the Standard Quantum Limit in Laser Interferometry*, Phys. Rev. Lett., **100**, 013601 (2008)

2007

- T. Corbitt, Y. Chen, E. Innerhofer, H. Mueller-Ebhardt, D. Ottaway, H. Rehbein, D. Sigg, S. Whitcomb, C. Wipf, and N. Mavalvala: *An all-optical trap for a gram-scale mirror*, Phys. Rev. Lett., **98**, 150802 (2007)
- H. Rehbein, H. Mueller-Ebhardt, K. Somiya, C. Li, R. Schnabel, K. Danzmann and Y. Chen: *Local readout enhancement for detuned signal-recycling interferometers*, Phys. Rev. D, **76**, 062002 (2007)

2005

- H. Rehbein, J. Harms, R. Schnabel and K. Danzmann: *Optical transfer functions of Kerr nonlinear cavities and interferometers*, Phys. Rev. Lett., **95**, 193001, (2005)